



Spin dynamics in magnetic nanoparticles

*Doctoral Thesis to obtain the degree of Philosophy Doctor
in Science and Technology*

Author: Elizabeth Martín Jefremovas

Supervisor: Luis Fernández Barquín

Department: Ciencias de la Tierra y Física de la Materia
Condensada

Date: October, 2021

Declaration

Dr. Luis Fernández Barquín, Catedrático de la Universidad de Cantabria, certifica:

Que la presente Memoria, titulada "Spin dynamics in magnetic nanoparticles" ha sido realizada, bajo su dirección, por Elizabeth Martín Jefremovas, y constituye su Tesis para optar al grado de Doctor por la Universidad de Cantabria.

Asimismo, emite su conformidad para que la presente Memoria sea depositada y se celebre, ulteriormente, la correspondiente Lectura y Defensa.

Y para que así conste, se firma en Santander, en el mes de Octubre de 2021.

Luis Fernández Barquín: _____

Abstract

This Thesis work studies the spin dynamics in ensembles of magnetic nanoparticles, where the magnetism stems from $4f$ and $3d$ orbitals. To this aim, five RCu_2 alloys with different compositions have been produced, where the Rare Earth (R) has been changed in order to scrutinise the magnetism of the resulting alloy. The studied alloys include **GdCu_2** , with no net angular moment (thus, non intrinsic magnetocrystalline anisotropy); **NdCu_2** , whose 5 crystalline electric field energy levels (doublets) are experimentally accessible by means of Inelastic Neutron Scattering; and finally **$\text{Tb}_{0.5}\text{Gd}_{0.5}\text{Cu}_2$** , **$\text{Tb}_{0.5}\text{La}_{0.5}\text{Cu}_2$** and **$\text{Tb}_{0.1}\text{Y}_{0.9}\text{Cu}_2$** , for which the *dilution* of TbCu_2 with R-ions, either magnetic or not, achieves to settle a tunable degree of magnetic disorder. All of them have been mass produced, nanoscaled via ball milling and well-characterised, using both microscopic and macroscopic experimental techniques.

Additionally to these $4f$ ensembles, the magnetic and structural properties of four different iron oxide nanoparticle ensembles (IONPs) have been investigated. The studied ensembles have encompassed the **commercial $\gamma\text{-Fe}_2\text{O}_3$ maghemite Synomag Nanoflowers (NFs)**, and the **Fe_3O_4 magnetite magnetosomes (BMs) synthesised by magnetotactic bacteria from the strain *Magnetospirillum gryphiswaldense***. Both maghemite and magnetite are considered nowadays outstanding magnetic materials candidates for biomedical applications, especially those connected to magnetic hyperthermia treatments. In this Thesis work, we have characterised the magnetic and structural properties of both Synomag NFs and BMs in great detail, and we have also compared their magnetic hyperthermia performance. Such a direct comparison between both IONPs is very useful for the technological transfer. Besides, we have gone one step beyond, by combining the (biomedical) potentialities of Rare Earth ions Gd^{3+} (contrast agent in Magnetic Resonance Imaging) and Tb^{3+} (luminescent bio-marker) with the advantages of BMs (biocompatibility, magnetic hyperthermia). This has been possible thanks to the **doping of magnetotactic bacteria with Gd^{3+} and Tb^{3+}** by the addition of GdCl_3 and TbCl_3 salts to the cell culture medium. A promising

future development is expected on the basis of this finding.

Resumen

Esta Tesis aborda el estudio de la dinámica de espín en sistemas de nanopartículas magnéticas cuyo magnetismo emerge de los orbitales $4f$ y $3d$. Con este objetivo, se han producido cinco sistemas de diferentes composiciones según RCu_2 , donde el elemento de Tierra Rara (R) ha sido variado con el fin de estudiar en detalle el magnetismo de la aleación resultante. De esta manera, se ha producido la aleación de **GdCu₂**, la cual no presenta momento angular neto (y por tanto, sin término intrínseco de anisotropía magnetocristalina); la aleación de **NdCu₂**, cuyos 5 dobletes energéticos definidos por el Campo Cristalino resultan experimentalmente accesibles por medio de Dispersión Inelástica de Neutrones; y las tres aleaciones de **Tb_{0.5}Gd_{0.5}Cu₂**, **Tb_{0.5}La_{0.5}Cu₂** y **Tb_{0.1}Y_{0.9}Cu₂**, para los que la *dilución* de TbCu₂ por medio de iones de Tierra Rara, ya sean magnéticos o no, permite alcanzar grado de desorden magnético *modificado a voluntad*. Este conjunto de aleaciones se ha nano-escalado mediante el uso de molienda mecánica y caracterizado en detalle, empleando para ello técnicas experimentales tanto microscópicas como macroscópicas.

Además de estos sistemas $4f$, se ha llevado a cabo el estudio de las propiedades magnéticas y estructurales de cuatro sistemas de nanopartículas de óxidos de hierro (IONPs). Los sistemas elegidos han sido las **Nanoflores (NF) comerciales Synomag, compuestas por maghemita, γ -Fe₂O₃**, y los **magnetosomas compuestos por magnetita, Fe₃O₄, (BMs), sintetizados por las bacterias magnetotácticas de la especie *Magnetospirillum gryphiswaldense***. Ambos óxidos de hierro, maghemita y magnetita, están llamados a ser hoy en día candidatos magnéticos prometedores para su aplicación biomédica, especialmente, para los tratamientos de hipertermia magnética. En esta Tesis se han caracterizado en gran detalle las propiedades magnéticas y estructurales de ambos Synomag NFs y BMs, además de haber comparado su rendimiento en hipertermia magnética. Esta comparación directa entre ambos candidatos es plenamente satisfactoria para conseguir una transferencia tecnológica eficiente. En este sentido, el trabajo descrito en esta Tesis pudiera constituir un importante paso adelante,

gracias a la combinación de la potencialidad (biomédica) de los iones de Tierra Rara Gd^{3+} (agente de contraste en Resonancia Magnética) y Tb^{3+} (biomarcador luminiscente) junto con las ventajas de los BMs (biocompatibilidad, hipertermia magnética), lo cual se ha logrado mediante el **dopado de las bacterias magnetotácticas con Gd^{3+} y Tb^{3+}** mediante la incorporación de sales de $GdCl_3$ y $TbCl_3$ al medio de cultivo celular. Este hito puede sentar las bases para un futuro desarrollo tecnológico.

Acknowledgements

I will begin this section by apologising, as it is going to be mainly written in Spanish. The fact that it is my mother tongue eases to get sentimental, and the vast majority of the people that are going to be mentioned are Spanish too. The rest of the Dissertation is going to be written in English, my scientific tongue, so there is nothing about to worry concerning science.

First of all, I will begin by acknowledging the Universidad de Cantabria and Gobierno de Cantabria for financial and technical support, specially, for awarding me the Concepción Arenal¹ PhD grant. This acknowledgement also holds for the technical support and access to beam time at large facilities, such as Laboratoire Léon Brillouin (LLB) at the CEA–Saclay, France, the Institut Laue–Langevin (ILL) in Grenoble, France, the Rutherford–Appleton Laboratory (ISIS), Oxford, United Kingdom, the BL22 CLAES beamline of the ALBA synchrotron, Barcelona, Spain, and the XAFS beamline of the Elettra synchrotron, Trieste, Italy.

Una vez realizada esta parte, comenzaré por agradecer a mi Director, Luis Fernández Barquín, todo el apoyo que me ha brindado. No sólo durante estos tres años, sino desde que aparecí por el Departamento, a finales de Julio de 2016, para interesarme por las Becas de Colaboración del Ministerio y la posibilidad de llevar a cabo un proyecto bajo su dirección. Te agradezco mucho lo tangible, pero especialmente, todos esos “intangibles”, que no son sino los detalles que marcan la diferencia.

A continuación, quisiera agradecerle a mi tutor, Luis Fernández Barquín. Me has dejado toda la libertad para desarrollarme como científica en este proceso formativo, y a la vez, siempre he sabido que podía contar contigo, no sólo para cuestiones puramente científicas. Tu calidad humana es de Nature para arriba.

¹Concepción Arenal was a Spanish journalist, legal expert and activist supporting feminism and the improvement of the living conditions of prisoners and social outcasts.

Aunque hayamos sido poco dados a verbalizar nuestro aprecio mutuo², a lo largo de este tiempo me has hecho el regalo más inesperado de todos, haciéndome experimentar el sentimiento de tener padre. Gracias por hacer germinar esta flor en medio de un campo en ruinas.

Quisiera agradecer también al Profesor Jesús Blanco toda su ayuda, dedicación y excelentísimo trato. El abordaje a los neutrones habría sido un naufragio sin la formación y el tiempo que me has dedicado. In the same way, I would like to express all my acknowledgement to Prof. Andreas Michels, first, for inviting me to join his group at the University of Luxembourg, for all the time he invested in teaching me about SANS, and second, for making me feeling home abroad. His kindness, as his scientific performance and dedication, are also beyond the outstanding standards. I will also acknowledge Prof. Peter Svedlindh for allowing me to join his group at the University of Uppsala to perform a PhD stay, especially, during the tough COVID times. Having the possibility to spend some time with people who are to me like Kobe Bryant or Lebron James was a really inspiring experience. Tack så mycket.

Por supuesto, me gustaría agradecer a todos los miembros del Grupo de Magnetismo y del CITIMAC (Jesús, Jose, Imanol, Luis Echandía...), y en especial, a Javi, por su ayuda en diferentes momentos de la Tesis, desde el manejo de aparatos y equipos hasta todos los papeleos y burocracias. Este equipo se completa con el Grupo de la Universidad del País Vasco, bios y físicos. Si fuera por ganas, iría uno por uno enumerandóos, pues siempre he podido contar con todos vosotros. No obstante, el espacio, a diferencia de mi gratitud, es limitado, así que, por favor, sentíos todos aludidos en estas líneas. Sí que me gustaría agradecer específicamente a las jefas, Malú, Alicia Muela y Ana, por permitirme y facilitarme siempre el acceso a vuestras dependencias, incluido el laboratorio bio, y por hacerme sentir siempre tan bien acogida. Fuera de nuestras fronteras, quisiera say thank you to Diego Alba, Françoise Damay, Philipp Bender, Shameek Vats, Mathias Bersweiler, Seda Ulusoy and Mariona Escoda i Torroella. Collaborating and sharing time with you has been an enormous pleasure.

Derivadas de estas interacciones a primeros vecinos, han surgido dos colaboraciones que traspasan, por mucho, las fronteras de la Física. Por un lado, mis compis big Henry y Camino. La vida en el infiernito ha sido mucho más cálida gracias a vosotros. Si tuviera que destacar un par de highlights del tiempo compar-

²quiero creer que algo de aprecio me has cogido, aunque sólo sea por agotamiento ☺.

tido, citarí­a ese inolvidable karaoke con Amaia Montero y Álex Ubago, junto con los martes temáticos. No obstante, sí que nos ha quedado pendiente mejorar, si es posible, la receta del fitcocho. A pesar de nuestra reticencia, Camino insistió en realizar la versión minimalista de la receta. La próxima vez nos jugamos los puestos de chef y pinches a los cocodrilos tragabolas. Por otro lado están mis beloved magterbias, Lucía Gandarias Albaina y Lourdes Marcano Prieto, con quienes no hay room escape con bici que se nos resista. Es difícil encontrar gente capaz de hacer el mundo más bonito desde tantos aspectos como lo hacéis vosotras. Qué suerte poder teneros cerquita.

Finalizo esta sección con el apartado más personal. Quizás no está bien que yo lo diga, pero tengo la enorme suerte de poder compartir vida y tiempo con gente que merecen mi más profundo agradecimiento. No voy a poder detallar a todas estas personitas tan fantásticas, así que me limitaré a enumerar unas pocas, sin perjuicio del resto. Araceli y su más que cuestionable gestión de tareas, pero brillante en la más importante de todas, compartir su corazón. Ana y los confidomingos, llevados hasta Luxemburgo. Ana Gesa, contigo, el tiempo parece detenerse entre visita y visita, pero correr sin descanso cuando estamos juntas. Gabi, infalible en gestiones de promoción y marketing, pero especialmente certera arrojando luz en los momentos más indicados. Este combo de gente maravillosa lo completan, cómo no, mis queridas ventanitas/puertitas. Puedo ser la más veterana, pero os aseguro que no dejo de aprender cada día que compartimos juntas. Con vosotras se gana la liga que de verdad importa. Mención especial para Julia Martínez González, la artista detrás de los *espiners*. Toda esta gente aquí citada tiene el don de hacer del mundo un lugar más bonito. Es un auténtico placer compartir vida con ellas. No voy a dejar fuera de esta lista a quien me ha acompañado durante un periodo muy importante de esta Tesis y de mi vida. Si algo he aprendido en este tiempo es que la nostalgia también tiene que tener su espacio. Cuánto de grande es el amor que compartimos no se explica con resúmenes, así que me limitaré a decirte que prometo cuidarlo hasta que cure bien.

Je voudrais aussi bien entendu remercier ma mère, qui non-seulement m'a aidée d'un point de vue personnel, mais aussi, du côté économique. Il est bien dommage qu'en 2021, la Science en soit toujours et encore au même point, du moins en Espagne. Merci pour ton soutien. Ces moments pendant le confinement à rédiger l'article des dilutions pendant la journée et à regarder Merlí en catalan le soir après avoir fait du sport dans le garage vont toujours faire partie de cette Thèse. J'espère pouvoir continuer à t'envoyer des cartes postales pendant longtemps.

Finally, I would like to thank you, the reader, for your time and dedication. I hope you will enjoy yourself as much as I did during the writing process.



Visual summary of some of the (non-scientific) milestones achieved during the 3 years of this Thesis work.

“El arte es todo aquello que hace que la vida pese menos. El triunfo suele disfrazarse de oro, pero componerse de fracasos. Nada de lo conseguido lo disfruté sin compartirlo. Estos catorce años sobre los escenarios me enseñaron que el éxito fue hacer de una quimera mi profesión. Que perseguir medallas y trofeos anestesian el proceso, donde pretendo vivir ahora. Que cuando persigues solamente un resultado, al alcanzarlo sólo hay vacío. Qué paradoja. Aprendí que triunfar no es algo cuantitativo y que la felicidad sólo te la regala el camino, por cansado que sea. Entiendo la música como una carrera de fondo en la que cada persona que te acompaña deja en ti una enseñanza nueva.”

Juancho Marqués. Documental “Hace un año”.

Contents

1	Introduction	1
2	Fundamentals: Theoretical background	9
2.1	Magnetic phenomena in nanoparticles	10
2.2	Interactions among the magnetic moments. RKKY indirect exchange	13
2.3	Spin dynamics: Length and time scales.	18
2.3.a	Spin Glass transitions	19
2.3.b	Ageing and memory effect phenomena.	22
2.4	Crystalline electric field. Spin waves.	23
2.4.a	Crystalline electric field	24
2.4.b	Spin waves	27
3	Experimental methods	31
3.1	Sample fabrication and preparation.	31
3.2	X-Ray techniques.	37
3.3	Neutron-scattering techniques.	42
3.3.a	Elastic neutron scattering	44
3.3.b	Inelastic neutron scattering	51
3.4	Microscopy. Transmission Electron Microscopy.	54
3.5	Magnetic measurements: Static DC and dynamic χ_{AC} regimes. . .	55
3.6	Thermodynamic properties: Specific heat measurements.	57
4	GdCu₂ magnetic nanoparticles	61
4.1	Magnetic properties	64
4.1.a	Static Magnetic Susceptibility: $M_{DC}(T, H)$	64
4.1.b	Dynamic Magnetic Susceptibility	69
4.2	Specific heat measurements	79

5	NdCu₂ magnetic nanoparticles	85
5.1	Magnetic order and disorder on NdCu ₂ nanoparticles	88
5.2	Inside the soul of the MNPs	107
5.2.a	Initial guide: Specific heat	108
5.2.b	The acid test: Inelastic Neutron Scattering	112
6	Tb_xR_{1-x}Cu₂ magnetic nanoparticles	125
6.1	Microscopic magnetic structure analysis: Neutron Diffraction	127
6.2	Magnetic characterisation	130
6.2.a	Static Magnetic Susceptibility: $M(T, H)$ characterisation	130
6.2.b	Dynamic Magnetic Susceptibility	136
6.3	Specific heat measurements	140
7	γ-Fe₂O₃ and Fe₃O₄ magnetic nanoparticles	145
7.1	Structural characterisation	150
7.2	Magnetic properties	156
7.2.a	Dynamic Magnetic Susceptibility	165
7.3	Magnetic Fluid Hyperthermia: NFs vs. Magnetosomes	172
8	Conclusions	179
A	XRD diffraction	189
B	Simulation of the $M(H)$ loops in bacteria	197
C	Surface contribution to the INS patterns: The choice of the N ratio	199

Chapter 1

Introduction

*“Tengo la nave afuera,
vamos a mi planeta”*

Daddy Yankee feat. Prince Royal

Magnetism is a very relevant discipline within the **Condensed Matter Physics and Materials research fields**. This is for sure due to the combination of both the potential technological applications, inherent to most magnetic materials, together with the attraction of the understanding of the fundamental phenomena giving rise to the macroscopic magnetic properties. Indeed, the magnetic behaviour of every magnetic material is the result of the existence of a magnetic coupling (caused by exchange interactions of a varied nature) and the role of anisotropy. Simplifying, and without aiming to be exhaustive, taking into account the most obvious magnetic coupling, known as direct exchange, it leads immediately to the Coulomb interaction and Pauli’s Exclusion Principle. Hence, it is directly connected to Quantum Physics; a *pôle d’intérêt indéniable* for any person attracted towards Physics. In a more general standpoint, every magnetic coupling is connected to the electronic structure, whose analysis constitutes actually the core of Condensed Matter physics. Furthermore, regarding the other key factor, **the magnetic anisotropy** (crystalline), this is connected to the spin orbit interaction and thus, to relativistic effects. The latter are still fascinating for the overall public, and physicists in particular. In short, from a fundamental point of view, the study of magnetic properties is related to basic physical concepts [1, 2].

Focusing on the simplest forms of static magnetic order, the **long-range ferromagnetic and antiferromagnetic couplings (large magnetic correlations lengths)** are continuously studied in new materials, yet nowadays, the trend is to

analyse complex magnetic materials that may provide relevant technical properties (multiferroics, magnetocaloric materials, skyrmions) [3, 4, 5]. In particular, the studies of materials with magnetic correlations of a length within the nanoscale has been flourishing over the last years [6, 7]. Any current conference about Magnetism is riddled with studies of skyrmionic materials, Spin Glasses, either ices or liquids, interfacial magnetism or core/shell nanoparticle ensembles¹. Moreover, not only is the community of Magnetism interested in the static arrangement within the materials, but it is also attracted to the study of the spin dynamics, being the works as well frequent currently [9, 10]. All this research is possible thanks to existence of high-performance techniques (e.g. electron energy loss spectroscopy, EELS, in high resolution transmission electron microscopes, HRTEM; angle-resolved photoemission spectroscopy, ARPES; or polarised small angle neutron scattering, to cite a few [11, 12, 13]), which are slowly becoming available for a large community of researchers in Magnetism. Notwithstanding, the phenomenal computational aid helping out in the interpretation of experimental data is the other fast development tool to consider [14].

On the other hand, in which concerns **short-range correlations**, researchers have addressed the interpretation of these giving rise to magnetic clusters, vortex states and the like, following the routes where there is some experience and availability of experimental tools. Progress within this field are made fast-paced thanks to the maturity state of Nanoscience. Indeed, the enormous room foresaw by R. Feynman has been gently filled, especially, throughout the last two decades. The fascination stemming from the mesoscopic scale is not a simple size reduction of the different materials, yet it has to do with the modifications that the main properties of a material undergo at this stage. **Each property of a material is determined by a particular correlation length**, which might be of several nanometers. A very extended strategy to study phenomena at the nanoscale is to produce ensembles of magnetic nanoparticles using a variety of routes (frequently of chemical nature [15]), as these systems provide an outstanding playground. Very frequently, the ensembles are formed by collection of quasi-spherical nanoparticles. Here, not only is the nanoparticle size responsible for the new emergent phenomena at the nanoscale, but also the combination of two different symmetry environments does play a significant role. In this way, one can distinguish between **(i) the nanoparticle core**, where the local symmetry environment is very alike to the bulk one; and **(ii) the nanoparticle surface**, with a lower symmetry and reduced coordination [16, 17, 18]. The combination of both environments in one

¹see, for example, the last ICM conference held in 2018 in San Francisco [8].

single nanoparticle may result in two different dynamics, the one ascribed to the core, and the one related to the surface. **As both spin dynamics coexist and take place at the same time**, they might generate two kinds of macroscopic behaviour, thus, giving rise to a **complex magnetic system**.

As indicated at the beginning of this Introduction, the nanometric size of these mesoscopic materials is of primer interest for applications. Advances in memory devices, spintronics and biomedical fields, to cite a few, take advantage of dealing with nano-devices, that can be implemented in chips and/or travel within the human body, getting attached to human cells [19, 20, 21]. Connected to the latter biomedical applications, it is overwhelming the huge amount of works concerning magnetic nanoparticles (MNPs) that have been devoted to Fe-oxides. The biocompatibility of these ensembles, together with their well-standardised synthesis processes, have been key to gather the attraction and efforts of the scientific community. Particularly, **there is one research line directly connected to magnetism which is aiming to employ the Fe-oxide MNPs (IONPs) for hyperthermia treatments** associated with cancer therapies [22, 23, 24]. Nevertheless, even if this is a very promising research line, there are some issues, related to the magnetic anisotropy of the ensembles, that are still open, and require a deeper understanding of the magnetic properties. More precisely, **a good understanding on the connection between the magnetic anisotropy, the particle size and how are the magnetic properties affected by the size reduction to the nanoscale merits more attention**. The vast majority of the research on these IONPs is carried out on ensembles produced by chemical routes [15]. However, some groups are trying to follow an alternative strategy by using **magnetotactic bacteria**, which seize the possibility of getting a magnetic response suitable for biomedical application with the aid of those living cells. These cells grow individual single domain magnetite nanocrystals, **magnetosomes**, whose size is below 50 nm, and are in the origin of the magnetic response [25].

In our group of Magnetic Materials of the Universidad de Cantabria, we are grabbing the chances provided by both synthesis strategies, chemical (*i.e.*, artificial) and bacteria (*i.e.*, natural). One of these chances was connected to the use of **artificially synthesised maghemite** (chemical routes) within a research work partially performed with the support of the European Union FP7 Project (NANOMAG) [26]. The objective was to define the magnetic structure and the correlations taking place at the nanoscale. within these $\gamma\text{-Fe}_2\text{O}_3$ MNPs. The idea was not only to provide a great characterisation of a great variety of IONPs, but also to determine the properties and measuring properties to standards in their biomed-

ical applications. As a consequence, we own experience on the interpretation of the magnetic behaviour of maghemite and magnetite phases². Furthermore, we have studied in detail the commercial Synomag **Nanoflowers** (fully maghemite), which display an attractive response for Magnetic Hyperthermia [28]. These NFs³ are formed by a multicore structure, as if they were *petals* forming a (*nano*)*flower*. Other analyses within our group using IONPs concentrate on the dipolar coupling of cluster IONPs [29, 30].

With such experience at hand, **it is now time in this Dissertation to face the challenge of acquiring a better understanding on the influence that the inner structure of these IONPS has in both the widely known Verwey transition and/or the low-temperature kink observed in magnetisation vs. temperature measurements [31]**. In this sense, previous results gathered in bacterial culture provided fine details on the magnetic response, especially affected the anisotropy connected to the spiral shape of chain of magnetosomes [32]. In addition, it has already been shown the effect of different cell culture procedures modifying the Verwey transitions [33]. Finally, slight variations in the chemical composition of magnetite magnetosomes are possible and have been investigated very recently [34, 35]. In short, we are now in a position to offer further information on the anisotropy and spin dynamics of the transitions found in these magnetosomes, which in a close cooperation with the group of Magnetism lead by Prof. M. L. Fdez-Gubieda at the University of the Basque Country, is to be described in this work.

It is here where the 4f intermetallic alloys come to court nicely. These ensembles offer advantages with respect to the magnetism associated to 3d orbitals. To cite a few, the **RCu₂ intermetallics**, being R a Rare Earth, **offer the following advantages:**

- **Switching between AF and FM states** is relatively easy, as this can be achieved by, simply, changing the non-magnetic Cu by Al [36, 37, 38, 39]
- The RCu₂ are **chemically stable** in time. No oxidation and/or changes in the valence state take place, as it is the case of magnetite, which transforms towards maghemite [40].
- R display a **large intrinsic magnetic moment**, compared to 3d-ones (note the difference, for instance, between the $\sim 10 \mu_B$ of Tb³⁺ and the typical \sim

²see, for instance, [27].

³supplied by Micromod Partikeltechnologie GmbH (Germany).

$4 \mu_B$ for magnetite [41]). This allows to better observe the subtle effects that are ascribed to the inherent disorder that goes along with the size reduction to the nanoscale.

- The **magnetic anisotropy**, that has a direct impact on the magnetic properties of a system, is more easily determined in the $4f$ ensembles.
- **There are also very powerful biomedical applications connected to the Rare Earth ions.** Here, it is worth mentioning the case of Gd^{3+} and Tb^{3+} . Whereas the former is widely used as a contrast agent in Magnetic Resonance Imaging (MRI), the later displays a performing luminescence, which allow to mark and signal, for instance, tumoral cells within a culture.

Furthermore, the role of exchange interaction and the magnetic anisotropy can be well-separated in the case of $4f$ ensembles. We have already pinpointed the relevance that the magnetic anisotropy has for the magnetic applications of the different materials (Magnetic Hyperthermia Therapy, memory devices...). Notwithstanding, **a good understanding on the way that exchange interactions take place is also key for attain a comprehensive picture of the mechanism beneath the magnetism.** The essential difference between $3d$ and $4f$ orbitals is related to their outer electrons. Whereas for the former $3d$, their large CEF splits the ground state multiplet before the spin-orbit interaction takes place, leading to a delocalisation of the electron wave functions, the latter $4f$ orbitals are internal, being their **magnetic moments localised**. This implies the existence of two different scenarios, one for the $3d$ Fe-oxides, where the electron wave functions of the neighbouring orbitals overlap via a p state anion (O^{2-}), and the one of $4f$ RCu_2 , where the exchange interactions propagate via the outer conduction electrons (indirect RKKY exchange).

Focusing on the latter $4f$ ensembles, their **indirect RKKY exchange** imply the existence of conduction electrons carrying quantum information. The particular spin state of a localised $4f$ electron couples (AF or FM) with the conduction electron, which interacts with the following $4f$ localised magnetic moment, yielding to an effective coupling between the $4f$ quantum angular moment states, even if their own orbitals do not interfere. Within the framework of the quantum phenomena related to magnetism, **crystalline electric field (CEF) single-ion excitations** and the collective excitations associated to **magnons** are a *hot topic*. This kind of excitations, that are intimately related to the spin dynamics, determine the energy level schemes of the condensed matter systems, which are at the basis of their particular behaviour. Indeed, the size reduction to the nanoscale affects the

properties of the different materials by directly altering their energy level schemes. Nonetheless, there are almost no reported works, and essentially, no works concerning $4f$ ensembles, to the best of our knowledge, where it has been disclosed and described **how the CEF and magnon schemes are disturbed in ensembles of nanoparticles**. A good understanding on this influence is critical to clearly be aware of how the nanoscale affects the propagation of excitations along nanocrystallites.

Initial studies of TbAl_2 and TbCu_2 have been tackled within our group [42, 43]. In the case of TbAl_2 , the alloy is Ferromagnetic (FM) in the bulk state, while a coexistence of this FM with a re-entrant Spin Glass-like phase has been observed in nanoparticles [42]. Also, correlations have been observed thanks to Small-Angle Neutron Scattering (SANS) [44]. Lately, the interest was biased towards TbCu_2 nanoparticles, which display an AF-core arrangement [39, 43]. Such results point also to a re-entrant SG behaviour for the surface magnetic moments, whereas in this case, the core kept a bulk-like AF order. Furthermore, [39, 43] provided a deep analyses on the microscopic magnetic structure, probed thanks to the use of Neutron Diffraction and Small-Angle Neutron Scattering. It can be easily deduced that a sensible continuation of this work would be to modify the Tb by other R components with different magnetic moment, such as Gd (absence of intrinsic anisotropy) or Nd (slightly different magnetic long-range order and feasible Crystalline Electric Field and magnon excitations). It is also natural trying to determine where (magnetic) percolation limits for the long-range order and/or the global Spin Glass-like state are found. This can be achieved by altering the chemical composition with $4f$ ions, either magnetic (Gd^{3+}) or non-magnetic (La^{3+} , Y^{3+}).

Bearing in mind the above considerations, it is easy to realise that **the following objectives are related to a deep study of a variety of RCu_2 compounds**. Consequently, we will try to extend the success of producing these new RCu_2 alloys with high-planetary ball milling process for, especially, analysing Inelastic Neutron Scattering, measurements. Another obvious objective is to study the macroscopic magnetic behaviour, focusing especially on the low temperature magnetic transitions of these alloys. If we are successful completing these objectives, a global understanding of these $4f$ magnetic nanoparticles will be achieved.

As derived from the introduction on the IONPs and the magnetotactic bacteria, we are here using the experience gathered in the understating of the very stable $4f$ intermetallic MNPs for the study of these IONPs. This applies especially to the

study of the transitions in the IONPs, which include both **Synomag maghemite Nanoflowers** and the **magnetite magnetosomes synthesised by magnetotactic bacteria**. Such a task will complete the objectives of this Thesis work, and will certainly pave the way for eventual future analyses of these materials, that already deserve the interest of the scientific community.

In short, if one wants to find a rationale of the work poured together here, it is clear that **the driving force is the study of the spin dynamics in ensembles of 3d and 4f nanoparticles**. It is a matter of fact that unravelling the spin dynamics beneath the magnetic transitions undergone by these ensembles of MNPs is key from both fundamental and applications viewpoints.

To this aim, the Thesis is structured as follows.

- Chapter 2: *Fundamentals: Theoretical background* serves as a general introduction to the **theoretical concepts** and equations that are going to be discussed along this Thesis.
- Chapter 3: *Experimental methods* sheds light into the **experimental techniques** involved in the sample production and in the measuring processes. Nevertheless, this chapter will particularly stress on the **details concerning the data analyses**, which, in the case of the Inelastic Neutron Scattering or specific heat measurements, include novel approaches to better account for the behaviour of magnetic nanoparticles.
- Chapter 4: *GdCu₂ magnetic nanoparticles* includes the experimental results together with the discussion of the data analyses corresponding to **six ensembles of GdCu₂ nanoparticles** of different sizes.
- Chapter 5: *NdCu₂ magnetic nanoparticles* is devoted to **NdCu₂**, for which the use of **neutron-based experimental techniques** (Neutron Diffraction, Small-Angle Neutron Diffraction and Inelastic Neutron Scattering) has been extensive. The use of these microscopic techniques was needed to unravel the complex spin dynamics of these nanoparticles.
- Chapter 6: *Tb_xR_{1-x}Cu₂ magnetic nanoparticles* presents three different **Tb_xR_{1-x}Cu₂ ensembles**, where we have played with the Tb³⁺ amount (x) and the R diluting ion (R = Gd, La, Y) to finely *tuning* the strength coupling of the RKKY interactions, leading to different kinds of magnetic disorder.

- Chapter 7: $\gamma\text{-Fe}_2\text{O}_3$ and Fe_3O_4 magnetic nanoparticles deepens into the magnetic properties of the 3d maghemite and magnetite nanoparticles. More precisely, a comparison between commercial **Synomag $\gamma\text{-Fe}_2\text{O}_3$ Nanoflowers and bacterial magnetosome**, which are cube–octahedral organelles formed by magnetite Fe_3O_4 , from structural to magnetic viewpoints, so as to their performance as magnetic hyperthermia agents, is settled. Additionally, the magnetic properties of Gd^{3+} and Tb^{3+} –doped magnetosome have been determined.

- Chapter 8: *Conclusions* gathers the **main conclusions of the Thesis**.

Chapter 2

Fundamentals: Theoretical background

*“¿De toas tus partes cuál decido?
Es que me gusta todo de ti.”*

Rauw Alejandro

The description of the main theoretical ingredients explaining the nanomagnetism have been reviewed in several publications [21, 45, 46, 47]. Nowadays, the field is, generally speaking, mature. Consequently, it seems adequate to focus uniquely on the issues that are of primer interest to the present work. A general discussion on the theoretical grounds on which the Superparamagnetic limit, the single domain magnetic relaxation processes, and the interfacial interplay between the nanoparticle core and surface environments have been thoroughly elaborated in precedent works. In particular, the models giving account for the $4f$ intermetallic magnetism have already been illustrated in recent works presented as PhD Dissertations at the University of Cantabria [48, 49].

Hence, this chapter aims to serve as an introduction to magnetic phenomena at the nanoscale, which are relevant for the particular discussion of the experimental results presented in this Dissertation. More precisely, **this Chapter will focus on the RKKY and Superexchange interactions and on the crystalline electric field (CEF) effects**. Furthermore, **it will also provide an overview on the main aspects concerning the spin dynamics (critical behaviour, rejuvenation phenomena, spin waves) of materials where magnetic disorder is present**. The presence of magnetic disorder is actually common in ensembles of magnetic nanoparticles [50].

2.1 Magnetic phenomena in nanoparticles

The last decade has witnessed the maturity of Nanoscience. The outburst of new phenomena and the possibility of fabricate almost *ad lib* materials has biased the interest and efforts of the scientific community towards this field [40, 51, 52, 53]. As the reader may already be familiar to, the key point of the mesoscopic scale is not connected to the size reduction itself, **but to the modification of the bulk (massive) behaviour of the materials**. Here it is where the term *correlation length* comes to light. A material exhibits some particular features, from the colour to the magnetic state, as long as the structural correlation length, ℓ , is greater than the property correlation length, for instance, the magnetic exchange correlation length, ℓ_{ex} . Therefore, if one reduces the particle size below the ℓ_{ex} , the magnetic state can be dramatically changed, for instance, from a pure Ferromagnetic (FM) state, where all the magnetic moments are aligned within a multi-domain structure, to a Superparamagnetic (SPM) single domain one, where the magnetization follows the thermal fluctuations above a certain temperature. The typical nanoparticle sizes for observing the nano-effects is below 50 nm, although it depends, of course, on the particular elements forming the magnetic nanoparticle (MNP) [54].

In addition to the appearance of new magnetic states when $\ell \sim \ell_{ex}$, one should care about **the role of surface magnetic moments**. This is especially the case when dealing with nanoparticles. It is a matter of fact that the proportion of these outer moments becomes more relevant the smaller the nanoparticle size gets. Assuming a ~ 2 -nm surface thickness, as it is typical according to several studies performed on diverse ensembles of MNPs [43, 55, 56], a nominal 15 nm-sized NP will have around 60% of the magnetic moments located at the surface. This proportion is, of course, relevant enough to modify the behaviour of the material with respect to the bulk situation by means of the **lower coordination and the reduced symmetry** of the surface moments, driven by the reduction of the particle dimensions.

Finally, a very interesting scenario can be figured out when the system exhibits **two spin dynamics**; **(i)** the one stemming from the magnetic moments located within the NP core; and **(ii)** the one corresponding to the surface (outer) ones. While the former usually remain almost unaltered with respect to the bulk situ-

ation, the surface tends to exhibit a more disorder-like phase, as the strength of the exchange interactions are changed at the surface due to, mainly, the lower coordination. Additionally, the CEF, which is extremely sensitive to the local symmetry environment, is also altered at the surface. We will explain, some lines below, how this effect is expected to modify the energy level splitting. And, last but not least, there is one more ingredient that makes the nanoscale *distress* even more interesting: **The onset of disorder**. It is clear that the outer atoms are the most exposed to any kind of modifications. Therefore, **slight modifications of the lattice positions** driven by the disorder contribution, which is inherent to any top-down approach, will show up for these surface atoms. As we are going to discuss a few lines later, the RKKY coupling is r -dependent, and slight modifications on the atomic positions **can result in dramatic changes from FM to AF couplings, resulting eventually in frustration and disorder**. These also applies for the case of MNPs where the Superexchange is at the basis of their long-range magnetism, as variations in those positions alter the overlap between the adjacent orbitals.

In the framework of this Thesis, **we have focused our attention on the different states that the magnetic moments can build depending on their degree of interaction**. More precisely, these states can be *either ordered or disordered* ones, but the key point is that *they are all settled by the magnetic interactions*. Given that the emergence of well-formed and interacting **disorder** states are found to be in the low-temperature region (typically, below 30 K), the entropy contribution stemming from the temperature does not play a role in the determination of the ground state. Therefore, the magnetically disorder states appear as a consequence of the minimisation of the internal energy term¹. Consequently, depending on the strength of these interactions, different configurations can be reached, that have been summarised in Fig. 2.1. This chart aims to provide a clear and visual idea of the different states involved in this Dissertation, and it is going to be explained in the following lines.

Starting from the less-interacting side, the **Superparamagnetic (SPM)** state depicts a situation undergone by single domain nanoparticles, where the cost of domain wall formation exceeds the energy contribution from the magnetostatic anisotropy. In this picture, all the magnetic moments within a nanoparticle are oriented coherently, giving rise to a single (super)moment. The relaxation of this

¹since my final degree project [57], I have become fascinated about the possibility that the least energetic configuration could be a disordered, rather than an ordered, one, at low temperatures. This is when my attraction to Spin Glasses started.

superspin follows a Néel–Brown law, which is typical for non–interacting entities [58, 59, 60]. This model assumes that the probability for a superspin reversal is given by a Néel–Arrhenius law due to thermal activation over an energy barrier, following:

$$\tau = \tau_0 \exp\left(\frac{E_a}{k_B T}\right) \quad (2.1)$$

being $E_a = KV$ the anisotropy energy barrier and τ_0 typically $\sim 10^{-9}$ s [58, 61]. This way, if the distribution of blocking temperatures T_B fits to this Arrhenius law, the magnetic moments relax almost independently one from each other, and either a blocked or a Superparamagnetic (SPM) state, depending whether the thermal energy is smaller or greater than the E_a , respectively.

To continue with, the **Spin Glass (SG)** state is found when the atomic magnetic moments interact with each other via frustrated interactions. These disorder state implies a spin dynamics very distinct with respect to the SPM framework, which is going to be detailed in Section 2.3. Very briefly, we will just anticipate here that these interactions give rise to memory effect or ageing phenomena, where the particular disorder configurations imposed by the exchange interactions are robust against thermal disorder. Here again, the different MNPs can interact dipolarly. As an extrapolation of this concept, strong dipolar interactions among MNPs can give rise to a Super Spin Glass state (SSG). Details on this SSG arrangement will be provided later on.

The following disorder state is the one of **Cluster Spin Glass (CSG)**, where there are regions within the MNP, rather than individual atoms, the ones responsible for the disorder state. This is to say, the frustration of the RKKY exchange does not come as a consequence of the interactions among individual magnetic moments, yet it is due to the interactions *among different regions of the MNP, formed by several magnetic moments*. The relaxation dynamics of these CSG take place at slower path with respect to the one of SGs, as it is going to be shown hereunder.

Finally, the right hands side of Fig. 2.1 sketches the situation concerning the **Superantiferromagnetic (SAF)** state. This is the case of MNP where the strength of the non–frustrated RKKY interactions is enough to couple the sufficient amount of magnetic moments to give rise a collective AF(FM) order state. Of course, the nanoparticle size should, at least, be greater than the magnetic unit cell, in order to host such an order configuration. The SAF state combines both AF order (within the core) plus a SG disorder (for the surface magnetic moments) [17, 59, 62]. This state is restricted to the mesoscopic scale, where the surface

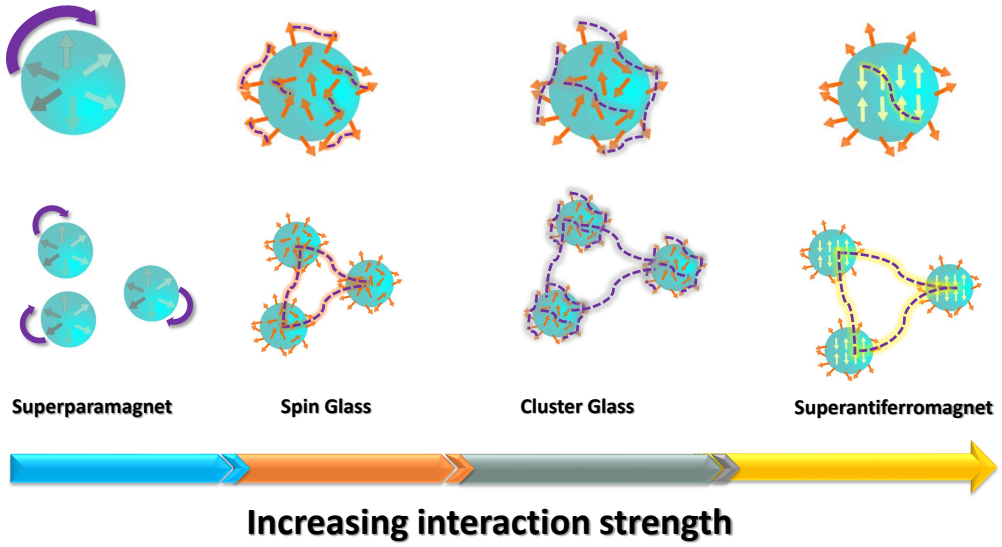


Figure 2.1: Representation of the different magnetic states that are going to be relevant within this Thesis work as a function of the strength interaction, from the non-interacting SPM ensemble (left) to the highly correlated Supermagnetism (in this case, Superantiferromagnetism) (right). The presence of some disorder is inherent to the existence of a surface.

disorder is relevant enough to induce a disordered magnetic state.

2.2 Interactions among the magnetic moments. RKKY indirect exchange

The general phenomenological expression for the exchange Hamiltonian between two spins \mathbf{S} at sites i and j reads as [63]:

$$\hat{H}_{ex} = \sum_{\alpha,\beta} J_{\alpha,\beta} S_{i,\alpha} S_{j,\beta} \quad (2.2)$$

being α and β the Cartesian coordinates x, y, z and $J_{\alpha\beta}$ the exchange tensor. This expression can be re-written into three contributions:

$$\hat{H}_{ex} = -J\mathbf{S}_i \cdot \mathbf{S}_j + \mathbf{D} \cdot \mathbf{S}_i \times \mathbf{S}_j + \mathbf{S}_i \cdot \boldsymbol{\Lambda} \cdot \mathbf{S}_j \quad (2.3)$$

where J is the scalar exchange integral (thus, isotropic), \mathbf{D} is the Dzyaloshinskii-Moriya vector, which gives account for the antisymmetric anisotropic exchange, and $\boldsymbol{\Lambda}$ is the anisotropy tensor, which reflects the symmetric anisotropic exchange.

In our case–study, the later two terms are negligible compared to the isotropic exchange $J_{i,j}$ [13, 50]. What is more, the energy of the isotropic exchange coupling depends exclusively on the relative orientation of the spins \mathbf{S}_i and \mathbf{S}_j . This way, a $J_{i,j} < 0$ value will favour an antiparallel (antiferromagnetic) orientation for the spins, whereas in the opposite situation, a ferromagnetic spin alignment will be settled.

Getting closer to the $J_{i,j}$ term, the fact that the wave functions of magnetic d and/or f electrons decreases exponentially with the distance from the nucleus may preclude their wave functions to overlap. In such a framework, the $J_{i,j}$ value becomes too small to couple the magnetic moments, meaning that no possible long–range magnetic order can be achieved. Indeed, an **intermediate entity**, able to connect the localised magnetic moments, is demanded to take part of the game. Provided that a *rider* is needed for the communication process to be achieved, one should then speak about **indirect exchange**. Here, we will restrict the explanation to the two kinds of indirect exchange mechanisms that are related to the compounds introduced in this Dissertation:

- (i) **RKKY:** The **Ruderman–Kittel–Kasuya–Yosida (RKKY) indirect exchange interaction** is the one that couples the $4f$ electron wave functions via the $5d$ and $6s$ conduction electrons (thus, restricted to metals). This way, the localised $4f$ spin states achieve to expand a long–range communication. The isotropic RKKY exchange interaction obeys the following expression [50]:

$$J_{RKKY}(r) = J_0 \frac{\cos(2k_F r + \phi)}{(2k_F r)^3}, \quad (2.4)$$

where k_F stands for the conduction electron Fermi wave vector and J_0 is of the order of ~ 1 eV [50, 64, 65].

- (ii) **Superexchange:** The **Superexchange** interaction applies in the case of the $3d$ magnetite and maghemite (bulk) systems. In this kind of exchange, which is restricted to insulators, the $3d$ electrons of the magnetic ions (Fe^{3+} and both Fe^{2+} and Fe^{3+} in maghemite and magnetite, respectively) are connected via the p electrons of non–magnetic *ligands* or *ions* (O^{2-} in the case of the aforementioned $\gamma\text{-Fe}_2\text{O}_3$ and Fe_3O_4), which act as a *bridge*. The exchange integral J_{PE} , within the framework of first order perturbation theory, can be expressed as [47]:

$$J_{PE}(r) = \int dr_1 dr_2 \phi_a(r_1) \phi_b(r_2) \frac{e^2}{|r_1 - r_2|} \phi_b(r_1) \phi_a(r_2) \quad (2.5)$$

where the electrons corresponding to nondegenerate orthogonal orbitals, represented as ϕ_a and ϕ_b , are exchanged between r_1 and r_2 position. This J_{PE} exchange is always positive (thus, FM) in the case of first order perturbation calculations. Nevertheless, within the framework of second order perturbation, where double occupancy is allowed through configuration interaction (*mixing*), the antiparallel spins can delocalise by hopping between neighbouring sites, which leads to an antiferromagnetic state. Particularly for the case of the inverse spinel structure of **magnetite**, the AF coupling of the trivalent Fe^{3+} located at the tetrahedral A-sites and the Fe^{3+} at octahedral B-sites leads to the compensation of their magnetic moments, resulting on a single contribution stemming from the Fe^{2+} located at octahedral B-sites. This results in a long-range **Ferrimagnetic** arrangement. The situation concerning **maghemite** is **very similar**, since the Fe^{3+} ions are also arranged into an inverse spinel structure. In this case, as for magnetite, the intensity of the magnetic moments depend on the different lattice positions, since one ninth of the Fe positions in the lattice are vacant. This also results in a long-range **Ferrimagnetic order**.

Indeed, the classical **dipolar interaction** deserves to be mentioned, since it is always present in any interaction involving magnetic moments [2]. Nevertheless, its strength is some orders of magnitude below the one corresponding to the above-mentioned indirect exchange mechanisms, meaning that the dipolar interaction can be roughly neglected when analysing the individual moments response. We will just briefly mention that the dipolar term also brings an angular dependence into the coupling scheme (thus, anisotropy), which contrasts with the isotropic RKKY and Superexchange. These two mechanisms, as defined above, only carry a radial dependency, yet they are not affected by the relative orientation of the magnetic moments. The angular dependency of the dipolar interaction can be inspected throughout the expression giving account for the energy between magnetic atoms, as:

$$E_{dip} = \sum_{r_{i,j}} \left[\frac{\mathbf{m}_1 \cdot \mathbf{m}_2 - 3(\mathbf{m}_1 \cdot \hat{\mathbf{n}}_{i,j})(\mathbf{m}_2 \cdot \hat{\mathbf{n}}_{i,j})}{r_{i,j}^3} \right], \quad (2.6)$$

where $\hat{\mathbf{n}}_{i,j}$ denotes a unit vector along the direction that connects the magnetic moments \mathbf{m}_i and \mathbf{m}_j . Note that, within the picture of MNPs, there are thousand of magnetic atoms involved in each of the MNP, leading to a super spin dipolar coupling. This would be at the origin for interparticle correlations.

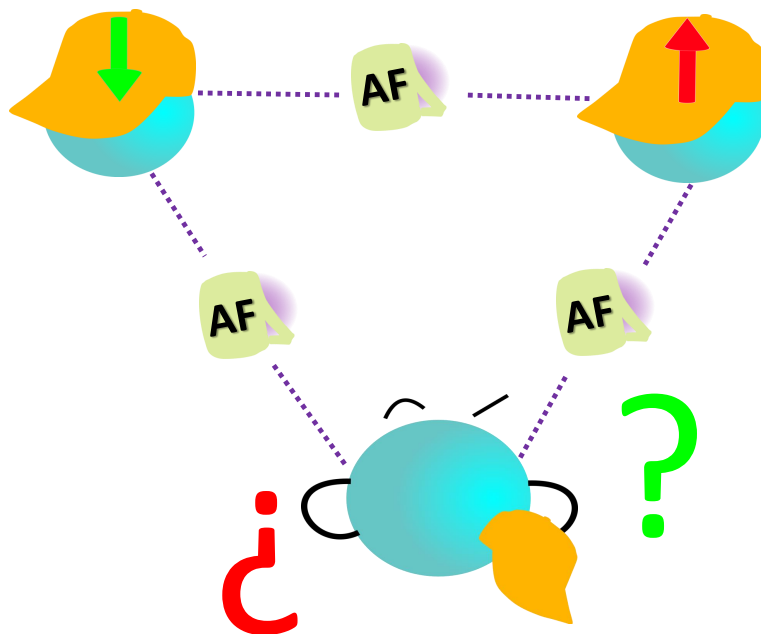


Figure 2.2: Simple sketch of magnetic frustration in a triangular AF lattice. From the point of view of the bottom magnetic moment (the one with the cap removed), the magnetic exchange coupling on the left imposes an upwards spin configuration, while, on the contrary, the right-side coupling demands this spin to point downwards. The bottom magnetic moment is not able to fulfil simultaneously both couplings getting thus, *frustrated*.

All in all, we have pictured so far a framework where the localised magnetic electrons are coupled via conduction electrons (RKKY, Rare Earths) or anions (Superexchange, Fe-oxides). Hence, the long-range magnetic order will solely depend upon the distance between two adjacent ions, giving rise to FM and/or AF orderings in the case of $4f$ Rare Earths, whilst in the case of Fe-based compounds, the typical coupling through Superexchange settles a long-range Ferrimagnetic configuration. A question that may naturally arise is **what would happen if there were a contradiction concerning the information carried by the riders**. For the shake of simplicity, we will explain what happens using the RKKY framework.

If the coupling *instructions* received by a particular magnetic moment are contradictory, the magnetic moment will not know how to arrange, and it will get *frustrated*. This frustration comes as a result of having interacting $4f$ moments (coupled via the itinerant $3d$ electrons) that cannot satisfy simultaneously all the requirements to achieve the lowest energy state. Serving as example, it could be that, for one particular magnetic moment, one first neighbour imposes a cou-

pling strength $J_i > 0$ (FM), whereas two second neighbours do $J_j < 0$ (AF). If $|J_i| = 2|J_j|$, the moment will not know which configuration should it adopt, given that the lowest energy state is not accessible, yet there is a *collection of low energy states, which do not include a particular one of the lowest energy*. This is the actual definition of frustration [50], which is a key ingredient for the disordered magnetic state known as **Spin Glass** (SG) to be settled. An illustrative example of such a frustration is the simplest triangular lattice with AF coupling, that can be inspected in Fig. 2.2.

Notwithstanding, **frustration itself is not enough to give rise to a SG phase**. The literature offers examples where geometrically-frustrated magnetic states are achieved without implying the setting of a Spin Glass, being the most common scenario the one that leads to a slow blocking towards a ground state dominated by large magnetic fluctuations [50]. One of the most typical example of such a frustrated (but not SG) state is the antiferromagnetic Kagomé lattice, which is found, for instance, in pyrochlores [66]. For a SG state to occur, it is crucial that, additionally to the competition between FM and AF RKKY interactions, **randomness must be present**. What is more, it is solely **the combination of frustration coupled with randomness the one able to rise a cooperative freezing process**, instead of a non-interacting *blocking* mechanism. This randomness can be of two types:

- (i) **Random-site occupancy:** The lattice positions corresponding to the non-magnetic (Cu in our case) and the magnetic ions (Gd, Nd, Tb) are promptly exchanged. This leads to an alteration of the **distance between R^{3+} – R^{3+}** .
- (ii) **Random-bond:** Here, it is the **coupling strength** the one which is altered. This occurs, when the lattice positions are maintained, but some magnetic ions are replaced by other ones, for instance, the half-replacement of Tb^{3+} by Gd^{3+} in $Tb_{0.5}Gd_{0.5}Cu_2$ alloys [67].

Certainly, both kinds of disorder can coexist, in both bulk and MNP states, as it is going to be shown afterwards in Chapter 6. Both kind of randomness result in either an *effective* alteration of the distance $r_{i,j}$ between the localised magnetic moments m_i and m_j , or in the strength coupling modifications. Given that the interaction coupling J_{RKKY} is of oscillating nature and r -dependent (see eq. 2.4), it is straightforward that the magnetic state may be switched by just tuning the distance and/or the strength coupling among the different magnetic moments. Fig. 2.3a showcases the typical RKKY oscillations, as a function of the distance between the magnetic moments, r . We have kept the Y-axis in arbitrary units in

order just to discuss how a frustrated state can be achieved. If we focus on $r_0 \sim 3.5 \text{ \AA}$, a value which is close to the mean $R^{3+}-R^{3+}$ distance in our RCu_2 alloys, the exchange coupling is negative (thus, AF). The same situation holds at $2r_0$. Nevertheless, a closer view to these oscillations allows easy to come up with the idea that minor alterations of the atomic distances r (or, alternatively, exchange coupling strength, J_{RKKY}) could easily lead to a cross-over from AF to FM (and viceversa). These modifications naturally appear when the NP state is achieved, as there is a strain contribution which slightly distorts the unit cell, thus, modifying the $R^{3+}-R^{3+}$ distance. Indeed, the partial-filling of the lattice with different R^{3+} , either magnetic (Gd^{3+}) or non-magnetic (La^{3+} , Y^{3+}), leads to the same effect. In any case, the alteration of the coupling between adjacent magnetic moments settles a competition between FM and AF couplings. **It is easy to see that this may finally result in a Spin Glass phase.**

To better realise this flexibility in the tuning of the sign of the magnetic coupling, Fig. 2.3b includes a scheme of the different degrees of magnetic order/disorder that can be achieved by finely-tuning the RKKY coupling strength, starting from a SAF $TbCu_2$ ensemble of MNPs, where the magnetic moments within the core are AF-ordered, being the outer surface ones forming a SG phase. The same situation holds for $GdCu_2$, yet the combination of both magnetic ions in the $Tb_{0.5}Gd_{0.5}Cu_2$ MNPs fall into the Super Spin Glass (SSG) regime, which is going to be further elaborated later on. On the non-magnetic dilution side, the dilution of Tb^{3+} with La^{3+} in $Tb_{0.5}La_{0.5}Cu_2$ is not that dramatic to destroy the AF ordering at the core, as the MNPs keep the global SAF of the parent $TbCu_2$ MNP ensembles. On the contrary, diluting $TbCu_2$ with 90 % of Y^{3+} already destroys the AF coupling at the bulk state, being the interactions among the magnetic moments progressively destroyed with the size reduction, yielding to the SPM $Tb_{0.1}Y_{0.9}Cu_2$ MNPs.

2.3 Spin dynamics: Length and time scales.

As it has been introduced in the previous section 2.2, frustration coupled with randomness may result in the onset of a disordered magnetic state, the one known as **Spin Glass**. This magnetic state imposes a very particular spin dynamics, which includes phase transitions, irreversibility and time-dependent magnetisation responses, to cite a few. This section will shed light into the theoretical details beneath the Spin Glass dynamics.

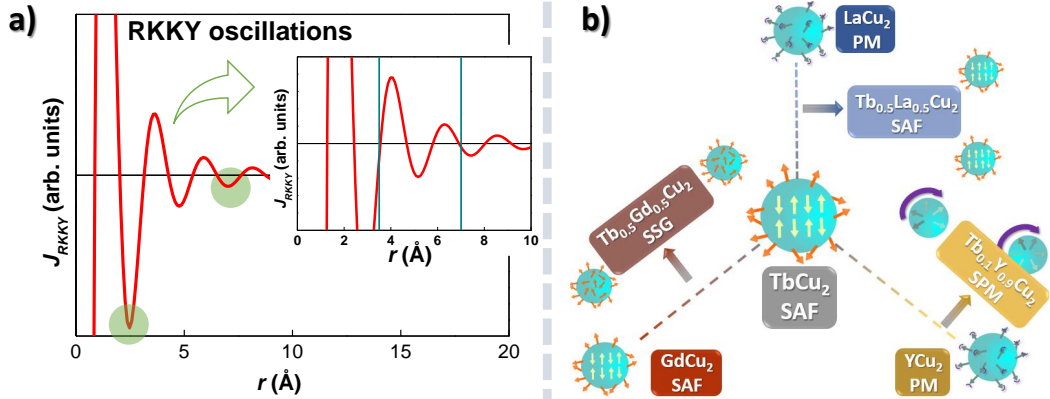


Figure 2.3: **a)** RKKY oscillations as a function of the distance r between adjacent magnetic moments. The inset zooms the region close to $r_0 = 3.5$ Å and $2r_0$. In **b)**, a visual sketch on the different magnetic disorder states that can be achieved by changing the R-content of the alloy is displayed, from the most interacting SSG disorder state found in the $\text{Tb}_{0.5}\text{Gd}_{0.5}\text{Cu}_2$ ensembles to the non-interacting Superparamagnetic $\text{Tb}_{0.1}\text{Y}_{0.9}\text{Cu}_2$. The $\text{Tb}_{0.5}\text{La}_{0.5}\text{Cu}_2$ ensembles, on the other hand, keep the bulk AF within the MNP core, constituting the so-called Superantiferromagnetic state. On the edges, LaCu_2 and YCu_2 fall in the Paramagnetic (PM) regime, where the thermal energy prevents the magnetic ordering of the moments.

2.3.a Spin Glass transitions

A phase transition signals a singularity in the thermodynamic potential. As a consequence, **phase transitions separate two different spin dynamics**. One could speak about *first-order* transitions, where the first derivative of the thermodynamic potential shows a finite discontinuity, or about *continuous* or *critical* transitions, where the first derivative is continuous, but second or higher are not [68]. The latter is the most common case for **magnetic transitions**, which are characterised by an **order parameter**. This parameter is equal to zero in the disordered phase (paramagnetic, PM) and non-zero in the ordered case, due to the symmetry breaking. For the case of SGs, Edward and Anderson proposed an order parameter, namely, q_{EA} , to give account for the spin-spin auto-correlation function [69], as:

$$q_{\text{EA}} = \lim_{t \rightarrow \infty} \langle s_i(\vec{0}) s_i(\vec{t}) \rangle \quad (2.7)$$

In the vicinity of the transition temperature T_f , the spin-spin correlation length becomes smaller than the coherence length ξ of the critical fluctuations. Accord-

ingly, below and above T_f , the length scales L_0 shorter than ξ will be governed by the critical fluctuations, as:

$$\xi \sim L_0 \left(\frac{T - T_{f,0}}{T_{f,0}} \right)^{-\nu} \quad (2.8)$$

being $T_{f,0}$ the static spin glass temperature, *i.e.*, when $f \rightarrow 0$ and ν a critical exponent. This ξ can be transformed into the a measurable time-domain according to a conventional critical slowing down as:

$$\tau = \tau_0 \left(\frac{T - T_{f,0}}{T_{f,0}} \right)^{-z\nu} \quad (2.9)$$

where $\tau = 1/2\pi f$, τ_0 is the relaxation time of a individual particle moment in the static limit ($f \rightarrow 0$), and $z\nu$ the critical exponent. Values for $z\nu$ between $5 < z\nu < 11$ are the ones traditionally ascribed to SGs, since they are considered to be within the *fragile regime* behaviour [70]. Indeed, it is worth mentioning the fact that the *true* SG phase is only reachable if $f \rightarrow 0$, as the relaxation towards equilibrium is only accomplished under that condition [50, 61]. Needless to say, the dynamic scaling should be experimentally probed by means of, indeed, dynamic $\chi_{AC}(T, f)$ susceptibility measurements.

Consequently, following the aforementioned picture, if $T > T_f$, the system will be in equilibrium on length (time) scales longer than ξ (τ), and a PM response will be retrieved from this phase. If the temperature is lowered **below T_g , a cross-over between critical dynamics on short length (time) scales and activated dynamics on long length (time) scales will take place, and a Spin Glass state will be settled.**

Additionally to the critical (power-law) scaling, SG transitions can also be characterised by means of the δ -parameter, which can be expressed as:

$$\delta = \frac{\ln(T_f)}{\log_{10}(2\pi f)} + k \quad (2.10)$$

This δ -parameter monitors the $T_f(f)$ dependence, which gives valuable information on the interactions (RKKY and/or dipolar) established among the magnetic moments [37, 39, 70, 71]. As a guide, one can consider δ values greater than 0.1 to be a clear indication of a nearly-independent relaxation of the entities, very similar to the Superparamagnetic fashion [60]. On the other hand, the interactions among the individual magnetic moments of canonical Spin Glasses lead to

a much faster relaxation dynamics, which is reflected by noticeably smaller δ values. Traditionally, δ values for canonical SGs have been reported to lie within the [0.002–0.004] range [50]. What about δ values included in the region in between the aforementioned values? As one may have anticipated, this interval accounts for a non-individual but still interacting spin dynamics, where the magnetic moments arrange in **clusters that freeze collectively**. The relaxation is then faster than that of a SPM state, but slower than the one of canonical SG. Examples of systems displaying this cluster-like behaviour (CSG) can be found, for instance, in $\text{Fe}_{91}\text{Zr}_9$, which displays $\delta = 0.066$ [72]. Super Spin Glass (SSG) nanoparticle ensembles also lie within this intermediate region between SPM and canonical SG [37, 61, 67, 73]. The magnetic moments (superspines) of the SSG nanoparticles interact, either directly via dipolar interaction, or indirectly via interaction mediated by the matrix material, leading to slower spin dynamics compared to SG, yet still interacting, in contrast with the SPM.

At this point, it very convenient to comment, even if briefly, the picture of the **droplet model**, given the fact that we are dealing with correlation and critical fluctuations lengths. For a complete description, we refer the reader to more complete overviews on this subject, *e.g.*, [74, 74, 75]. Here, as it is common, we will restrict ourselves to the point of view provided by the Ising Edwards–Anderson model, where only the nearest-neighbours interactions are considered [69]. It is also advisable to avoid any singularity related to the phase transition, and hence, we will depict the picture not too close to T_f . Therefore, the equilibrium state at each temperature would consist of a particular ground state plus thermally activated droplet excitations of several sizes. These droplets, that are *protected* by energy barriers, encompass a low-energy cluster of spins with volume L^d and fractal surface L^{d_s} [68], and can be thermally activated.

Finally, the freezing transition associated with the entrance in a Spin Glass state is not only frequency, but also, field dependent. This $T_f(H)$ behaviour is better inspected in the static regime, which is experimentally achievable by measuring $M_{\text{DC}}(T, H)$. Although there are several models to give account for this dependence, it is the model proposed by de Almeida and Thouless the one that seems to provide the best fitting to the experimental data. Accordingly, their proposed:

$$H(T) \propto \left(1 - \frac{T_f(H)}{T_f(0)}\right)^m \quad (2.11)$$

being m is 3/2 within the mean field framework. The viability of this dependence is going to be checked-out in Chapters 4 and 6.

2.3.b Ageing and memory effect phenomena.

So far, the spin dynamics related to magnetically-disordered states (SG, SSG, SPM...) has been characterised by means of $\chi_{AC}(T, f)$ measurements. More precisely, eqs. 2.9 and 2.10 deal with the in-phase $\chi'(T, f)$ component. Nevertheless, the out-of-phase χ'' component also carries very powerful information related to the spin dynamics, as it accounts for the dissipation connected to (SG) phase transitions. Furthermore, the time-dependent phenomena that are going to be introduced hereunder are going to be better traced by the χ'' component, rather than by the χ' one.

In this sense, the out-of-equilibrium dynamics in non-ergodic systems (Spin Glass, either SG or SSG) also gives rise to two appealing **time-dependent phenomena**, which are the **ageing and memory effect**. The presence of these two phenomena guarantees a high correlation among the magnetically frustrated interactions. Within the framework of SGs, they are the RKKY interactions the ultimate responsible for providing a strength coupling relevant enough for these phenomena to become noticeable [76, 77, 78, 79, 80].

Beginning with the **ageing**, magnetically frustrated spin systems are characterised by the existence of a broad distribution of the spin fluctuation times. A unique ground state, in the sense of being the one where all the interactions are minimised, is not accessible, as already mentioned, forcing the system to adopt, at $T = T_f$, a configuration where not all the conditions are satisfied *simultaneously*, and the spin fluctuations freeze at a finite experimental time scale. Thus, at temperature values below $T < T_f$, the ergodicity of the spin system is broken down [81, 82, 83, 84, 85, 86]. Consequently, the system will show a kinetic slowing-down dynamics (meta-stable equilibrium), **which can be experimentally probed as a time-decay of the magnetization**. This relaxation follows a logarithmic-like dependency for the case of canonical SGs [76, 87]. This is the experimental evidence that the system is relaxing towards the thermodynamic equilibrium, which cannot actually be reached for the global SG state, but it does for some small spin clusters [88]. The particular time dependence is known as *ageing*, and it gets more visible in the low field and low frequency measurements [76].

Provided that the field changes are small enough (which always holds in the case of the performed χ_{AC} measurements of this Thesis work), the magnetisation

M vs time t , $M(t)$, responds linearly to the applied magnetic field, H , applied after a waiting time t_w . Given that the SG is out of equilibrium on experimental time scales, the instant $t = 0$ is fixed as the moment when the SG is quenched to any temperature, as long as there is a non-equilibrium state. This means that the waiting temperature, T_w , can be chosen above or below T_g indistinctly. As we have already commented a few lines above, although both in-phase and out-of-phase components of χ_{AC} display this phenomenon, it is usually studied in the out-of-phase component, where these kind of subtle effects get more noticeable [76]. Assuming that the relaxation rate $\left[\frac{\delta M_{t'=1/\omega}}{\delta \ln(t')} \right]_{t_w}$ is a slowly varying function of $\ln(t')$ (which holds in the low frequency and field limit), the out-of-phase component shows a time dependency that reads [76]:

$$\chi''(\omega; t) \approx -C \left[\frac{\delta M_{t'=1/\omega}}{\delta \ln(t')} \right]_{t_w} \quad (2.12)$$

being C a constant. This equation evidences the direct relationship between $\chi''(t)$ and $\left[\frac{\delta M_{t'=1/\omega}}{\delta \ln(t')} \right]_{t_w}$, as both decrease with t .

On the other hand, the other time-dependent phenomena, which are the **memory effects**, are also an exclusive manifestation of frustrated systems with broken ergodicity [77, 82, 84, 89]. These effects show up when a SG system, that has been cooled upon making a stop (halt) at a particular $T < T_g$ during a sufficiently long t_w (usually, $t \sim 10^3$ s), is re-heated. In this line, as $T \lesssim T_g$, the magnetization value drops, as the system keeps a memory of each isothermal ageing, where an evolution towards equilibrium was developed. The system is said to *rejuvenate*, as some particular *disorder domain* configurations are *imprinted* to it. This implies that some spins would arrange into those *clusters*, as their disorder configurations are more energetically favourable².

2.4 Crystalline electric field. Spin waves.

The last section of this *Fundamentals* Chapter is devoted to the single-ion crystalline electric field and magnon collective excitations (spin waves). A good understanding of how these excitations alter the energy level schemes is key to figure out the spin dynamics of the target ensembles. Accordingly, this section will provide

²this effect provides the basis of a thermal memory cell [90], which could act as a *warehouse* for a byte by means of simple thermal manipulation [88].

a detailed description on the CEF and spin waves basis, focusing on the NdCu₂ case–study.

2.4.a Crystalline electric field

In eq. 2.3, we have provided the Hamiltonian exchange term. Indeed, this term has to be taken into account in the Hamiltonian that describes the whole system, which includes more terms, as:

$$\mathcal{H} = \mathcal{H}_0 + \mathcal{H}_{Ex} + \mathcal{H}_a + \mathcal{H}_{CEF} + \mathcal{H}_{SO} + \mathcal{H}_Z \quad (2.13)$$

where the first term gathers the kinetic and Coulombic repulsion energies, the \mathcal{H}_{Ex} is the exchange term already introduced in eq. 2.3, the \mathcal{H}_a is the anisotropy term, the \mathcal{H}_{CEF} stands for the crystalline electric field (CEF) contribution, the \mathcal{H}_{SO} stands for the Spin–Orbit (SO) interaction and the latest \mathcal{H}_Z is the Zeeman term. Hybridization (mixing), Dzyaloshinskii–Moriya, dipolar and other possible terms have been neglected due to their minimal influence to the global spin system [50].

We will focus hereunder on the last three terms. First of all, it should be noted that **the scenario changes dramatically depending upon we are dealing with 3d or 4f ions**. Given that the magnetism displayed by the former 3d is caused by the electrons filling the most external shell, $\mathcal{H}_{CEF} \gg \mathcal{H}_{SO}$. This yields to a situation on which the CEF splits the ground state multiplet, followed by a distortion of the symmetry driven by the Jahn–Teller effect [2]. As a result of the latter spontaneous distortion, the 3d ions are no more well–described by the J quantum number, since their angular momentum L is *switched–off*. This means that 3d are considered as S –state ions [2, 91], being this S the right quantum number. On the other hand, **in the case of 4f intermetallics**, $\mathcal{H}_{SO} \gg \mathcal{H}_{CEF}$, which implies that the ground state multiplet is firstly split by the Spin–Orbit interaction, and then, the CEF splits the J eigenstates. This leads to a playground where the 4f ions **are well–described by the J quantum number**, which has several implications that are going to be developed hereunder. Finally, the last contribution, \mathcal{H}_Z , accounts for the Zeeman interaction, which comes to play in both 3d and 4f ions. This interaction splits the sub–levels (either S or J eigenstates) in the presence of an external field, which opens new accessible states. This field can be either externally applied and/or a local field caused just by an ordered magnetic configuration, such as FM or AFM.

Therefore, it is then straightforward to expect that the CEF splits the $(2J+1)$ -fold degeneracy of the ground state. What is more, within the localised framework, the fact that the separation energies between the different J multiplets are, generally, one order of magnitude greater than the perturbation energies caused by the surrounding atoms, transitions to energy levels above the ground state multiplet can be neglected in practice. Consequently, **electrons will be occupying energy levels corresponding solely to the splitting of the ground state multiplet**. Seizing the opportunity that the analyses is providing us, we will focus our efforts on the evaluation of the CEF effect in the magnetic $4f$ ions from hereunder.

They are the **electron–electron interactions caused by the electrostatic interaction** between the aspherical $4f$ charge distribution of one particular R^{3+} , and the aspherical electrostatic field arising from the neighbours, **the ones that account for the CEF splitting**. Indeed, this electrostatic interaction is the ultimate responsible for the intrinsic magnetocrystalline anisotropy of these $4f$. Just as a reminder, we would like to stress at this point that all the considerations that are going to be presented assume that the energy of the incomplete $4f$ shell is always below the energy of the Fermi level. This situation forces the $4f$ electrons to be well-localised, preventing the alloys to display mixed/fluctuation–valence phenomena [50, 92, 93]. Moreover, given that the experimental data and efforts are only available in detail (see Chapter 5) to the Nd^{3+} ions, we will provide a general overview on the CEF effects in R, stressing on some particularities of the $NdCu_2$ intermetallic alloy.

Accordingly, we will expand now the \mathcal{H}_{CEF} term already introduced in eq. 2.13. This contribution accounts for the potential energy that experience the $4f$ electrons due to the electrostatic interaction with the already mentioned aspherical electrostatic field [94]:

$$\begin{aligned}\mathcal{H}_{CEF} &= e \sum_i V_{CEF}(r_i) \\ V_{CEF}(r) &= \sum_{l,\alpha} Y_{l,\alpha} r^l Z_{l,\alpha}(\Theta, \Phi)\end{aligned}\tag{2.14}$$

where the expansion of $V_{CEF}(r)$ is made by means of Tessarial harmonics (defined in [95]), instead of using the spherical ones, which offers the advantage of dealing with real functions. We will not deepen into the mathematical elaborations and considerations, but we would just like to mention that working with the Tessarial harmonics, together with the fact that only the ground state multiplet

is needed to be addressed, allows to transform the $f(x_i, y_i, z_i)$ polynomials in J_α ($\alpha = x, y, z$) operators, by means of the *Stevens' operations equivalents* [96]. This transformation is extremely helpful, since the J_α operators act on the $4f$ shell as a whole, on the contrary of what the polynomials x_i, y_i, z_i do in $V_{CEF}(r_i)$, as they act on individual $4f$ electrons. Thereby, the \mathcal{H}_{CEF} reads as:

$$\mathcal{H} = \sum_i \sum_{\ell, m} O_\ell^m B_\ell^m(i) \quad (2.15)$$

being O_ℓ^m and B_ℓ^m the Stevens operators and CEF parameters, respectively. The computation of the CEF parameters from a microscopic approach is a very challenging problem, since some of the assumptions and approximations made are not exact. In this way, even if minor, there is an overlap between the other electrons belonging to the particular R ion with the $4f$ ones of the neighbour ions. Furthermore, the conduction electrons can also play a role in the CEF determination [97, 98]. To avoid undesired complications, in the case of the NdCu_2 results presented in this Thesis, the CEF parameters have been taken from experimental data [93, 99, 100, 101, 102].

The description of the CEF Hamiltonian corresponding to the NdCu_2 alloy (orthorhombic CeCu_2 -type crystal structure, $Imma$ space group) takes into account that the Nd^{3+} ions are located at Wyckoff position 4e with point-group symmetry C_{2v} , together with the fact that the ten-fold degenerate Hund's rule ground-state multiplet ${}^4I_{9/2}$ (total angular momentum $J = 9/2$) is split by the CEF into five doublets. The fact that the next multiplet state is located several hundreds of meV higher in energy [103] keeps the above mentioned approximations safe. Therefore, the CEF Hamiltonian (eq. 2.15) of C_{2v} symmetry, only the terms $\ell = 2, 4, 6$ and $m = 0, 2, 4$ and 6 with $m \leq \ell$ are involved [95]. The CEF parameters are experimentally determined thanks to specific heat, magnetic susceptibility and inelastic neutron scattering measurements in the paramagnetic region [93, 99, 100, 101, 102]. Briefly, these results suggest a doublet CEF ground state formed by $|0\rangle = 0.049|\pm 9/2\rangle + 0.891|\mp 7/2\rangle - 0.373|\pm 5/2\rangle - 0.230|\mp 3/2\rangle + 0.111|\pm 1/2\rangle$ in the basis $|J, M_J\rangle \equiv |M_J\rangle$, which is responsible for the uniaxial orthorhombic easy-axis single-ion anisotropy. The first excited state is $|1\rangle = \mp 0.025|\pm 9/2\rangle \pm 0.309|\mp 7/2\rangle \pm 0.306|\pm 5/2\rangle \pm 0.284|\mp 3/2\rangle \mp 0.854|\pm 1/2\rangle$ located at an energy of 2.9 meV. The second excited level is $|2\rangle = -0.010|\pm 9/2\rangle + 0.120|\mp 7/2\rangle + 0.724|\pm 5/2\rangle - 0.675|\mp 3/2\rangle + 0.079|\pm 1/2\rangle$ at 5.0 meV [99]. The remaining two $J = 9/2$ levels lie at higher energies. These theoretical considerations will be useful to understand how the CEF takes place in our NdCu_2 ensembles of MNPs (explained in detail in Chapter 5).

2.4.b Spin waves

So far, we have assumed paramagnetic RCu_2 intermetallic ensembles, where no long-range magnetic order is settled and the magnetic moments are disordered by means of thermal fluctuations. Nevertheless, this is an uncompleted picture, since most of the RCu_2 intermetallics (and, in particular, NdCu_2) display an antiferromagnetic order state [93]. The presence of magnetic exchange interactions causes the emergence of collective excitations, the **spin waves**. These dispersive excitations, quantised as quasiparticles that obey Bose–Einstein statistics (**magnons**), provoke slight deviations from the equilibrium positions of the magnetically-ordered spins [2] (see sketch in Fig. 2.4a). These deviations can be viewed as coupled *precessions* of the magnetic moments about the equilibrium direction. These *precessions* are quantised in different modes, which are known as **magnons**. These quasiparticles are linear combinations of single-ion excitations from the ground state to the first excited molecular-field state [92, 104]. It is worth mentioning here the difference between FM and AF orderings with respect to the spin wave propagation. The translational symmetry of ferromagnets allows to a clear understanding on the spin wave propagation, which has been nicely reviewed in several textbooks [1, 2, 105]. However, the situation concerning antiferromagnets is more tricky. Whereas for conventional antiferromagnets, this translational symmetry is obeyed in each of the sublattices, when the AF order is more complex (e.g. incommensurate arrangements), the study of magnons is far from being a simple matter. Here, we will briefly describe the **spin wave dispersion for a commensurate AF structure** (along a -direction) as [1]:

$$\hbar\omega_q = 4 J S \sin(qa) \quad (2.16)$$

being q the wave vector transfer and a spin–spin distance (equal to the magnetic unit cell parameter).

A simple Taylor expansion of the sinusoidal term³ in eq. 2.16 at q values near $q = 0$ will lead to easily observe that **the dispersion relation is linear for small values of q** . Furthermore, this dispersion relation implies a variation in the sublattice magnetisation and specific heat according to $T^{3/n}$ [1], yet it is very tricky to be experimentally distinguished from the phonon contribution. Note the contrast, still for $q \rightarrow 0$ values, between the linear dispersion relation of spin waves

³AF dispersion at $q \rightarrow 0$: $\hbar\omega_q \propto q - \frac{q^3}{3!} + \frac{q^5}{5!} + \dots$

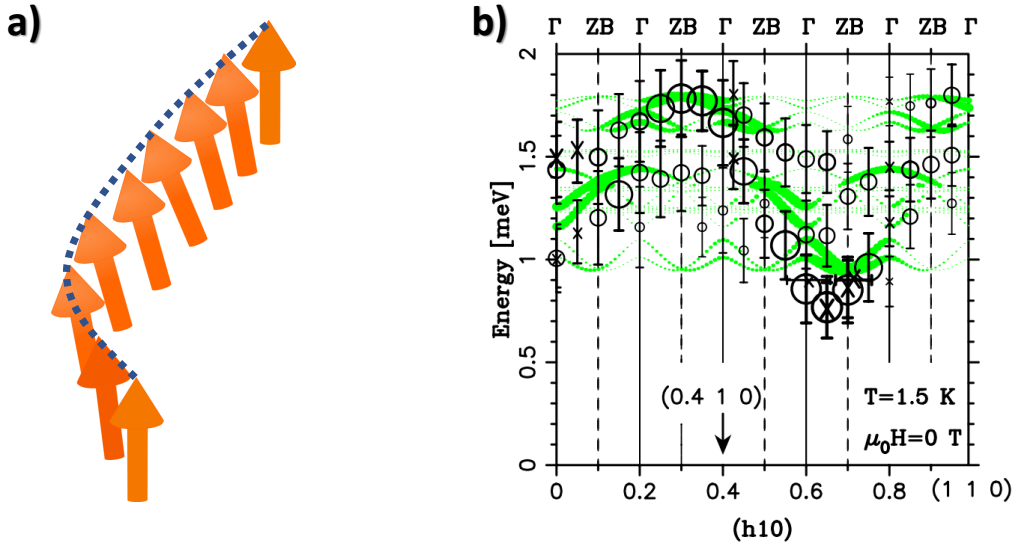


Figure 2.4: **a)** Sketch of a spin wave propagation in the simplest case of a linear array FM-coupled magnetic moments. The spin waves provoke slight deviations of the magnetic moments with respect to their equilibrium position. We have represented the FM case for the sake of simplicity. **b)** Dispersion curves of the magnetic excitations along (h 1 0) in the AF phase NdCu_2 single crystal, taken from [102]. The calculation (green lines) are compared to the experimental data (\circ and \times). Vertical lines indicate the center and the zone boundary of the magnetic Brillouin zone. The arrow marks the position of the magnetic propagation vector, (0.4 1 0), in the AF1 region.

in AF, and the **quadratic dispersion followed by the spin wave dispersion undergone in FM (and Ferrimagnets) at $q \rightarrow 0$** [106]. This quadratic relation is retrieved by making the same Taylor expansion around $q = 0$ of the cosinusoidal term⁴ that for appears in the dispersion relation of FM (and Ferrimagnets), which reads [1, 2, 94]:

$$\hbar\omega_q = 2 J S \left[Z - \sum_{r_c} \cos(q \cdot r_c) \right] \quad (2.17)$$

being the sum evaluated over the Z vectors r_c connecting the central magnetic moment to its nearest neighbours. Besides, a simple inspection of both eqs. 2.16 and 2.17 also allow us to conclude, that **both AF and FM dispersion curves evidence a gap at $q = 0$** . The occurrence of this gap has been ascribed to the magnetocrystalline anisotropy [1, 94], which may shift the values of $E(q)$ curves.

⁴FM dispersion at $q \rightarrow 0$: $\hbar\omega_q \propto 1 - \frac{q^2}{2!} + \frac{q^4}{4!} - \dots$

Luckily, the NdCu_2 alloy, analysed in Chapter 5, displays a long-period commensurate propagation vector, where the magnetic unit cell is ten times the length of the body-centred orthorhombic unit cell. This corresponds to a period of 20 atomic Nd^{3+} layers along the a axis. Besides, no trace of the bulk incommensurate structure is found in the nanoparticle state, which eases the way. Here again, we will try to keep the mathematical descriptions as simplest as possible. Thereby, we will not describe the mathematical treatment of these magnetic excitations, since it is out of the scope of this Dissertation. We would like to mention, very briefly, that the spin wave contribution to the Hamiltonian can be also described by means of the Stevens' operators, taking into account the Random Phase approximation (RPA) and sticking within the Mean-Field (MF) approximation [107, 108]. In this framework, magnons are expected to reproduce well the Callen-Callen theory, provided that the number of accessible energy states is not limited [92, 109].

It should also be noted that the spin wave propagation is affected by the magnetoelastic effect, which is always present in Rare Earth ions [110], since it couples the magnetic moments and the lattice. Therefore, modifications in the unit cell parameters have an impact on the magnetic state, that obviously affect substantially the spin wave propagation. The alteration of the spin wave propagation comes as a result of both the static deformations of the crystal, that are a source of anisotropy, and the interference of the dynamic time-dependent modulations of the magnetic moments with the lattice vibrations (magnon-phonon interaction) [94].

Finally, in order to connect (shortly) this theoretical background to the experimental observations, it is worth mentioning that obtaining experimental results from the dispersion curves in real samples of polycrystals and nanoparticles is beyond the realistic possibilities. Even if one aims to account for the $\hbar q$ dependencies of eq. 2.16 in the experimental curves, as, for instance, the ones shown in Fig. 5.12 of Chapter 5, the realistic experimental conditions of polycrystals and nanocrystallites preclude the direct application of the text-book eq. 2.16 to the data. Furthermore, the determination of such dispersion curves is challenging even for the case of a single crystal [1, 94, 111]. Fig. 2.4b showcases the study carried out by M. Rotter *et al.* in a NdCu_2 single crystal [102]. There, it can be seen that the experimental data themselves do not allow to clearly identify all the magnetic modes taken place in this AF structure. The reasons for this are both the rapid variation of the scattering intensity, and the limitations regarding the experimental resolution, which imply non-negligible uncertainties around each data. **The cooperation between numerical modelling** (which are out of the scope of this

Thesis work) **plus experimental data is essential to disclose the static and dynamic properties of this kind of complex magnetic systems.**

Chapter 3

Experimental methods

*“¿Dónde estás, que no te veo? Sin
ti me siento feo.”*

Chris Viaz feat. Young Vene

This chapter will provide an overview on the different steps that are involved in the sample fabrication and the measuring processes. The latter have been schematically displayed in Fig. 3.1. More precisely, **this recapitulation will stress on some of the model considerations that connect the experimental observations to the underlying physics of the different samples**, given the fact that the general features and basic performance of the instrumental tools have already been explained in great detail in precedent works (e.g., [34, 48]). Furthermore, among the different experimental techniques, the ones which have provided the most powerful results presented in this work were the neutron-based ones. These encompass Neutron Diffraction (ND), Small-Angle Neutron Diffraction (SANS) and Inelastic Neutron Scattering (INS). Therefore, a more careful description of these techniques will be provided in the following.

3.1 Sample fabrication and preparation.

The first step concerns the sample fabrication, which has been performed differently depending on the sample origin of magnetism ($4f$ or $3d$). In this way, **the $4f$ alloys** (RCu_2 , $R = \text{Gd, Tb, Nd, La, Y}$) were fabricated from the starting products (i.e., from the purchased bulk ingots), producing the polycrystalline pellets in an **arc furnace** (MAM-1 Johanna Otto GmbH) under an Ar atmosphere (99.99%).

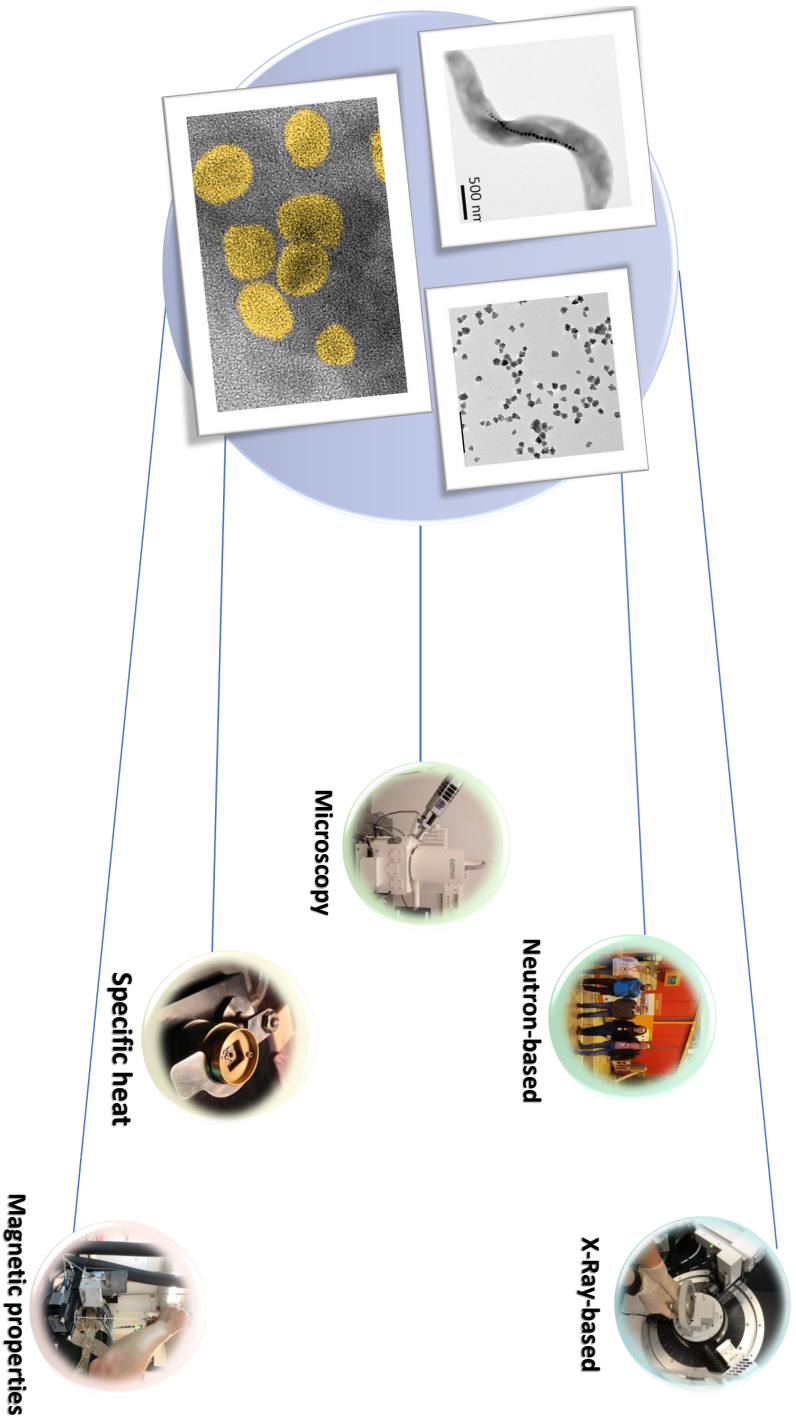


Figure 3.1: Sketch on the different experimental techniques used along this Thesis work. Sample preparation comes, of course, in a previous step. Whereas X-Ray-based and Transmission Electron Microscopy bring, generally speaking, information on the structure, magnetic and thermodynamic (specific heat) techniques allow to understand the macroscopic sample properties. Neutron-based techniques provide information on the microscopic structure, magnetism and collective excitations of the materials.

Stoichiometric amounts of R (>99.9%) and Cu (99.999%) pure metals, were put together to obtain large (~ 5 g) quantities. In order to ensure a good homogenisation, the resulting pellets were turned upside down and re-alloyed for, at least, six times. The reduction of mass after this remelting step was minimal ($\lesssim 0.01\%$).

After this arc-melting process, **the reduction of particle size was achieved using a high-energy planetary ball mill** (Retsch PM 400/2) with carbon-tungsten (WC) air-tight containers. For this, the pellets were crushed in an agatha mortar, placing the resulting coarse-grained powder inside the WC containers, together with a precise number of WC balls. The ratio ball:sample weight was 12:1, as the common practise indicates excellent results [39, 112]. The containers were sealed off under Ar atmosphere (99.99%) in a glove box to minimise the presence of oxygen that might oxidise the RCu_2 alloys. At this point, it is worth recalling that, if at all, this oxide were present, it would not appear as more than one or two surface layers. In any case, its low ordering temperature (antiferromagnetic transition $T_N = 13$ K in the case, for instance, of nano Gd_2O_3 [113]) minimises the influence in the intrinsic RCu_2 transitions found at higher temperatures. The nanometric size of the alloys was adjusted by selecting different milling times ($t = 0.5, 1, 1.5, 1.75, 2$ and 5 h). Note that the milling time is short, which allows not only to avoid the eventual formation of R_2O_3 , but it also opens the possibility to get nanometric samples right away. The grinding was carried out with rotation speed of 200 rpm in successive steps of 5 min of clockwise rotations followed by anti-clockwise rotations with a 5 min intermediate stop. The whole procedure is sketched in Fig. 3.2.

Additionally, some measurements (Small-Angle Neutron Scattering, SANS, and Specific heat, c_P), required the alloys to display a particular shape. More precisely, these techniques imposed the powders to be pressed, in order to form compact pellets (circular disks in the case of SANS). This has been achieved by using a Specac's Atlas Series hydraulic press, applying 2 tons (SANS) and 1 ton (c_P).

The procedure above described and sketched in Fig 3.2 connects with a long-debated question on how to proceed in the characterisation of MNPs. Recent examples of the different techniques for MNPs are well described in [21, 114]. As a consequence of the discussions shared in the EU project Nanomag with the participation of standardisation institutes (e.g., NPL in UK, or PTB, in Germany), it was proposed that techniques should be classified in three categories: *standard*, *medium* and *advanced* [115]. Thereby, in our case, Transmission Electron Microscopy (TEM), static $M_{DC}(T, H)$ and dynamic $\chi_{AC}(T, f, t)$ susceptibility

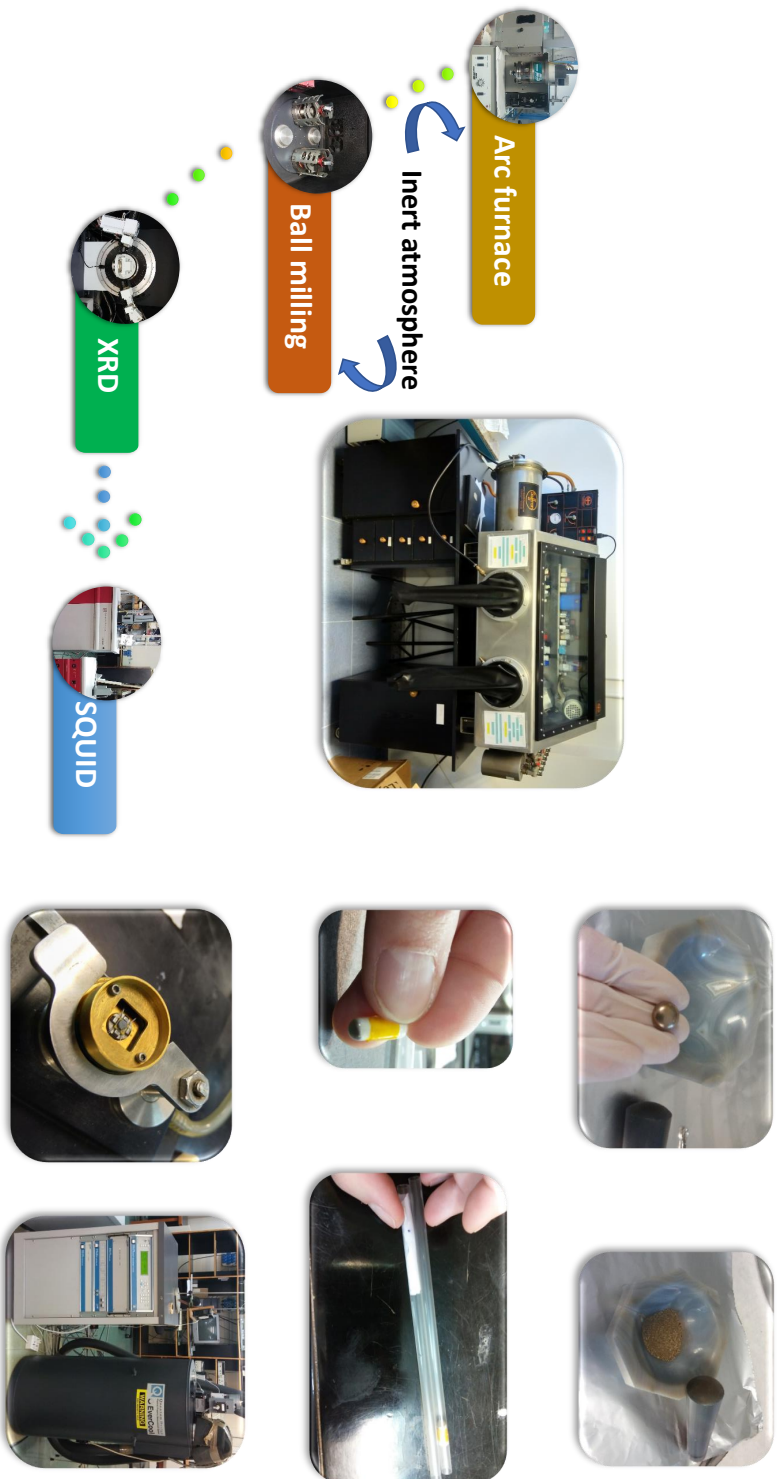


Figure 3.2: The cycle on the left represents the regular measuring processes, from the sample preparation to the magnetic measurements, performed at the University of Cantabria. Pictures on the right showcase some of the details encompassed by the different sample preparations. For instance, magnetometry measurements required the sample powder to be placed within gelatin-capsules closed with kapton tape mounted in plastic straws (see middle figures on the right).

will belong to the *standard* category, XRD, to the *medium*, and, finally, Neutron-techniques (ND, SANS and INS, explained below), to the *advanced* ones. This classification is not irrelevant when looking for technology transfer.

The situation concerning the synthesis of **3d IONPs** is completely different. On the one hand, **commercial Synomag Nanoflowers (γ -Fe₂O₃) were supplied by Micromod Partikeltechnologie GmbH (Germany)**. These MNPs were synthesised following a polyol method [116, 117], which ensures their size, shape and chemical purity. On the other hand, the **bacterial magnetosome (kept inside the bacteria, *intracellular*, or extracted) were supplied by our collaborators at the University of Basque Country (UPV/EHU)**. The magnetosomes are cube–octahedral magnetite Fe₃O₄ nanoparticles of size $\langle D \rangle \sim 40$ –45 nm synthesised by magnetotactic bacteria from the *Magnetospirillum gryphiswaldense* strain MSR–1 (DMSZ 6631). Bacteria were cultured microaerobically at 28°C for 48 hours in Flask Standard Medium (FSM), as described by Heyen and Schüler [118], supplemented with 100 μ M iron (III)–citrate to support magnetosome formation. Briefly, culture was carried out in three 1 L–bottles at 28°C under microaerobic conditions (bottles loosely capped and without shaking). Cells were collected after 120 h when well–formed magnetosomes were present. Bacteria magnetosomes (BM) have been measured either in the whole cells (*intracellular*), which has been the case of XRD, XANES, DC–magnetometry and dynamic AC–susceptibility measurements; or extracted from the bacteria (*extracellular*), which has been the one for TEM and AC magnetometry.

For the preparation of whole bacteria samples, the cells were harvested by centrifugation, fixed in 2% glutaraldehyde, and washed three times in mQ water. The fixed and washed cells were freeze–dried, resulting in a powder sample. Complementary, magnetosomes were extracted following the protocol described by Grünberg et al. [119] with minor modifications. The cells were collected by centrifugation, suspended in 20 mM HEPES–4 mM EDTA (pH = 7.4), and disrupted using a French press at $P = 1.4$ kbar. The lysated cells were sonicated, promoting the separation of magnetosomes, and centrifuged at 600 g for 5 min, to remove cell debris. Then, magnetosomes were collected from the supernatant by magnetic separation and rinsed 10 times with 10 mM HEPES–200 mM NaCl (pH = 7.4). Finally, the isolated magnetosomes were re–dispersed in deionized water (pH 7.4), sterilised in autoclave (115°C, 15 min), and stored at 4°C in a conventional fridge. The stability of the magnetite magnetosomes against oxidation is secured during several weeks.

Additionally to the undoped BMs, there are in the literature some recent and promising works reporting the possibility to include some elements, such as Co, Cu or Mn, to the magnetosome structure, by a process that is called *doping* [120, 121, 122]. By incorporating such *3d* elements to the magnetosome structure, the magnetic properties of the BMs get altered, displaying greater coercivity and/or remanence, as it has been shown, for instance, in [34]. Within the framework of this Thesis work, **we have aimed to go one step beyond**. Given our solid background on *4f* magnetism, we decided **to dope the BMs with Gd³⁺ and Tb³⁺ ions**. This is totally new in the literature, since there are no works, to the best of our knowledge, where bacteria were grown in a medium containing a controlled amount of R-ions, except from that of Shimoshige *et al.* [123], where the incorporation of Sm ions into *Magnetospirillum magneticum* strain RSS-1 was achieved. Given the lack of previous investigations, we decided to mimic the strategy followed to get Co and Mn doping in magnetotactic bacteria shown in [34, 35]. Thereby, the Gd³⁺/Tb³⁺-doped bacteria were cultured following the same procedure that the one commented before for the undoped bacteria, but adding different concentrations of GdCl₃/TbCl₃ hexahydrate salts to FSM medium. Of course, given that free R ions can be toxic, before moving forward, it was mandatory to check the living conditions and motility of bacteria, which was carried out by optical microscopy and optical density (*OD*) measurements. What we observed is that not only bacteria could grow in this medium, but also they synthesised magnetosomes. This preliminary test allowed us to proceed to the growth of bacteria.

For this purpose, the Minimum Inhibitory Concentration (MIC), this is to say, the concentration of R salts at which the growth of bacteria was hindered, was needed to be determined. The results for the cultures are shown in Fig. 3.3, where the OD at 565 nm at different concentrations for the bacteria grown in the presence of the R-salts are shown. This OD is based on the amount of light scattered by the culture of each single well. A Synergy HTX Multi-Mode Microplate Reader (BioTek) was used for this purpose. Given that the MIC value is determined as the cut-off point of cell-growth, according to Fig. 3.3, we decided to work with a concentration of 100 μM of R salts and 100 μM of Fe (Gd[100:100] and Tb[100:100] from hereinafter). Additionally, we grew bacteria with a concentration of 10 μM of R salts and 100 μM of Fe, [10:100], to check whether the crystallinity of the magnetosomes could be altered by a lower concentration of R.

transmission mode using a double Si crystal monochromator oriented in the [111] direction. A reference Fe-sample was measured for determining the position of the bacteria Fe-K edge ($E = 7112$ eV).

Data analysis was performed by using FullProf suite program [124] (XRD) and the Athena package of Demeter software [125] (XANES). We would like to focus more on the XRD analyses, as this technique has extensively been used throughout this work to verify the crystalline structure of the $4f$ and $3d$ ensembles, so as to determining the mean nanoparticle size and microstrain of the NPs. After the detailed description of the XRD analyses, a brief description of the XANES analyses will be included.

Beginning with the XRD analyses considerations, **the quantification of the nanocrystalline structure was achieved by performing a Rietveld refinement** [126]. Despite the fact that the precision of the parameters is usually less in ensembles of NPs than in perfect polycrystalline samples, if one follows a careful fitting procedure, the definition of the nanostructure is solid and supports other structural techniques [127, 128].

The theoretical intensity profile, $y_{c,i}$, used in the Rietveld calculations includes the following contributions:

$$y_{c,i} = y_{b,i} + \sum_{\phi} S_{\phi} + \sum_{\vec{h}} I_{\phi,\vec{h}} \Omega_{\phi,\vec{h},i} \quad (3.1)$$

being $y_{b,i}$ the background intensity, S_{ϕ} the scale factor of phase ϕ , $I_{\phi,\vec{h}}$ the integrated intensity, which includes the Lorentz factor, absorption correction, preferred orientation, structure factor and special corrections such as detector efficiency. Finally, $\Omega_{\phi,\vec{h},i}$ accounts for the profile peak function.

The refinement of the patterns has been performed using the least-squared method, taking as variables both instrumental and structural parameters of the sample. The aim was, therefore, to minimise the expression:

$$\chi^2 = \sum_{i=1}^n w_i (y_i - y_{c,i})^2 \quad (3.2)$$

where y_i is the intensity for the $2\theta_i$ experimental data, $y_{c,i}$, the calculated profile and $w_i = 1/\sigma_i^2$ weights the data errors for each i . Then, the agreement

between the experimental and the calculated pattern is shown by means of the Bragg factor, R_B , defined as:

$$R_B = \frac{\sum_i |y_i - y_{c,i}|}{\sum_i |y_i|} \quad (3.3)$$

Given that, our measurements are performed in nanocrystalline compounds at a finite temperature with not ideal point-like source of radiation, theoretical Dirac-delta shaped peaks are not expected. Actually, the peaks broaden in both Lorentzian and Gaussian shapes. It is thanks to this peak broadening that one can extract information about the size of the crystalline particles and their microstrain [128, 129]. To access this information, it is compulsory to correctly evaluate the contribution to the peak broadening that arises from the instrument as well. This is parameterised by a resolution function (Cagliotti parameters [130, 131]), and was obtained from a LaB₆ calibration. This compound presents numerous Bragg reflections, being hence frequently used as a calibration standard.

At this point, it is necessary **to connect the crystal domain size to the actual size of the nanoparticles**. From the fundamental point of view, the contribution to the peak broadening due to the NP size is calculated by the Scherrer equation 3.4:

$$B(2\theta) = \frac{\Upsilon \cdot \lambda}{\zeta \cos(\theta)} \quad (3.4)$$

Being $B(2\theta)$ the peak width measured in rad, λ the wavelength for the diffracted beam and ζ the size of the coherent crystalline domains of the diffraction. Υ takes into account the shape and the method used to determine size distribution. The majority of the NPs concerned in this work display, as shown by TEM images, quasi-spherical shape. In such a case, $\Upsilon = 0.9$, as indicated in [114]. In addition, the same factor is used for the case of the 3d NPs, for the same reason. The connection then between the crystal domain ζ and the mean NP size $\langle D \rangle$ is straightforward according to [132]:

$$\langle D \rangle = \frac{4}{3} \zeta \quad (3.5)$$

On the other hand, **the microstrain contribution** to the peak broadening, η , arises, mainly, from the milling process, although the size reduction to the nanoscale also implies slight distortions in the crystalline unit cell. This generates not uniform crystalline distortions that give rise to local variations of lattice distances among crystalline sites. This contribution can be easily calculated following:

$$B(2\theta) = 4\eta \cdot \tan(\theta) \quad (3.6)$$

As it comes naturally, the latter microstrain contribution is more relevant at high angles, whereas the former size contribution becomes heftier at low angles. So, at this point, one can easily obtain an estimation of the nanoparticle size and microstrain by inspecting the peak broadening arising from the XRD pattern. It seems clear then that the sticking point is related to the way that this peak shape is considered, as the peaks are, actually, a convolution of both Gaussian or Lorentzian profiles. If one fits the peaks into just one of these two options, different values of Full-Width-at-High-Maximum, $FWHM$, will be obtained, leading to different $\langle D \rangle$ and η . Therefore, a more realistic and precise scenario would be considering the peak shape according to a Voigt profile, which is constituted by the convolution of Gaussian and Lorentzian ones. This Voigt profile can be approximated, without loss of accuracy, to a Pseudo-Voigt $pV(X)$ description, which consists on a linear combination of both Lorentzian (L) and Gaussian (G) profiles. Both L and G display the same $FWHM$. The relevant information about micro-structure and size and microstrain effects are deduced from:

$$pV(x, \eta, H) = aL^p(x, H) + (1 - \eta)G^p(x, H) \quad (3.7)$$

This function employs H and η parameters instead of using the form factors H_L and H_G . Nevertheless, one can write eq. 3.7 in terms of H_L and H_G using the Thompson-Cox-Hastings equations, that connect the form factors of a Voigt and a pseudo-Voigt [133] as:

$$H = H_G^5 + 2.69269H_G^4H_L + 2.42843H_G^3H_L^2 + 4.47163H_G^2H_L^3 + 0.07842H_GH_L^4 + H_L^5 \quad (3.8)$$

and

$$\eta = 1.36603 \frac{H_L}{H} - 0.47719 \left(\frac{H_L}{H} \right)^2 + 0.11116 \left(\frac{H_L}{H} \right)^3 \quad (3.9)$$

The parametrisation of $pV(x)$ by means of the form factors H_L and H_G is of primer interest, since it provides information on the microstructure and on the size and microstrain. These contributions are accessed by following:

$$\begin{aligned} H_G^2 &= \left(U + (1 - \xi)^2 D_{ST}^2 \right) \tan^2\theta + V \tan\theta + W + \frac{I_G}{\cos^2\theta} \\ H_L &= (X + \xi D_{ST}) \tan\theta + \frac{[Y + F(S_Z)]}{\cos\theta} \end{aligned} \quad (3.10)$$

where U , X (isotropic) and D_{5T} (anisotropic) are the parameters connected to the microstrain; and Y , I_G (isotropic) and $F(S_Z)$ (anisotropic) are related to the size. Finally, ξ sets the lorentzian contribution to the microstrain. Since the instrumental contribution is well defined by the measured Cagliotti parameters, the parameters V and W of eq. 3.10 should be ignored.

Jumping onto the brief description of X-Ray Absorption, this measuring technique is not related to the scattering, but to the *absorption* of the photons by the atoms, mainly, via the photoelectric effect [134]:

$$E_{kin} = \hbar\omega - E_0 \quad (3.11)$$

being E_{kin} the kinetic energy of the incident electrons, $\hbar\omega$ the energy of the incoming X-rays and E_0 the binding energy. The absorption process takes places, provided that $\hbar\omega > E_0$, according to:

$$I_t = I_0 e^{-\mu(E)th} \quad (3.12)$$

being I_t the intensity transmitted through the sample, I_0 the intensity of the incident X-ray, $\mu(E)$ the absorption coefficient, and th the thickness of the sample.

When a core level electron is promoted to a free-state above the Fermi energy level, a sharp increase of the absorption coefficient is retrieved. This feature in the spectrum is typically known as the *absorption edge*. Depending on the E_{kin} , the excited electron can promote to a higher energy level, but still on the same absorbing atom (localised state), or it can reach the continuum states and propagate into the material. If this is the case, these electrons interact strongly with the potentials of the surrounding atoms, giving rise to fine structure oscillations (XAFS) that modulate the μ . There are two regions that can be distinguished for the XAFS: the near-edge (XANES) and the extended, EXAFS. In this Thesis work we have focused on the XANES, which typically extends from a few eV below the absorption edge up to 100–150 eV above the edge. From the latter measurements, information on the electronic properties and the local geometry around the absorber atom are gained [135].

More precisely, **we have used XANES to identify and quantify the amount of γ -Fe₂O₃ and Fe₃O₄ phases in the NFs and in the BMs.** To this aim, we have used the **linear combination analysis (LCA) method**, where the normalised spectrum of the sample, μ_{exp} , is fitted to a linear combination of normalised

spectra of the reference compounds, μ_j , weighted to the atomic fraction of each phase by a factor α_j , according to:

$$\mu_{\text{exp}} = \sum_j \alpha_j \mu_j \quad (3.13)$$

This method is rather straightforward, provided that the reference patterns display a good quality, and has been widely used in a variety of research fields, such as biology or material science [40, 136, 137].

3.3 Neutron–scattering techniques.

The use of neutrons is key to unravel the structural and magnetic features in both bulk and nano alloys, particularly, for the RCu_2 . In this way, $4f$ alloys can be considered as a playground which gathers attractive phenomena, such as crystalline electric field (CEF) excitations, complex magnetic arrangements (helical, incommensurate...) and/or inter/intra particle correlations [110, 111, 138]. These appealing phenomena, though, impose the use of neutrons to be defined with precision at the **microscopic scale**. Although the previous section has showcased the potentialities of the X–Ray based techniques, here, it is important to recall that they have no associated magnetic moment. This implies that *the magnetic structure* gets, in practice, *invisible* for X–rays¹. Furthermore, whereas the scattered X–ray photons interact with the electronic cloud surrounding the nuclei, **the non–charged neutrons penetrate the Coulombic barrier**. This allows neutrons to interact dipolarly with the nuclear spins, so as with the magnetic moment of the unpaired electrons. Thereby, we gain access not only to the nuclear structure, but also, to the magnetic one. Furthermore, another difference between neutrons and X–rays is that the scattering length of neutrons depends, additionally to the scattering elements, on their particular isotope state and on the quantum angular momentum number of the nucleus–neutron system, $I \pm 1/2$. Hence, some of the scattered waves will have definite relative phases, thus, being able to build interferences (coherent scattering), whereas there will also be a contribution to the scattering stemming from neutrons that interact randomly with each nucleus of the sample (thus, without interfering). Another difference with XRD concerns that the scattering length of XRD (form factor) shows a dependence on the atomic

¹polarisation analyses using, for example, X–ray magnetic circular dichroism allow to extract a different magnetic information.

number, which hampers the distinction between isotopes and/or with adjacent elements in the periodic table. Furthermore, light elements, such as C, N or O, cannot be detected by XRD, yet they are visible to neutrons. Taking all this into account, **we are going to use of neutrons to unravel how the magnetic structures develop once the nanoparticle regime is entered**, but also, **to disclose some particularities about the microscopic magnetic structure in some of the bulk 4f alloys**.

In the following, we would not dare to give a deep-saturated mathematical equation-based description on the Neutron Diffraction process, as there are already several works and textbooks in the literature where all these issues have been addressed in great detail. I would like to refer the reader to [138, 139, 140, 141, 142]. Nevertheless, when working with neutrons, providing a good definition of the magnitudes, geometries and processes that are going to be taken into account is essential.

Hence, we will begin by introducing the well-known *master* equation that describes the process where an incoming neutron is scattered by a material. This interaction is quantified by the differential scattering cross-section, which is normalised to the solid angle $d\Omega$, the incident neutron flux ϕ and the number of atoms constituting the incoming beam, N , as:

$$\left(\frac{d\sigma}{d\Omega}\right)_{k_i, \sigma_i, \lambda_i \rightarrow k_j, \sigma_j, \lambda_j} = \frac{1}{N\phi d\Omega} \sum_{k_j} W_{k_i, \sigma_i, \lambda_i \rightarrow k_j, \sigma_j, \lambda_j} \quad (3.14)$$

where the initial states of the sample λ_i and the neutron, k_i, σ_i , are changed to λ_j, k_j, σ_j , respectively. The term $W_{k_i, \sigma_i, \lambda_i \rightarrow k_j, \sigma_j, \lambda_j}$ stands for the number of transitions per second from state i to the state j , and Φ is the flux of incident neutrons. This term can be evaluated using Fermi's Golden rule as:

$$W_{k_i, \sigma_i, \lambda_i \rightarrow k_j, \sigma_j, \lambda_j} = \frac{2\pi}{\hbar} |\langle k_j \sigma_j \lambda_j | \mathcal{V} | k_i \sigma_i \lambda_i \rangle|^2 \rho_{k_i \sigma_i}(E(i)) \quad (3.15)$$

being \mathcal{V} the interaction potential between the neutron and the sample, and $\rho_{k_i \sigma_i}(E(i))$, the density of the final scattering states per unit energy interval. Here, we assume an isotropic short-ranged scattering behaviour for \mathcal{V} (Born-approximation), a framework within the first-order perturbation theory applies, and, consequently, Fermi's Golden rule holds true. Additionally, this microscopic scattering cross section $\frac{d\sigma}{d\Omega}$ defined by the *master* equation is related to the macroscopic differential

cross-section per volume V as:

$$\frac{d\Sigma}{d\Omega} = \frac{N}{V} \frac{d\sigma}{d\Omega} \quad (3.16)$$

Finally, as it is well-known, **scattering processes can be elastic**, where the structure factor that contains information about the atomic positions is given by $S(q)$, **or inelastic**, for which this factor does also contain information on the fluctuations of the atoms, $S(q, \hbar\omega)$. The latter Inelastic Neutron Scattering (INS) process allow typically to access information on the single-particle crystalline electric field (CEF) and collective magnon excitations processes (as examples, but also, to the phonon spectrum, certainly). The q values accessible by using this technique lie within the range 10^{-2} – $10^{-11} \text{ \AA}^{-1}$, corresponding to energy excitations between 10^{-5} – 100 meV , which are the typical values for energy level transitions. The point that neutrons carry information of both nuclear and magnetic natures makes this technique so powerful, as it provides mainly information regarding phonon and CEF, as well as magnon excitations. The following two subsection will bring some details to these scattering processes.

3.3.a Elastic neutron scattering

The elastic neutron scattering can be defined assuming the momentum-transfer (scattering vector, q) to be described as the difference between the initial and the final states of the neutron vector k :

$$q = k_i - k_f \rightarrow \text{Elastic} : k_i = k_f = \frac{2\pi}{\lambda} \quad (3.17)$$

being the neutron energy change:

$$\Delta E = E_i - E_f = \frac{\hbar^2}{2m_n} (k_i^2 - k_f^2) \rightarrow \text{Elastic} : \Delta E = 0 \quad (3.18)$$

Neutron Diffraction (ND) and Small Angle Neutron Diffraction (SANS) techniques are included within this elastic regime. The former provides information on the nuclear and magnetic structures in an angular range very similar to the typical one of in-house XRD ($5^\circ \lesssim 2\theta \lesssim 120^\circ$). On the other hand, SANS focuses on the scattering process that take place in the low-angle regime, generally, $2\theta \lesssim 5^\circ$. This range may be accessible in the Small-Angle X-ray scattering technique as well, but no experiments have been carried out so far in our samples. Given the analyses of the magnetic dynamics of MNPs carried out in this Thesis,

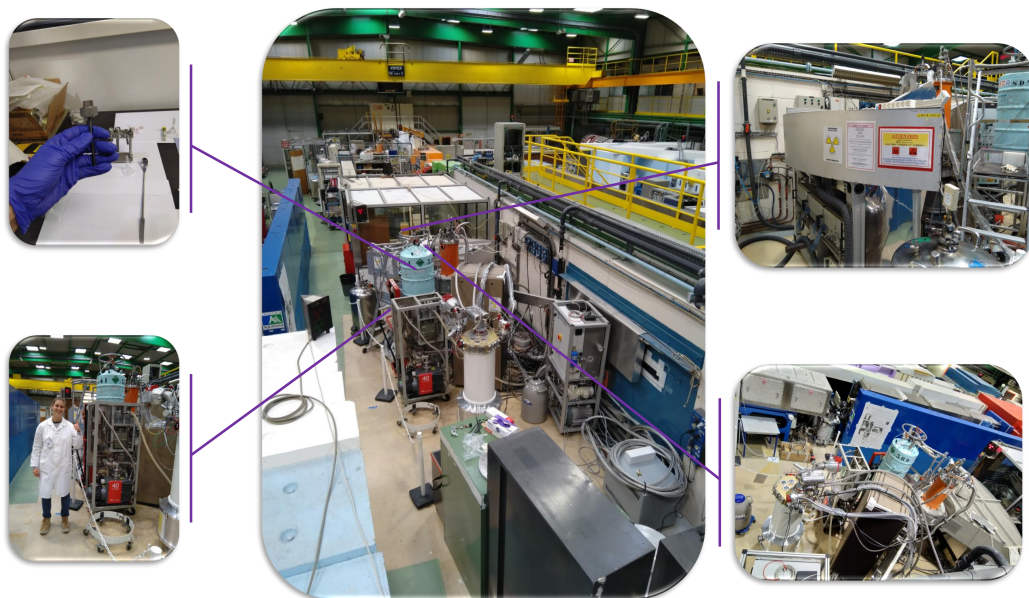


Figure 3.4: G4.1 detector located at LLB (Laboratoire Léon Brillouin) at the CEA–Saclay. The accessible dispersion angle lies within the range $3^\circ \leq 2\theta \leq 105^\circ$, with a step of 0.02° . Patterns have been measured with $\lambda = 2.432 \text{ \AA}$ (cold neutrons) at different low temperatures thanks to the use of an *orange* cryostat. This is clearly visible standing close to the neutron guide and beside a liquid He (blue) Dewar. The powder alloys were mounted in the sample holder, as shown in the top–left image.

accessing the small angle region was, nearly, mandatory. Thanks to these measurements, we may reveal the correlations among the magnetic moments, that are usually of the order of a few nanometers. The SANS technique is unique in this sense, as it opens the path to study microstructural and magnetic inhomogeneities at a length scale between $\sim 1\text{--}300 \text{ nm}$ [13, 143]. The fact that a variety of macroscopic magnetic properties, including bulk and, of course, nanoscaled materials, are realised within this range, this technique sparkles on its own.

ND experiments were conducted at the G4.1 instrument located at Laboratoire Léon Brillouin (LLB) at CEA–Saclay, France, and at D1B instrument, located at Institute Laue–Langevin (ILL), in France. The latter ND measurements were carried out by PhD. María de la Fuente Rodríguez. The wavelength of the neutrons was $\lambda = 2.426 \text{ \AA}$ and 2.520 \AA (thermal cold neutrons), respectively. Patterns were collected at several temperatures between $T = 1.5 \text{ K}$ and 15 K under no magnetic applied field. The measuring time for each pattern was set to 8 h in order to ensure a high signal–to–noise ratio. Fig. 3.4 provides an overview on G4.1

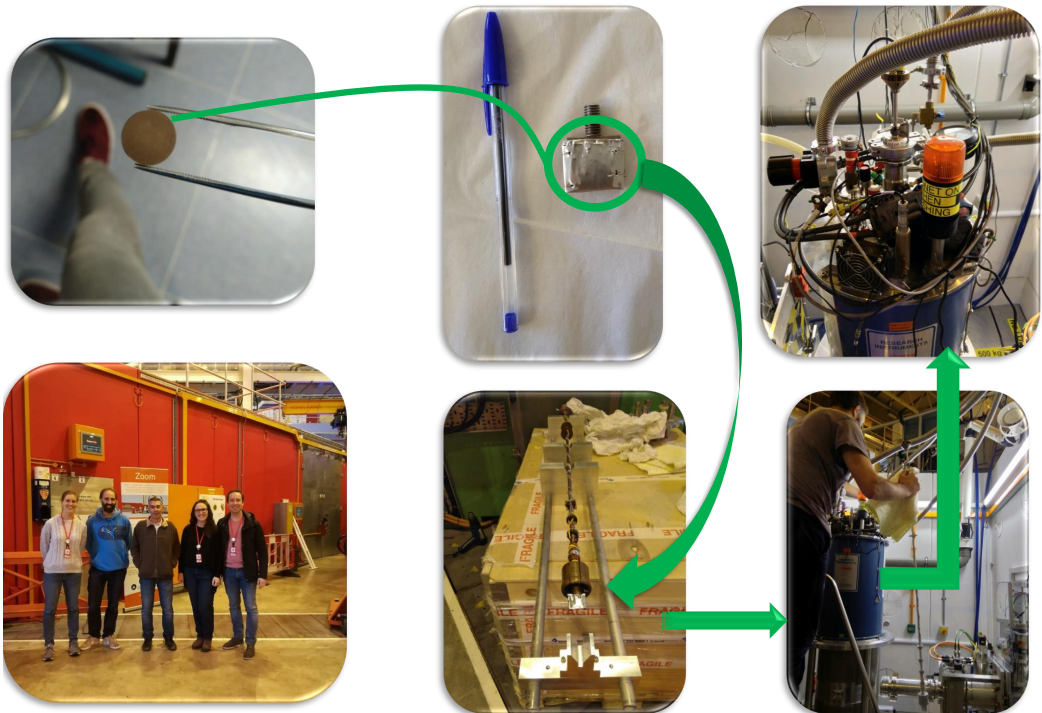


Figure 3.5: Some illustrative images regarding the SANS measurements performed with ZOOM instrument, located at the Rutherford–Appleton Laboratory (ISIS) large facility, in Oxford, United Kingdom. The NdCu_2 powder alloys are compacted in pellets (disks of 1 mm thickness and 10 mm diameter) and mounted in the sample holder (aluminium–foiled). It is important to find a balance between the required amount of sample, that has to be enough to be measured, and the need to avoid multiple–scattering processes, which implies thinner disks. The use of a cryostat allowed to reach temperatures around 2 K and magnetic fields up to 3 T (Oxford instruments).

instrument, where some zones are shown with a closer detail. For instance, on the top-left picture, a closer view to the sample holder, which is placed inside an *orange* cryostat, can be inspected. On the top-right side, a front-view of the detector, which consists on a lineal multi-detection system made of 800 cells of BF_3 , is shown.

SANS measurements were performed using the ZOOM instrument located at Rutherford–Appleton Laboratory ISIS large facility, Oxford, United Kingdom. The measurements were performed in both $k \perp$ and $k \parallel$ geometries (explained below), for a temperature range between $T = 2\text{--}15$ K and applied magnetic fields $\mu_0 H = 0\text{--}3$ T. Fig. 3.5 illustrates some of the aspects of that SANS experiment, including the compacted-powder samples (pellets), the sample holder and the cryostat, which allows to access temperatures as low as 2 K. The detector distance to the sample can be changed in order to select a particular q range, which in our case, was of $0.04\text{--}4$ nm^{-1} . It is worth reminding at this point that RAL–ISIS is an spallation source, where neutrons are pulsed (50 Hz) and a time-of-flight detection procedure is natural. This contrasts with LLB and ILL, where a continuous flux of neutrons is provided by the nuclear reactor.

A detailed background description of neutron diffraction is available in several precedent works, *e.g.*, [13, 138, 141]. Therefore, here we will just concentrate on the most important features concerning the SANS, which have merited attention during the development of the Thesis work.

As it was described before, **the scattering cross-section contains information of both the nuclear and the magnetic structures**. Within the elastic framework, and in order to keep the mathematics as simple as possible, we would just write the radially-averaged unpolarized macroscopic differential SANS cross-section per unit of volume, $\frac{d\Sigma}{d\Omega}(q)$, as a sum of a nuclear $\frac{d\Sigma_{nucl}}{d\Omega}(q)$ plus a magnetic contribution, $\frac{d\Sigma_{mag}}{d\Omega}(q)$, as:

$$\frac{d\Sigma}{d\Omega}(q) = \frac{d\Sigma_{nucl}}{d\Omega}(q) + \frac{d\Sigma_{mag}}{d\Omega}(q) \quad (3.19)$$

Each contribution is expanded according to:

$$\frac{d\Sigma_{nucl}}{d\Omega}(q) = \frac{8\pi^3}{V} \left| \tilde{N}(q) \right|^2 \quad (3.20)$$

where the $\tilde{N}(q)$ denotes the Fourier transform of the nuclear scattering-length density, and V is the scattering volume. The second term, $\frac{d\Sigma_{mag}}{d\Omega}(q)$, requires a

more careful description, which is going to be developed hereunder.

The magnetic scattering SANS cross-section will display a dependence upon the magnetic applied field, H_0 , is applied either parallel or perpendicular to the incoming k . This dependency is, obviously, not retrieved in the nuclear cross-section, since it does not carry information on the magnetization state of the sample. Of course, there could be intermediate situations between the parallel and perpendicular geometries, but, given that the vast majority of SANS experiments are performed employing these two scattering geometries, we will restrict our dissertation to them. In principle, a *purely* nuclear SANS signal should be recovered in the $k \parallel H_0$ geometry, while the $k \perp H_0$ shall carry nuclear plus magnetic information, if the sample magnetization is saturated at the applied H_0 . In this scenario, the scattering section of each component will read as:

$$\left(\frac{d\Sigma}{d\Omega}\right)_{par}(q) \approx \frac{8\pi^3}{V} \left(|\tilde{N}|^2 + b_H^2 |\tilde{M}_s|^2 \right) (k \parallel H_0) \quad (3.21)$$

and

$$\left(\frac{d\Sigma}{d\Omega}\right)_{perp}(q) \approx \frac{8\pi^3}{V} \left(|\tilde{N}|^2 + b_H^2 |\tilde{M}_s|^2 \sin^2(\theta) \right) (k \perp H_0) \quad (3.22)$$

where we have assumed that, at H_0 , the sample is completely saturated along z direction, *ie.*, $M(r) = \{0, 0, M_z = M_s(r)\}$; the constant $b_H = 2.91 \times 10^8 \text{ A}^{-1}\text{m}^{-1}$ [13]; and, for the perpendicular scattering geometry, θ accounts for the angle between the H_0 and the momentum-transfer vector, q .

This way, it is a very common straight-forward procedure to obtain the $\left(\frac{d\Sigma}{d\Omega}\right)_{perp}(q)$ by subtracting the $\left(\frac{d\Sigma}{d\Omega}\right)_{par}(q)$ from the total measured SANS cross-section at the saturation field. In this situation, the remaining $\left(\frac{d\Sigma}{d\Omega}\right)_{perp}(q)$ at saturation displays two different regions, traditionally known as the (*magnetic*) *Guinier* (low q) and *Porod* (high q) laws [144, 145]. These read, respectively, as:

$$\frac{d\Sigma_{mag}}{d\Omega}(q) \cong \frac{d\Sigma_{mag}}{d\Omega}(q=0) \exp\left(-\frac{q^2 R_{GSM}}{3-s}\right) \quad (3.23)$$

where R_{GSM} the radius of giration ($R_{GSM} = \sqrt{\frac{3}{5}}R$ in the case of spheres) and s an a -dimensional factor that contains information of the particle shape ($s = 0$ in

spheres). This approximation is valid for $q < 1.3/R_{GSM}$ [142].

At larger q , the $\frac{d\Sigma_{mag}}{d\Omega}(q)$ follows the Porod law:

$$\frac{d\Sigma_{mag}}{d\Omega}(q) \propto q^{-D} \quad (3.24)$$

being D an exponent related to the scattering inhomogeneities of the sample [144]. For smooth interfaces, $D = 4$, but this number can be, even, non-integer and/or greater than 4 [146, 147].

So far, we have outlined the framework adequate for the case where the sample magnetization is completely saturated at the applied magnetic field. Nevertheless, one may wonder about **what happens for the applied fields that are below the saturating one**. In this situation, an extra contribution to the SANS scattering cross-section comes to light, which is called as the *spin-misalignment* term, $\frac{d\Sigma_{SM}}{d\Omega}$. It has been proven that **this mesoscopic spin-misalignment (SM)** is an **important ingredient driving the magnetic behaviour** [13, 148]. We will give hereunder a very brief summary on the understanding of these deviations, that span a few nanometers. Although for the case of our samples, the implementation of the ensuing expressions is yet to be adequately implemented, we have considered of interest to grasp an understanding of this theoretical elaboration. It is important bearing in mind that we are concerned to magnetic SANS effects, thus, all the development will concern the \perp geometry.

Consequently, the above mentioned eq.3.22 should include a term giving account for the SM, *ie.*:

$$\left(\frac{d\Sigma}{d\Omega}\right)_{perp}(q) = \frac{d\Sigma_{res}}{d\Omega}(q) + \frac{d\Sigma_{SM}}{d\Omega}(q) \quad (3.25)$$

where the $\frac{d\Sigma_{res}}{d\Omega}(q)$ is simply, the term of eq. 3.22, and the $\frac{d\Sigma_{SM}}{d\Omega}(q)$ is expanded as:

$$\frac{d\Sigma_{SM}}{d\Omega}(q) = \frac{8\pi^3}{V} b_H^2 \left[\left| \tilde{M}_x \right|^2 + \left| \tilde{M}_y \right|^2 \cos^2\theta - \left(\tilde{M}_y \tilde{M}_z^* + \tilde{M}_y^* \tilde{M}_z \right) \sin\theta \cos\theta \right] \quad (3.26)$$

where it has been assumed that the sample saturation magnetization is along the z -axis, *ie.*, $\tilde{M}_s \sim \tilde{M}_z$. Thus, the \tilde{M}_x and \tilde{M}_y give account for the Fourier transforms of the magnetization out of the saturation direction, which is, actually, the spin-misalignment. This SM term can be described by means of two response functions,

$$\frac{d\Sigma_{SM}}{d\Omega} = \underbrace{S_H(q)R_H(q, \theta, H_i)}_{\text{anisotropy inhomogeneities}} + \underbrace{S_M(q)R_M(q, \theta, H_i)}_{M_s \text{ inhom}} \quad (3.27)$$

where the first term takes into account the spatial variations $M(r)$ due to the anisotropy field, and the second one accounts for the ones due to fluctuations on M_s . Each term can be expanded as:

$$S_H(q)R_H(q, \theta, H_i) = \frac{8\pi^3}{V} b_H^2 \left| \tilde{H}_P(q) \right|^2 \frac{p^2}{2} \left(1 + \frac{\cos^2\theta}{(1 + p\sin^2\theta)^2} \right) \quad (3.28)$$

being \tilde{H}_P the Fourier transform of the magnetic anisotropy field, and

$$S_M(q)R_M(q, \theta, H_i) = \frac{8\pi^3}{V} b_H^2 \left| \tilde{M}_z(q) \right|^2 \frac{p^2 \sin^2\theta \cos^4\theta}{(a + p\sin^2\theta)^2} + \frac{2p\sin^2\theta \cos^2\theta}{1 + p\sin^2\theta} \quad (3.29)$$

where p is defined in both eq. 3.28 and 3.29 as:

$$p(q, H_i) = \frac{M_s}{H_{eff}(q, H_i)} \quad (3.30)$$

with

$$H_{eff}(q, H_i) = H_i(1 + \ell_{ex} H_i^2 Q^2) \quad (3.31)$$

being ℓ_{ex} the exchange correlation length, already introduced in Chapter 2, and H_i the external applied magnetic field.

Therefore, the analyses of the SANS measurements would not be only restricted to the saturation field, but also, **details on the micromagnetic SANS structure could be accessed using the data corresponding to intermediate fields below saturation**. The next step will be to implement a program where

a generalisation of the magnetic Guinier–Porod law [145] could be realised. At this moment, this is still under development, and we are still trying to polish the different fitting routines². Although the SANS data presented in Chapter 5 cannot be analysed with the detail that is described here, it is expected that a future continuation of this work will require the concepts briefly described above.

3.3.b Inelastic neutron scattering

The inelastic neutron scattering (INS) studies physical processes implying a change in the energy of the incoming neutrons. Actually, this kind of scattering is always present in measurable condensed–matter systems, given the fact that, at $T > 0$, every atom is never completely still, but it is vibrating around the lattice equilibrium position due to the thermal energy. The more atoms vibrate and the more time they spend out of their equilibrium position, the greater this inelastic (structural) contribution gets. Nevertheless, compared to the elastic scattering, the INS contribution is several orders of magnitude smaller. As a result, the elastic signal may mask that from inelastic scattering, and the INS may therefore be only visible in the form of an attenuation of the Bragg peaks (Debye–Waller factor). However, the interest of determining the energy lost by neutrons when interacting with matter is of primer interest, since **it carries very powerful and rich information on the quantum states, magnon excitations or phonon propagation**, among others [94, 138, 149]. Just an acknowledgement for neutron scatterers, N. Brockhouse was awarded a Nobel prize in 1994³ supported by his investigations in INS, together with C. Shull, whose work was devoted to the development of neutron diffraction.

The use of Inelastic Neutron Scattering opens the path to analyse the single and/or collective excitations of energy that are included within the range of 10^{-5} –100 meV. As for the case of elastic neutron scattering, the INS signal encompasses two contributions: one stemming from the scattering with the nuclei, and a second one, which emerges from the interaction of the neutron spin with the unpaired electrons. The former is related to phonons, whereas the second carries information on **the single–particle excitations**, such as the ones driven by **crystalline electric field (CEF) effects**, but also, on **collective magnetic excitations associated with the propagation of the spin waves within the ordered region (magnons)** [94, 138]. In principle, **CEF excitations should**

²stay tuned for incoming publications.

³the same year I was born! ☺

be dispersionless, while **phonon and magnons should display an E vs. q dependence**. A simple way to distinguish whether a dispersion excitation is of nuclear origin (phonons) or magnetic is to follow such $E(q)$ variation. If the excitation energy transfer increases along with the wave vector transfer q , the excitation is triggered by phonons. On the contrary, if the energy transfer decreases as the q increases, one should expect a magnetic origin for the excitations [150]. Just to give a little background on these measurements, the first reported experimental observations of spin waves using this technique were made by Bjerrum Møller and Houmann at Risø [151]. Their work paved the way to the understanding of these collective excitations in magnetic structures, yet their determination in AF structures remains, still nowadays, challenging [92].

Before moving forward, one may reckon, at this point, about **how to experimentally distinguish between magnon excitations and the Zeeman splitting of the different multiplets**. The provenance of the former have been already explained in Chapter 2, whilst the latter came as a consequence of the appearance of local fields within the magnetic ordered region. These local fields are gathered in a single term, \mathcal{H}_m , which is introduced to the CEF Hamiltonian (see eq. 2.14), and provokes a splitting of the energy level multiplets. This opens the access to new sub-energy levels, to which the electrons can promote, leading to the appearance of extra peaks in the INS pattern. **A strong temperature dependency of the peak intensity, together with the observation of a gap**, are features usually ascribed to **magnons (spin waves)**, and are usually not retrieved for the case of the simply Zeeman splitting transitions.

To ease the reading of the INS description, we consider that it is better to focus on the main expressions that allow the experimental analyses of the data. We refer the reader to follow [92, 94, 138], where a deeper understanding is provided. Hence, we will describe the INS contribution by the term:

$$\frac{d\sigma}{d\Omega d(\hbar\omega)} = \frac{k_f}{k_i} S(q, \hbar\omega) \quad (3.32)$$

being $S(q, \hbar\omega)$ the INS intensity. The total integrated scattering intensity, $\int d(\hbar\omega) S(q, \hbar\omega)$, is independent of T , and falls off with q quadratically in the case of magnetic excitations. On the contrary, for the case of phonons, as we have already mentioned, an increase with q and T is observed [138]. This is usually inspected in the so-called *contour plots*, as it is going to be shown in Chapter 5. Regarding the magnetic contribution to INS, we will just briefly mention that only the magnetization components that are perpendicular to q contribute to the

scattering–cross section [138].

Another way to experimentally probe these excitations is to represent the measured $S_{mag}(q, \hbar\omega)$ vs. the $E_{transfer}$. There, according to the theoretical background provided in Chapter 2, **the outburst of peaks**, that account for the transitions between the energy levels corresponding to the splitting of the ground state multiplet due to the CEF, will emerge (apart from the instrumental background, sure). Needless to say, these peaks display non–zero width, rather than a Dirac–delta shape, due to the thermal disorder and quantum nature of electrons. Additional peaks shall emerge in the magnetic ordered phase due to the multiplet splitting caused by the Zeeman effect and/or to the magnon density state that cause the spin wave excitations [93, 94, 99], as it has already been said.

The INS analyses provided in this Thesis work focus on an ensemble of NdCu₂ with 13 nm–sized MNPs. It is worth recalling at this point that this is the first time that INS is performed in $4f$ ensembles of MNPs. In addition to the limited access to beam time, the INS technique requires the use of great amount of sample, in particular, of MNPs (~ 10 g), to get a sufficient signal–to–noise ratio, which is undoubtedly a *sticking point* for using this technique. As we have commented in the sample preparation, here, the use of the ball milling technique is key, since it provides a great amount of highly crystalline MNPs in a relatively easy and efficient way. To complete the results of the MNPs, we provide also a comparison with the NdCu₂ bulk alloy. This was accomplished by analysing the experimental data reported by E. Gratz *et al.* in [99]. We would have rather measured the bulk alloy by our own too, but the access to beam time is very limited and, unluckily, there was no time left to be invested on the NdCu₂ bulk alloy.

Accordingly, the NdCu₂ 13 nm–sized MNPs were measured using the neutron time–of–flight spectrometer IN4 located at ILL (France) with incident energies of $E_0 = 8.8, 16.7, \text{ and } 66.7$ meV, at three different temperatures, $T = 1.5, 5.25$ and 10 K. All spectra were collected and corrected for background, absorption, and self–shielding, and normalised to vanadium, by PhD. María de la Fuente Rodríguez. On the other hand, data for bulk alloy were performed by E. Gratz *et al.* on a polycrystalline sample using IN4 and IN6 time–of–flight spectrometers, at ILL too, with incident energies of $E_0 = 3.17$ (IN6), 12, 17, and 50 meV, at temperatures $T = 1.5, 3, 4.5$ and 10 K [99]. These spectra were also corrected for background, absorption and self–shielding, and put on an absolute intensity scale by a standard vanadium calibration [99].

Both data sets were analysed using Igor software by programming a non-linear fit. Several fitting functions were tried, to finally converge to a straight line background plus Gaussian peak-shape:

$$I = \underbrace{a \cdot E(q, \hbar\omega) + b}_{\text{background}} + \underbrace{\sum_i A_i \cdot e^{-4 \ln(2) \frac{E(q, \hbar\omega) - E_{0,i}}{FWHM_i^2}}}_{\text{Gaussian}} \quad (3.33)$$

being A_i the amplitude for peak i , $FWHM$ the Full-Width at High Maximum and $E_{0,i}$ the centre of the i -peak, which stands for the energy level position E_0 . One should remember that both A_i and $FWHM$ define together the peak area, which is related to the probability of transitions to i -level.

3.4 Microscopy. Transmission Electron Microscopy.

Transmission Electron Microscopy (TEM) is a powerful technique which allows to gain access to the nanoparticle morphology (shape) and size. In our case, the images were recorded employing the direct electron beam (Bright Field mode). In the case of $4f$ alloys, High-Resolution and EDX (Energy Dispersive X-Ray) spectroscopy techniques were also used in order to get an insight to the crystallographic planes in the NPs and to verify their chemical composition, respectively. Besides, Scanning Electron Microscopy (SEM) was performed to gain information on the sample morphology of bulk and some of the biggest $4f$ MNPs. These measurements were performed with the help of Ms. Seda Ulusoy at the clean room of the Ångström Laboratory, located at the Uppsala Universitët, with a Zeiss 1550 Gemini, working in topographic contrast mode. The samples were mounted on a rotary sample holder and sputtered with Au to enhance their contrast.

The sample preparation for **TEM measurements was different depending upon the origin of the sample magnetism**. In this way, the $4f$ MNPs required to suspend the solid powder in ethanol under ultrasonic vibration. Then, two drops of the suspension were applied to carbon films on copper grids. These measurements were performed on a Jeol JEM 2100 electron microscope (JEOL, Japan) at the TEM facility of the Universidad de Cantabria (SERMET) and at the Stockholm University (Ms. Seda Ulusoy), operating at an accelerating voltage of 200 kV. On the other hand, in the case of $3d$ MNPs, TEM was performed on

Synomag NFs and magnetosomes (extracted from the bacteria) adsorbed onto 300 mesh carbon-coated copper grids. The images were obtained with a JEOL JEM-14000Plus electron microscope (SGIker, UPV/EHU) at an accelerating voltage of 120 kV (Ms. Lucía Gandarias Albaina). The particle size distribution in both 4f and 3d was analysed in several images using a standard software for digital electron microscope image processing, ImageJ [152].

3.5 Magnetic measurements: Static DC and dynamic χ_{AC} regimes.

The magnetic characterisation encompasses both static DC magnetization and dynamic AC susceptibility, $M_{DC}(H, T)$ and $\chi_{AC}(T, f, t)$ measurements, respectively. To this aim, Quantum Design QD-PPMS and QD-MPMS (SQUID) instruments were used intensively. Additionally, for the case of BMs, a Vibrating Sample (VSM) magnetometer was also employed to measure the hysteresis loops at room temperature, with the collaboration of PhD. Iñaki Orue. The way these instruments work is well-known and has already been explained in other Dissertations in great detail (e.g., [34, 48]), so we will not repeat here those descriptions. Briefly, we will just mention that the static $M_{DC}(H, T)$ measurements have been performed in a wide range of temperatures ($T = 2\text{--}300$ K) and fields ($\mu_0 H \leq 9$ T). In the case of the $\chi_{AC}(T, f, t)$, a broad range of frequencies ($f = 1.7$ Hz–10 kHz) could be accessed.

Additionally to the conventional Zero-Field cooling (ZFC)-Field Cooling (FC) protocols performed in the static $M(T)$ regime, that have been very widely described elsewhere⁴ [34, 48], here, we would like to give some brief remarks on the **two quantities that we have introduced in [37] to better account for the strength of the Spin Glass frustrated interactions. These are the Irreversibility Area, IA, and the Full-Width at Half-Maximum of the SG ZFC- $M(T)$ cusp, FP.** To obtain the IA, ZFC and FC M_{DC} values are subtracted and normalised to the maximum FC M_{DC} value. Then, the IA is obtained as the integration of the resulting curve. Obtaining the FP, on the other hand, requires to measure the FWHM from the normalised M/M_{max} vs. T/T_f curves. Both quantities are, consequently, dimensionless. These two quantities display opposite

⁴just as a brief description, the ZFC-FC protocol starts with the cooling of the sample under no external applied field (ZFC). Then, a magnetic field is applied, and the magnetisation is measured upon warming. Without removing the field, the sample is cooled again (FC), and the magnetisation is measured, either during the cooling process or upon warming.

behaviours, given that the value of IA tends to increase when the presence of the SG phase in the MNP ensembles is strong, as the magnetic irreversibility gets stronger. On the other hand, the FP behaves exactly opposite: the more robust the SG phase, the faster the magnetic moments freeze, leading to a sharper SG peak. Therefore, the greater IA and the smaller FP , the more robust the SG state.

Regarding the dynamic χ_{AC} measurements, apart from the conventional $\chi_{AC}(T, f)$ measurements, here we would like to stress some details on the time-dependent aging and memory effect phenomena measurements that we have performed. As these effects are very subtle, since they are traced using the out-of-phase component $\chi''(T, t)$, we have used the MPMS-SQUID device installing the Reciprocating Sample Option (RSO), at both Universidad de Cantabria and Uppsala Universit et. This allows to enhance the sensitivity of the instrument up to $M \sim 10^{-8}$ emu. There exist in the literature several works providing different protocols to trace these time-dependent effects, employing both static M_{DC} and dynamic χ_{AC} measurements [77, 87, 153, 154]. Here, we have decided to use dynamic χ_{AC} susceptibility, as it allows to detect in more detail the subtleties concerning the spin dynamics. More precisely, we have constraint to the lowest measurable frequencies ($f = 0.17$ to 2 Hz) and oscillating fields ($\mu_0 H = 0.1$ and 0.313 mT), in order to tune the measurements to the slow dynamics of the frustrated magnetic moments.

Concerning the **ageing**, we have followed the protocol described in [76], whereas memory effects and *rejuvenation* have been performed according to [77, 87, 153]. Accordingly, the relaxation of the Spin Glass phase towards equilibrium (ageing) was followed by measuring the out-of-phase component, χ'' vs. t , at a fixed f and T , for a period of time no less than $t \sim 4 \cdot 10^3$ s. Just as a recall of what was mentioned in Chapter 2, a time-dependent response for the χ'' is expected in a SG phase. Furthermore, the robustness of the SG phase was traced via the *temperature cycling* measuring protocol. In this measuring procedure, the $\chi''(t)$ is measured at $T < T_g$ (typically, $0.8T_g$) for a time enough to the SG phase to relax towards equilibrium ($t \sim 10^4$ s). Then, the temperature is raised a $\Delta T \sim 10\%$, for different temperature values close to T_g , below and above. Afterwards, the temperature is lowered back to the initial T and the $\chi''(t)$ is measured again. By doing this, **one can observe whether the initial SG domain configuration (droplet) is maintained along with a new domain configuration (droplets within droplets), or whether a completely new SG phase is set.** A schematic visual representation of this protocol is shown in Fig. 3.6

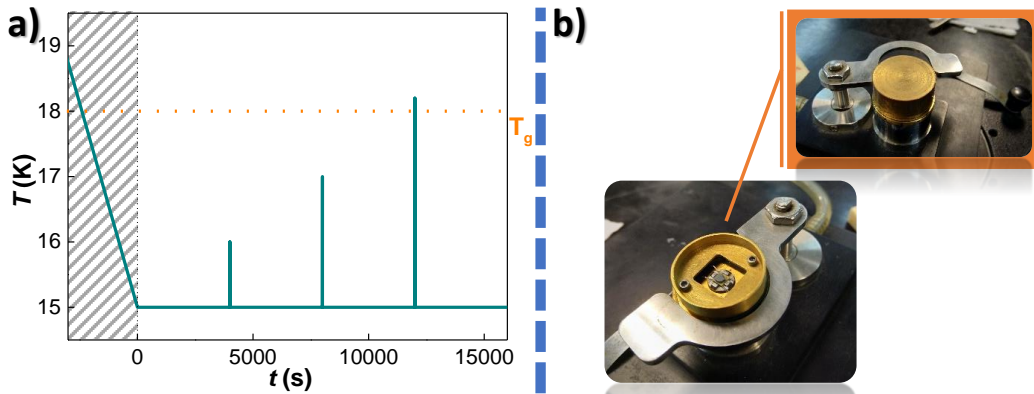


Figure 3.6: **a)** Sketch of the temperature cycling protocol. The aging measurement starts at $t = 0$, when the temperature is lowered to the chosen T_w . **b)** Detailed view on the specific sample holder, suitable for c_p measurements also performed under an external applied field.

In which respects the **memory effect phenomena**, these appear after having waited for a period of time, t_w , at a temperature value T_w within the SG phase, *ie.*, $T_w < T_g$, as explained in Chapter 2. Therefore, the way to detect those effects is to first, measure the $\chi''(T)$ dependence without making any pause, *ie.*, as it is conventionally done. This is the way to obtain the *reference curve*, which, within this Thesis work, has been measured upon warming. Then, the temperature is cooled upon T_w , where a stop of, typically, $t \sim 10^3\text{--}10^4$ s, is made. Once the waiting is resumed, the cooling is continued down to the same T than the reference's one. Finally, the $\chi''(T)$ is measured upon warming without making any stop. It is, precisely, on this second warming measurement where the memory effects will appear, in the form a drop of the $\chi''(T)$ at $T \lesssim T_w$, as already explained in Chapter 2. Examples of these memory effects will be shown in Figs. 4.4 or 5.8.

3.6 Thermodynamic properties: Specific heat measurements.

The thermodynamic properties of the $4f$ alloys were studied by measuring the specific heat at constant pressure, (c_p). Data were measured using the Heat Capacity option of the QD-PPMS instrument at $T = 2\text{--}300$ K and $\mu_0 H \leq 8$ T following the relaxation method [155]. The experimental details on the sample holder (puck) or sample preparation have already been reported before [48], and there is few to be added. We will just mention that we have employed a specific sample holder (see

Fig. 3.6b), which is suitable for the application of high magnetic field in samples with high magnetic moment, as it is the case of the 4f MNPs. This avoids the eventual lift-off of the pellets.

Attention is deserved to the **data analyses** of the c_P , as **a new approach of the fittings for ensembles of NPs has been elaborated**. This goes along with the fact that c_P measurements are not that common in nanoparticle ensembles, which already might attract the attention of the MNP community. Although research on the c_P response of nanoparticles has been studied in the last years (e.g. [156, 157]), **the analyses where a clear separation between the c_P stemming from the core (order, bulk-like symmetry) and the one from the surface atoms (disorder, symmetry breaking) are very scarce**. To this matter, it is worth mentioning a work by B.X. Wang *et al.* [158], where a theoretical model that accounts for these double NP behaviours in copper oxide NPs has been proposed. However, a full understanding of the c_P response regarding nanoparticles where the magnetic and CEF contributions are relevant is still missing. To fill in this gap, a simple description that takes into consideration these two behaviours is going to be shown hereunder.

Thereby, as it is commonly known, $c_P(T)$ measurements may carry information on the magnetic and CEF excitations. It is very common to assume the c_P to be constituted by the addition of the phononic c_{ph} , electronic c_{el} (metals) and magnetic plus CEF $c_{mag+CEF}$ contributions:

$$c_P = c_{ph} + c_{el} + c_{mag+CEF} \quad (3.34)$$

The former two contributions are usually grouped in a single term, labelled as $c_{lattice}$, which needs to be subtracted from the total c_P in order to obtain the $c_{mag+CEF}$, that carries information concerning magnetic transitions and single-ion (CEF) and collective excitations (magnons). Therefore, **a good estimation of the $c_{lattice}$ contribution is key to unravel the $c_{mag+CEF}$** . Traditionally, two different approaches have been invoked when dealing with the $c_{lattice}$. They are **(i)** the one that consists on the extrapolation of the $c_{lattice}$ measured in the PM region according to a Debye model [159]; and **(ii)** the one that assumes this $c_{lattice}$ to be that of the non-magnetic isostructural compound [93, 160], including a mass-renormalisation factor [161] for accounting the different molar masses. Nevertheless, these two approaches failed in giving a good account for the $c_{lattice}$ in MNP ensembles, **as the modifications of the bulk properties (local symmetry, coordination environment...) are neglected**. Furthermore, the experimental evidences indicate a softening of the phonon modes at the MNP

surface [67, 157, 162], ascribed to the reduced symmetry and enhanced distortion. Indeed, **a more subtle analysis when dealing with the specific heat response of MNP ensembles is needed**. Here, we propose to account for the existence of the two different local coordination and symmetry environments (core and surface) *by splitting the $c_{lattice}$ into two different contributions*: **(i)** the one that accounts for the **nanoparticle core**, and **(ii)** the one that is responsible for the **nanoparticle surface**. Both contributions are weighted by a factor N , that accounts for the surface-to-volume ratio. Accordingly, we will address N_c and N_s for the proportion of magnetic moments located within the MNP core and at the MNP surface, respectively. A 2 nm-thickness has been assumed as a reasonable estimation for the surface, based on several studies performed on diverse ensembles of MNPs, where the surface thickness has been stated to be around ~ 2 nm [43, 55, 56]. Accordingly, the c_p reads as follows:

$$c_{lattice} = N_c \left[\gamma_c \cdot T + 9R \left(\frac{T}{\theta_D^c} \right) \int_0^{\theta_D^c/T} dx \frac{x^4 \cdot e^x}{(e^x - 1)^2} \right] + \quad (3.35)$$

$$+ N_s \left[\gamma_s \cdot T + 9R \left(\frac{T}{\theta_D^s} \right) \int_0^{\theta_D^s/T} dx \frac{x^4 \cdot e^x}{(e^x - 1)^2} \right]$$

being the N_c value, calculated according to:

$$N_c = \frac{V_{core}}{V_{MNP}} = \left(\frac{r_{core}}{r_{MNP}} \right)^3 \quad (3.36)$$

and the N_s value obtained by just subtracting $1 - N_c$.

Therefore, the use of eq. 3.34 leads to the fitting of 5 free parameters, $\gamma_{c,s}$, $\theta_D^{c,s}$ and N_c , as $N_s = 1 - N_c$.

Once the $c_{lattice}$ is estimated, the $c_{mag+CEF}$ contribution is obtained by simply subtracting it from the experimental c_p , as it is traditionally done. The resulting $c_{mag+CEF}$ would then carry information on both the magnetic excitations (c_{mag}) and c_{CEF} . The latter contribution can be calculated theoretically as:

$$c_{CEF} = \frac{1}{kT^2} \left[\sum_i E_i^2 p_i - \left(\sum_i E_i p_i \right)^2 \right] \quad (3.37)$$

where $p_i = \frac{e^{-E_i/kT}}{\sum_j e^{-E_j/kT}}$ the Boltzmann factor.

Chapter 4

GdCu₂ magnetic nanoparticles

*“Soy aquella niña de la escuela,
la que no te gustaba, ¿me
recuerdas?”*

Lola Índigo

The first insight into the RCu₂ family will be devoted to the **GdCu₂** alloy. Gd³⁺-ions display a half-field 4*f* shield, leading thus to a total angular $L = 0$. As a consequence, no spin-orbit interaction is settled, there are no CEF effects retrieved, and the magnetocrystalline contribution to the anisotropy vanishes. Therefore, this **S-state ion** is convenient to study the RKKY exchange interactions themselves, given the fact that there will not be any influence of the electron-electron interactions caused by electrostatic interaction between the aspherical 4*f* charge distribution of one particular Gd³⁺ and the aspherical electrostatic field arising from the neighbours. This brings Gd³⁺ to a situation that could be interpreted as an intermediate state between the 4*f* magnetic intermetallics and the 3*d* compounds.

Furthermore, Gd³⁺ displays, together with Tb³⁺, **the highest de Gennes factor**, $dG = (g_J - 1)^2 J(J + 1)$, among the RCu₂ series ($dG = 15.75$ and 10.5 , respectively). Within the RKKY model, the dG is expected to be proportional to the ordering temperature, T_N [93]. Thereby, both GdCu₂ and TbCu₂ display the highest critical T_N values (40.2 K [163] and 48 K [164], respectively). According to the aforementioned values, a cross-over between the maximum values of dG and T_N is observed, which underlines the fact that the RKKY interactions are not enough to account for the magnetic interactions, and higher-order crystalline and molecular-field parameters, so as quadrupole and magnetoelastic interactions,

should be invoked to fully understand how the magnetic interactions are settled [110, 165]. In any case, the fact that we are dealing with the alloy displaying the second highest T_N among the RCu₂ series ensures the existence of strong AF coupling, which, together with the lack of angular moment, makes GdCu₂ an excellent candidate to study the RKKY coupling.

While the knowledge about magnetic Nanoscience has already become mature, it is very surprising that the works focused on $4f$ intermetallic nanoparticles are so scarce. This is more so, considering these constitute the best ensembles to unravel the magnetism (indirect RKKY coupling, the effect of crystalline electric field...) at its basis. Indeed, the fascination of these ensembles is not limited to disclose fundamental physics, yet they have shown their suitability for a plethora of applications, from permanent magnets [166, 167] to medical applications [53, 168, 169], to cite a couple of them. Furthermore, given the well-known fact that finite-size effects alter the magnetic properties, owing to the symmetry breaking and the reduced coordination environment for the surface atoms (see [170] or [171]), *there is plenty of room at the bottom* concerning the determination of how the $4f$ magnetism is affected at the mesoscopic scale. To fill in this gap, some groups started to unveil, in the last two decades, the magnetic properties of RX₂ intermetallics at the nanoscale. One of the initial examples was the mechanically-milled GdAl₂ [172, 173]. This alloy, which is a conventional FM in bulk state [36], undergoes a transformation to a re-entrant spin glass when it is nanoscaled. The bulk $T_C \sim 170$ K [174] survives together with the emergence of a freezing transition at $T_f \sim 65$ K [172, 175]. The FM state is strong, since it stays almost unaffected upon milling times as great as $t = 590$ h [176], where the crystalline structure is destroyed, and the alloy gets amorphous.

Particularly, in the last few years, our group started investigations on TbCu₂ MNPs produced using low milling times. In bulk TbCu₂, an AF state is present, instead of the FM one of TbAl₂ [38, 93, 164, 177]. Previous investigations on TbAl₂ MNP ensembles reported the coexistence of $T_C \sim 100$ K with a low-temperature SG state at $T_f \sim 45$ K [42]. The question that remained open was then to determine the impact of the size reduction on the AF RKKY interactions in ensembles of TbCu₂ MNPs. To this aim, in the second decade of the 2000s, our group focused on the fabrication of these TbCu₂ MNPs and on their characterisation, from structural to magnetic viewpoints. Concerning the fabrication process, it was very surprising that, already at $t = 0.5$ h, nanometric sizes around 25 nm were achieved [39]. This contrasts with the metallurgical situation of TbAl₂, which required $t = 70$ h to obtain a similar MNP size [42]. Coming to the magnetism, a

low temperature Spin Glass-like transition emerged at $T \sim 15$ K for the TbCu₂ MNPs, coexisting with the bulk Néel transition ($T \sim 48$ K). Both transitions are held up to $t = 15$ h, where the global AF state was destroyed, and thus, the T_N is no more retrieved [39, 43]. The crystalline structure, so as the magnetic unit cell, were also kept in the MNP ensembles, with minor modifications with respect to the bulk one [43, 178].

Given that these works demonstrated the possibility to obtain, in relatively low milling times, crystalline magnetic nanoparticle ensembles of TbCu₂, we decided to mimic this procedure to obtain (*S*-state) GdCu₂ MNPs. Accordingly, **six ensembles of GdCu₂ MNPs have been produced**, employing milling times of $t = 0.5\text{h}, 1\text{h}, 1.5\text{h}, 1.75\text{h}, 2\text{h}$ and 5h . Additionally, a master bulk alloy was produced and measured, to be used as a reference. By keeping the milling process that short, the bulk orthorhombic *Imma* CeCu₂-type crystalline structure was preserved almost unaltered in the MNPs, which guarantees the good degree of crystallinity (see Appendix A for a detailed explanation on the crystalline structure). The maintenance of the crystalline structure within the MNPs was key to our **main purpose**, which was to **study the modifications driven by finite-size effects**, avoiding the effects caused by the amorphisation of the alloys [127, 179, 180]. Indeed, there is a microstrain contribution inherent to the grinding that distorts the crystalline array of ions, but still far from turning the sample into an amorphous arrangement. The Rietveld refinements on the XRD patterns (Appendix A) indicate mean MNP sizes of $\langle D \rangle$ 40(5), 32(5), 25(5), 18(3), 10(1) and 7(1) nm, which are comparable with the ones of TbCu₂ ensembles [39]. As occurs in the TbCu₂ MNPs, the milling times needed to achieve nanometric sizes in GdCu₂ ensembles are drastically reduced from those reported for GdAl₂ [36]. For instance, with only $t = 1.5$ h, a mean particle size of $\langle D \rangle \approx 25$ nm is reached for GdCu₂, whereas $t = 120$ h were needed to achieve such a size in GdAl₂. It seems that alloying these R with Cu in this stoichiometric proportion 1:2 leads to a softer mechanical behaviour with respect to the Al situation.

Regarding the structural characterisation, the high neutron absorption rate of Gd [181] prevents us to evaluate not only its crystallographic (nuclear) state, but also, the magnetic moment structure by neutron diffraction. Thus, the crystalline arrangement could only be verified by means of XRD. Therefore, the results and discussions presented hereunder will be mainly focused on the magnetic properties. Fortunately, we also could gain access to the thermodynamic properties of this alloy by means of specific heat measurements, which were clearly helpful to have an insight to the energy level schemes.

4.1 Magnetic properties

This section will deep into the magnetic properties of the GdCu₂ ensembles of MNPs. We will first provide and discuss the static $M_{DC}(H, T)$ characterisation, in order to get a first idea about how the magnetic transitions take place in these MNPs. Afterwards, dynamic $\chi_{AC}(T, f)$ and $\chi_{AC}(t)$ measurements will be commented, with the aim of disclosing the particularities of the spin dynamics and interactions. Thanks to the $\chi_{AC}(T, f, t)$ measurements, the existence of different blocking mechanisms taking place simultaneously at these MNP ensembles will be disclosed.

4.1.a Static Magnetic Susceptibility: $M_{DC}(T, H)$

The static magnetic susceptibility analyses will begin by the determination of the magnetisation behaviour as a function of the temperature, *i.e.*, $M_{DC}(T)$. These measurements serve as an initial guide to picture the magnetic transitions undergone by the GdCu₂ ensembles. In order to study the possible field-irreversibility of the MNPs, we have performed Zero-Field Cooled (ZFC) and Field Cooled (FC) measurements. Fig. 4.1a includes these protocols performed at constant field $\mu_0 H = 10$ mT for all the nano-scaled GdCu₂ alloys. In order to clearly see every data set, two Y-axis scales have been used, one for milling times $t \leq 1.75$ h (top), and a second one, for $t \geq 2$ h (bottom). Besides, given that the results concerning the 0.5h-milled MNPs are masked by the rest of the data sets, we have shown them separately on the right. While the AF Néel transition is only present for low milling times ($t \leq 1.75$ h, top figure), all the data sets exhibit magnetic irreversibility below the freezing temperature, $T_f \sim 25$ K. This freezing temperature reveals the transition corresponding to a Spin Glass-like phase.

Bearing in mind the aforementioned situation concerning TbCu₂ MNPs [39, 43], we can state **the magnetic state of the greatest MNPs** ($\langle D \rangle \geq 18$ nm, *i.e.*, $t \leq 1.75$ h) building up to a **Superantiferromagnetic (SAF)** state, where the magnetic moments located within the core retain the AF coupling order, while the ones located at the surface constitute the disordered SG phase. For clarity purposes, a sketch of the SAF arrangement has been included in this Fig. 4.1a. It is worth noting that the T_N value is not affected by the size reduction, as it

is always found at 42 K, which agrees with the one of the bulk alloy. Notwithstanding, the intensity of this Néel transition gets progressively softened with the milling, down to $t = 2\text{h}$ ($\langle D \rangle = 10(1)\text{ nm}$), where it is completely removed. This indicates a reduction of the AF-coupled moments, driven by both the increasing microstrain, η , and the surface-to-core ratio. The former η is due to slight distortions of the atomic positions, r , which effectively modify the exchange coupling among the Gd³⁺ atoms, leading thus to the frustration of some of the RKKY interactions¹. On the other hand, an increase of the surface magnetic moments implies a greater *spin canting*, which detaches the magnetic moments from the AF state. These canted spins will promote the onset of a magnetically disordered phase. **For milling times $t \geq 2\text{h}$** , the AF-order is completely removed, since there is no fingerprint of the Néel transition in the $M_{DC}(T)$ curves, as it can be inspected in the bottom panel of Fig. 4.1a. At this point, we can anticipate, thanks to the $\chi_{AC}(T, f)$ characterisation shown hereunder, that one should figure out a **Super Spin Glass (SSG)** state [182, 183], where all the spins participate to this global frustrated state. The SSG arrangement has been sketched in the inset of this bottom panel of Fig. 4.1a. In any case, what is clear from the $M_{DC}(T)$ analyses is that **the SG cusp intensity shoots up dramatically for $t = 2\text{h}$ and 5h -milled MNPs**, with respect to the situation concerning lower milling times. In this way, although it increases smoothly within the range $t = 0.5\text{--}1.5\text{h}$, and from $t = 2\text{h}$ to 5h , between $t = 1.5\text{h}$ and $t = 1.75\text{h}$, the value gets doubled, but, what is more, from $t = 1.75\text{h}$ to $t = 2\text{h}$, it gets a four-fold increase. This scrutiny of the SG cusp variation has not been reported before, even not for the case of TbCu₂ *cousins* MNPs.

In order to find out more information on the freezing process, the T_f vs. $\mu_0 H$ behaviour has been analysed. The results follow the dependence showed in de Almeida–Thouless line (eq. 2.11) with $m = 3/2$, which agrees well with the mean field framework for Spin Glasses [184, 185]. The exception to these fittings are the results concerning the 0.5h milled MNPs, highlighting the prevalence of the AF order within this ensemble.

Table 4.1 includes the main results, together with the parameters obtained from Curie–Weiss fittings² performed in the region $T > T_N$ at $\mu_0 H = 0.1\text{ T}$. The results for the Curie Temperature θ_P show positive values in the whole range of sizes. This fact is indicative of FM interactions among magnetic moments [1]. As long as the AF-moments are relevant ($t \leq 1.5\text{h}$), θ_P stays almost constant at

¹just as a recall, in eq. 2.4 and Fig. 2.3, the coupling dependency with r was depicted.

²Curie–Weiss law: $M/H = \frac{C}{T - \theta_P}$, being $C = \frac{n\mu_0\mu_{eff}}{3k_B}$ [2].

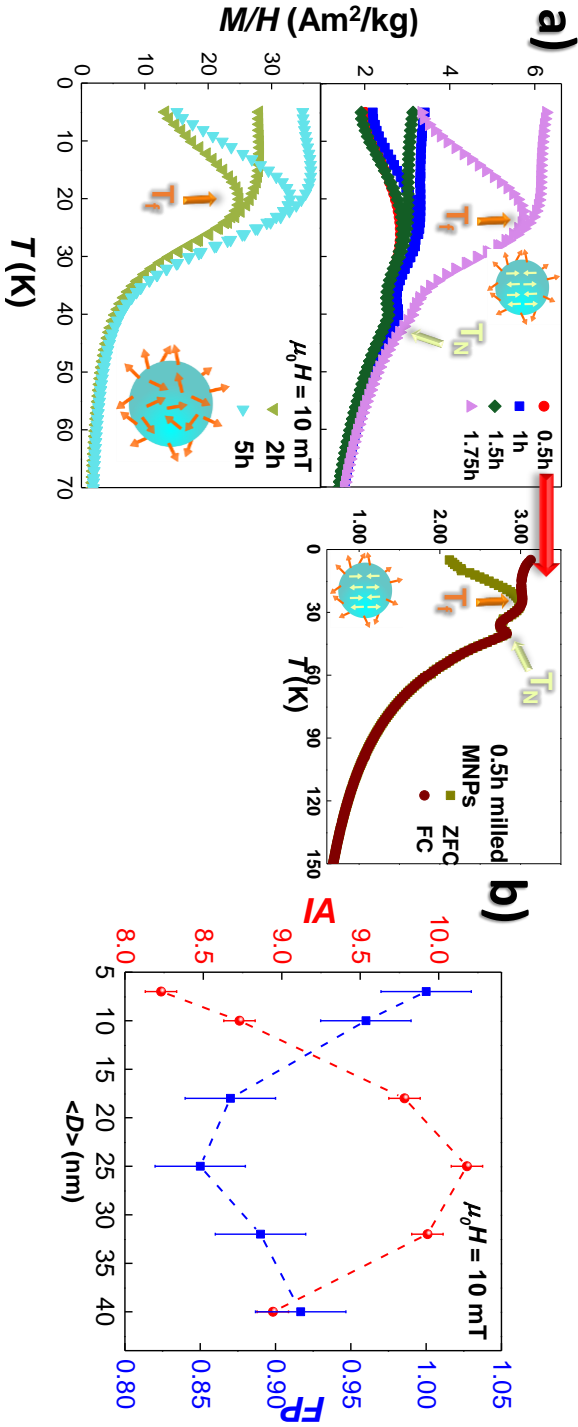


Figure 4.1: **a)** ZFC-FC curves of $M_{DC}(T)$ measured at $\mu_0 H = 10$ mT. Top includes the GdCu₂ MNPs $t \leq 1.75$ h, where T_N (yellow arrow) and T_f (orange arrow) coexist (i.e., $\langle D \rangle \geq 18$ nm). Measurements corresponding to the largest MNPs ($\langle D \rangle = 40(5)$ nm, $t = 0.5$ h) are represented individually at the right side, where different colours have been employed to distinguish between the ZFC branch (dark yellow) and the FC one (brown). Bottom displays $t \geq 2$ h, where the T_N is suppressed. Sketches for the SAF (top) and SSG (bottom) states have been included as insets. **b)** Evolution of the Irreversibility Area ΔA (red spheres) and the Spin Glass sharpness FP (blue squares) with respect to mean diameter size $\langle D \rangle$ for the different GdCu₂ ensembles.

$\theta_P \sim 8$ K, a value that is in good agreement with the one obtained for the bulk alloy, $\theta_P^{bulk} = 8.05(2)$ K. Notwithstanding, the θ_P value increases for $t = 1.75$ h (~ 10 K). The increase is even more dramatic, for the case of $t \geq 2$ h–milled (~ 20 K), when the cross–over from a surface SG–like phase to a SSG global state takes place. Curie–Weiss fittings also provide quantitative values for the μ_{eff} , which, on the contrary, are not affected by the milling. This is congruent with the fact that the magnetism of these MNPs is solely due to the Gd³⁺–ions. We will just mention that the experimental results are slightly above the one expected theoretically, $\mu_{eff}^{theo} = g_J \mu_B \sqrt{J(J+1)} = 7.94 \mu_B$, (where $J = 7/2$, obviously). This agrees well with the reported (experimental) values of $\mu_{eff} = 8.14 \mu_B$ and/or $\mu_{eff} = 8.7 \mu_B$ in either single crystal [186] or polycrystalline alloys [187] respectively. The enhancement of conduction–electron interaction has usually been claimed to be beneath this finding [188].

Table 4.1: Experimental values of the T_f measured at $\mu_0 H = 0.25$ mT together with the irreversibility temperature obtained from the axis extrapolation of the AT line described in eq. 2.11, T_{irrev} . The θ_P and μ_{eff} obtained from the Curie–Weiss fittings are also included.

t (h)	$\langle D \rangle$ (nm)	T_f (K)	T_{irrev} (K)	θ_P (K)	$\mu_{eff} (\frac{\mu_B}{Gdat})$
0.5	40(5)	32(1)	–	8.16(2)	8.762(1)
1	32(5)	31(1)	26.4(3)	8.03(2)	8.876(1)
1.5	25(5)	30(1)	27.4(4)	8.17(7)	8.763(1)
1.75	18(3)	28(1)	24.0(3)	10.6(3)	8.697(1)
2	10(1)	24.2(5)	21.7(2)	21.7(3)	8.452(1)
5	7(1)	24.3(5)	21.6(2)	23.0(2)	8.703(1)

On the way of the $M_{DC}(T)$ analyses Fig. 4.1b displays the evolution with the mean MNP size of the IA and FP quantities, elaborated in chapter 3. Just as a reminder, the greater IA and the smaller FP , the more robust the SG state. It is very worth noting the occurrence of a maximum (minimum) in this Fig. 4.1b for the IA (FP) measured in the 1.5h–milled alloy. This result points to $\langle D \rangle = 25(5)$ nm MNP–size ($t = 1.5$ h) as the one where the SG phase is the most robust. This is in principle, striking, as for that size, a well–defined AF–core still remains. Nevertheless, this situation is well–understood by taking into account what really matters to a SG state. Accordingly, the RKKY interactions depend on actually two sources of frustration, the one that comes inherent to the disorder introduced

by the size reduction (increasing surface-to-core ratio and microstrain), and the intrinsic competition between FM and AF interactions. The latter rivalry between exchange interactions contributes to the disorder SG phases, as it has already been discussed for FM order in [189]. Therefore, it would not be unreasonable to consider our SAF MNPs to be formed by two spin networks, from which frustration arises: **(i) the one, mostly corresponding to the spins within the core**, with competing FM–AF RKKY interactions, and **(ii) the second one, mainly related to the spins at the surface**, where the increasing microstrain introduced by the milling, together with the symmetry-breaking and local coordination reduction gives rise to a greater magnetic disorder.

Once the $M_{DC}(T)$ at different constant applied H fields has been analysed, it is time to move to the $M(H)$ results, measured at a constant T value, to inspect the magnetisation under external applied field. This will allow access to get, mainly, information on the anisotropy of the GdCu₂ MNPs. Accordingly, Fig. 4.2a displays the $M_{DC}(\mu_0 H)$ hysteresis loops measured at $T = 5$ K. There, it can be seen that none of the alloys reaches the magnetic saturation at the highest applied field, $\mu_0 H = 5$ T, as it is the case for the bulk alloy (see inset). Furthermore, the M_{DC} at this $\mu_0 H = 5$ T (depicted in Fig. 4.2b, blue squared) increases dramatically when the AF arrangement is removed ($t \geq 2$ h), a fact that agrees well with the increasing FM couplings established among some magnetic moments (which are favoured by the spin canting at the surface). Also, in the absence of AF order, the shape of the M vs. $\mu_0 H$ curve changes, as there is a negative bending of the M between $\mu_0 H = 1.5$ T to $\mu_0 H = 5$ T, which was positive for the SAF ensembles and, in this case, it is reflecting a reduction in the anisotropy. What is more, if we inspect in more detail the $M(\mu_0 H)$ curves for both SSG MNPs, a value of $M \sim 5 \mu_B$ is reached at $\mu_0 H = 5$ T, which corresponds to $\sim 70\%$ of the theoretical saturation value $M = g_J \cdot J = 7 \mu_B$ ($J = 7/2$, $g_J = 2$). This is greater than the $\sim 55\%$ value observed in TbCu₂ NPs at the same magnetic field [39], which underlines the lower anisotropy for GdCu₂ MNPs. This is well-understood according to the lack of magnetocrystalline anisotropy of Gd³⁺-ions. The left inset of this Fig. 4.2a includes a zoom-in of the central region of the hysteresis loops, where both the coercive field and the remanent magnetic moment can be observed. For clarity purposes, the $\mu_0 H_C$ vs. MNP size, $\langle D \rangle$, has been depicted in Fig. 4.2b, together with the $M(\mu_0 H = 5$ T) value (dark yellow circles and blue squares, respectively). There, a maximum for $\mu_0 H_C$ can be noticed for $\langle D \rangle \sim 18$ nm ($t = 1.75$ h-milled) MNPs, where the $M(\mu_0 H = 5$ T) also increases dramatically. A similar effect has been reported for the case of FM-MNPs, where the **cross-over from multi-domain to single-domain MNPs** was claimed to be triggering this

rise [1, 2]. It is very plausible that our GdCu₂ ensembles could hold within this picture, *i.e.*, AF domain walls could be set for $\langle D \rangle \lesssim 20$ nm, whilst their energy cost will not be compensated for smaller MNPs. Later on, dynamic $\chi_{AC}(T, f, t)$ analyses will confirm this preliminary scenario.

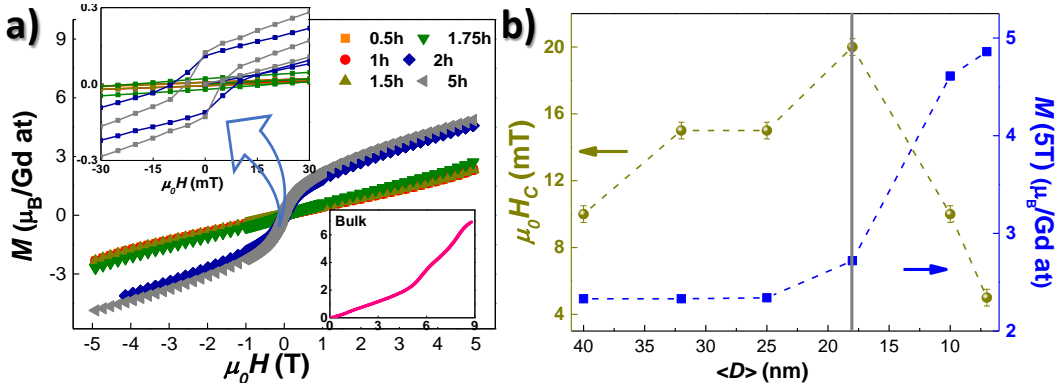


Figure 4.2: **a)** Magnetic moment per Gd atom vs. the external applied field (hysteresis loop) measured at $T = 5$ K for the ensembles of GdCu₂ MNPs. The left inset provides a closer look to the central region $\mu_0 H \sim$ mT to better observe the coercive field $\mu_0 H_C$ and remanent magnetisation M_r . The right inset shows the bulk alloy measured up to $\mu_0 H = 9$ T. In **b)**, the evolution of the $\mu_0 H_C$ (dark yellow red spheres) and $M(\mu_0 H = 5$ T) (blue squares) with the MNP size $\langle D \rangle$ (reverse axis) at $T = 5$ K is plotted. The gray line marks the limit size for which the cross-over from multi-domain to single-domain AF takes place.

Finally, considering the coexistence of FM and AF interactions in some of our samples, we have investigated the presence of an eventual Exchange Bias. The loops were measured after cooling down to both $T = 5$ and 2 K in a presence of $\mu_0 H = 5$ T. However, the measurements (not shown) indicate that no shift in the $M(H)$ loop for any of the studied alloys. This absence of shift is not so surprising considering that the exchange anisotropy effect is weak when the interface of the core and the surface of the NPs presents a large atomic roughness [16].

4.1.b Dynamic Magnetic Susceptibility

As we have already mentioned in Chapter 3, dynamic magnetic susceptibility is a powerful technique that provides valuable information on the spin dynamics [50, 179, 190]. Thereby, thanks to the $\chi_{AC}(T, f)$ and χ_{AC} vs. time, t , analyses, we have gained access to a very complete insight into the magnetic moment interactions and dynamics. This has been specially enlightening in the case of these

GdCu₂ ensembles, given the lack of microscopic ND measurements. To this aim, we will present first the *conventional* $\chi_{AC}(T, f)$ measurements. Then, the measurements tracing the memory and ageing phenomena will be shown and discussed.

To begin with, Fig. 4.3 includes the $\chi_{AC}(T)$ components (in-phase χ' and out-of-phase χ'') measured at the lowest frequency of $f = 0.17$ Hz (Figs. 4.3a and b) and in a range of frequencies between 100 and 10000 Hz (Figs. 4.3 c–f); measured at an alternating field of $h = 0.131$ mT (no bias field). Starting with Figs. 4.3a and b, the occurrence of two humps, ascribed to the freezing and the Néel transitions, can be easily observed up to 1.75h-milled MNPs. Whereas the former T_f value slightly shifts with the milling time (MNP size) (see Table 4.2), the T_N stays constant at 40.2 K for all the ensembles. **Once the 1.75h of milling time (18 nm MNP size) is overcome, the AF transition is removed**, which agrees with the M_{DC} characterisation. Far from being surprising, this finding reinforces the idea of a **cross-over between a SAF state and a SSG-like one at $\langle D \rangle \lesssim 18$ nm**. Nonetheless, by just observing at first glance the out-of-phase component shown in Fig. 4.3b, one should be shocked by a striking feature. In this way, the freezing transition provokes a dissipation process, recorded in the $\chi''(T, f)$ at $T_g = 18$ K, which is expected for Spin Glass transitions [50, 191]). Nonetheless, *there is also dissipation connected to the Néel transition*. This is absolutely unprecedented, as no dissipation should be probed in the vicinity of a second-order transition [1]. The dissipation takes place in the form of two humps, located very close to the T_N , at $T_{d1} = 33.5(5)$ K and $T_{d2} = 40.0(5)$ K. Furthermore, the peaks get broaden and reduce their intensity with the milling, being almost wiped-out for the $t = 2$ h and 5h ensembles, where the AF collective state is already lost. This finding allows to connect this high-temperature disorder contribution to the AF state, more precisely, to the existence of *antiferromagnetic domain walls*, in which there exist uncompensated magnetic moments that are *magnetically* disordered. This has already been proposed for AF grain boundaries in [192], and is congruent with the static $M_{DC}(H)$ characterisation shown before (Fig. 4.2b). There, the H_C vs. $\langle D \rangle$ representation displayed a maximum for these 18 nm-sized MNPs. If one takes into consideration their MNP core size, which is $\langle D \rangle \sim 14$ nm, and given that the domain wall thickness lies around 1–1.5 nm [42], it is clear that these 1.75h-milled (18 nm-sized) MNPs are close to the limit size for domain walls to occur.

The fact that this high-temperature dissipation takes the form of two cusps, rather than a single one, is congruent with the antiferromagnetic microstructure, that has been unravelled thanks to muon spectroscopy resonance and neutron

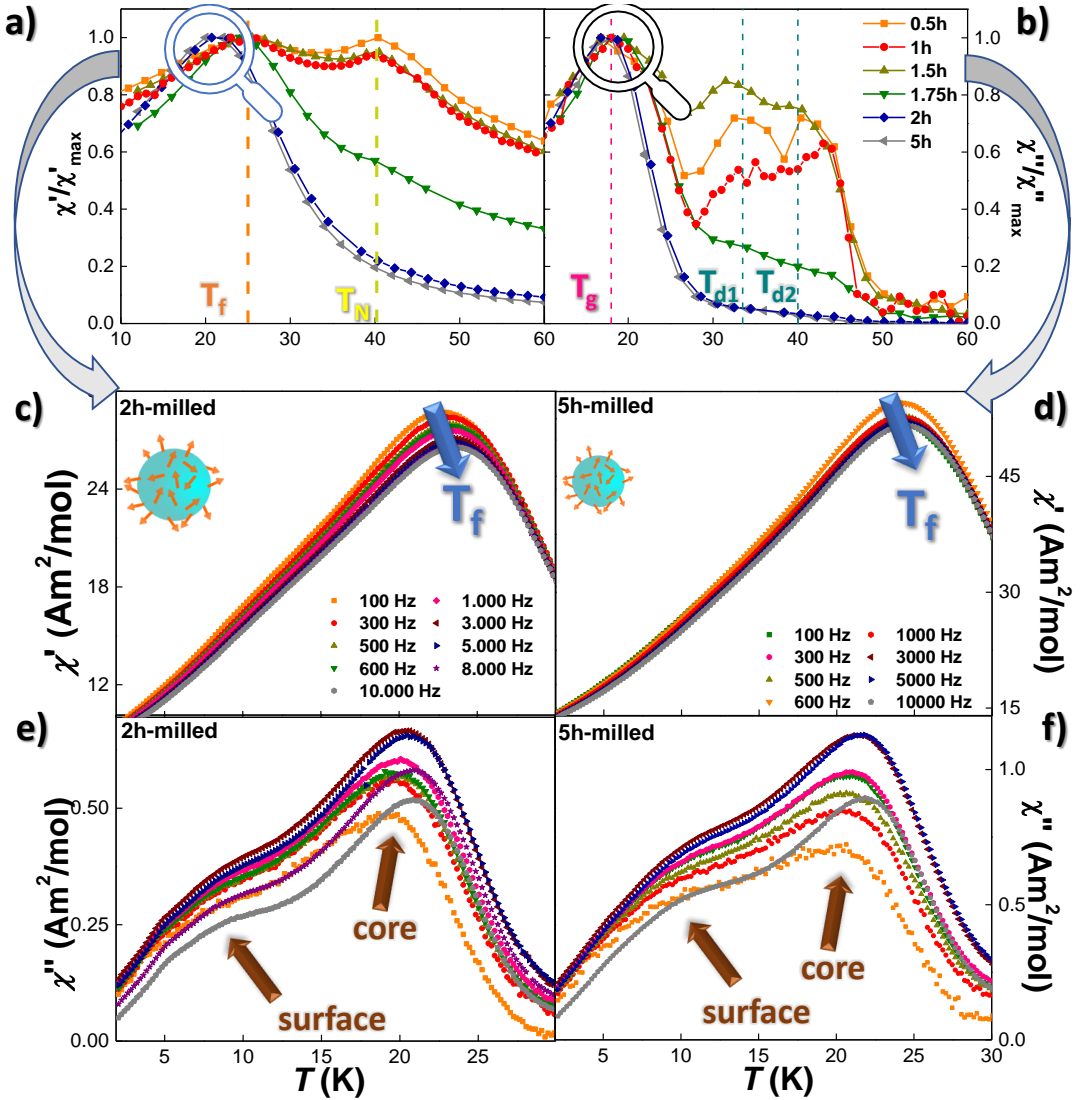


Figure 4.3: a and b) include the normalised $\chi'(T)/\chi'_{max}$ and $\chi''(T)/\chi''_{max}$ components, respectively, measured at $f = 0.17$ Hz and $h = 0.131$ mT. The χ'_{max} (χ''_{max}) correspond to the value of the Spin Glass peak. The orange and yellow dashed lines in a) mark both $T_f \approx 25$ K and $T_N \approx 40$ K transitions corresponding to the 1.5h milled MNPs. In b), additionally to the glass $T_g \approx 18$ K, the positions of $T_{d1} \approx 33.5$ K and $T_{d2} \approx 40$ K peaks in the vicinity of the Néel transition have been marked. c) and e) (d) and f) display the $\chi'(T)$ ($\chi''(T)$) components measured several f the 2h (left) and 5h (right) SSG MNPs. The T_f and the freezing of the surface and core moments have been marked with blue and brown arrows.

diffraction analyses [193, 194, 195]. In this way, the commensurate magnetic structure of bulk GdCu₂ [195] carries a non-collinear cycloidal propagation, where the small cantings of the Gd³⁺ lead to left-handed and right-handed cycloids [193, 194]. This results in the existence of two different types of domain walls, which translate into two different contributions to dissipation in the macroscopic $\chi_{AC}(T)$. The finding of fingerprints for AF domain walls in our GdCu₂ MNPs is particularly interesting, since these AF domain walls are on target nowadays, owing to their potential applications on the Spintronic field, such as spin wave polarizer and retarder [196] and/or ultra-fast switching dynamics [197].

Let us now focus on the low-temperature spin dynamics. Figs. 4.3 c–f include the in-phase $\chi'(T)$ component (Figs. 4.3c and e) and the out-of-phase $\chi''(T)$ (Figs. 4.3d and f) for the SSG 2h and 5h-milled MNPs. A right-shift towards higher temperature values of T_f is obtained in all the ensembles, which constitutes a typical fingerprint of SG phases [84, 175]. As it has already been introduced in Chapters 2 and 3, very powerful information on the spin dynamics can be obtained by quantifying this displacement *via* the scaling to some critical exponents. Therefore, Table 4.2 includes the obtained values for the δ -parameter (eq. 2.10), $z\nu$, τ_0 and $T_{f,0}$, obtained according to eq. 2.9.

Table 4.2: δ -shift parameter, relaxation time τ_0 of individual particles for $f \rightarrow 0$, freezing transition temperature T_f and critical exponent $z\nu$ for all of the GdCu₂ MNPs, obtained following eqs. 2.10 and 2.9.

T (h)	$\langle D \rangle$ (nm)	δ	τ_0 (s)	$T_{f,0}$ (K)	$z\nu$
0.5	40	0.0280(2)	10^{-8}	24.3(4)	7.7(3)
1	32	0.0180(1)	10^{-8}	26.5(2)	6.1(2)
1.5	25	0.0160(1)	10^{-13}	25.14(2)	8.1(2)
1.75	18	0.0160(5)	10^{-13}	24.13(2)	8.7(3)
2	10	0.0136(6)	10^{-11}	22.58(4)	4.9(2)
5	7	0.0263(1)	10^{-8}	23.20(4)	4.2(2)

To begin with the discussion of values of δ -parameter are found to lie above those typically attributed to the canonical SG state systems, [0.002–0.004], where the concentration of the magnetic impurities is very diluted [50]. Also the results for our MNPs are far from the ones obtained in archetypal re-entrant SG systems [198, 199], as commonly found in other intermetallic SSG MNPs [39, 43]. In any case, we are still far below the upper limit of $\delta = 0.1$ expected for SPM systems

[60, 79], and close to the ones reported for Cluster Spin Glass [73, 179]. This reveals a tendency of the magnetically-disordered moments to form different arrays, within each one the spins are coupled and respond as a whole, which leads to a cooperative relaxation process. The results arising from the power-law scaling are consistent as well, since the obtained $z\nu$ values are inside the *fragile regime* behaviour ($5 < z\nu < 11$) [70]. Here, it is worth noting that this exponent drops to almost half of its value when the AF state is destroyed ($t \geq 2h$), which evidences that the MNPs dynamics achieves a more glassy behaviour [79].

The $T_{f,0}$ values are always kept below the experimental ones, as expected, and get reduce at the lowest MNP sizes, according to a less-robust SG phase. What is more, fact that all of the obtained $T_{f,0}$ are only 2 K deviated with respect to the T_{irrev} values obtained after the extrapolation of the AT-line fitting discussed above, is indicative of a good agreement between both static and dynamic characterisations [185]. Finally, τ_0 values are pretty close to those corresponding to SG phases, again, far from the ones expected for SPM ensembles [200, 201]. **The 1.5h and 1.75h-milled MNPs (25 and 18 nm-sized, respectively) evidence the two fastest relaxation processes, indicating the greatest interactions among the disordered magnetic moments.** It is worth reminding that faster spin dynamics imply greater magnetic interactions, where, for the case of SG-like phases, all the spins freeze as a whole. This is very distinct from the *blocking* mechanism, where the particle magnetic moments are *detached* from each other particle, being the blocking state set from the individual arrest of the magnetic moments (slower dynamics, hence).

Paying now more attention to the dissipation associated with the Spin Glass low-temperature transition, Figs. 4.3e and f allow to observe a double-peak structure near the glass T_g transition. To clarify the definitions, here we are calling *glass temperature*, T_g , the temperature at which the maximum of the dissipation is located. This T_g is, of course, associated to the freezing T_f , being, obviously, $T_g < T_f$ [50]. The double-peak structure for the low temperature T_g can only be detected at the higher f side, *i.e.*, f between 100 and 10.000 Hz, and **it is indicative of a two-step freezing process**, just in the same way as it has also been observed in Fe/ γ -Fe₂O₃ core-shell SSG nanoparticles [73, 202]. Accordingly, **the core and surface magnetic moments freeze separately**, giving rise to a first hump, found at $T \sim 7$ K, which accounts for the surface moments spin dynamics, and a second one, owing to the core magnetic moments, located at $T \sim 13$ K. The fact that this double-freezing mechanism can only be disclosed for the greater f can be understood as a matter of *decoupling*. This way, only

when the probing f reaches ~ 100 Hz, can become tuned to the alloy fundamental harmonics, provoking the decoupling of the surface and core magnetic moments, which will response on each own.

Given the variety of spin disorder dynamics evidenced in the GdCu₂ ensembles (low-temperature SG, high temperature uncompensated spins, SSG state for the smallest MNPs, etc.), it was very worth addressing the ageing and memory effect phenomena with the aim of accessing more information on the coupling among the spins. As we have already introduced in previous chapters, these are helpful to evaluate the robustness of the magnetically frustrated RKKY interactions among the moments. Accordingly, these two phenomena probe the existence of highly-correlated RKKY-frustrated spins, thus, they are restricted to the out-of-equilibrium dynamics of non-ergodic systems (SGs) [50, 76, 77, 78, 203]. It should be noted, at this point, that the protocols associated to the ageing and memory effects are not so commonly performed, as they require very high sensitive MPMS-SQUID magnetometers, besides they are time-consuming. In the case of the measurements presented in this Dissertation, the MPMS-SQUID (both at Uppsala and Cantabria) had to be equipped with the Reciprocating Sample Option (RSO), in order to gain access to sensibility up to $\sim 10^{-8}$ emu.

Beginning with **the largest MNPs** (40 and 32 nm-sized, 0.5 and 1h-milled ensembles), **they have not evidenced the occurrence of memory effects associated with the low temperature SG transition** ($T_g = 18$ K). This indicates that **the AF state within these MNPs is robust against disorder**, and it encompasses a great amount of magnetic moments. This prevents the frustrated interactions to correlate a great amount of spins, which hampers the building of a solid randomly disordered *domain* configuration. As we have already introduced in Chapter 2, a drop in the magnetisation at $T < T_w$ should be recorded if the system dynamics is that of a non-ergodic ensemble of magnetic moments. Given that, for these ensembles, no drop neither time-dependence response in the χ'' vs. T representation are observed, both phenomena should be discarded.

Nonetheless, **the situation concerning the MNPs of sizes below 25 nm** (*i.e.*, milled for $t \geq 1.5$ h) is different, as **both memory effects and ageing phenomena are probed**. As it can be seen, Fig. 4.4 includes the memory effects (left-panels) and temperature cycling protocols (right-panels) measurements for the SAF 1.5h-milled (25 nm) MNPs (top) and the SSG 5h-milled (7 nm) ones (bottom). These specific MNP sizes correspond to the ones with the greatest frustration (1.5h), and to the most robust SSG phase (5h-milled), respectively.

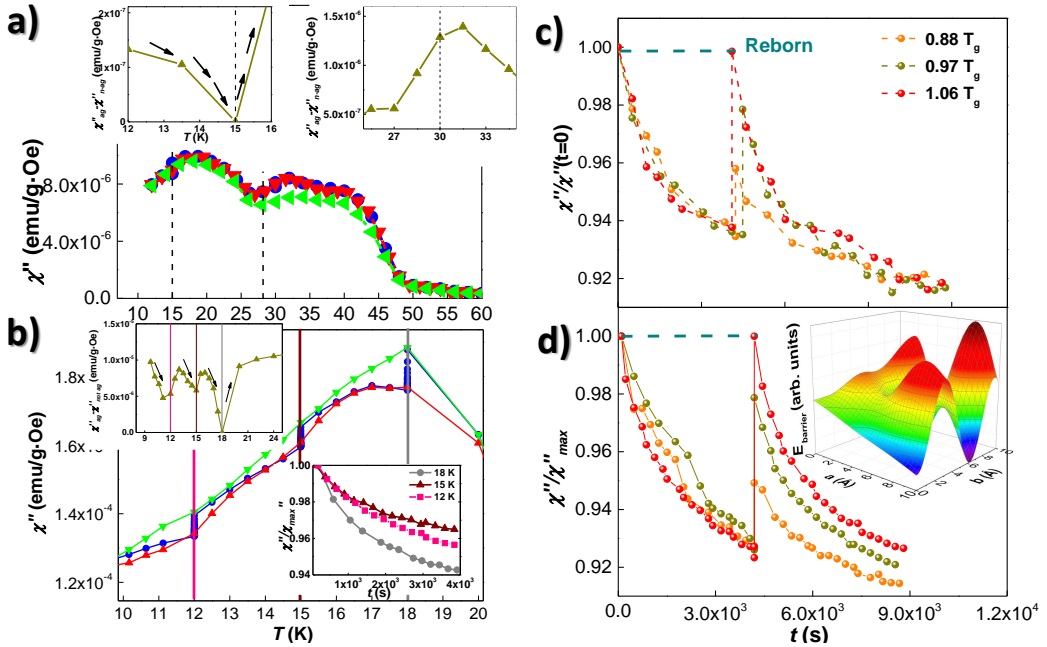


Figure 4.4: Out-of-phase χ'' component of GdCu₂ 1.5h (top, **a**) and **c**) and 5h (bottom, **b**) and **d**) milled MNPs measured at $f = 0.2$ Hz and 0.17 Hz, respectively. Memory effects are evidenced in **a**) and **b**), as a drop in the $\chi''_{aged} - \chi''_{not\ aged}$ susceptibility is measured below $T_w = 15$ K (**a**) and $T_w = 12, 15$ and 18 K (**b**)) (see top insets). No memory effects are evidenced at $T_w = 30$ K. Bottom inset in **b**) displays the relaxation of $\chi''(t)$ at T_w . **c**) and **d**), display the relaxation measured at $T_w = 15$ K before and after applying three different ΔT . It can be seen that the SG state is completely reborn when the rise is of $\Delta T = 1.06T_g$. The inset of **d**) shows a sketch of the energy-barrier landscape, where two different energy barriers, corresponding to distinct domain configurations, are depicted.

Starting the discussion with the 25 nm-sized MNPs, the occurrence of both memory effects and ageing phenomena connected to the low temperature surface SG transition can be clearly observed in Fig. 4.4a. These memory effects can be traced in $\chi''(T)$ curve measured upon warming, which has been recorded after having made a stop at $T_w = 15 \text{ K} = 0.83T_g$ while cooling down. Particularly, the memory of the surface SG phase is probed in the form of a drop in the in the difference between $\chi''_{aged} - \chi''_{notaged}$ at $T \lesssim T_g$, which is clearly depicted in the top left-inset of Fig. 4.4a. Here, we would like to give a brief explanation on this effect, which could serve as an example to follow the main concepts related to the out-of-phase phenomena already commented in Chapters 2 and 3. In this way, starting from the high temperature-side, the MNPs are progressively cooled down to their freezing transition, temperature at which a particular disorder configuration is settled. This disorder state is further cooled down to $T = T_w < T_g$, where it is *aged* for some (long-enough) time. While this halt takes place, the magnetically-disordered moments are relaxing towards equilibrium, letting the *disordered-domain configuration* to be settled. The slower the magnetic moments relax during this halt, the most stable the disorder configuration is, which means that the interactions among the frustrated spins are more robust. Once the waiting time is over, the T is subsequently cooled down, which implies the *freezing* of this equilibrium state. Then, when the MNPs are warmed, once T approaches the T_w , the sample magnetic moments *recall* that they achieved a metastable *equilibrium state*³ at T_w . Thus, this leads to a drop of the $\chi''(T)$ component at $T \lesssim T_w$. To probe this effect, the use of low-frequency AC fields remains essential, in order not to perturb the very delicate non-equilibrium dynamics of the SG systems [204]. Therefore, the observation of a drop in the $\chi''_{warming}(T)$ curve reveals the non-ergodic interacting nature of the frustrated SG phase achieved at $T_g = 18 \text{ K}$. This low temperature Spin Glass transition will also evidence aging phenomena, as it can be seen from the relaxation of the $\chi''(t)$ shown in Fig. 4.4b. The decay of the magnetisation with time follows the same trend as was found in other Spin Glasses [68, 77, 205]. In which concerns the high-temperature dissipation, no memory effects are found, as there does not exist a drop (see top right inset). This observation, opposite to the low-temperature transition, supports the non-interacting nature of this disorder contribution. This finding further backs up the idea previously raised that they are the uncompensated magnetic moments arranged within the AF-coupled core which are at the basis of this non-interacting disorder.

³not an actual equilibrium state, since we are dealing with non-ergodic dynamics.

The situation concerning the low-temperature dissipation corresponding to the 5h-milled SSG MNPs reads equally. Memory effect phenomena are displayed by the SG transition, as it can be seen in Fig. 4.4b. There, the $\chi''(t)$ was recorded at three different temperature values, 12, 15 and 18 K, which represent 0.66 , 0.83 and $1T_g$, respectively. The out-of-phase component displays memory effects for each of them (notice the drop in $\chi''_{aged} - \chi''_{notaged}$ in the top inset in Fig. 4.4b), being the relaxation undergone at $T_w = 18$ K the one taking place faster (see bottom inset), as expected [87].

In order to access more information on the robustness of the SG phase, we have also performed temperature cycles, following the protocol already stated in Chapter 3. Figs. 4.4c (1.5h) and d (5h) include these measurements, performed at $T = 15$ (Fig. 4.4c) and at $T = 18, 15$ and 12 K (Fig. 4.4d), with cycles of $\Delta T \approx 0.88, 0.97, 1.06$ and $1.11T_g$. First of all, both MNP ensembles achieve a completely reborn SG landscape (*rejuvenation*) when the cycling step is performed above T_g ($\Delta T \geq 1.06T_g$), as the χ'' post-cycle is equal to the former χ'' pre-cycle. Therefore, we have restricted our analyses to $\Delta T \leq 1.06T_g$. Also, one can observe that the smaller the ΔT , the slower the relaxation towards equilibrium, which indicates that larger free-energy barriers are built. This reveals that the *domains* of correlated spins are larger [77]. Still close to the *rejuvenation limit*⁴, the cycle performed at $\Delta T = 0.97 T_g$ brings more light into the dynamics of the SG state established at different MNP sizes.

Interestingly, **the SG freezing dynamics corresponding to the most robust SAF (1.5h) and SSG (5h) MNPs behave in a very similar fashion.** In this way, the $\chi''/\chi''(t=0)$ value at both 1.5h and 5h (25 nm and 7 nm, respectively) MNPs after the cycle performed at $\Delta T = 0.97T_g$ is around $\chi''/\chi''(t=0) = 0.98$, whereas it is already $\chi''/\chi''(t=0) = 1$ (fully recovered) for 1.75h and 2h (18 and 10 nm-sized) ones (not shown). This implies that the domains built for the former (1.5 and 5h) are larger, as the particular SG configuration is not completely *reborn* after the cycling. The reason beneath this feature can be deduced following the thread of the previous magnetic characterisation. This pointed the most interacting SG phase to be settled at 1.5h-milled MNPs. Once the SSG state is established, the smaller the MNPs, the more robust the frustrated interactions among the spins get, which yields naturally to 5h-milled (7 nm) MNPs to be more robust compared to 2h (10 nm)-ones.

⁴see Chapter 2.

Moving now to the smallest ΔT , the effect of a finite overlap length scale $\ell_{\Delta T}$ can already be observed at this $\Delta T = 0.88T_g$, as the $\chi''(t = t_{\Delta T})$ displays a non-zero value. This rise is enhanced as the step ΔT does, until the initial value is met, *i.e.*, $\chi''(t = t_{\Delta T}) = \chi''(t = 0)$. This is explained as follows. At $t = 0$, the Spin Glass ordered regions, that can be viewed as *domains*, start to develop with time, growing in size. This leads to a particular *metastable* spin configuration, namely, L_1 . The rise of temperature ΔT would then lead to a situation in which the larger clusters start to break down, while a new domain configuration (L_2) appears, *i.e.*, two SG domain configurations coexist. Therefore, several different length scales (time scales) are present. This has also been reported in previous works on Fe_{0.5}Mn_{0.5}TiO₃ and CdCr_{1.7}In_{0.3}S, to cite a few [76, 77]. This domain landscape is sketched in the inset of Fig. 4.4d.

As a summary of the magnetic properties of the GdCu₂ MNPs, we can conclude the following. First, we have observed two magnetic regimes depending upon the MNP size: The one of **larger MNPs**, $\langle D \rangle \geq 18$ nm, where there co-exists an ordered AF core plus a disordered SG surface, meaning that a **Superantiferromagnetic state** is settled; and **the one corresponding to MNPs below a critical size of $\langle D \rangle \leq 10$ nm**, where the AF structure vanishes and all the magnetic moments built up into a **SSG state**. Thanks to the $\chi_{AC}(T, f)$ and $\chi_{AC}(t)$ analyses, we have been able also to disclose **two particularities concerning the spin dynamics within each SAF and SSG arrangements**. This way, there is **a non-interacting spin disorder phase**, connected to the uncompensated magnetic moments forming AF domain walls, which contrasts with the interacting nature beneath the surface SG-like phase. On the other hand, when the MNPs are globally disordered in to the **SSG state**, **a two-steps freezing process of the spins has been observed**, where the surface moments freeze before the ones located within the core. **The occurrence of two different spin dynamics** within each global state (SAF and SSG) supports the existence of **two-length scales in the GdCu₂ MNPs**, a fact that has also been observed in nanocrystalline Gd [206]. In that work, F. Döbrich et al. showed the occurrence of two length scales, the one with defect cores of the grain boundaries, which was around 5 nm, and a larger one, of around 20 nm, which accounts for the anisotropy of the whole crystallite. This observation would back up our conclusion of the existence of a double contribution to disorder in our GdCu₂ MNP ensembles.

4.2 Specific heat measurements

As we have already commented in chapters 2 and 3, thanks to the specific heat analyses, one can obtain information on the magnetic transitions undergone by the sample. Besides, an insight to the CEF, which, in the case of GdCu₂, does not apply, can be gained. Following the analysis procedure of eq. 3.34, we have separated the measured c_P as a sum of the $c_{lattice}$ and the $c_{mag+CEF}$. For the particular case of Gd³⁺ ions, given their S -state, the CEF contribution vanishes, remaining only the c_{mag} one. In any case, the sticking point of the analyses was related to the former $c_{lattice}$, as we have already commented in detail in Chapter 3. Therefore, we have analysed the c_P of the GdCu₂ ensembles **by taking into account both core and surface environments according to eq. 3.35. Each contribution is weighted by the proportion of magnetic moments located within the core and at the surface**, which are estimated, according to eq. 5.1, to be $N_c = 2.7, 2.4$ and 1.8 and for 1.5h, 2h and 5h, respectively, and, indeed, $N_s = 1 - N_c$.

Table 4.3: Values for surface Sommerfeld coefficient γ^s and Debye Temperature, θ_D^s , for GdCu₂ 1.5h, 2h and 5h-milled MNP ensembles, obtained according to eq. 3.34.

t (h)	γ^s (mJ(molK ²) ⁻¹)	θ_D^s (K)
1.5	22.8(1)	225(1)
2	27.9(2)	259(1)
5	33.9(1)	265(2)

According to this procedure, the green line in Fig. 4.5a represents the obtained $c_{lattice}$ for 1.5h milled MNPs (given as an example). Values of $\gamma^c = 6.7(2)$ mJ(molK²)⁻¹ and $\theta_D^c = 277(3)$ K have been obtained, which agree well with the ones obtained for bulk alloy (not shown), and reported for polycrystalline bulk GdCu₂ [207]. The obtained γ^s and θ_D^s values have been inserted in Table 4.3. There, it can be seen that both parameters increase with the size reduction, a fact that is expected, according to the increasing surface disorder (γ^s) and surface-to-core ratio (θ_D^s). The inset of this figure shows the magnetic entropy S_{mag} against the temperature. This S_{mag} is obtained according to:

$$S_{mag}^{exp} = \int_0^{300} \frac{c_{mag}}{T} dT \quad (4.1)$$

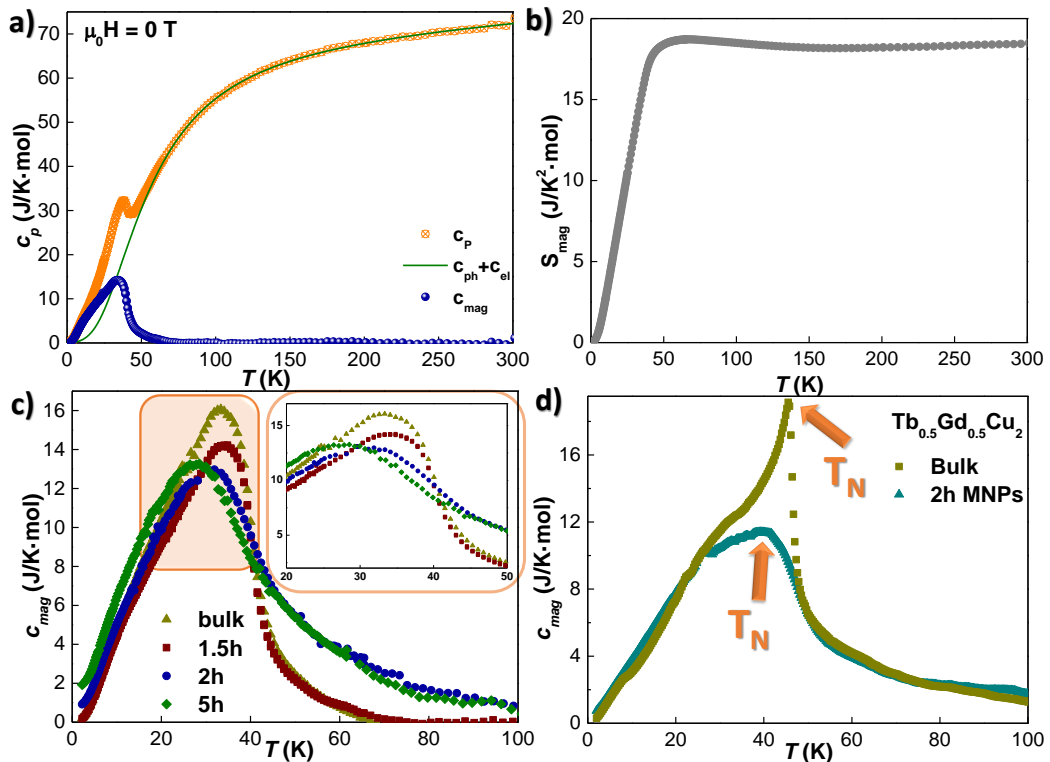


Figure 4.5: **a**) Measured specific heat (orange) together with the $c_{lattice}$ (green) and the c_{mag} contributions for GdCu₂ 1.5h milled MnPs. **b**) Magnetic entropy for bulk GdCu₂ alloy, where it can be seen that saturation is almost achieved around $T_N = 40$ K. **c**) c_{mag} contribution corresponding to bulk, 1.5h, 2h and 5h-milled MnPs. Inset zooms the region surrounding the hump contribution to c_{mag} . **d**) c_{mag} contribution corresponding to Tb_{0.5}Gd_{0.5}Cu₂ bulk and 2h milled MnPs alloy. All the measurements (**a**)–**d**) have been performed under no external applied field.

The experimental magnetic entropy is slightly greater with respect to the theoretical value $S_{mag}^{theo}(300K) = R[\ln(2J + 1)] = 17.29$ J/mol·K² as $S_{mag}^{exp} \sim 18$ J/mol·K², a fact that is revealing that the $c_{lattice}$ has been slightly underestimated.

Coming now to Fig. 4.5b, a depiction of the $c_{mag}(T)$ is provided for the bulk, 1.5h, 2h and 5h-milled alloys. Indeed, it is important taking into account that, for milling times $t \leq 1.5$ h, the MnPs display two sources of c_{mag} . On the one hand, **the AF-coupled magnetic moments give rise to a λ -like peak shape anomaly**, located at $T \sim 40$ K. This contribution should show a slight left-shift with the size reduction, as the reduction of the number of AF-coupled bulk materials have evidenced this tendency [208, 209]. On the other hand, at temperatures

below T_N , a Schottky-like type contribution emerges, which can be traced in the form of a broad hump [210]. In the case of GdCu₂, the occurrence of this Schottky should be ascribed to the Zeeman splitting of the eight-fold degenerate energy level, rather than to a spin wave propagation and/or CEF effects [93, 160]. The fact that the excess of c_{mag} drops to zero for $T > T_N$, rules out the possibility of a CEF-motivated contribution to c_P . This lack of CEF contribution is congruent with the S -state of Gd³⁺, and has already been reported for GdCu₂ single-crystal [211] and GdCu_x bulk antiferromagnets [207]. Both AF and Zeeman contributions are so close one to each other that they overlap, resulting on a single broad cusp, rather than in two separated signatures.

When $t \geq 2h$, a broad cusp with a tail that extends up to $T \sim 100$ K. The cusp intensity is reduced with respect to the one of bulk and 1.5h milled alloys, and moves towards lower temperatures, $T \sim 31$ (2h) and $T \sim 27$ K (5h). The situation for these SSG MNPs reads very similar to the one of the bulk and 1.5h-milled alloys. Even though the AF interactions are not strong enough to give rise to a collective well-defined ordered state within the smallest MNPs, they still exist within the sample, as they are a basic requirement for magnetic frustration [50]. Consequently, it could be possible that some regions of the MNPs give rise to an *effective* local field, which splits the multiplets (Zeeman splitting), resulting on a contribution to the c_{mag} . Of course, as the AF order interactions are further damaged (increasing disorder caused by the milling), this splitting gets smaller. Consequently, the hump appears at lower temperature values, moving from $T \sim 31$ (2h) to $T \sim 27$ K (5h). The tail (asymptotic decrease to zero of the c_{mag}), which was not observed for larger MNP sizes (lower milling times), shall be ascribed to the **SG-frustrated moments**, which may give rise to (tiny) contributions to the specific heat [50, 210, 212, 213].

For the shake of clarity, we are advancing here the great advantage of using Gd³⁺-ions, as they provide a probe for disclosing these c_{mag} subtleties. As an example, we have decided to include in Fig. 4.5c the c_{mag} contribution coming from a Tb_{0.5}Gd_{0.5}Cu₂ alloy at both bulk and MNP state. Even with a 50% Tb³⁺ content, the influence its CEF splitting masks the SG contribution to the specific heat. In consequence, it is impossible to disclose, already at the bulk state, the subtle details concerning the SG tail. A more detailed analysis on this Tb_{0.5}Gd_{0.5}Cu₂ system will be provided in Chapter 6.

To sum up, **an evolution from a Superantiferromagnetic to a completely**

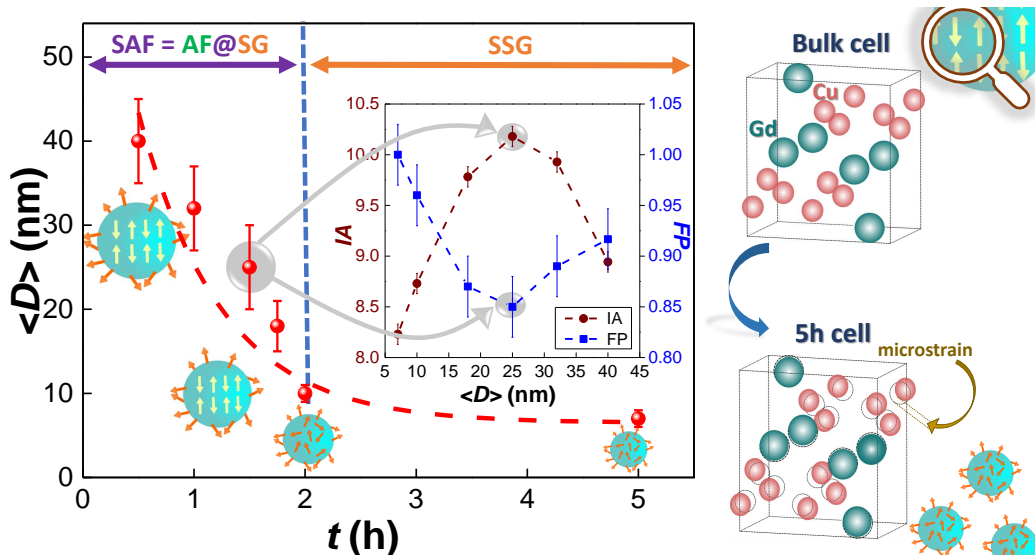


Figure 4.6: Mean NP size $\langle D \rangle$ as a function of milling time t for the six produced ensembles of GdCu₂. The inset depicts the IA and FP parameters at $\mu_0 H = 10$ mT

disordered global Super Spin Glass state as a function of the MNP size has been shown by the GdCu₂ ensembles. Note in Fig. 4.6 how the amount of magnetically disordered moments increase as the MNP size decreases with increasing the milling time, t . These magnetic, that are *detached* from the AF order state, give rise to a Spin Glass–like disorder state, which stems as a consequence of the frustration of the RKKY indirect exchange interactions.

Along with the finite–size effects (lower coordination, symmetry breaking), the microstrain, even if minimal, plays a key role, as it distorts the aspherical $4f$ charge distribution by altering the lattice position of the Gd³⁺ from their bulk situation. This may also lead to the frustration among the RKKY interactions, as it has already been explained in Chapter 2. By pushing this microstrain beyond, but still far from getting an amorphous alloy, one can come to a situation where the collective AF order state breaks down, and the magnetic state of the NPs undergoes a transition to a Super Spin Glass ensemble. This is the situation that takes place when a **limit size $\langle D \rangle \sim 18$ nm is overcome.**

Finally, the inset of this Fig. 4.6 brings the reader’s attention to one singular fact, which is that, on the contrary of what one may think at first glance, **the maximum frustration of the RKKY interactions is achieved for 25 nm–sized MNPs, where there still exist a robust AF collective state** (see in the

inset the maximum (minimum) of the IA (FP). This result can be understood in terms of a balance between a strong competition between FM–AF interactions (frustration, SG) and the AF interactions themselves, that are required to be strong enough to participate in the competition.

Chapter 5

NdCu₂ magnetic nanoparticles

*“Sólo por que es mi niña,
cualquiera se encariña.”*

Wisin feat. Myke Towers

Among the light Rare–Earths, Nd³⁺ ions display an electronic configuration $4I_{9/2}$, with 3 unpaired electrons. This half–integer spin configuration leads Nd³⁺ to be considered as Kramers ions, which implies that the energy levels are, at least, doubly degenerated. Furthermore, from the point of view of the magnetic structure, the Kramers nature of Nd³⁺ also forces the magnetic moments to be fully saturated when $T \rightarrow 0$ K [138]. To do so, the magnetic moments usually collapse at low temperature into a square–wave modulation, and the appearance of higher order harmonics is expected [138].

As it has already been stated in Chapter 2, the large spin–orbit interaction makes the lowest multiplet J to be enough to describe the energy state. This is a great advantage to study the CEF schemes and the possible splitting of the multiplets when a magnetic state is set, as it eases the theoretical and computational efforts [111]. Particularly, as the electronic configuration of Nd³⁺ is well–described by $J = 9/2$, where the splitting caused by the CEF is expected to give rise to 5 energy levels, the one corresponding to the ground state + 4 excited levels. These energy levels are actually doubly–degenerated (Kramers). The separation between each doublet is, at least, of around 2–3 meV, which is more than enough to be detected by means of Inelastic Neutron Scattering (INS).

From the point of view of magnetism, **NdCu₂** has evidenced a **very complex**

antiferromagnetic structure already at bulk state. In this way, the magnetic moments arrange, at $T \rightarrow 0$ K, into a commensurate–square up modulated magnetic structure, where the propagation vector is $\tau = (0.6, 0, 0)$, and the harmonic associated with $3\tau = (0.2, 0, 0)$ [213]. Although higher order harmonics should appear, there is only one reported study where, thanks to the use of a single crystal instead of polycrystalline powder sample, the 5τ harmonic has been detected [214]. Then, at the reorientation temperature $T_R \sim 4.4$ K, there is a change in the AF structure, as a first–order transition takes place and the magnetic structure builds incommensurate with the crystal lattice, following $\tau = (0.612, 0.042, 0)$ [213, 214, 215]. This incommensurate structure keeps a sinusoidal modulation up to $T_N = 6.5$ K, where the second–order transition from AF to PM takes place, and the magnetic order is wiped out.

The crystalline structure is that of the orthorhombic CeCu₂–type one, with space group *Imma* (No. 74). The Nd³⁺ ions occupy the *4e*-sites (0, 0.25, *z*), whereas Cu atoms are located at the *8h* position (0, *x*, *y*). Values for *x*, *y*, and *z* are found to lie near $x \sim 0.0506$, $y \sim 0.1659$, and $z \sim 0.5383$. Lattice parameters for this bulk unit cell have been found to be $a = 4.3843(4)$, $b = 7.0326(6)$ and $c = 7.4194(15)$ Å.

Fig. 5.1 illustrates the state of the art of the bulk NdCu₂. As we will deepen in the particular details along this chapter, here, we will just provide a small *flavour* of this alloy. Accordingly, the main features of NdCu₂ bulk alloy are the orthorhombic crystalline structure, represented in Fig. 5.1a, the presence of two magnetic transitions, clearly depicted in Fig. 5.1b in the M_{DC} , its low–temperature commensurate phase, shown in closer detail in Fig. 5.1c, and, finally, the CEF splitting of the $J = 9/2$ multiplet into the aforementioned–mentioned 5 doublets (Fig. 5.1d), as revealed by INS.

The research carried out in the NdCu₂ MNPs shown along this Chapter was focused on determining whether the AF structure was kept in the NP regime, more specifically, how do size–effects and microstrain affect the two transitions that take place in this alloy. To do so, ND, SANS XRD, magnetic $M_{DC}(T, \mu_0 H)$ and dynamic $\chi_{AC}(T, f, t)$ characterisation, and specific heat measurements have been carried out. What is more, **we have been able to study, by means of INS measurements, how the change of symmetry environments (reduced coordination) and dimensionality (2D–surface vs. bulk–core) affect the CEF splitting and magnon (spin waves) propagation across ensembles of 13 nm–sized MNPs.** The main results will be elaborated hereunder.

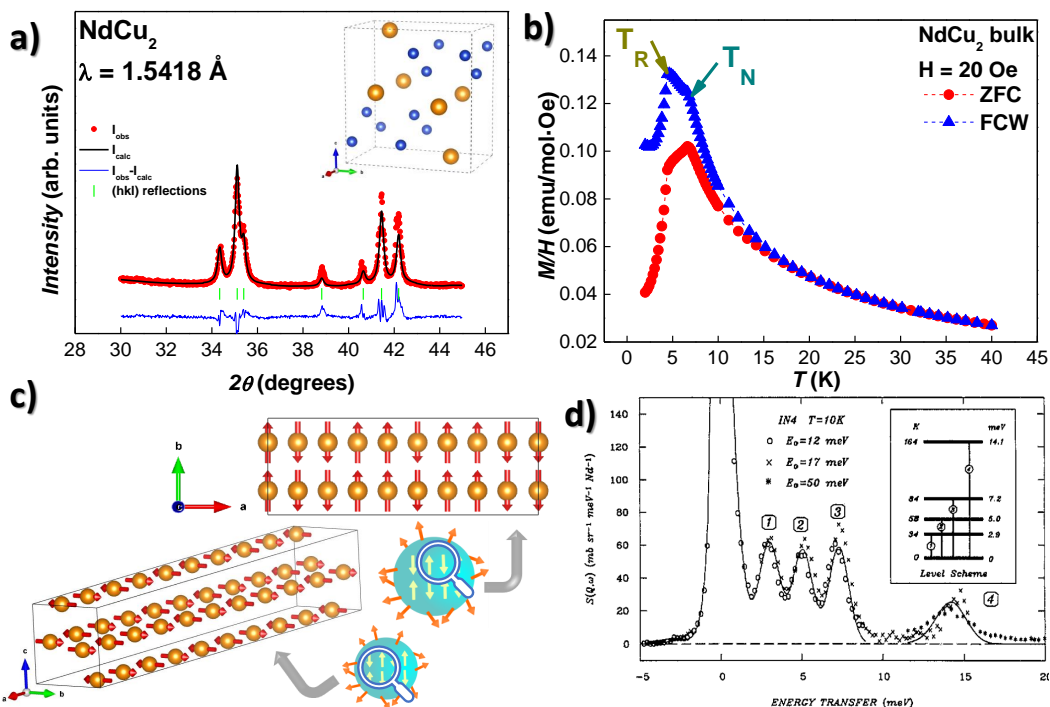


Figure 5.1: **a)** XRD patterns together with the Rietveld refinements performed on NdCu₂ bulk alloy. Inset displays the unit cell, where the Nd-ions are in yellow and the Cu-atoms, in blue colour. **b)** Displays a M/H vs. T ZFC-FC, where the position for the reorientation and Néel transitions (T_R and T_N , respectively) are marked with arrows. **c)** displays a sketch on the magnetic commensurate unit cell, with comprises 20 crystalline cells along a direction, 10 along the ferromagnetically-coupled b - c planes. **d)** shows the INS spectrum for NdCu₂ bulk in the PM region, where the splitting of the ground state $J = 9/2$ by the CEF leads to 5 energy levels. This spectrum is taken from [99].

5.1 Magnetic order and disorder on NdCu₂ nanoparticles

The first step to follow a sensible rationale, already applied in the other alloys introduced along this Thesis, was to verify that the bulk orthorhombic crystalline structure was kept within the nanoparticles. We address the reader to Appendix A to check out the XRD interpretation, where all the Bragg peaks are indexed congruently within the *Imma* orthorhombic structure. The Rietveld refinements disclose a minimal lattice distortion (below 0.1%) for the MNPs, whose mean particle size $\langle D \rangle$ and microstrain η have been calculated to $\langle D \rangle = 18.3(1.0)$ nm and $\eta = 0.62(7)$ %, and $\langle D \rangle = 13.0(5)$ nm and $\eta = 0.59(1)$ % for $T = 2$ h and 5h, respectively. The achieved low Bragg factors¹ ($R_B < 2\%$ in both MNP sizes) reinforce the reliability of the performed refinements.

Once the crystalline structure of NdCu₂ MNPs is secured, a closer insight to the magnetic structure is necessary. As we have explained in the introduction of this chapter, the questions that have to be faced concern, on the one hand, the AF Néel transition (bulk, $T_N = 6.5$ K [93]), and, on the other hand, the incommensurate–commensurate transition (bulk, $T_R = 4.2$ K [93]). To disclose both issues, we have employed Neutron Diffraction (G4.1, LLB, CEA–Saclay, France) and Small–Angle Neutron Scattering (ZOOM, RAL–ISIS, UK) measurements. We will begin by presenting the ND results, and afterwards, the SANS ones.

Beginning with the **ND analyses**, Fig. 5.2 includes the ND patterns, together with the the Rietveld refinements (Thompson-Cox-Hastings equations, [133]), at $T = 15$ K (PM) and $T = 1.5$ K (AF, commensurate) for the 2h (Figs. 5.2a and b) and 5h–milled MNPs (Figs. 5.2c and d), respectively. Rietveld refinements on the PM region (Figs. 5.2a and c) allow to access structural (nuclear) information, since no magnetic order is contributing here. According to these calculations, a mean MNP size of $\langle D \rangle = 16.5(4)$ nm (Bragg factor $R_B = 2.6\%$) for 2h–milled and $\langle D \rangle = 12.7(1)$ nm ($R_B = 2.4\%$) for 5h–milled MNPs are obtained, respectively. These values are congruent with the ones obtained by means of XRD analyses (see Append A).

$${}^1R_B = \frac{\sum_i |I_i - I_i^{\text{calc}}|}{\sum_i |I_i|}$$

The variation of temperature in the ND experiment allows to analyse the volume modification of the lattice. This is especially useful in systems where (structural) phase transitions, anomalies in the thermal expansion coefficient and/or magnetoelastic effects are present. Precisely, the Rietveld analyses conducted on both the non-magnetic (nuclear) and the magnetic structures allow to observe the occurrence of **magnetoelastic effect**, which is characteristic of RCu₂ [110]. In this sense the unit cell volume V reduces with decreasing T , yet it shrinks more dramatically once the AF state is settled. This is clearly depicted in the inset of Fig. 5.2a, from which a change in the decrease rate $\frac{\Delta V}{\Delta T}$ is obtained depending upon the magnetic state. Accordingly, the $\frac{\Delta V}{\Delta T}$ is ≈ 42 times and 33 times greater for $T < T_N$ than for $T > T_N$ (PM state). This magnetoelasticity, that is common in RCu₂ intermetallics [99, 110], softens for $t = 5$ h milled MNPs due to the reduction of the number of AF-coupled magnetic moments.

Paying now more attention to the magnetic state at $T = 1.5$ K, in Figs. 5.2b and d, the outburst of extra peaks associated with the magnetic periodicity can be easily observed, especially, in the region $18.5^\circ < 2\theta < 24^\circ$ (see the insets). Both the sharpness and the scattering intensities of these magnetic peaks are reduced with respect to the bulk, as a result of finite-size effects [111]. In order to give account for these AF peaks, we have employed a **commensurate square-up modulation description**, in the same way as for the bulk alloy [213]. The magnetic cell consists therefore of ten crystallographic unit cells along the a -direction, being the moments separated by $a/2$ with respect to each other. Each of them is oriented along the b -direction, being the b - c planes ferromagnetically aligned. This structure is the same as the one sketched on Fig. 5.1c. This magnetic cell would then extend up to ~ 43 Å, a value that is smaller with respect to the MNP core diameter of 5h-milled MNPs, ~ 90 Å. Thereby, the MNP core can host an AF arrangement [216]. Furthermore, the magnetic Rietveld refinements point to a nuclear size slightly larger than the magnetic one, as $\langle D_N \rangle = 16.5(4)$ nm ($R_B = 2.4$ %) and $\langle D_m \rangle = 15.5(3)$ nm ($R_B = 6.64$ %) for 2h-milled MNPs, and $\langle D_N \rangle = 12.6(6)$ nm ($R_B = 1.56$ %) and $\langle D_m \rangle = 12.4(3)$ nm ($R_B = 4.7$ %) for 5h-milled ones.

The sine-wave modulation propagates according to $\tau = (0.6, 0, 0)$ and the harmonic associated with $3\tau = (0.2, 0, 0)$. No higher harmonics could be detected, as these are too subtle to be detected on polycrystals. Experiments conducted on a NdCu₂ single-crystal were able to detect up to the the 5τ harmonic [214]. As it has already been mentioned, a modulation in the intensity should be recovered for the Kramers Nd³⁺ ions [138]. To this aim, we have described this

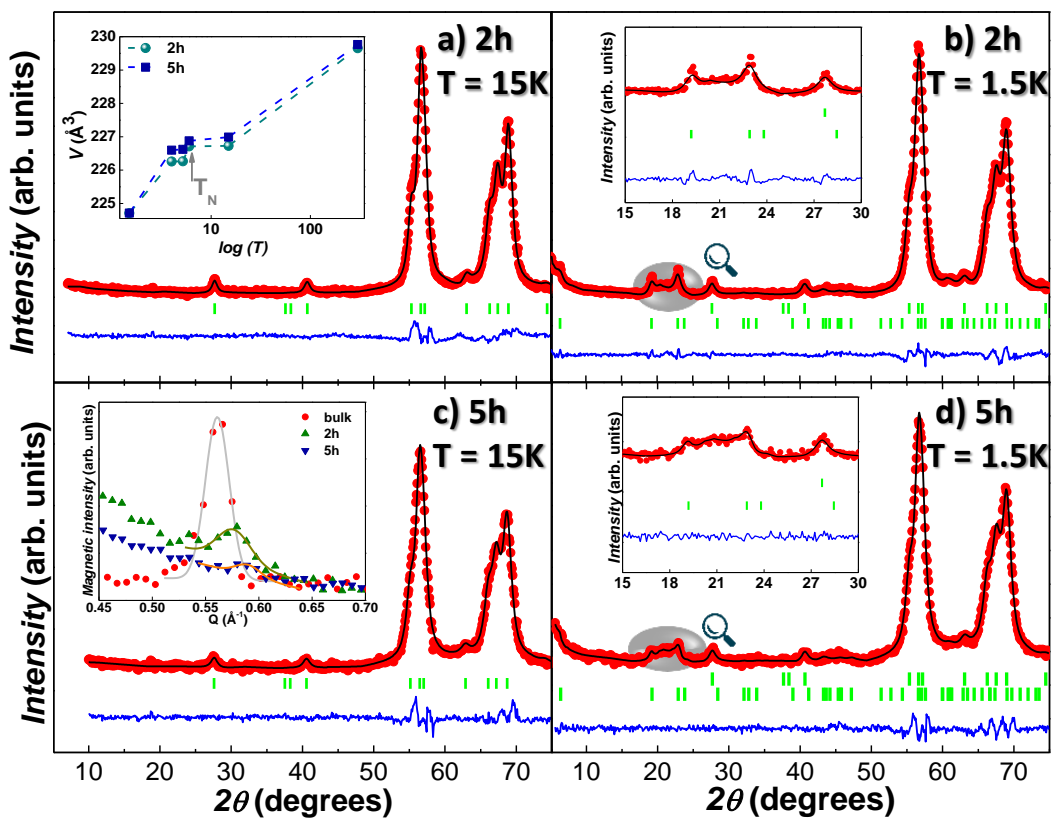


Figure 5.2: Neutron diffraction patterns ($\lambda = 2.426 \text{ \AA}$) and Rietveld refinements for **a), b)** NdCu₂ 2h-milled and **c), d)** 5h-milled MNPs measured at $T = 15 \text{ K}$ (**a)** and **c)**) and $T = 1.5 \text{ K}$ (**b)** and **d)**), which correspond to the PM and magnetic ordered regions respectively. The inset in **a)** shows the reduction of the unit cell volume with decreasing temperature. The position of the Néel transition is marked by the gray arrow. The inset in **c)** shows the progressive disappearance of the magnetic peak located at $q \approx 0.55 \text{ \AA}^{-1}$ with size reduction. The insets in **b)** and **d)** allow to observe in closer detail the broadening of the magnetic reflection within the range $18.5^\circ < 2\theta < 24^\circ$.

modulation according to the sine-wave modelled by the following Fourier series: $\mu = \mu_\tau \sin(2\pi\tau R_i/a + \phi_1) + \mu_{3\tau} \sin(6\pi\tau R_i/a + \phi_3)$, where $R_i = 0, a/2, a, \dots, 5a$. This description results in magnetic moments of $\mu_\tau = 2.76(6) \mu_B$ (2h-MNPs) and $\mu_\tau = 2.64(6) \mu_B$ (5h-MNPs), associated with the first harmonic τ , and $\mu_{3\tau} = 0.94(3) \mu_B$ and $\mu_{3\tau} = 0.98(3) \mu_B$ with the third 3τ ($R_B = 10.7\%$ for 2h-MNPs and $R_B = 6.7\%$ for 5h-MNPs). These values give $M_0 = \pi/4 \cdot \mu_\tau = 2.2(1) \mu_B$ and $M_0 = \pi/4 \cdot \mu_\tau = 2.0(5) \mu_B$ magnetic moments values for 2h and 5h-MNPs, respectively, and are smaller than the maximum theoretical magnetic moment of $3.27 \mu_B$. This finding, which has also been observed previously in the bulk alloy [99], can be understood by the CEF influence on the Nd³⁺ ions [217]. **The decrease of the magnetic moment value with the MNP size confirms the reduction of the AF-coupled entities.**

The presence of a disordered moment arrangement, connected to the existence of interfaces, could, in principle, give rise to **interparticle correlations**. To verify this, the magnetic scattering intensity has been plotted vs. q , in the inset of Fig. 5.2c. There, the observation of a rise for the low- q region ($2^\circ < 2\theta < 15^\circ$, i.e., $q < 0.665 \text{ \AA}^{-1}$), unveils the existence of such correlations, that are triggered by the dipolar interactions among MNPs [43, 67]. The reduction of the AF-coupled magnetic moments with size reduction is also supported by the gradual removal of the intense bulk magnetic peak located at $q \approx 0.55 \text{ \AA}^{-1}$, $2\theta \approx 12.4^\circ$, as this peak gets progressively broadened and displaced to higher q values with the size reduction.

Once the particularities regarding the second-order Néel transition have been disclosed, the question that should be faced is **whether there is or not a transition connected to the reorientation of the magnetic moments**, which has been classified as a first-order one. As it was reported in [213, 214, 215], the magnetic moments of the bulk alloy undergone a transition from a low-temperature commensurate structure to an incommensurate arrangement at $T_R \sim 4.2$ K. Getting an answer to this question is important not only from a fundamental viewpoint, yet it drives some implications connected to powerful applications. In this sense, it has been reported that incommensurate arrangements give rise to helical structures [138]. Provided that helix is a kind of configuration very suitable for hosting magnetic skyrmions [218], having the possibility of disclosing the helicity on the NdCu₂ MNPs is key to rise, or not, these nano-alloys to a potential position for these exotic spin textures to occur.

To scrutinise the occurrence of a reorientation in the MNPs, in Figs.5.3a, c

and e, we have included the ND patterns, together with the Rietveld refinements (Bragg factor $R_B < 10\%$ in all of the cases), for the three NdCu₂ alloys (bulk, ~ 18 nm and ~ 13 nm), measured at $T = 5.2$ K (*ie.*, in the region $T_R < T < T_N$). The refinements in the bulk alloy represented in Fig. 5.3a show a change in the propagation vector to $\tau = (0.612, 0.042, 0)$ with no higher harmonics, as expected from [213, 214, 215]. However, **this description does not hold within the MNP regime, where the magnetic structure keeps the commensurate arrangement up to T_N** . Specific heat measurements (shown afterwards) will further confirm this statement, as no trace for transition at T_R is detected in the MNPs.

One interesting feature of the patterns shown Figs.5.3a, c and e concerns the way that the magnetic peaks located at $18^\circ \leq 2\theta \leq 25^\circ$, which correspond to (0 0 0) and (1 1 0) reflections, smooth as the MNP size decreases. This brings to the fore the progressive loss of the AF ordering, together with the appearance of microstrain. In addition, the rise in the intensity observed for the MNPs at $2\theta < 7^\circ$, ($q < 0.316 \text{ \AA}^{-1}$) unveils again the existence of interparticle correlations. These will be related, thanks to the magnetic measurements, to the Spin Glass state of these surface magnetic moments, a fact that is very common in RCu₂ MNPs [43, 67, 219].

The right panel of Fig. 5.3, which encompasses Figs. 5.3b, d and f, depicts the evolution of the magnetic moment associated with each harmonic, M_τ (left axis) and $M_{3\tau}$ (right axis), with the temperature. These values have been obtained as $M_\tau = \pi/4 \cdot \mu_\tau$ and $M_{3\tau} = \pi/4 \cdot 3 \cdot \mu_{3\tau}$ for the fundamental (left axis) and third harmonic (right axis), respectively. A decrease in the value of the magnetic moment with the decreasing of the MNP size can be observed, which is congruent with the progressive loss of the AF-coupled entities. The comparison with the Brillouin function for $J = 9/2$ (red-dashed line) shows a reasonable agreement.

All in all, **thanks to the ND analyses, it can be concluded that the bulk commensurate AF structure is definitely kept within the MNP core**. The **finite-size effects and microstrain** associated with the nanoparticles **prevent the commensurate-incommensurate transition to take place in the studied MNP sizes**. Besides, the rise of the scattering signal in the low-angle (low- q) region announces a **correlation among the disordered magnetic moments**. This disorder phase is congruent, as it will be shown afterwards in the magnetic characterisation section, with a Spin Glass-like state. According to Chapter 3,

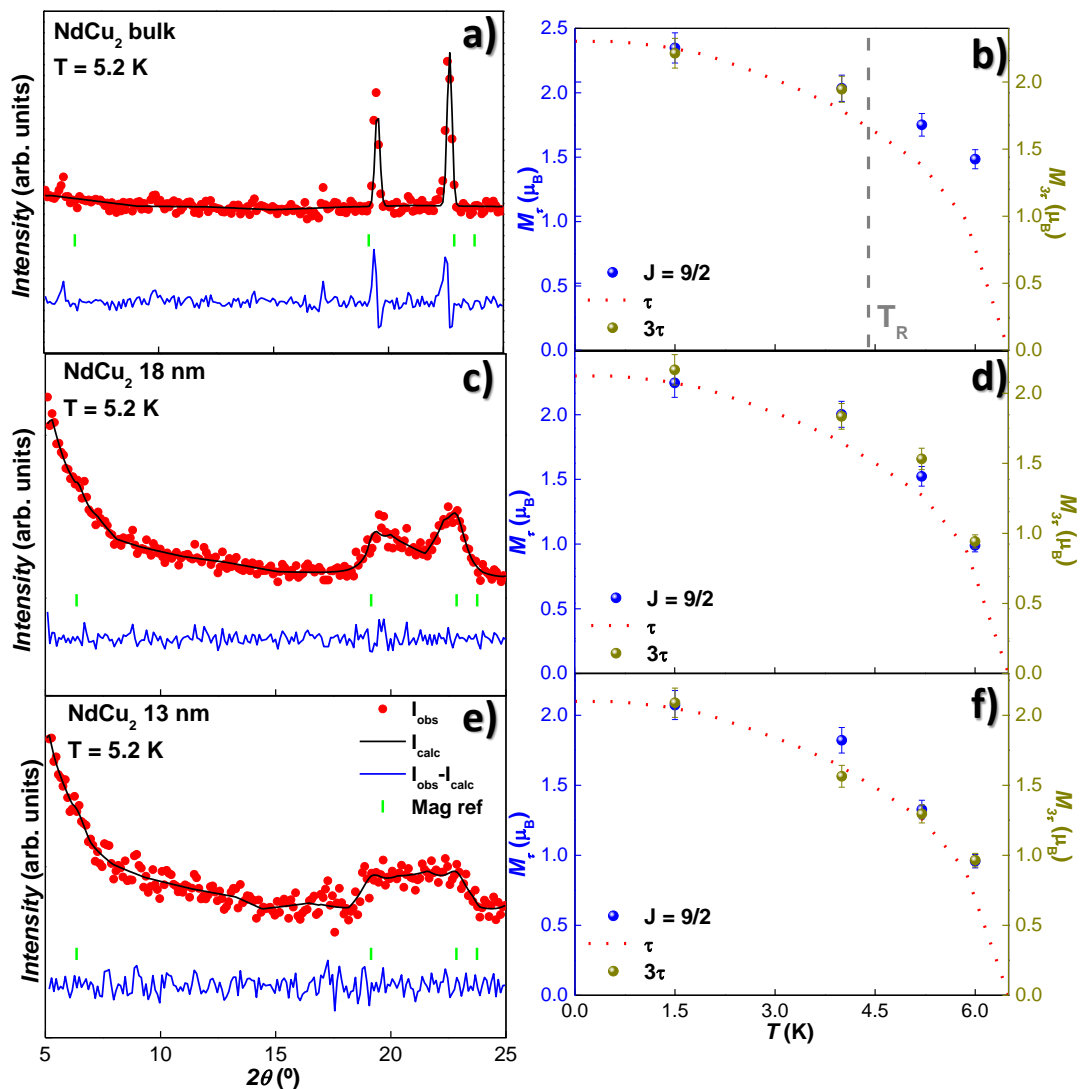


Figure 5.3: Left-side panels **a**), **c**), and **e**) show neutron diffraction patterns ($\lambda = 2.426 \text{ \AA}$) and Rietveld refinements measured at $T = 5.2 \text{ K}$ for NdCu₂ bulk, 18 and 13 nm-sized MNPs, respectively. The patterns display the region $5^\circ \leq 2\theta \leq 25^\circ$, where the intensity of the magnetic reflections is most noticeable. Right-side **b**), **d**), and **f**) display the temperature-dependence of the unit cell magnetic moment. It is worth noting that the commensurate-incommensurate transition only takes place for the bulk alloy (see gray dashed-line in **b**)).

information concerning the correlations among the magnetic moments, from the ones among the magnetic moments, to the ones within the different magnetic unit cells, can be accessed by using SANS. Therefore, we have accessed the low- q region of the NdCu₂ neutron scattering by means of this sophisticated technique.

Not only are the **correlations within the nanoparticle regime of primer interest**, but the complex magnetic structure of NdCu₂ makes also appealing to study the SANS coming from the bulk alloy. This complex magnetic structure hosts a combination of AF-coupled magnetic moments along the a -direction and FM-coupled b - c planes, which leaves **the possibility of an helix arrangement to be settled**. If this was the case, the period of this helix, which is of, normally, a few tens of nanometers, should be detected in the form of a peak in the SANS region. Notwithstanding, it is very surprising the fact that there are no reported studies, to the best of our knowledge, elucidating whether NdCu₂ could carry an helical configuration. Even the detailed study undergone by R.R. Arons *et al.* [213] does not even mention this possibility, which would definitely boost the interest towards the alloy. Indeed, a similar type of helix configurations are very suitable, for instance, to hosting magnetic skyrmions [218]. One possible reason for this lack may be related to the inherent complexity of the techniques needed to face this question (*e.g.*, muon-resonance spectroscopy or SANS), plus the limited access to them, as they require the use of a large facility. Needless to say, a deep and solid background to manipulate and to interpret the data are mandatory, which enhances the difficulty. In our case, we were awarded with allocation and beam time at RAL-ISIS to measure 3 NdCu₂ alloys, bulk, 2h and 5h-milled MNPs.

We will introduce first the results concerning the SANS measurements performed on the **bulk NdCu₂** alloy. These were taken within the q -range 0.04–4 nm⁻¹ (real space distance d between 157–1.57 nm), and are represented in Fig. 5.4. This figure includes the elastic differential SANS cross-section $\frac{d\Sigma}{d\Omega}$, measured at $k \perp$ geometry, as a function of the momentum transfer q . The SANS patterns are almost field-independent in the whole $\mu_0 H$ measured range for all the measured temperatures, even the ones concerning the magnetic state ($T < 6.5$ K). These features can be observed in both Figs. 5.4a ($T = 2$ K, $\mu_0 H$ between 0 and 3 T) and 5.4b ($\mu_0 H = 0$ T, $T = 2.1, 4.8$ and 11.3 K). The fact of measuring a field-independent SANS contribution in the NdCu₂ bulk alloy is actually surprising, as a field-dependence should be observed according to the two spin-flip metamagnetic transitions that undergoes the alloy, from a pure AF state ($\mu_0 H < 0.75$ T) to a Ferrimagnetic arrangement (0.75 T $< \mu_0 H < 2.7$ T) and then, to a FM phase [215, 220]. For the shake of clarity, the inset of Fig. 5.4a includes a sketch on the

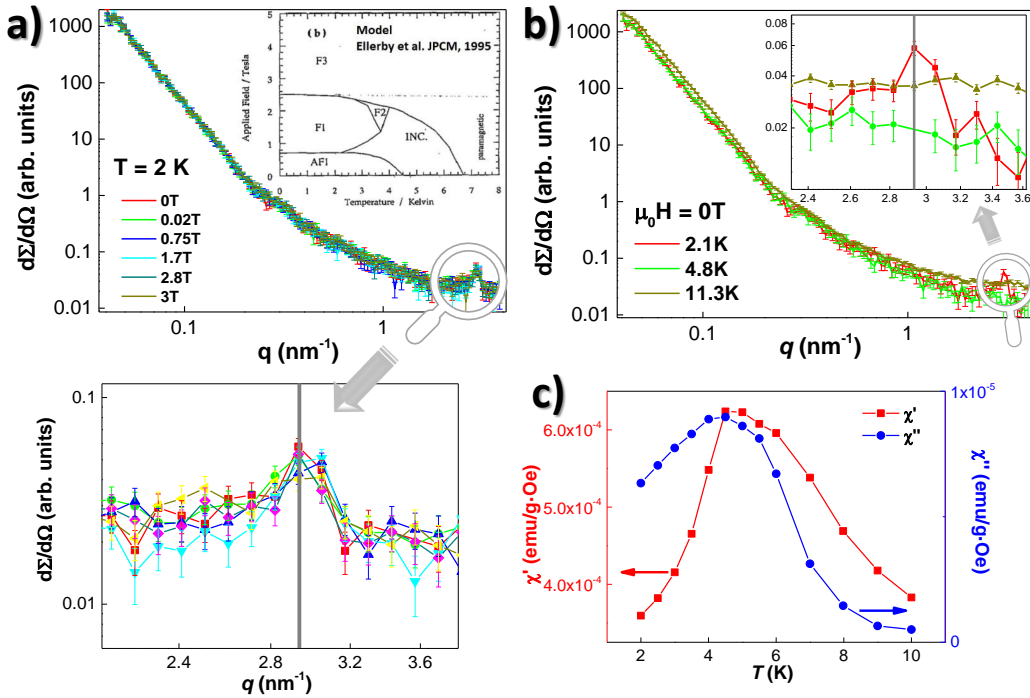


Figure 5.4: Differential SANS cross-section $\frac{d\Sigma}{d\Omega}$ vs. momentum transfer q (log-log scale) measured for NdCu₂ bulk alloy at **a)** $T = 2$ K at different applied fields $\mu_0 H$ and **b)** at different temperatures under no applied field. Bottom inset in **a)** depicts a closer inspection to the high- q peak is given at $T = 2$ K. The top inset shows the modelled-magnetic phase diagram of bulk NdCu₂, where the magnetization is shown as a function of the temperature (diagram taken from ref. [215]). Inset in **b)** zooms-in the q region between 2.3 and 3.6 nm⁻¹ to better check the variations in the SANS intensity near the magnetic peak. **c)** showcases the in-phase χ' and the out-of-phase χ'' components vs. the temperature measured at $f = 0.2$ Hz and $h = 0.313$ mT, where two peaks can be inspected from the χ' at $T_R = 4.5(2)$ K and $T_N = 6.0(2)$ K. A broad cusp in the χ'' component is recovered in the vicinity of both transition temperatures.

magnetic phase diagram of NdCu₂, taken from [215]. Depending on the temperature and applied field, the NdCu₂ alloy undergoes up to 5 different magnetic states (apart from the obvious PM state). The reason for this lack of field-dependence in our NdCu₂ alloy has nothing is not intrinsic to the NdCu₂ itself, but to the sample (pellet) and its inherent porosity. In this way, an incipient *plateau* can be observed in the low- q region ($q \approx 0.04$), corresponding to real space distances of $d \sim 150\text{--}160$ nm. This reveals the presence of large scattering objects within our samples, that are not connected to the NdCu₂ itself, but to the presence of pores. The fact that **(i)** this SANS contribution does not show a dependence on either the field or the temperature (nuclear-like SANS signal), and **(ii)** it will also appear at the same values in the MNP regime (Fig. 5.5), further supports this pore-origin.

This way, the nuclear contribution to the scattering of the sample pores masks the own SANS contribution stemming from the NdCu₂. This strong nuclear scattering precludes a grain-boundary origin, as it gives rise to smaller scattering contributions [221]). Furthermore, the fact that the asymptotic decay of the SANS cross-section does not follow the Porod law $\frac{d\Sigma}{d\Omega}(q) \propto q^{-D}$, where D is an integer number $1 \leq D \leq 4$ [13, 144], but it does with $D \sim 3.4\text{--}3.6$, which corresponds to surface fractal structures [222], further supports the pore origin of this nuclear-like scattering [146, 223, 224]. These pores come as a result of the compaction process followed during the sample preparation, a feature that has been observed previously in other SANS works, e.g., [225]. This porosity is inherent to the followed rational for the SANS analyses; it is advisable to compare powders of bulk NdCu₂ and powders of nanocrystalline NdCu₂. Hence, the magnetic SANS low- q contribution arising from NdCu₂ is restricted.

Nevertheless, the influence of the porosity form factor vanishes at the high- q region, which means that the NdCu₂ scattering can be then unveiled. Therefore, we will restrict our analyses to this high- q region (zoomed in the bottom inset of Fig. 5.4a, $q > 2.2 \text{ nm}^{-1}$), bearing in mind, of course, that we are approaching the resolution limit of the instrument, which decreases as increasing q . In any case, **the observation of a peak located at $q \approx 2.930 \text{ nm}^{-1}$ is crystal clear**, and very relevant, at $T = 2$ K (see Figs. 5.4a and b). The aforementioned q value corresponds to a real space distance $d \approx 2.1$ nm, which is near 5-times the a parameter of the crystallographic unit cell. This reveals that the AF-RKKY exchange magnetic cell involves a great amount of magnetic moments, since it correlates up to 5 nuclear cells. The $\chi_{AC}(T)$ measurements (Fig. 5.4d) supports this correlation, as the presence of a cusp in the $\chi''(T, f)$ component at $T \lesssim T_N$ reveals that a large number of individual magnetic moments feel an additional correlation

than that of the long-range AF correlation. Furthermore, these short-range AF interactions are robust, since this peak remains almost unaffected even when $\mu_0 H = 3$ T is applied, as it can be clearly seen from the bottom inset of Fig. 5.4a.

The magnetic nature of this peak is further confirmed by inspecting the $\frac{d\Sigma}{d\Omega}$ vs. T dependence in Fig. 5.4b, as this peak is wiped out when the bulk alloy undergoes the transition from the commensurate phase to the incommensurate one (*i.e.*, $T > 4.2$ K), which is more noticeable in the inset. As a consequence of the change in the propagation vector from $\tau = (0.6, 0, 0)$ to $\tau = (0.612, 0.042, 0)$, a modification in the correlation among the magnetic moments takes place. This modification, even if slight, is enough for altering the periodicity of the magnetic structure along the b direction, as the b - c planes are not exactly FM-aligned. Thereby, the period along the b -direction changes from 10 to 23 crystallographic unit cells [214]. This might imply that we could recover a peak, but located at lower q values, *ie.*, masked by the nuclear pore scattering.

In any case, the survival of the AF state at $T = 4.8$ K is clear, as the SANS intensity remains close to the one corresponding to $T = 2$ K, even if we do not observe any magnetic peak (see Fig. 5.4b, inset), and, obviously, thanks to the evidence gathered thanks to the ND results. Both SANS contributions ($T = 2$, red, and 4.8 K, green line) are well below the one corresponding to the PM phase ($T = 11.3$ K, dark yellow line). This is expected, since a rise in the scattering signal due to the increasing disorder should be recovered in the non-magnetic state.

The question that NdCu₂ hosts or not an helix configuration cannot be unambiguously disclosed with the data at hand. The small tilt in the b - c planes plus the incommensurability of the magnetic structure could, certainly, argument in favour of the helimagnetic order. Nevertheless, the pore contribution masks the possible helix peak, which would be a definite proof of the helicity². At this point, a definitive statement cannot be raised. Of course, we would aim to disclose this issue by requesting more beam time, focusing our efforts on the high- q range, with a greater counting time to gain better statistics, and, indeed, trying to fix the porosity of the samples by applying greater pressure to the pellets, or, simply, directly using the pellets prepared after the arc-furnace.

To continue with SANS analyses, we will present the results concerning the MNPs. It is worth recalling at this point that, according to ND, the incommen-

²in the case of an helimagnetic order, one should also found the existence of tiny satellite peaks in the neutron diffraction patterns [138].

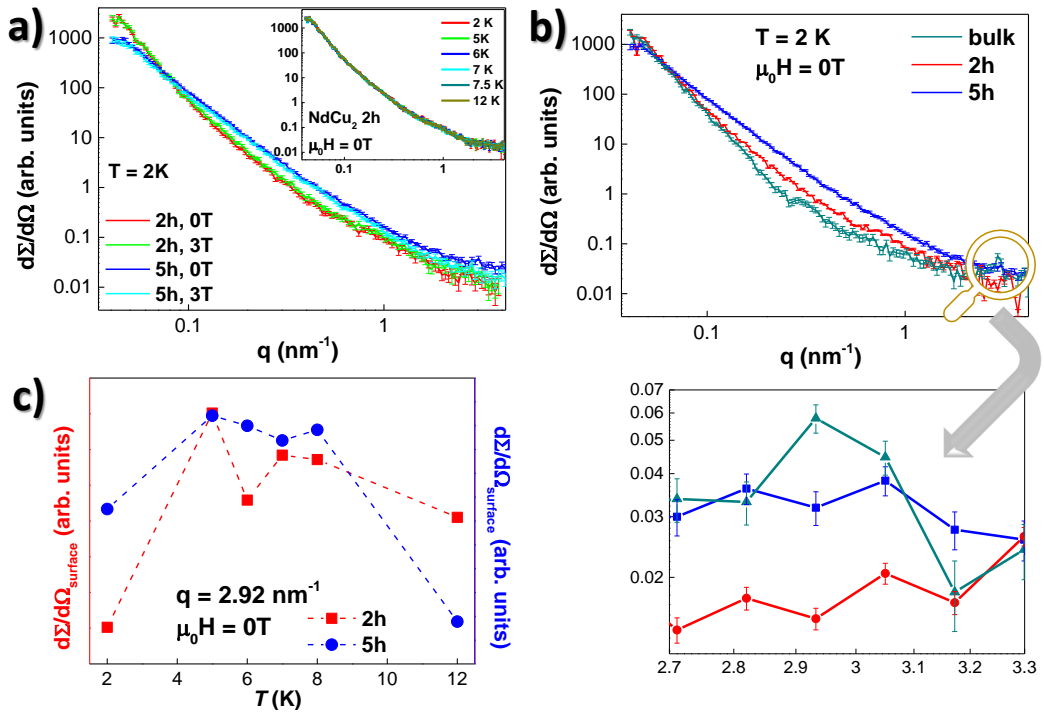


Figure 5.5: Differential SANS cross-section $\frac{d\Sigma}{d\Omega}$ vs. momentum transfer q (log–log scale) measured at $T = 2\text{ K}$ for NdCu₂ 2h and 5h MNPs under no applied field and under $\mu_0 H = 3\text{ T}$. The inset shows the SANS measured for the 2h–milled alloy under no external applied field at different temperatures between 2 and 11.3 K. **b)** Comparison between the bulk (dark–cyan) and the MNPs (red and blue, respectively) is provided, where they can be seen both the bending and the increase of the SANS contribution with the reduction of the MNP size, in good agreement with the reduction of AF–coupled moments. The bottom inset provides a closer look to the high– q peak, where no trace for the AF peak is recovered for the MNPs. **c)** displays the $\frac{d\Sigma}{d\Omega}$ at $q = 2.92\text{ nm}^{-1}$ at different measured temperatures. The bulk contribution has been removed, weighted by the N factor, in order to unmask the surface contribution to the SANS.

surability of the magnetic structure is lost when entering the MNP regime. This is not actually surprising, given the weakening of the AF interactions in the mesoscopic scale, compared to the bulk. In this sense, the increasing spin disorder results in a loss of magnetic transitions, particularly, the *weaker* ones, which is the case of this commensurate–incommensurate transformation. Later on, c_P or $\chi(T, f)$ measurements will confirm the loss of this transition in the MNPs.

Fig. 5.5a includes the $\frac{d\Sigma}{d\Omega}$ of the **MNPs** (2h and 5h–milled) measured at $T = 2\text{ K}$ under no external applied field and at the highest field ($\mu_0 H = 3\text{ T}$). Once again, no field dependence is observed, as the nuclear–scattering triggered by the

sample pores may mask the SANS contribution stemming from the MNPs. This prevents the observation of weak features or peaks associated with the nano-size of the samples, which one would expect to observe a hump super-imposed to the asymptotic SANS decay at q values close to the MNP sizes ($q \approx 0.35$ and $\approx 0.48 \text{ nm}^{-1}$ for 2h and 5h-milled, respectively). Nonetheless, it is possible to mention the presence of a flattening of the SANS contribution corresponding to the 5h-milled alloy (see Fig. 5.5b), a fact that reflects that the scattering entities within the 5h-milled alloy are smaller compared to the 2h-milled ones. Additionally, the SANS measured at different temperatures do not display any extra feature for any of the MNPs. As an example, the inset of this Fig. 5.5a displays the SANS measured at several temperatures for the 2h-milled MNPs.

It is clear, from the comparison between the bulk, 2h and 5h-milled MNPs included in Fig. 5.5b, and zoomed for the region around $q \approx 2.93 \text{ nm}^{-1}$ in the bottom inset, that the AF bulk peak is smeared out in the MNPs. The suppression of this peak can be an indication that the **deviations from the pure commensurate order**, which is connected to complex helimagnetic-like behaviour, **are clearly suppressed by the reduction of size and microstrain**. This underlines how subtle is the deviation from the pure commensurate structure, as the AF order within the MNP cores is well-maintained, according to the previous ND.

In which respects to the overall SANS intensity variation in the region close to the $q \approx 2.93 \text{ nm}^{-1}$ peak (bottom inset of Fig. 5.5b), it decreases between bulk and 2h-milled MNPs. This is a sign that the AF commensurate structure gets better defined in the 2h-milled MNPs, which leads to a reduction of the SANS intensity. When the MNP size is further reduced from 2h to 5h-milled MNPs, this SANS intensity recovers a value close to the bulk one. This recovering may be directly associated with the scattering entities, which are smaller, and also to the loss of AF-coupled entities.

In Fig. 5.5c we have represented the SANS cross-section corresponding to the MNP surface. To isolate this contribution from the one corresponding to the whole MNP, the core elastic total SANS cross-section, $\frac{d\Sigma}{d\Omega}_{bulk}$ (assumed to be equal to the bulk one), has been subtracted from the $\frac{d\Sigma}{d\Omega}_{MNP_s}$. Of course, in order to take into account the core size, a weighting factor N has been employed, being this N estimated according to eq. 5.1, in the same way as in [219]:

$$N = \frac{V_{core}}{V_{MNP}} = \left(\frac{r_{core}}{r_{MNP}} \right)^3 \quad (5.1)$$

The resulting $\frac{d\Sigma}{d\Omega_{surface}}$ is then represented in Fig. 5.5c, where, a peak located at $T \sim 4.8$ K appears clear. This peak appears in both 2h and 5h-milled ensembles, and is triggered by the surface Spin Glass-like magnetic moments. The observation of a peak in SANS measurements connected to a SG phase has already been observed in re-entrant Spin Glasses [226, 227]. Additionally to this peak, a second one, located at $T \sim 8$ K, also appears in both ensembles, being broadened for the 5h-milled MNPs. This peak, located at $\sim 2T_f$, may be ascribed to short-range correlations, that may hold up to even a few degrees above T_f . Of course, this evidence should be taken with care, as it is a result of a subtraction, and probably, would merit more work and the use of extra measurements, such as polarised SANS and/or micromagnetic simulations [13].

The study of the microscopic magnetic structure of the NdCu₂ MNPs has revealed the existence of an AF-coupled core plus a SG-like disordered surface. More over, there are clear signs that **the slight deviations from the pure commensurate state found in the bulk alloy at $T = 2$ K are modified by the size reduction and the microstrain**. It is necessary now to complete the magnetic characterisation by measuring macroscopic magnetisation, in order to disclose some details that may escape the resolution of neutron diffraction techniques. To this aim, static $M_{DC}(T, H)$ and dynamic $\chi_{AC}(T, f, t)$ measurements will be presented and discussed in the following.

Beginning with the static magnetisation, Figs. 5.6a and b show the magnetic susceptibility M_{DC}/H vs. temperature T Zero Field Cooling-Field Cooling (ZFC-FC) curves measured at $\mu_0 H = 10$ mT for NdCu₂ 2h and 5h milled MNPs, respectively. The observation of an irreversibility in the low temperature region ($T \lesssim 5.5$ K), as the ZFC-FC branches separate, already points to the existence of a magnetic disordered (Spin Glass-like) state. According to ND, from here, it is safe to conclude that such a state to be promoted by the surface magnetic moments. We cannot miss the existence of an AF-ordered nanoparticle core, which should leave a trace in the form of a cusp in the $M(T)$ signal at $T = T_N$. However, a closer look to both freezing and Néel transition temperature values let us realise how close to each other they are. In this way, $T_f \approx 5$ K, (see χ_{AC} below), while $T_N \approx 6$ K. As a result, both contributions overlap, giving rise to a single broad maximum located at $T \approx 5.5$ K.

Nonetheless, the existence of AF-like interactions is well supported by Curie–Weiss fittings (displayed in the insets of Figs. 5.6a and b), where negative values for the paramagnetic Curie temperature, θ_P , are obtained for both MNP sizes ($\theta_P = -9.2(3)$ K and $\theta_P = -7.8(2)$ K, respectively). It should be noticed the progressive rise of the θ_P value as the MNP size reduces, which highlights the weakening of the AF-like interactions together with the possible emergence of FM-like ones, as is common in RCu₂–MNPs [37, 39, 67]. The reason for these FM-like interactions to occur has already been explained in Chapter 4, in terms of the increasing uncompensated magnetic moments, which have evidenced a tendency to develop weak FM [228, 229]. Curie–Weiss fittings also provide quantitative information on the magnetic effective moment, μ_{eff} , which lies close to $\mu_{eff} \approx 3.80\mu_B$ for both MNP ensembles. This value is slightly higher than the theoretical value, calculated as $|\mu_{eff}| = g_J\mu_B\sqrt{J(J+1)} = 3.62\mu_B$, a very common feature in RCu₂ alloys [67, 186]. According to [188], it is the anisotropic magnetic hyperfine interaction which is at the basis of this effect.

Figs. 5.6c (2h) and d (5h) include the M vs. μ_0H measurements performed up to $\mu_0H = 5$ T at a constant temperature value $T = 2$ K (i.e., below T_f), where three salient features can be underscored. First, it is worth noting how the bulk metamagnetic transitions disappear progressively with the size reduction, in good agreement with the weakening of AF order and the existence of feeble FM. As it can be seen, the metamagnetic transition located at $\mu_0H = 2.75$ T still survives for 2h milled MNPs (marked with a pink arrow in Fig. 5.6c), whilst the one located at $\mu_0H = 0.75$ T [215] is not present at none MNP ensembles.

Second, non-negligible values of the coercive field μ_0H_C and remanent magnetization M_r are found for both MNP ensembles (zoomed in the insets), which clearly brings out the presence of magnetic SG disorder. What is more, the μ_0H_C value becomes greater with the size reduction, from $\mu_0H_C = 4.08(5)$ mT for the 2h-milled to $\mu_0H_C = 5.23(5)$ mT for 5h-milled MNPs. The M_r follows the same path, as it increases from $M_r = 0.062(1)\mu_B/Nd^{3+}$ to $M_r = 0.094(1)\mu_B/Nd^{3+}$. These two facts indicate a rise of the SG-coupled magnetic moments. At this point, we would like to mention that these μ_0H_C and M_r values are notably larger with respect to the ones for SSG GdCu₂ MNPs [37] or SAF TbCu₂ MNPs [39] of similar size, which highlights the greater magnetic anisotropy of Nd³⁺ with respect to Gd³⁺ or Tb³⁺.

Third, as it can be seen, none of the MNP ensembles reaches saturation at $\mu_0H_C = 5$ T, being $M(5\text{ T}) \approx 1.40\mu_B/Nd^{3+}$ in both cases. This value is also far

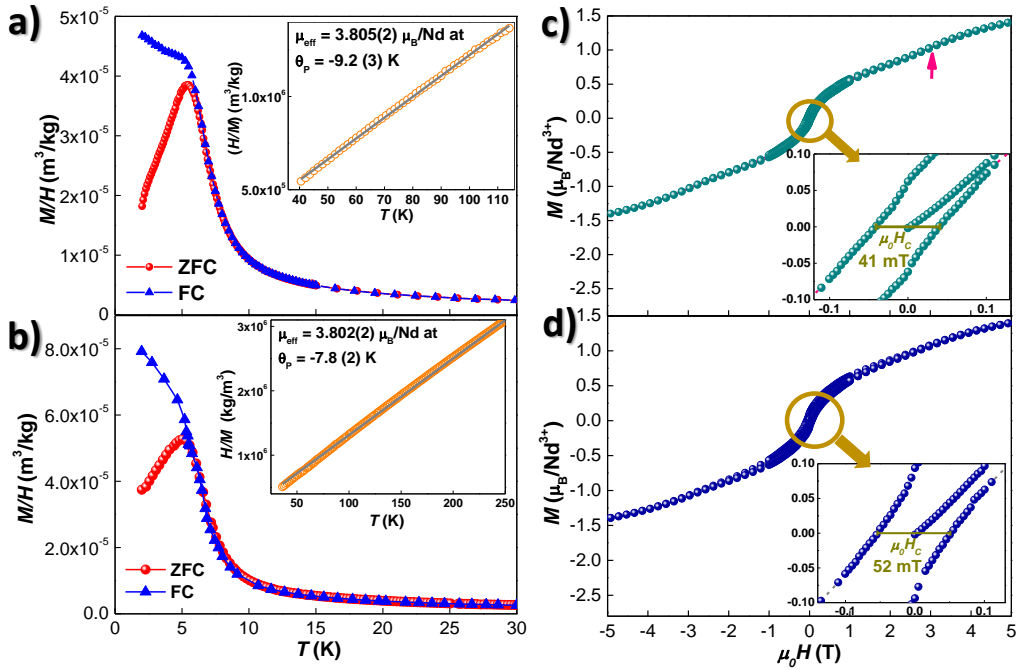


Figure 5.6: **a)** and **b)** show the magnetic susceptibility M_{DC}/H vs. temperature T measurements performed at $\mu_0 H = 10$ mT for 2h and 5h-milled NdCu₂ MNPs, respectively. The red curves illustrate the measurements performed following the Zero-Field Cooling (ZFC) protocol (i.e., cooling under no applied magnetic field), whereas the blue ones have been measured following the Field-Cooling (FC) protocol (i.e., cooling under $\mu_0 H = 10$ mT). Insets show Curie-Weiss fittings of the measurements taken at $\mu_0 H = 0.1$ T, from which values for the magnetic effective moment μ_{eff} and paramagnetic Curie temperature, θ_p , have been extracted. **c)** and **d)** show the $M(\mu_0 H)$ loops measured at $T = 2$ K. According to the emergence of a SG state, both MNP ensembles develop coercivity ($\mu_0 H_C \approx 50$ mT) and remanence ($M_r \approx 0.06\mu_B/\text{Nd}^{3+}$ and $M_r \approx 0.09\mu_B/\text{Nd}^{3+}$, respectively), which are displayed in a closer view in the insets. The pink arrow in **c)** remarks the survival of the bulk metamagnetic transition located at $\mu_0 H = 2.75$ T for 2h-milled NPs.

from the theoretical saturation $\mu_z = g_J \cdot J\mu_B = 3.27 \mu_B$ and below the reported value of $M(25 \text{ T}) = 1.9 \mu_B/\text{Nd}^{3+}$ in [217] for bulk polycrystalline NdCu₂. In addition, the values of $M(5 \text{ T})$ in the MNP state are below that of the $M(5 \text{ T}) \approx 1.45 \mu_B/\text{Nd}^{3+}$ in a polycrystalline bulk alloy. This indicates that the surface contribution to the magnetic anisotropy is larger than the magnetocrystalline one acting together with the AF ordering.

Going now to the dynamic $\chi_{AC}(T, f)$ analyses, Fig. 5.7 includes the in-phase $\chi'(T, f)$ (top panel) and out-of-phase $\chi''(T, f)$ components (bottom), where left-side panels (Figs. 5.7a and b) correspond to NdCu₂ 2h-milled MNPs and the

right-side ones (Figs. 5.7c and d), to 5h-milled ones. A maximum in $\chi'(T, f)$ occurs at around $T \approx 5.6$ K for 2h and $T \approx 5.5$ K for 5h-milled MNPs. This maximum, which evidences dissipation in $\chi''(T, f)$, reduces its value and shifts towards higher temperatures when increasing the frequency, which is a fingerprint of freezing transitions [50, 175]. In addition to this SG-cusp, a maximum in $\chi'(T, f)$ corresponding to the AF Néel transition should be observed at $T = T_N$. Here again, the fact that we only observe one single broad peak in $\chi'(T, f)$ is a consequence of the proximity of both T_N and T_f values.

In order to obtain more information about the freezing dynamics, we have analysed the frequency dependence by determining both δ -shift parameter, according to eq. 2.10³, and the critical slowing down law, following eq. 2.9⁴. First, δ -shift parameter values are 0.0218(7) for 2h and 0.0301(3) for 5h-milled MNPs, respectively, which are larger with respect to the ones reported for canonical Spin Glasses [50], but still below the upper limit of SPM ensembles [60]. Furthermore, the obtained values are smaller than the ones corresponding to SAF TbCu₂ [39] or SAF Tb_{0.5}La_{0.5}Cu₂ MNPs [67], which suggests **a more interacting SG dynamics in NdCu₂ MNPs**.

Second, the T_f -shift along with the f scale up according to the aforementioned dynamical critical slowing down law (see insets in Figs. 5.7a and c). For these scalings, fitting parameters of $T_{f,0} = 5.36(3)$ K, $\tau_0 = 9.88(8) \cdot 10^{-11}$ s and $z\nu = 5.87(3)$ for 2h-milled MNPs and $T_{f,0} = 5.05(1)$ K, $\tau_0 = 1.0(1) \cdot 10^{-10}$ s and $z\nu = 5.05(1)$ for 5h-ones have been obtained. These are close to the values reported for Tb_{0.5}La_{0.5}Cu₂ SAF MNP ensembles [39, 67] and lie within the expected range for SGs [70].

Finally, given the slight increase of δ -shift parameter, τ_0 and $z\nu$, together with the slight decrease of the $T_{f,0}$ as the MNP size decreases, a reduction in the interaction among the magnetic moments with the size reduction can be stated. This finding has already been observed for SAF GdCu₂ MNPs (see Chapter 4), where it has been shown how the disappearance of the AF RKKY interactions harms the interactions among the magnetically disordered moments, resulting in a weakened SG state. Of course, congruent with the ND characterisation, no trace for the bulk reorientation temperature ($T_R \sim 4.5$ K) is found at the nanoparticle state.

$$^3\delta = \ln(T_f)/\log(2\pi f) + k$$

$$^4\left(\frac{T-T_{f,0}}{T_{f,0}}\right)^{-z\nu}$$

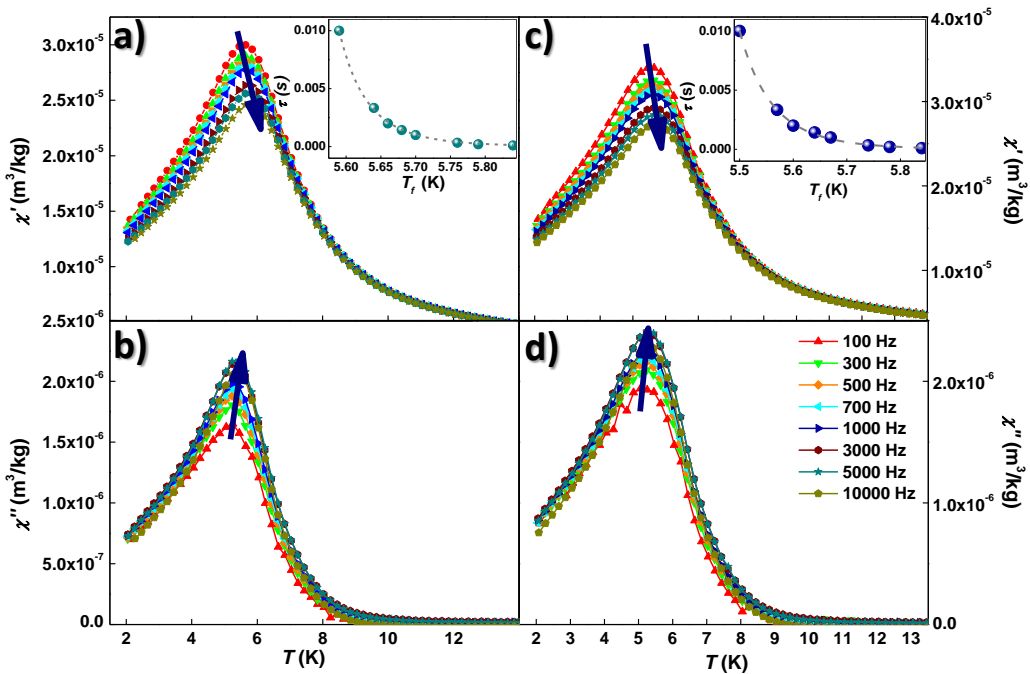


Figure 5.7: In-phase $\chi'(T, f)$ (top panel, **(a)** and **(c)**) and out-of-phase $\chi''(T, f)$ (bottom panel, **(b)** and **(d)**) components of the dynamic susceptibility $\chi_{AC}(T, f)$, measured applying an oscillating field $h = 3.13$ Oe, for $T = 2$ h (left, **(a)** and **(b)**) and $T = 5$ h (right, **(c)** and **(d)**) NdCu₂ MNPs. The shift of the maximum associated with the SG state with the frequency of h is marked with dark blue arrows. Insets exhibit in closer detail the $\tau \equiv 1/(2\pi f)$ vs. T_f dependence, where a scaling to a dynamical critical slowing down behaviour (power law) is recovered, confirming the freezing (SG) nature of this transition. $\chi''(T, f)$ component displays dissipation associated with the SG state.

In order to inspect the robustness of the SG phase we have analysed the time-dependant $\chi_{AC}(t)$ response. Figs. 5.8a and c (left-side) include the memory effect and ageing measured for the 2h and 5h-milled MNPs, respectively. The measurements are focused on the temperature region $T < 10$ K, given that the alloys entered the PM region already at $T = 7$ K. The glass temperature T_g of these MNPs, determined according to the emergence of a peak in the out-of-phase $\chi''(T, f)$ component, was located at $T_g = 3.8(1)$ K in both ensembles. Therefore, the waiting temperature, T_w , was fixed at $T_w = 3.2$ K, which corresponds to $T_w \approx 0.86 T_g$. As it can be observed in Figs. 5.8a and c, **both MNP ensembles evidence memory effects upon warming**, as a drop of the magnetization is recovered in the difference between $\chi''_{aged} - \chi''_{notaged}$ at $T \lesssim T_g$ (see insets). The relaxation of the $\chi''(t)$ (Figs. 5.8b and d) follows the same trend as the one of GdCu₂ MNPs (see chapter 4), which is also congruent with other SGs [68, 77, 203, 205].

With the aim of accessing more information about such robustness, we have performed temperature cycles, following the protocol already described in Chapter 3. Figs. 5.8b and d include these measurements, performed at $T = 3$ K with cycles of $\Delta T \approx 0.84, 0.94, 1.05$ and $1.11T_g$. As it can be seen, the smaller the ΔT , the slower the relaxation, which indicates that larger free-energy barriers are built, meaning that the *domains* of correlated spins are larger [77]. Paying now more attention to the rise in the $\chi''(t)$ at $t > t_{\Delta T}$, the effect of a finite overlap length scale $l_{\Delta T}$ can already be seen at $\Delta T = 0.84T_g$, as the $\chi''(t = t_{\Delta T})$ increases with respect to $\chi''(t \lesssim t_{\Delta T})$. This rise is enhanced as the step ΔT does, until the initial value is met, *ie.*, $\chi''(t = t_{\Delta T}) = \chi''(t = 0)$. The situation reads equally as the one already explained for the case of GdCu₂ MNPs. Just as a reminder, we will briefly mention that, at $t = 0$, the magnetic moments freeze in some particular disordered configuration, imposed by the frustration of the RKKY interactions. This leads to a particular *meta-stable* spin configuration, L_1 .

The rise of the temperature ΔT would then lead to a situation very alike to the one of GdCu₂ already explained in the previous Chapter 4. Accordingly, the larger clusters start to break down while a new domain configuration (L_2) appears. This way, **two SG domain configuration coexist**; which implies the existence of different length scales (time scales), in the same way as reported in previous works [76, 77]. This 2D domain-wall landscape is sketched in the inset, for distances below 1 nm. The coexistence of both domains is maintained even for $\Delta T = 1.05T_g$, *ie.*, above the T_g , indicating the stiffening of this SG phase. Then, when $\Delta T = 1.11T_g$, the energy barriers of the larger clusters arranged in

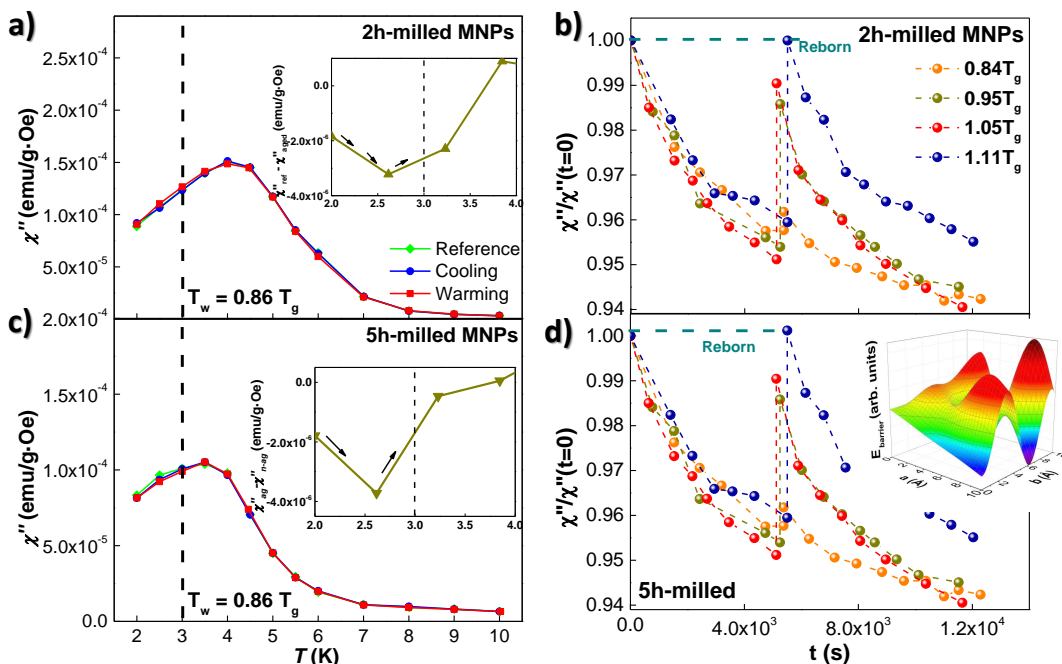


Figure 5.8: Out-of-phase χ'' component of NdCu₂ measured at $f = 0.2$ Hz as a function of the temperature (left-side) and time (right-side) for 2h (a) and b)) and 5h-milled (c) and d)) MNPs. In a) and c), memory effects are evidenced when measuring upon warming after having wait for $t \sim 4 \cdot 10^3$ s at $T = 3$ K = $0.86 T_g$ (see insets). b) and d) display the $\chi''(t)$ recorded at $T = 3$ K before and after applying 4 ΔT (cycles) to verify the strength of the SG phase. It can be seen that the SG state is completely reborn when the rise is of $\Delta T = 1.11 T_g$. The inset of d) shows a sketch of the energy-barrier landscape, where two different energy barriers, corresponding to distinct domain configurations, are depicted.

L_1 become smaller compared to the energy driven by the temperature. Thus, this former domain is completely destroyed, and the SG state **is completely reborn**.

Finally, it is worth mentioning that both memory and temperature cycling measurements have been performed for the bulk alloy as well, in order to see whether the incommensurate–commensurate transition of the magnetic structure could carry frustration that might give rise to a SG state. Nevertheless, no trace for memory effects nor relaxation are evidenced in the bulk alloy at any temperature surrounding the $T_R \approx 4.5$ K. This ensures that the transition from the commensurate phase to the incommensurate one is accomplished without the weakening of any magnetic AF order, as the magnetic moments keep well–aligned in the square–up structure.

5.2 CEF and magnon propagation: An insight into the quantum soul of NdCu₂ MNPs

Once the magnetic structure has been characterized, from both microscopic and macroscopic viewpoints, an insight into the quantum nature of the NdCu₂ MNPs has been undergone. More precisely, this will focus on the single–ion crystalline electric field (CEF) and the collective magnon excitations. At this point, it is worth mentioning that the works devoted to these excitations on MNP ensembles are very scarce. In this way, only a few studies have showed direct evidence of the presence of spin waves in hematite and maghemite MNPs [148, 230, 231]. This constitutes a room to be filled, since the propagation of spin waves is attracting a lot of attention nowadays [232, 233]. Besides, the knowledge about the CEF effects in 4*f*–MNPs is extremely scarce, if not absent, which is actually surprising, given that R alloys constitute a fair playground to probe them.

Apart from the basic interest inherent to the determination and understanding on how the bulk collective excitations develop at the nanoscale, a precise determination on the role that the core and the surface/interface of the MNPs play on this process is a must for disclosing the MNP dynamics, which is at the basis of several problems concerning quantum magnetism (*e.g.*, [234, 235, 236]). Finally, a good understanding on the CEF in R–alloys is also crucial, as long as it affects remarkable technological properties related to their use as permanent magnets [237] or, more recently, to their energy–saving magnetocaloric behavior [238]. Given the efforts that are devoted nowadays to replace bulk materials by MNPs at the afore–

mentioned applications, the influence that particle size, microstrain, and surface effects have on the CEF and the magnetic excitations should be disclosed *urgently*.

The very first step to disclose these **CEF and magnon collective excitations** is to analyse the **specific heat** response. These measurements can be used as an initial guide to unveil CEF and magnon excitations. Later on, thanks to the **Inelastic Neutron Scattering** analyses, we will confirm these preliminary insights, and also, complete the information on CEF and collective excitations.

5.2.a Initial guide: Specific heat

As it has been shown in the previous Chapter 4, specific heat analyses bring information on the magnetic transitions undergone by the sample. Nevertheless, the main aim, in the case of NdCu₂, is to use these measurements to unveil information on the splitting driven by the CEF. The way we have analysed the c_P follows the explanations already given in Chapters 3 and 4, where the core and surface environments are taken into account, and thus, we will avoid unnecessary repetitions.

Therefore, the green line in Figs. 5.9a and d represent the obtained $c_{lattice}$, from which $\gamma^s = 22.82(2) \text{ mJ}(\text{molK}^2)^{-1}$ and $\theta_D^s = 281(4) \text{ K}$ for 2h, whereas $\gamma^s = 21.5(5) \text{ mJ}(\text{molK}^2)^{-1}$ and $\theta_D^s = 240(6) \text{ K}$ for 5h-milled MNPs. These values are, as expected, greater than the bulk ones, which have been obtained from the analyses of the measurements as $\gamma^{bulk} = 12.14(13) \text{ mJ}(\text{molK}^2)^{-1}$ and $\theta_D^{bulk} = 224.7(6) \text{ K}$, which are in good agreement with the ones reported in [99]. Therefore, the $c_{mag+CEF}$ (blue dots) can be safely obtained by just subtracting the $c_{lattice}$ from the measured c_P . This $c_{mag+CEF}$ contribution is represented in closer detail in Figs 5.9b and e.

Insets in Figs. 5.9a and b depict the magnetic entropy S_{mag} against the temperature, obtained, as for the case of GdCu₂ (see Chapter 4), according to:

$$S_{mag}^{exp} = \int_0^{300} \frac{c_{mag+CEF}}{T} dT \quad (5.2)$$

None of the MNP ensembles reach the theoretical value $S_{mag}^{theo}(300\text{K}) = R[\ln(2J+1)] = 19.14 \text{ J/mol}\cdot\text{K}^2$, as $S_{mag}^{exp} = 17.4(1)$ and $16.8(1) \text{ J/mol}\cdot\text{K}^2$ (2h and 5h, respectively). This fact is expected, as there are around 20% (40 % for 5h) of surface moments distorting the bulk AF state and CEF splitting, which results on a poorer definition of the single and collective excitations. Ergo, the contribution to the

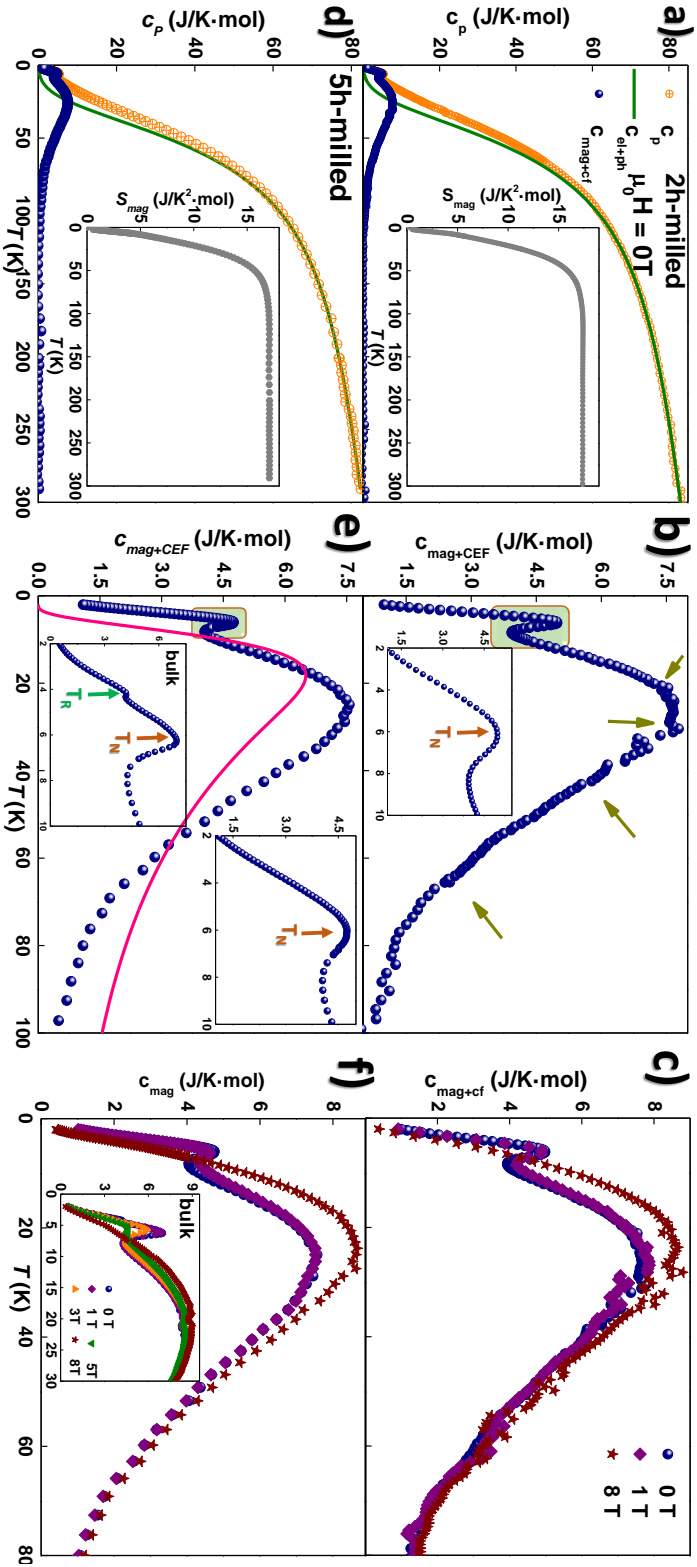


Figure 5.9: a) (2h) and d) (5h) display the measured specific heat (orange) together with the c_{Griffice} (green) and the $c_{\text{mag+CEF}}$ contributions. Insets include the magnetic entropy, where it can be seen that almost 90% of the total value is reached at 70 K. b) and e) depict in greater detail the $c_{\text{mag+CEF}}$ contribution, where the inset zooms the region surrounding the AF Néel transition. There, no trace for the reorientation at T_R is recovered, as it is the case of the bulk (bottom inset in e)). The pink line corresponds to the calculated contribution arising from the CEF, c_{CEF} , obtained according to eq. 3.37. c) and f) show the $c_{\text{mag+CEF}}$ contribution measured under $\mu_0 H = 0, 1$ and 8 T. The inset in f) shows the $c_{\text{mag+CEF}}$ for the bulk alloy measured at several fields between 0 and 8 T.

entropy (CEF and magnetic) is reduced. Besides, the value of S_{mag}^{exp} around T_N is ≈ 3.56 J/mol·K², which is also below the expected value $S_{mag}^{theo}(T_N) = R[\ln(2)] = 5.76$ J/mol·K² for a completely removal of the two-fold spin degeneracy of the crystal field ground state doublet. These facts (reduced S_{mag} at both 300 K and T_N) also occurred in polycrystalline bulk NdCu₂ in [99] or CeCu₂ [239], where they were argued in terms of short-range correlations effects.

Moving on now to Figs. 5.9b and e, the emergence of a hump above $T_N \approx 6$ K can be clearly observed. This broad peak, which is located between $10 \text{ K} \lesssim T \lesssim 80 \text{ K}$, corresponds to the **Schottky anomaly**, characteristic of systems where there is a discrete number of energy levels that are thermally accessible. In this line, when an appreciable amount of electrons gain enough energy to undergo a transition from a lower level to a higher energy-one, the internal energy of the system changes. This sudden change is reflected in the c_p in the form of a broad peak that usually exceeds the $c_{lattice}$ contribution. When the highest level is fully populated, the situation goes back to the starting one, where it was the lowest energy level the one fully occupied, and no contribution to the c_p is detected [210]. This finding is of fundamental interest, as it is indicating that the **CEF level schemes remain almost unaltered in spite of the size reduction and the microstrain of the MNPs**. Of course, INS should confirm this preliminary assumption, but it is a promising result to tempt to go beyond and trying to observe this effect by using the aforementioned technique.

A closer look to Fig. 5.9b allows us to see the occurrence of four humps, marked with dark yellow arrows, located at $T \approx 18, 32, 45$ and 80 K, which correspond to $E \approx 3.1, 5.5, 7.8$ and 13.8 meV respectively. These energy values are very close to the ones corresponding to the CEF splitting reported in [99] and to the ones that are going to be obtained from the INS measurements, and is congruent with the assumed CEF origin for the splitting. The inset zooms-in the low-temperature region, where no trace for the reorientation is recovered, in good agreement with the neutron diffraction results. The intensity of the AF peak is greater than the one corresponding to 5h-milled MNPs, but lower than the bulk-one (Fig. 5.9e), in good agreement with the progressive loss of AF order as the MNP size reduces.

Fig. 5.9e also includes the calculated c_{CEF} (according to eq. 3.37). There, it can be seen that the temperature value at which the maximum Schottky contribution is found, $T^{Schmax} \sim 80$ K, shifts up to higher temperatures for the experimental data, as $T_{exp}^{Schmax} - T_{calc}^{Schmax} \approx 8$ K. This mismatch between the experimental and the calculated contributions to the specific heat was also detected for the bulk

parent alloy, being indicative of the existence of temperature–dependent interactions, such as magnetoelastic effect and/or short–range correlations among Nd³⁺, also reported in [99]. In order to access more information, we have removed these temperature–dependent interactions by normalising both experimental and calculated contributions to their respective temperature value for which the Schottky anomaly is maximum (T/T_{max}^{Schmax}). We prefer to lead the reader to the observation of Fig. 3 in [219] in order not to complicate excessively the observation of Fig. 5.9e. In that figure of [219], it can be seen that the experimental c_{mag} falls to zero above the Schottky anomaly faster than expected according to the calculated c_{CEF} . This indicates that **the CEF $|9/2\rangle$ multiplet is poorly defined**, as its contribution to the specific heat is smooth. Later on, the INS results will confirm this macroscopic–insight to the CEF schemes statements. The bottom inset of this Fig. 5.9e includes the low–temperature bulk $c_{mag+CEF}$, where, by contrast to what happens for the MNP ensembles, a peak at $T = T_R$ is obtained, reflecting the commensurate–incommensurate first–order transition.

The field dependence of the $c_{mag+CEF}$ contribution is displayed in Figs. 5.9c (2h) and f (5h). There, we have employed $\mu_0 H = 0, 1$ and 8 T. The Néel transition is barely affected at 1T, whereas it is wiped out at 8 T. This is congruent with the $M(\mu_0 H)$ characterisation shown before, as the AF state is completely destroyed when the applied field is greater than 2.7 T. Inset in Fig. 5.9f includes the $c_{mag+CEF}$ contribution corresponding to the bulk alloy, where a clear drop in the intensity associated with the AF transition is observed at $\mu_0 H = 3$ T. By further increasing the field, it can be seen how the AF interactions still survive at $\mu_0 H = 5$ T. Given that both the modelisations and the experimental ($M\mu_0 H$) study presented in [213] stated a completely removal of the AF arrangement at such a magnetic field, our results are indicating the existence of AF interactions, but not enough to rise a collective AF state. According to the phase diagram presented in [213], included in Fig. 5.4a, the magnetic moments are FM–oriented (F1). A further increase of the field to 8 T completely destroys the AF interactions, as no trace for the Néel transition is noticed.

To sum up, the macroscopic insight to the CEF levels sets a sparkling scenario of the MNPs. **A maintenance of the CEF levels in the nanoparticles shall be anticipated** according to the c_p results. Also, the splitting of the energy levels lies on values that are experimentally accessible by means of INS as well.

5.2.b The acid test: Inelastic Neutron Scattering

Inelastic Neutron Scattering has been employed to further investigate the behaviour of the single and collective excitations. Even if there are some solid arguments in favour of these excitations to take place in the MNPs, the literature concerning INS in NdCu₂ only include a study of the magnetic excitations in the field-induced ferromagnetic phase (F3) in a single-crystal sample [240], and the one carried out by E. Gratz *et al.* on a bulk polycrystalline alloy [99]. No reported works on NdCu₂ (or, even, 4*f*-compounds) MNPs have been reported so far. Therefore, we are presenting here the first contribution⁵ on INS in 4*f* ensemble of MNPs. Given the limited access to beam time, only the 5h-milled MNP ensembles could be measured. We have used, therefore, the INS data published by [99] for the bulk is an excellent reference-point in order to establish a deep comparison with our MNPs. Indeed, it holds true that the aforementioned research was carried out 3 decades ago. However, we both employed the IN4 instruments at the ILL, for which the reliability and resolution of the detectors have not been pretty much changed for the last 30 years. Therefore, from our point of view, the comparison with the bulk reported data of [99] is sensible, being the conclusions and statements shown hereunder safe.

Given the extension of the results, this section will develop as follows: First, the main features regarding the bulk alloy will be introduced and analysed, in order to set the basic concepts of this reference. Then, a detailed description on the 5h-milled MNP INS contribution will be given, including a comparison with the bulk. Finally, the surface contribution to the INS will be disclosed.

Bulk NdCu₂

As it has already been mentioned, data for **NdCu₂ bulk** were taken from [99]. Their NdCu₂ sample consisted on a polycrystalline alloy obtained by induction melting and annealed for 1 week. E. Gratz *et al.* focused on three temperature values, $T = 10, 4.5$ and 3 K using incident neutron energies, E_0 , between 12 and 50 meV. Apart from IN4, they also employed the IN6 instrument to gain access to the subtle details surrounding the splitting of the lowest doublets (energy transfer window between -0.5 – 2 meV) that took place at the magnetic state ($T = 1.5$ K), using incident neutron energy of $E_0 = 3.17$ meV.

⁵published in [219].

Starting at the PM region ($T = 10$ K), Fig. 5.10a shows the $S(Q, \hbar\omega)$ vs. the energy transfer for their experimental data and our fittings. Data were collected at $E_0 = 12, 17, 50$ meV, and have been added together, taking into account their own backgrounds and energy transfer windows, given that each E_0 focuses the counting on different energy values. The outburst of 4 peaks can be clearly observed, being their corresponding fitting parameters inserted in Table 5.1. First of all, the energy transfer position of each peak, E_i obtained from our fittings is in good agreement with the reported ones by E. Gratz *et al.* [99]. Additionally to these 4 peaks, it is very worth mentioning the emergence of a peak, at $E_0 = 10.5(4)$ meV, that does not correspond to the splitting driven by the CEF. This peak, that was not mentioned in [99], is also retrieved at the MNP measurements (see Fig. 5.11). Thanks to the contourplots of the MNPs (see, for example, Figs. 5.12c or i), where a tiny contribution at around 10 meV that can be inspected, the phonon–origin of this peak will be discussed later on, since there is an increase of the signal with q .

Table 5.1: Coefficients of the fitting of the NdCu₂ bulk data collected by E. Gratz *et al.* [99] at $T = 10$ K at the IN4 instrument. Background corrections (modelled as a straight line) have been performed. All the parameters have been obtained following eq. 3.33.

	$ 0\rangle$	$ 1\rangle$	$ 2\rangle$	$ 3\rangle$	$ 4\rangle$
Amplitude	222(14)	60(3)	64(3)	72(3)	21(2)
FWHM	1.59(6)	1.70(12)	1.35(9)	1.32(7)	2.4(4)
E_i	0.11(1)	2.91(4)	5.14(4)	7.32(3)	14.5(1)

Going now to the data analysis concerning the magnetic region ($T < T_N$), we will first focus on the data collected at IN4 instrument ($T = 4.5$ and 3 K). Fig. 5.10b shows the experimental data (E. Gratz *et al.*, [99]) together with our performed fittings. It is worth noting the emergence of a peak, already at $T = 4.5$ K, at energy transfer value of $E = 1.47(2)$ meV. This peak was argued in [99] to appear as a consequence solely of the Zeeman splitting of the CEF doublets. Nevertheless, the aforementioned study also left the possibility of spin waves to also trigger this peak. Taking into account the intensity of this peak, together with the data measured at $T = 1.5$ K and for the MNPs (see below), the key role of magnons at this peak appears clear, rather than being a simply splitting of the ground state CEF multiplet. As the temperature is decreased to $T = 3$ K, the peak gets more intense, as expected for these kind of collective excitations, that

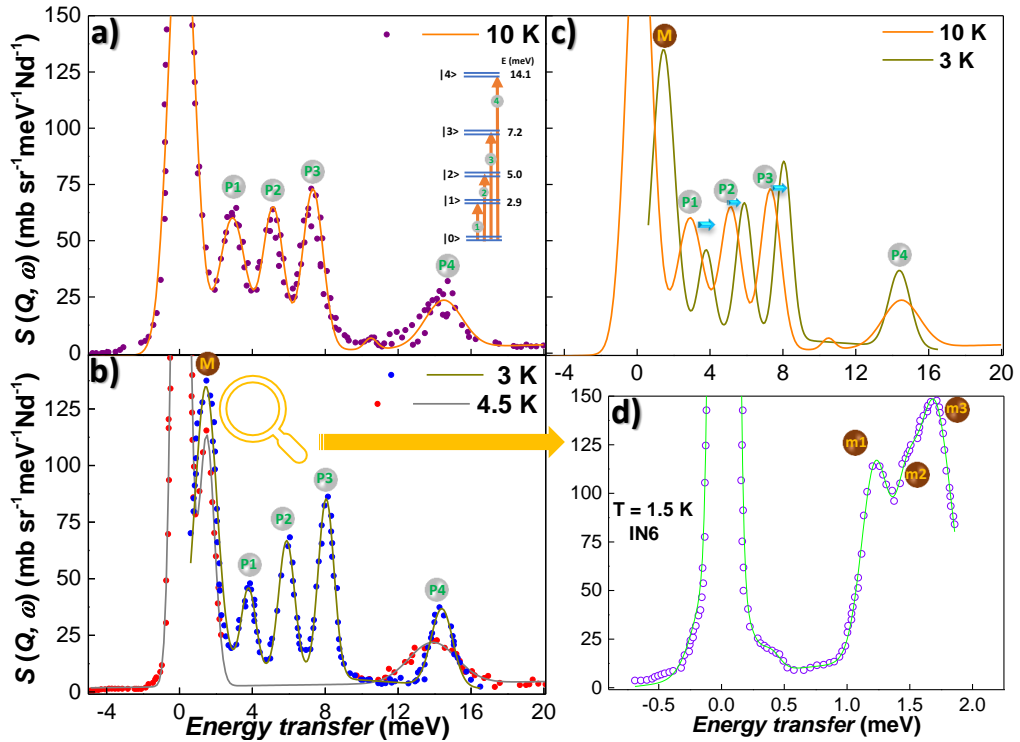


Figure 5.10: Scattering function $S(Q, \omega)$ as a function of the energy transfer at **a)** $T = 10$, **b)** 4.5 and 3 and **d)** 1.5 K. The inset in **a)** includes the CEF splitting level schemes. The experimental data were collected by E. Gratz *et al.* [99] using IN4 instrument (**d)** with IN6), whereas the lines give account for the fitting performed following eq. 3.33. In **c)**, a comparison between the fittings for 10 and 3 K is provided, where it can be seen the outburst of a magnon peak at $T = 3$ K and the temperature–peak shift driven by magnetoelastic effects.

get better defined as the temperature entropy is removed.

Comparing now the magnetic and PM spectra (Fig. 5.10c), two features can be detected: First, there is an energy shift towards higher energy transfer values as the temperature is decreased, which reveals the existence of **magnetoelastic effects**, a fact that is not surprising in R-based systems [110]. Second, **a slight reduction of the peak area ($height \times FWHM$) corresponding to the first excited level is obtained**, compared to the situation at $T = 10$ K. This slight modification, which implies a **reduction in the probability of transition**, can be understood owing to both the **Zeeman splitting and the magnon spectra**. The former Zeeman splits the multiplets, as it has already been explained in Chapter 2, while the later magnon excitations give rise to different magnon modes. Thereby, there appear new accessible levels below $|1\rangle$, which implies a reduction of the probability transitions to this $|1\rangle$. Additionally, the Zeeman splitting of the multiplets located at greater energy transfer values actually happens, yet it is too subtle compared to the experimental sensitivity to be detected.

Finally, Fig. 5.10d includes the data collected using IN6 at $T = 1.5$ K and $E_0 = 3.17$ meV. The better resolution can be seen at first glance, as the energy windows is now between -0.5 and 2 meV, essential to disclose the details concerning the spin wave propagation. Table 5.2 includes the parameters for the fittings. There, it can be seen that the magnetic peak, labelled as **M**, actually consists of the convolution among three peaks, **m1**, **m2** and **m3**. According to [99], these correspond to the **magnon density-of-states** of NdCu₂, which displays a gap below 1 meV, as nor peak nor hump takes place at this energy range. Indeed, it would have been of primer interest to also measure the bulk alloy using this IN6 instrument at T values closer to the T_R . This would have brought more light into how the magnon density-of-states gets affected by the reorientation of the magnetic moments. Nevertheless, this is not a possible follow-up work line, as IN6 instrument is dismantled.

To sum up, the bulk INS spectra have provided a good overview on the CEF splitting concerning NdCu₂, where the **ground state + 4 excited levels** are clearly seen. Once the magnetic state is established, the CEF multiplets split, as a consequence of the Zeeman term to the Hamiltonian, and the **onset of magnon excitations**, with a certain density-of-states is visible. The question is now *whether it is possible to observe these features in an ensemble of MNPs*, or the microstrain and surface symmetry-breaking affect the CEF splitting so dra-

Table 5.2: Coefficients of the fitting of the NdCu₂ bulk data collected by E. Gratz *et al.* [99] at $T = 1.5$ K at IN6 instrument. Background corrections (modelled as a straight line) have been performed. All the parameters have been obtained following eq. 3.33.

	$ 0\rangle$	m1	m2	m3
Amplitude	$2.8(1.5)\times 10^3$	101 (8)	59 (7)	129 (6)
FWHM	0.126 (9)	0.26 (2)	0.20 (3)	0.32 (2)
E_i	0.0213 (10)	1.228 (9)	1.466 (13)	1.692 (7)

matically that no well-defined energy level can be retrieved.

Nanoparticle state

Once the CEF and magnon schemes for bulk NdCu₂ have been provided, we will now **move into the MNP regime**. One may reckon at this point that the bulk schemes remain almost unaltered within the MNP core, as the precedent characterisation has claimed this inner moments to be almost equal to the bulk arrangement. On the contrary, little is known concerning what would happen to the outer magnetic moments, but it can be conjectured to consider the NP surface as an interface. In [241], L. T. Baczewski *et al.* studied the influence of interface effects on a Rare-Earth CEF in Fe–Tm and Fe–Nd multilayers. According to their work, a modification of the CEF Hamiltonian, in the form of a second-order term, is observed. This came in a consequence of the change of the symmetry surrounding the Nd³⁺ ions, altered by the presence of interfaces. Thereby, it would not be unreasonable to expect a modification of the CEF schemes at the MNP surface, where the bulk symmetry is broken. Even if the distortion can be minor, the highly dependence of the CEF on the electrostatic potential created by the charges in the vicinity of the 4*f* electrons of each R ion [93, 94] results in a modification of the CEF schemes.

Additionally to the inherent complexity of the INS technique, one extra hindrance related to the NdCu₂ crystalline structure arises. In this way, whereas CEF levels are easily evaluated in high symmetry cubic R–intermetallics [242, 243], alloys displaying tetragonal or orthorhombic crystalline structures add complexity to the calculations [242, 243]. There have been recent attempts to broaden the knowledge on CEF dealing with very complex structures, as in non-periodic TbCd₆

quasicrystals [244] or nanocrystalline pure Tb [245]. Nevertheless, the works are, still, very scarce, being the majority of the efforts devoted to, as we have already said, Fe–oxide MNPs [190, 230, 246]. Even at these, only a few studies have shown directly the presence of spin waves in ensembles of MNPs of hematite and maghemite by INS [148, 230, 231], which reinforces the challenge we are aiming to tackle.

Far from discouraging us, this absence in the literature pushed us forward to reveal the CEF schemes. As it has already been said, we gained measuring time at IN4 instrument (ILL) to perform INS on NdCu₂ 5h–milled MNPs. These measurements were taken by PhD. María de la Fuente, who also did the data curation (background, absorption, self–shielding and normalization to vanadium). Patterns were measured at three incident neutron energies, $E_0 = 8.77, 16.67$ and 66.68 meV, at three temperature values, $T = 10, 5.25$ and 1.5 K. The results are going to be presented as follows: First, the experimental data, together with the fittings, are going to be shown and discussed for the three measured temperatures. Then, we will focus only on the data sets acquired at $T = 10$ K (PM) and 1.5 K (AF). Since these particular temperature values match the ones measured in the bulk alloy by E. Gratz *et al.*, it will be then possible to isolate the INS surface contribution from the response coming from the whole MNP.

Fig. 5.11a displays the three data sets plus the performed fittings. The Y–axis scale is arbitrary, as we wanted to clearly compare, in one single picture, the three temperature sets, which correspond to the SAF state, the vicinity of the freezing transition and the paramagnetic state, according $\chi_{AC}(T, f)$ results. Non–surprisingly, the INS spectra display 4 humps at energy transfer values that are compatible with the bulk ones. An additional peak, located at $E \sim 10.5$ meV (marked with a blue arrow), is also retrieved at the MNPs, yet the experimental resolution hampers its observation when the magnetic phase ($T < 6.2$ K) is established. Notwithstanding, the contour plots (see below Fig. 5.12) will allow us to pinpoint the phonon origin beneath this peak. The CEF levels schemes are sketched in the right–side of this Fig. 5.11a, where the shadows around each multiplet represent the existence of a distribution of energies around each level, due to the microstrain. Still on this Fig. 5.11a, the emergence of a magnon–peak can be seen at $T = 5.25$ and 1.5 K, *ie.*, the magnetic state. This peak gets more intense as the temperature is lowered, as expected owing to the better establishment of the AF state. Accordingly, we can state the **CEF splitting and magnon collective excitations to be taking place at the NdCu₂ MNPs**. Finally, magnetoelastic effects are observed with temperature, as it was the case of the bulk alloy. The

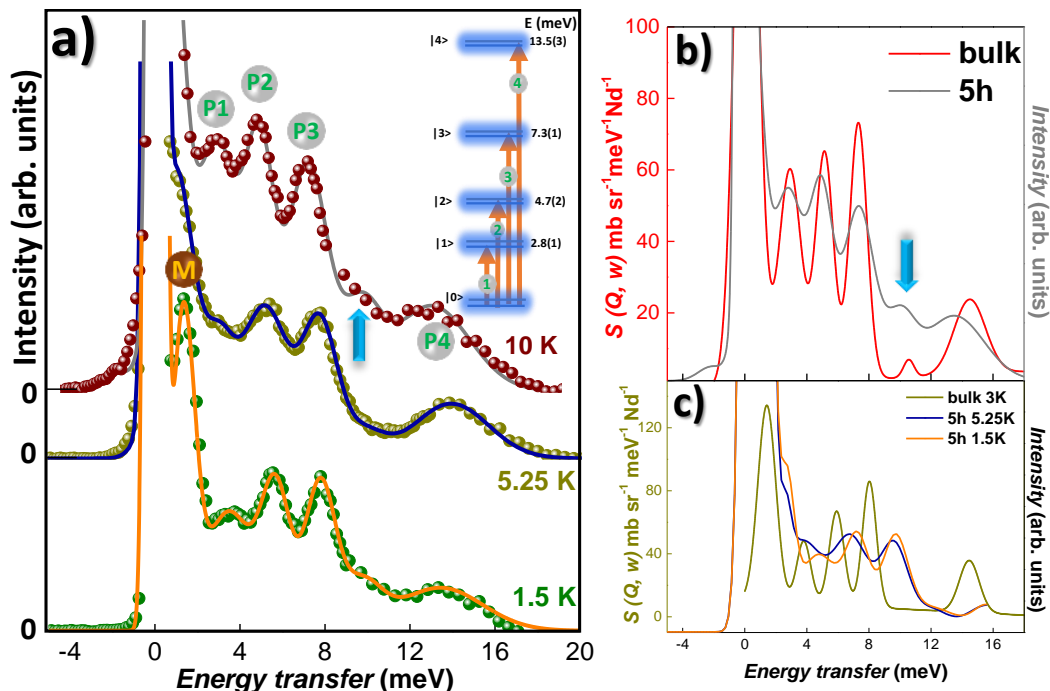


Figure 5.11: a) Inelastic neutron scattering intensity integrated over the q range from 1.11 to 3.06 \AA^{-1} as a function of the neutron energy transfer E , at temperatures $T = 10 \text{ K}$ (top), 5.25 K (middle) and $T = 1.5 \text{ K}$ (bottom) for NdCu₂ MNPs measured at IN4 instrument. The fittings to the data have been made assuming a Gaussian peak shape. The position of the phonon-like peak at $\sim 10.5 \text{ meV}$ has been marked with a blue arrow. On the right-hand side, the CEF levels corresponding to the PM region, together with the measured energy values of P1–P4 have been included. The (blue) shaded is a sketch of the distribution of energies cause the transition decoherence. In **b)** and **c)**, a comparison between the bulk and the MNPs is provided for both PM (**b)**) and magnetic state (**c)**), for which only the $E_0 = 17$ (bulk) and 16.7 meV (MNPs) data have been included, as bulk data were limited at this E_0 . It is striking to observe that the energy transfer values at which the bulk CEF peaks emerge remain almost unaltered at the MNPs, whereas the relative intensities are clearly affected by the size reduction.

explanation for this magnetoelasticity has already been discussed for the bulk alloy and in the ND results.

At this point, the scenario is connected to a situation that is unprecedented, in the sense that there are no reported works showing the CEF and magnon collective excitations at an ensemble of $4f$ MNPs. However, there is no new physics running at this point, in the sense that all the aforementioned statements could have been guessed provided that the MNP core behaved like the bulk NdCu₂. Nevertheless, **there is one finding that is worth mentioning at this stage**. If we compare the relative peak intensities of the bulk and MNPs (see Figs. 5.11b and c), it can be seen that **the almost-constant relative peak intensities of the bulk alloy are not kept for the MNPs**. Also in Fig. 5.11c, **a shift of the magnon peak is unveiled**. Thanks to the more subtle analyses presented in Fig. 5.13, more light will be brought into what is actually happening. Hence, at this step, we will just bring this finding close to our attention, keeping *the hype*.

Information on the energy dispersion relation can be gained from the 2D E vs. q representations. In this sense, Fig. 5.12 depicts the obtained INS spectra as *contour plots*, where the scattering intensities are plotted as a function of the neutron energy transfer and the wave vector transfer (dispersion curves). Within the PM region, all the excitations corresponding to energy transfer from the ground state to the four excited levels can be distinctly seen (see Figs. 5.12g–i). The data collected at the higher incident energy $E_0 = 66.7$ meV (Figs. 5.12c, f and i) show that the total splitting ~ 13.5 meV is lower than that of bulk NdCu₂, ~ 14.1 meV, at all the measured temperatures. Spectra collected at lower incident energies of 8.8 and 16.7 meV show the different dispersion-less excitations from the ground state to the first three excited CEF levels (~ 2.8 , ~ 5.0 , and ~ 7.3 meV). These levels are the same as in bulk NdCu₂ within experimental precision [99]. In the magnetic state, at $T = 1.5$ K (Fig. 5.12a–c) and $T = 5.25$ K (Fig. 5.12d–5.12f), the CEF excitations at low energies (< 3 meV) are strongly modified by the magnetic ordering and the exchange interactions, leading to a dispersive propagating transverse magnetic excitation [99, 100, 102, 240], which is seen as a substantially broadened peak due to the powder averaging in our nanocrystalline sample. Also, they are better defined at $T = 1.5$ K than at $T = 5.25$ K, which is expected. The CEF levels that lie at 4.7 and 7.3 meV in the paramagnetic phase move up in energy to 5.7 and 7.8 meV, respectively, while higher lying levels are essentially unaffected by the magnetic order.

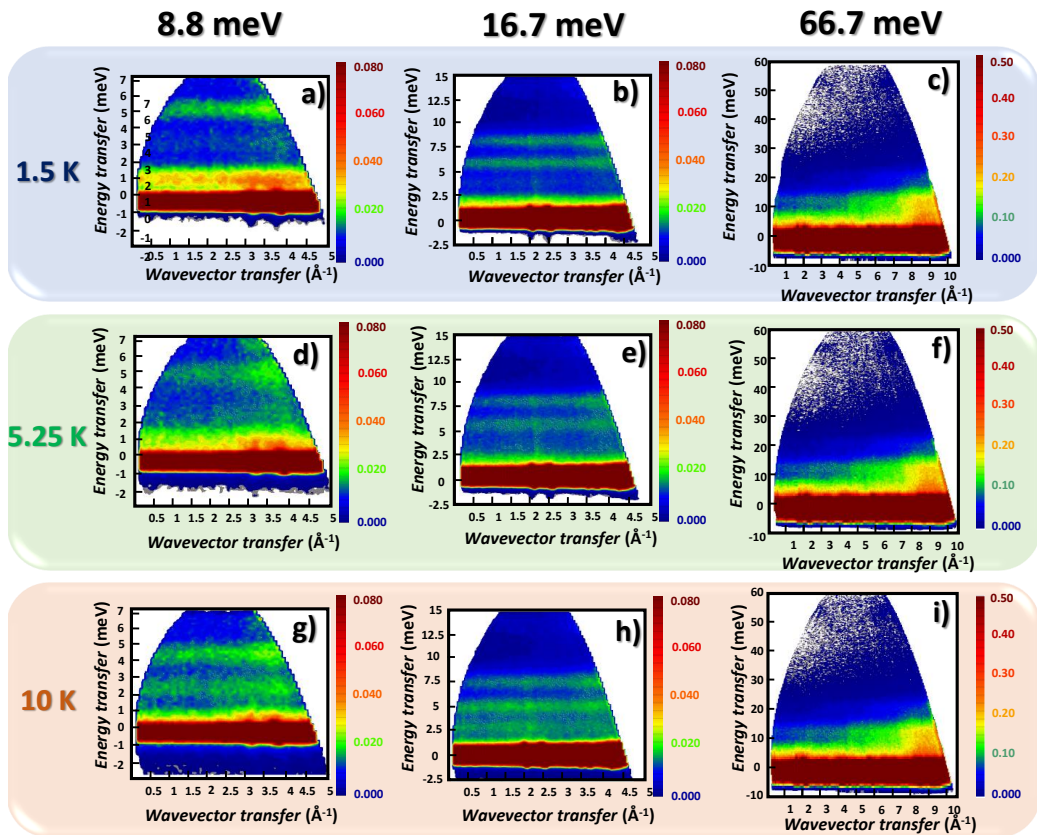


Figure 5.12: Contour plots of the scattering function $S(Q, \hbar\omega)$ as a function of wave vector and energy of 5h-milled NdCu₂ nanoparticles measured at $T = 1.5$ K (top), $T = 5.25$ K (middle) and at $T = 10$ K (bottom), for incoming neutron energies of $E_0 = 8.8, 16.7,$ and 66.7 meV (left to right).

Nanoparticle surface

So far, the situation does not seem to be very tricky. The only sticking point was related to the experiment itself, but the data look relatively *user friendly* at first glance. Nevertheless, Fig. 5.11 left one important piece that didn't fit into the puzzle, in the form of a **slight modification on the relative peak intensities**. Our hunch was that we were observing the surface effect, but no safe conclusions could be directly extracted from the experimental INS data themselves. As the MNP signal includes both core and surface contributions, we could not disclose the origin of this effect, even if the most reasonable scenario points to surface influence. Here again, the lack of reported studies that could be used as a guide for interpretation is hindering the progress. Nevertheless, it is here that the originality of our approach emerges. All the precedent characterisation (ND, SANS, c_P , M_{DC} , χ_{AC}) has backed the bulk-like behaviour for the core magnetic moments. Therefore, it should not be considered a drawback or misstatement the idea that the INS contribution would behave equally. If we could, then, **subtract the core contribution to the total MNP INS, the remaining signal will account for the surface**. To do so, we have used the data collected by E. Gratz *et al.* for bulk NdCu₂ to subtract them from the total INS MNP signal. Therefore, the surface contribution to the INS is obtained simply by:

$$S_{\text{surface}}(q, \hbar\omega) = S(q, \hbar\omega) - 0.3 S_{\text{core}}(q, \hbar\omega), \quad (5.3)$$

Figs. 5.13a and b show the resulting $S_{\text{surface}}(q, \hbar\omega)$ intensity (*Intensity*, in arbitrary units) at $T = 10$ K, PM state and $T = 1.5$ K, SAF state, respectively, as a function of energy transfer for a wave vector of $q = 1.75 \pm 0.5 \text{ \AA}^{-1}$, obtained by combining data sets taken at different incoming energies. It is here that **the most striking result comes, as both CEF (P1–P4) and collective magnetic excitations can be clearly observed**. This is pretty stunning, as it is indicating that **the bulk CEF energy level schemes and magnon excitations are well preserved even at the surface of the MNPs**. At this point, we would like to mention that we are aware of the uncertainty linked to the estimation of the N factor as 0.3. Therefore, in order to verify the maintenance of the CEF and the magnon peaks in the $S_{\text{surface}}(q, \hbar\omega)$, we have tried several values for the ratio $N = N_{\text{core}}/N_{\text{MNP}}$, being N_{core} and N_{MNP} the number of magnetic moments located within the core and at the whole MNP, respectively. Indeed, the greater the N , the smaller the proportion of the magnetic moments located at the MNP surface gets. We refer the reader to the figure included in Appendix C, where the resulting $S_{\text{surface}}(q, \hbar\omega)$ is shown, after having subtracted from the whole $S(Q, \hbar\omega)$ the $S_{\text{core}}(Q, \hbar\omega)$, weighted by the indicated N factor. There, it can be seen how

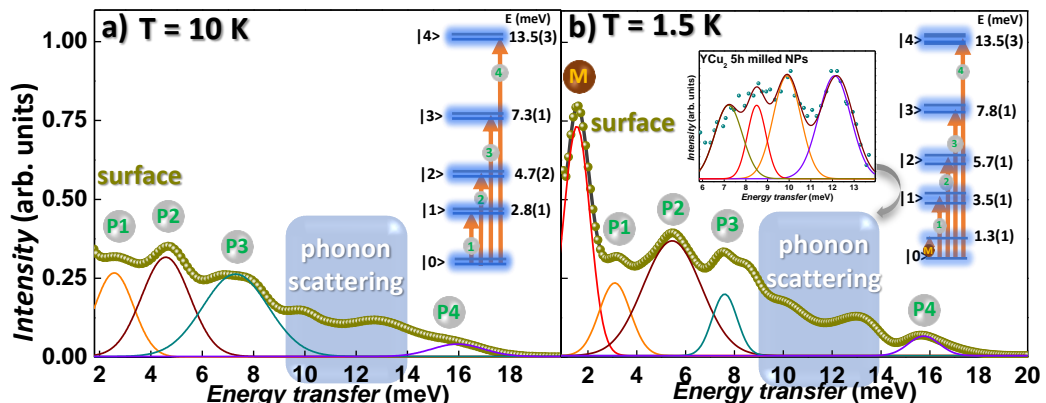


Figure 5.13: $S_{\text{surface}}(q, \hbar\omega)$ obtained following eq. 5.3 for the PM region at $T = 10$ K **a**) and the ordered region at $T = 1.5$ K **b**). The observation of the four CEF peaks, plus the magnon, at the surface contribution to the INS is actually unprecedented. Inset in **b**) includes a zoom vision of the isostructural YCu₂ 5h-milled MNPs, where a phonon contribution is non-negligible within the range $E \sim 6$ –14 meV. A sketch on the CEF+magnon schemes is provided in the right-side of both figures.

the peaks associated with the CEF remain in all of the patterns, no matter the N value. Given this situation, we have assumed $N = 0.3$, as it is the most reliable value, according to the approximations and the experimental data shown before.

Furthermore, quantitative information can be obtained by inspecting in closer detail both $S_{\text{surface}}(q, \hbar\omega)$ contributions. First, concerning the paramagnetic phase ($T = 10$ K, Fig. 5.13a), a left-shift of the energy transfer values can be determined for transitions from the ground state to the first and to the second excited levels. In this way, CEF excitations are found at $\hbar\omega_{P1} = 2.6$ and $\hbar\omega_{P2} = 4.6$ meV for the MNP surface, whereas they were found at $\hbar\omega_{P1} = 2.9$ and $\hbar\omega_{P2} = 5.0$ meV for the bulk state [215]. This fact reveals a **softening of the CEF splitting**, which can be ascribed to the less symmetric crystalline environment in the proximity of the MNP interfaces. As we have already mentioned [241], the interfaces play a role in the CEF definition, therefore, it is not surprising to observe a modification at the surface. Of course, the softening may also affect the higher energy excitations (P3 and P4), but the presence of phonon-scattering makes difficult to determine precisely their energy transfer values. Particularly, this scattering becomes rather strong in the energy range from 9 to 14 meV (blue-shadowed region in 5.13), which complicates the precise determination of the P4 position. The non-magnetic isostructural YCu₂ MNPs INS (see inset in Fig. 5.13b) confirms the phonon scattering. Finally, the poor definition of the $|9/2\rangle$ multiplet (*i.e.*, P4 excitation) was already foreseen by the specific heat analyses.

From the total MNP INS contribution, a change of the relative peak areas between P1 and P2 was already anticipated. There, we did not deep into the final reason for this effect to occur, but we will now focus on this fact. In this way, **whereas an almost homogeneous ratio between the peak areas $P2/P1$ was found in bulk NdCu₂, the value $P2/P1$ is almost 30% decreased at both the surface and the whole MNP state.** This is revealing a **partial inhibition of the transitions from the ground state to the first excited level**, which reveals that the bulk local-symmetry environment is slightly distorted at the MNPs. The structural microstrain η is at the basis of this distortion. Even if minimal ($\eta < 1\%$), it slightly changes the cation distribution surrounding the Nd³⁺ ions, thus, provoking the decoherence of some CEF excitations. Of course, this distortion should also be affecting P2–P4 transitions, but its effect is almost not noticeable within the experimental resolution, given that the distortion is very subtle ($\eta < 1\%$). Therefore, it can only be detected for the most intense excitation (*i.e.*, from the ground state to the first excited level, P1). Given that this partial inhibition from the ground state to the first excited level is close, but slightly greater at the whole MNP $S(q, \hbar\omega)$ than the one at the $S_{\text{surface}}(q, \hbar\omega)$, both the core and surface microstrain are definitely playing a role. Therefore, we can state that the intermediate regions between the AF-ordered MNP cores and SG-disordered surfaces in MNPs play the same role as *interfaces* do in multilayers, where a modification of both CEF level splittings and ground-state wave functions was reported (*e.g.*, in Fe–Nd multilayers [241]).

Furthermore, the **magnetically ordered phase** ($T = 1.5$ K, Fig. 5.13b) shows the **co-existence of collective magnetic excitations and CEF levels**, which is actually unprecedented, as the loss of periodicity at interfaces is well-known to affect the magnetic interactions. Here, the lowest energy excitation (peak labelled **M**) related to a transverse spin wave mode generated from the AF NdCu₂ ground state, is slightly shifted in energy ($\hbar\omega \approx 1.6$ meV) with respect to the bulk ($\hbar\omega \approx 1.4$ meV [99]). There are two possible scenarios to give account for this effect: **(i)** an enhanced anisotropy of the MNPs, which implies the shift of the modes towards greater energy values; and/or **(ii)** a stiffening of the magnon excitations in the MNPs, as greater energy transfer $\hbar\omega$ implies larger frequency (ω), being the latter proportional to the coupling constant between the adjacent magnetic moments. In the picture of the latter boosted exchange interactions, a shift on the Néel transition with respect to the bulk situation should have been recovered, since the AF state may be more robust. Nevertheless, the proximity of both T_f and T_N makes very tricky to observe this effect. By contrast what is un-

doubtedly is the enhancement of the anisotropy constant K in the MNPs, as it has been evidenced by the static $M(T, \mu_0 H)$ characterisation. Given that K is directly connected with the energy gap in the spin waves dispersion relation, small variations in the K value result in a modification of the energy of the magnon modes, as it has been shown, for instance, in [247]. Therefore, **we consider the anisotropy to be playing the main role in the shift of the magnon peak**. Furthermore, it is also very likely that the microstrain does also play a role in our MNPs, since it drives slight modifications of the interatomic distances among the magnetic moments (r) located at the surface. Given that $J_{RKKY} \propto \frac{2k_{FR} \cdot \cos(2k_{FR}) - \sin(2k_{FR})}{r^4}$, these minor modifications in r could effectively modify the coupling among the adjacent magnetic moments, leading to an enhancement of the exchange interaction among them.

To summarise, thanks to our procedure, some conclusions can be raised associated with the NdCu₂ MNP landscape. **First**, the INS in the PM region ($T = 10$ K) showed that **transitions to the first excited level are partially inhibited with respect to the bulk alloy**. This partial inhibition is deduced from the decrease in the intensity for transitions from the ground state to the first excited level, and can be attributed to a distortion of the local-symmetry environment surrounding each Nd³⁺-ion. As the distortion of the crystalline structure is below 1%, according to XRD or ND, this effect is weak, *i.e.*, it is only detected for the first excitation, which is the most intense one. **Second**, concerning the magnetic state, ($T = 1.5$ K), **a positive shift in the energy associated with the collective magnon excitations has been detected**. The modification of the spin wave energy is slightly modified, surely due to the increasing anisotropy connected to the size reduction to the nanoscale. Indeed, further INS experiments using different resolutions and/or other MNP ensembles may be helpful to complete these statement.

Chapter 6

Tb_xR_{1-x}Cu₂ magnetic nanoparticles

“Este party es un safari.”

J. Balvin

So far, we have studied the magnetic interactions in ensembles of GdCu₂ and NdCu₂ MNPs, where the frustration of the RKKY exchange interactions came, mainly, as a consequence of the size reduction to the nanoscale. Additionally to this, there can be found in the literature several examples where the frustration was achieved already at the bulk state, by replacing some of the magnetic R³⁺-ions by non-magnetic Y³⁺-ones, thus, *diluting* the RKKY exchange interactions [93, 160, 248, 249]. Nevertheless, there are no works, to the best of our knowledge, where both procedures are combined simultaneously, *ie.*, a *dilution* using non-magnetic 4*f*-ions *plus a size reduction to the nanoscale*. What is more, there are no reported studies providing a complete picture of what would happen if one **combines** two different kinds of magnetic R in a single crystal lattice (not a two-phased material), where the strength of the exchange interactions would vary in intensity, rather than being just switched on/off.

Apart from the fundamental interest that these combinations offer to the basic understanding of the RKKY propagation, the Tb_xR_{1-x}Cu₂ alloys that are going to be introduced in this section offer a rich variety of magnetic disorder states, which include the SSG Tb_{0.5}Gd_{0.5}Cu₂, the SAF Tb_{0.5}La_{0.5}Cu₂ or the SPM-like Tb_{0.1}Y_{0.9}Cu₂ MNPs. This way, by finely selecting the *x* proportion and the suitable R combination (Tb and Gd, La or Y), the capability to control the magnetic moment orientation in frustrated magnets, via the intraparticle interactions, is

achieved. A deep understanding of this control is essential for the emerging applications such as the Giant Magnetocaloric effect [250, 251, 252] or spintronic devices [4, 6, 253], where controlling the magnetic disorder, together with a precise definition of the complex magnetic structures involved, is key.

In this chapter, we are exploring the different degrees of frustration and magnetic disorder in three series of diluted bulk and NPs alloys, using the antiferromagnetic $TbCu_2$ bulk alloy as a starting point. Gd^{3+} , La^{3+} and Y^{3+} have been chosen as diluting ions, giving rise to **$Tb_{0.5}Gd_{0.5}Cu_2$, $Tb_{0.5}La_{0.5}Cu_2$ and $Tb_{0.1}Y_{0.9}Cu_2$** compositions. Whereas La^{3+} and Y^{3+} are non-magnetic, we have selected Gd^{3+} as magnetic ions due to the fact that Gd^{3+} displays, after Tb^{3+} , the largest magnetic orbital moment J among the Lanthanides [93]. This condition makes the Tb–Gd combination to be, in principle, the most suitable one to observe a possible enhancement of the random-bond disorder. Milling times were fixed to $t = 2$ h and 5 h, as these allowed to achieve nanometric sizes around 10 nm with a minor degree of microstrain [37, 39, 42].

As for the precedent $GdCu_2$ and $NdCu_2$, the structural characterisation made by means of XRD of these $Tb_xR_{1-x}Cu_2$ ensembles (bulk and MNPs) has been included in the Appendix A. Briefly, it is worth mentioning here the fact that all the produced alloys consistent with a single crystallographic phase of the orthorhombic $CeCu_2$ -type crystal structure ($Imma$ space group), as it is found for the parent bulk RCu_2 alloys ($R = Tb, Gd, Y$). This should not be surprising at this point, but we would like to stress the fact that we only found *a single phase*, not two phases, one corresponding to pure $TbCu_2$ and a second one of RCu_2 . This was achieved thanks to the melting process, which includes several re-melting steps in the arc-furnace, thanks to which the pellets were homogeneous. There is another detail, regarding the crystalline structure of the diluted alloys, that might have been problematic: The case of **$LaCu_2$** . This alloy is an exception for the RCu_2 orthorhombic $Imma$ structure, as it **crystallises in the hexagonal $P6/mmm A1B_2$ -type one** [254]. This implies that the crystalline structure of the $Tb_{0.5}La_{0.5}Cu_2$ alloy could consist of a mixture of both orthorhombic and hexagonal phases. Nonetheless, this risk is bypassed, since **the Rietveld refinements reveal unambiguously that only a single phase of the orthorhombic $Imma$ structure is present**. This is explained owing to the lower energy-cost that the orthorhombic structure has with respect to the hexagonal AB_2 -type [93]. The situation regarding the crystalline structure turns then back to be close to the one of $GdCu_2$ and/or $NdCu_2$, keeping the situation, at least at this point, simple.

6.1 Microscopic magnetic structure analysis: Neutron Diffraction

As it has already been anticipated, the stability of the bulk orthorhombic (*Imma*) crystalline structure was verified by means of XRD in all the produced alloys (bulk and nanoparticle state). This supports again the ball-milling route as an useful (and relatively simple) nanoparticle production method, where the final ensembles retain the crystallinity of the bulk state (provided the milling time is below a certain upper limit, of course [39, 255]). Appendix A showcases the Rietveld refinements performed in all of the samples, thanks to which particle sizes around 10 nm for 2h and 7 nm for 5h-milled alloys have been revealed. The question that naturally arises is, consequently, what happens to the magnetic structure in these $Tb_xR_{1-x}Cu_2$ alloys. According to the previous analyses regarding $NdCu_2$ shown in Chapter 5, the nanoparticle cores retained the bulk magnetic unit cell [213]. This also happened in the $TbCu_2$ ensembles, as reported in [43]. Consequently, one could expect a similar scenario held by these $Tb_xR_{1-x}Cu_2$ nanoparticles. Nevertheless, one should take into account the fact that **we have modified the alloy already at the bulk state** by the chemical substitution of the Tb-sites. By altering the *effective* distance between the Tb^{3+} ions, the RKKY exchange interactions are no more the same as the ones in the parent $TbCu_2$ bulk alloy, which might lead to a modification in the magnetic arrangement that has nothing to do with the size reduction. Although ND analyses on $Tb_{0.5}Y_{0.5}Cu_2$ bulk alloy have pointed out the stability of the parent $TbCu_2$ magnetic structure within the alloy, with an obvious reduction of T_N caused by the reduction in the Tb^{3+} amount [93, 249, 256, 257, 258], it is clear that a detailed study on the microscopic magnetic structure is mandatory in both bulk and MNPs *diluted* ensembles.

Given that the access to the neutron beam time is very limited, we decided to focus on the $Tb_{0.5}La_{0.5}Cu_2$ bulk and nano ($t = 2h$) alloys, as Gd^{3+} prevent the $Tb_{0.5}Gd_{0.5}Cu_2$ alloy to be studied by means of ND [181], and the dilution of $TbCu_2$ with non-magnetic Y^{3+} ions has been nicely reported [93, 249, 256, 257, 258]. Thereby, the ND measurements on the $Tb_{0.5}La_{0.5}Cu_2$ system were performed at D1B instrument (Institute Laue-Langevin, ILL, France) by PhD María de la Fuente Rodríguez, using a wavelength $\lambda = 2.520 \text{ \AA}$. Several temperatures between $T = 5 \text{ K}$ and 300 K were selected according to the magnetic state of the alloy¹. As for the case of $NdCu_2$, each of the patterns was measured for 8h so as to get a high signal/noise ratio.

¹see the “Magnetic characterisation” a few pages below.

ND patterns corresponding to the bulk alloy are included in Figs. 6.1a and b. Fig. 6.1a gathers the patterns collected for all the temperatures. It is worth noting the emergence of magnetic Bragg peaks for the measurements collected at $T \leq 20$ K. As an example, the two ones located within the range $28^\circ < 2\theta < 33^\circ$ have been zoomed. This fact is congruent with the antiferromagnetic Néel transition that takes place at $T_N = 33.1(1)$ K (see magnetic characterisation below). According to the Rietveld refinements ($R_B^{nuclear} = 8.2\%$ and $R_B^{mag} = 10.7\%$) of the patterns collected at $T = 5$ K included in Fig. 6.1b, **the magnetic structure is a collinear commensurate AF**. In this case, as Tb^{3+} is not a Kramers ion, no modulation in the intensity should be recovered [138]. The magnetic unit cell consists of 6 pairs of AF-coupled Tb^{3+} ions, aligned along the a -direction separated by $1/2a$, following a distribution according to $+ - - + - - \dots$. The non-Kramers nature of the ground state ($J = 6$) prevents this alloy to display a modulation in the intensity. In addition, TbCu_2 displays a different temperature dependence of the magnetic moments depending upon their Miller index [178]. Hence, the ones indexed with an odd Miller index (h, k, l) decrease faster, whereas the ones indexed with even $h + k + l$ and $(h \pm 1/3, k, l)$ retain a greater value of the magnetisation up to higher temperatures. The magnetic unit cell, which includes, as we have already said, 6 crystallographic unit cells, propagates thus according to vectors $\tau_1 = (0, 0, 0)$ and $\tau_2 = (1/3, 0, 0)$, where 4 Tb^{3+} are located at τ_1 and the remaining 8 occupy the τ_2 positions. This **double temperature dependence also holds for the $\text{Tb}_{0.5}\text{La}_{0.5}\text{Cu}_2$ alloy**, as the value for the magnetic moments are found to be $\mu_1 = 6.68(3) \mu_B$ and $\mu_2 = 4.71(5) \mu_B$. The maximum theoretical magnetic moment for Tb^{3+} is $9.72 \mu_B$; a value that is notably greater, so is the experimental value of $8.8 \mu_B$ found for the TbCu_2 parent alloy [43]. This discrepancy can be understood by means of **spin canting and the disorder environment**, as half of the Tb^{3+} sites are filled with non-magnetic La^{3+} ions. This is a fact that distorts the crystalline (and magnetic) structure. The thermal evolution of the μ_1 is plotted in Fig. 6.1c, together with the results coming from the MNPs. There, a Brillouin dependence with $J = 6$ is obeyed, as expected.

Coming now to the **MNP state**, ND patterns in Fig. 6.1c evidence the outburst of a magnetic structure at $T \leq 20$ K, as it was the case for the bulk alloy. The AF Néel transition, located at $T_N = 27.1(1)$ K, accounts for this emergence. According to Rietveld refinements on the $T = 10$ K pattern shown in Fig. 6.1d ($R_B^{nuclear} = 5.3\%$ and $R_B^{mag} = 5.8\%$), **the magnetic structure perfectly fits the one already explained for the bulk alloy**. Thanks to Rietveld refinements, **a magnetic size of $\langle D_{mag} \rangle = 12.3(3)$ nm and nuclear one of $\langle D_{nucl} \rangle =$**

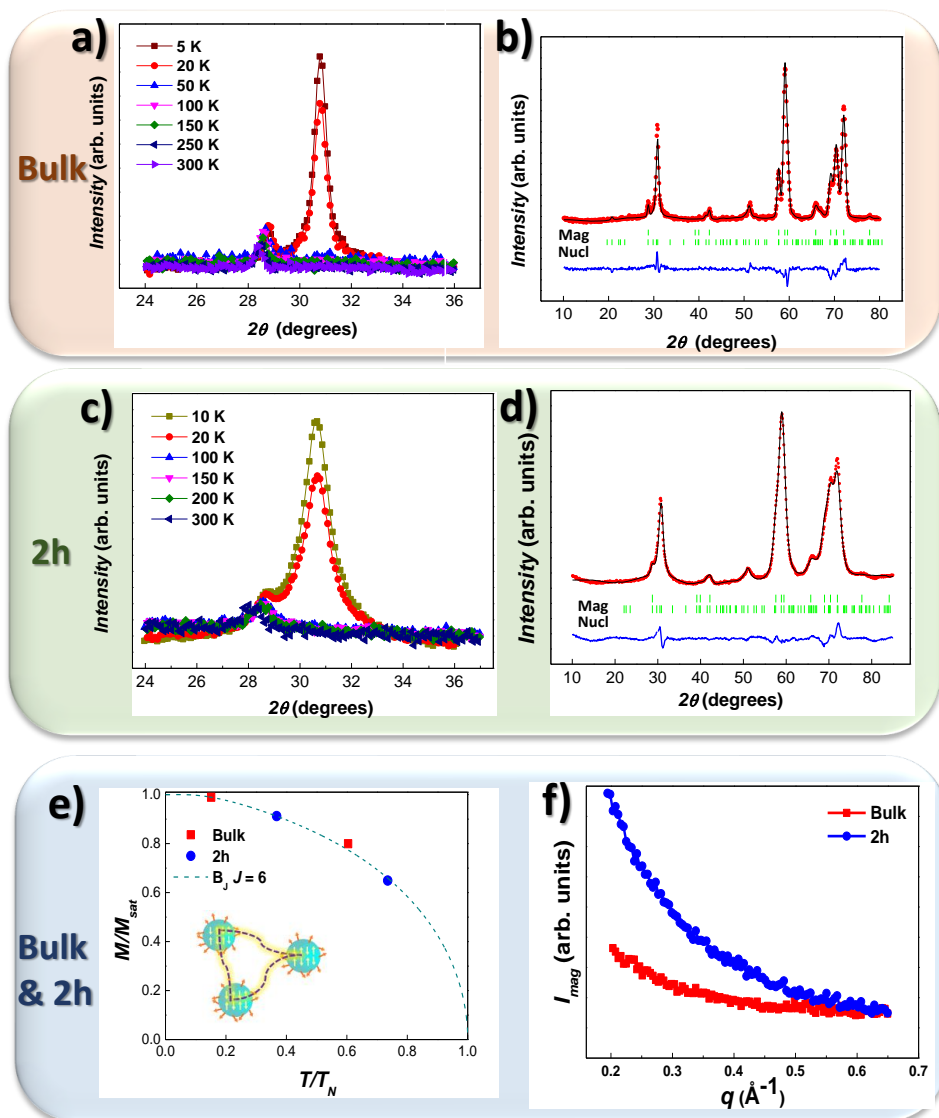


Figure 6.1: ND patterns measured using $\lambda = 2.520 \text{ \AA}$ for $Tb_{0.5}La_{0.5}Cu_2$ bulk (top panel) and 2h-milled MNPs (middle panel). In **a)** (**c)**), patterns for all the measured T values are shown, where the emergence of magnetic Bragg peaks is clear for the $T < 20$ K measurements in the region around $2\theta \sim 30^\circ$. In **b)** (**d)**), data collected at $T = 5$ K ($T = 10$ K) are displayed together with the Rietveld refinements, which show an almost perfect match with the experimental values (see bottom blue line, which reflects the difference between $I_{obs} - I_{calculated}$, (blue line)). **e)** showcases the evolution of the magnetisation per Tb^{3+} atom (normalised to M_{sat}) with the temperature for bulk (red) and 2h milled MNPs (blue) is depicted. The dark cyan-dotted line represents the Brillouin function calculated with $J = 6$. **f)** depicts the variation of the magnetic intensity in the low q region ($q < 0.665 \text{ \AA}^{-1}$) for bulk (red) and 2h MNPs (blue) at $T = 20$ K. There, the rise in the magnetic signal of the MNPs is unambiguous.

13.8(4) nm are obtained. This leads to a single-domain situation.

Finally, Fig. 6.1f focuses on the low- q region ($2^\circ < 2\theta < 15^\circ$ i.e., $q \lesssim 0.665\text{\AA}^{-1}$) of both bulk and MNP ensembles, measured at $T = 20$ K. It can be seen how the magnetic signal increases for the MNPs, which points to **the existence of interparticle correlations**. As for the NdCu_2 case, the provenance of these correlations is due to the increasing disorder of the magnetic moments, which is driven by both size reduction and microstrain. Such correlations could be very likely related to a Spin Glass phase, as the magnetic characterisation will confirm hereunder the SAF state of these MNPs.

6.2 Magnetic characterisation

As for the precedent Chapters, the magnetic characterisation has been performed in both static $M_{DC}(H, T)$ and dynamic $\chi_{AC}(T, f)$ regimes. No time-dependency measurements were included in this case, as the magnetic (disorder) state of the alloys was unambiguously distinguished.

6.2.a Static Magnetic Susceptibility: $M(T, H)$ characterisation

Beginning with the M vs. T measurements, Fig. 6.2a–c shows the ZFC–FC performed at low field ($\mu_0 H = 10$ mT) for $\text{Tb}_{0.5}\text{Gd}_{0.5}\text{Cu}_2$, $\text{Tb}_{0.5}\text{La}_{0.5}\text{Cu}_2$ and $\text{Tb}_{0.1}\text{Y}_{0.9}\text{Cu}_2$, respectively. The temperature values corresponding to the observed transitions, together with the values obtained from a Curie–Weiss fitting performed on the data measured at $\mu_0 H = 10$ mT have been included in Table 6.1.

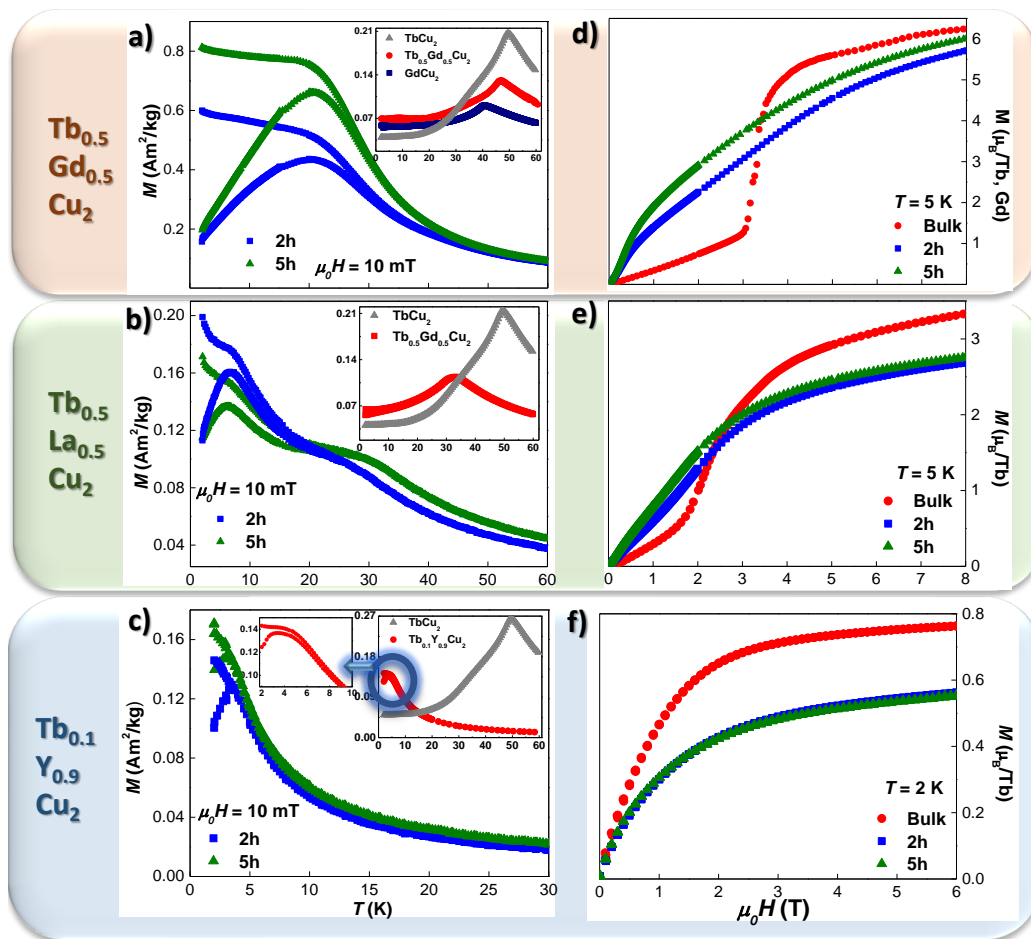


Figure 6.2: **a)–c)** display the ZFC–FC magnetisation curves for $Tb_{0.5}Gd_{0.5}Cu_2$, $Tb_{0.5}La_{0.5}Cu_2$ and $Tb_{0.1}Y_{0.9}Cu_2$ MNPs, respectively, measured at $\mu_0 H = 10$ mT. Insets show the bulk diluted alloy (red circles) with respect to the non diluted parents $GdCu_2$ (dark blue squares) and/or $TbCu_2$ (gray triangles). The y-axis has been re-scaled in all of the alloys for clarity purposes. **d)–f)** include the M vs. $\mu_0 H$ measured at $T = 5$ K for $Tb_{0.5}Gd_{0.5}Cu_2$ and $Tb_{0.5}La_{0.5}Cu_2$, whereas the data for $Tb_{0.1}Y_{0.9}Cu_2$ MNPs have been measured at $T = 2$ K, respectively. In all of the cases, the blue squares give account for the $t = 2$ h, whereas green triangles have been employed for the $t = 5$ h–milled MNPs.

Table 6.1: Néel temperature (T_N), freezing transition (T_f), paramagnetic Curie temperature (θ_P) and effective magnetic moment (μ_{eff}) obtained from Curie–Weiss fitting of FC measurements taken at $\mu_0 H = 100$ mT for the different produced alloys. The asterisk * indicates the blocking T_B instead of T_f .

Alloy	$t(\text{h})$	T_N (K)	T_f (K)	θ_P (K)	$\mu_{eff} (\frac{\mu_B}{\text{at}})$
$\text{Tb}_{0.5}\text{Gd}_{0.5}\text{Cu}_2$	bulk	47.2(1)	absent	19.9 (5)	9.26(1)
	2h	absent	19.7(1)	16.1(1)	9.31(3)
	5h	absent	21.2(1)	13.2(3)	9.86(1)
$\text{Tb}_{0.5}\text{La}_{0.5}\text{Cu}_2$	bulk	33.1(1)	absent	20.3(2)	10.23(2)
	2h	27.1(1)	6.2(1)	10.2(7)	10.16(2)
	5h	26.3(1)	7.0(1)	7.3(1)	10.29(4)
$\text{Tb}_{0.1}\text{Y}_{0.9}\text{Cu}_2$	bulk	absent	4.1(1)	2.84(1)	10.53(2)
	2h	absent	3.5(1)	-0.34(4)	10.56(2)
	5h	absent	3.0(1)*	-0.79(4)	10.76(6)

The first system that is going to be analysed is the $\text{Tb}_{0.5}\text{Gd}_{0.5}\text{Cu}_2$ series. As it can be seen from Fig. 6.2a, **no trace of an AF arrangement is retrieved in the MNP state**, whilst the bulk alloy clearly retains this transition, located at $T_N = 47.2(1)$ K. This value lies between those corresponding to bulk GdCu_2 ($T_N = 40.2(1)$ K [37, 163]) and TbCu_2 ($T_N = 49.1(1)$ K [43, 93]). The magnetisation value at this transition is also located between the parents' ones (almost 2.25 times larger than the one of GdCu_2 and 1/3 of the value of TbCu_2), which is expected for this intermediate stoichiometry. Nevertheless, what is worth noting is the occurrence of an irreversibility, as the FC branch retains a higher magnetisation at $T \lesssim 18$ K. This is a clue for the existence of a Spin Glass state, which would be triggered by the random–bond disorder plus the competition between AF and FM interactions. The latter competition is revealed by the positive value of the paramagnetic Curie temperature $\theta_P \approx 20$ K (see Table 6.1). The presence of a disordered magnetic phase already at the bulk state has also been displayed by other intermetallic alloys containing Gd, such as the polycrystalline Gd_4PtAl [259] or the GdCu_2 already introduced in this Thesis. The latter GdCu_2 displayed a $\theta_P \approx 20$ K, which agrees well with the one obtained in this $\text{Tb}_{0.5}\text{Gd}_{0.5}\text{Cu}_2$ bulk alloy. The irreversibility is more evident in the NP ensembles, where a freezing transition is unveiled, thus, giving rise to a **Super Spin Glass state** (SSG) [60, 173]. As it has already been discussed, the evolution from a pure bulk AF state to a NP SSG is commonly found (see the GdCu_2 or the 3d NiO compounds [260]). The SSG,

that emerges below $T \sim 20$ K, gets more robust as the MNP decreases, according to the rise in both the magnetisation (1.5 times) and the freezing transition temperature values ($\frac{T_f^{7nm} - T_f^{9nm}}{T_f^{9nm}} \approx 8\%$). The value of θ_P still holds positive for the MNPs, but shows a smooth reduction with size. Such a finding is concomitant with a progressive weakening of the FM interactions, that can be provoked by the increasing number of surface magnetic disordered moments. Finally, the obtained μ_{eff} values do not display appreciable size-dependence, and lie slightly below the ones reported for parent TbCu_2 and GdCu_2 [37, 39].

The situation concerning the **$\text{Tb}_{0.5}\text{La}_{0.5}\text{Cu}_2$** series is notably different. Here, opposite to what happened in $\text{Tb}_{0.5}\text{Gd}_{0.5}\text{Cu}_2$, **the bulk AF transition**, that takes place at $T_N \approx 33$ K, **does also survive in the MNPs** (see Fig. 6.2b). The bulk alloy also evidences irreversibility at $T \lesssim 20$ K, triggered once again by competing FM-AF interactions. In which concerns the MNPs, there is of course a reduction in both the magnetisation and the temperature of the Néel transition, which emerges naturally from the increasing disorder. The former magnetisation is diminished to half of the TbCu_2 value (see inset), as what also the case for $\text{Tb}_{0.5}\text{Y}_{0.5}\text{Cu}_2$ single-crystal [249]. Concerning the latter, a reduction of $|\Delta T_N(9nm)| = \frac{T_N(9nm) - T_N(bulk)}{T_N(bulk)} \approx 20\%$ can be quantified, which is almost twice the reduction that was obtained in the case of pure TbCu_2 NPs [39]. The half filling with a non-magnetic R^{3+} ion is at the basis of these findings, and back up the claim of the weakening of the RKKY exchange interactions to be solely affected by the replacement of Tb^{3+} ions by non-magnetic R^{3+} , regardless of the particular element. Besides the Néel transition, a freezing-like one is also observed in the MNPs at $T_f \sim 6-7$ K. Thereby, a **Superantiferromagnetic state** (SAF) shall be ascribed, which meets the ND measurements as well, shown above. As for the case of $\text{Tb}_{0.5}\text{Gd}_{0.5}\text{Cu}_2$, the positive value of θ_P gets reduced along with the MNP size, and no significant size-dependence of the μ_{eff} values is found.

Finally, the **$\text{Tb}_{0.1}\text{Y}_{0.9}\text{Cu}_2$** series will end the present discussion. Here, it should be stressed that the AF order state is destroyed already in **bulk** (see inset of Fig. 6.2c), since the magnetic percolation limit is overcome. This is coherent with the lack of both metamagnetism and hysteresis reported for this alloy [248, 261]. Particularly, in [261], a critical value of $x_c = 0.15$ was stated as the minimum concentration of Tb^{3+} -ions needed to give rise to a global AF state. Nonetheless, despite the weakening of the RKKY, the magnetic moments do interact among them, owing to the *plateau* observed in the FC branch at low temperatures. Later on, dynamic $\chi_{AC}(T, f)$ will disclose the **Cluster Spin Glass**

nature behind this effect. As it can be seen in Table 6.1, the transition temperature reduces along with the size, underlying the weakening of the interactions among the magnetic moments. This situation is in clear contrast with the one corresponding to $Tb_{0.5}Gd_{0.5}Cu_2$ and $Tb_{0.5}La_{0.5}Cu_2$, and can be ascribed to the reduced Tb-content of these MNPs. This way, bearing in mind that only 10 % of the moments are magnetic in $Tb_{0.1}Y_{0.9}Cu_2$, a reduction in the MNP size goes along to, obviously, a reduction of the total amount of the Tb^{3+} contained in each one. The less Tb^{3+} , the weaker the RKKY interactions. This *smoothed* competition yields to a less interacting ensemble of magnetic moments, and a weaker SG state is, therefore, settled. So much so that the **5h-milled MNPs** are no more interacting SG, yet they behaviour should be ascribed to an almost independent blocking process. A de Almeida–Thouless analysis fails giving account for the T_B vs. H dependency, as expected for non-interacting entities [184, 185]. The rise, rather than a *plateau*, in the FC branch for $T < T_B$ supports the evolution from a CSG in the bulk state to a weak interacting SPM state in 5h-milled NPs. The θ_p values fall near to zero at these MNP ensembles, and the μ_{eff} values lie again very close to the experimental value of $TbCu_2$ [39].

Isothermal $M_{DC}(\mu_0H, T)$ measurements of the diluted alloys are shown in Fig. 6.2. A temperature of $T = 5$ K was employed for both $Tb_{0.5}Gd_{0.5}Cu_2$ and $Tb_{0.5}La_{0.5}Cu_2$, whereas a $T = 2$ K was needed for the $Tb_{0.1}Y_{0.9}Cu_2$ dilution, as the disorder SG (SPM) states appeared at $T \leq 4$ K. Beginning with the **bulk ensembles**, it is worth first mentioning the **metamagnetic transitions** located at $\mu_0H = 3.33(1)$ T for $Tb_{0.5}Gd_{0.5}Cu_2$ (Fig. 6.2d) and $\mu_0H = 2.31(1)$ T for $Tb_{0.5}La_{0.5}Cu_2$ (Fig. 6.2e). Whereas the shape of the metamagnetic transition of **$Tb_{0.5}La_{0.5}Cu_2$** is more similar to a **spin-flop** mechanism, the one for **$Tb_{0.5}Gd_{0.5}Cu_2$** is **spin-flip** like, pointing to a **greater anisotropy for the latter alloy** [262]. Provided the S -state of both Gd^{3+} and La^{3+} ions (thus, a lack of magnetocrystalline contribution to the anisotropy), it is very plausible that the difference between the atomic radii of Tb^{3+} and La^{3+} , which is more dramatic than the one between Tb^{3+} and Gd^{3+} [263], enhances the random-bond disorder, leading to an increased anisotropy for the La-content alloy. Needless to say, **no trace for metamagnetic transition is found for bulk $Tb_{0.1}Y_{0.9}Cu_2$** (Fig. 6.2f), according to its CSG state. Indeed, the $Tb_{0.1}Y_{0.9}Cu_2$ alloy also displays the smallest anisotropy value of the produced dilutions, as the magnetisation reaches almost the saturation at $\mu_0H = 4$ T, while the magnetic saturation is not reached for $Tb_{0.5}Gd_{0.5}Cu_2$ or $Tb_{0.5}La_{0.5}Cu_2$ at even $\mu_0H = 8$ T. All the obtained $M(\mu_0H)$ values for each alloy can be easily understood according to their Tb^{3+} content. Beginning from the low-content side, a value of $M(6\text{ T}) = 0.765(1) \mu_B / Tb$ is found for the $Tb_{0.1}Y_{0.9}Cu_2$ bulk alloy,

which is almost 10 times decreased with respect to the $TbCu_2$ value at same μ_0H [39]. Then, at $\mu_0H = 8$ T, the magnetisation reaches $\approx 89\%$ and $\approx 50\%$ of the $TbCu-2$ value for $Tb_{0.5}La_{0.5}Cu_2$ and $Tb_{0.5}Gd_{0.5}Cu_2$, respectively. A few lines below, when presenting the Arrott plot analyses, fine details concerning the bulk state will be disclosed for these later two alloys.

We will move now to the **MNP ensembles**. A non-surprising reduction of the magnetisation is derived at the MNP state, due to both the canting of the magnetic surface moments and the increasing distance among them magnetic moments with respect to the bulk state. Once the NP state is set, the anisotropy of the MNPs increases, by means of the growing spin canting, that increase as the lattice microstrain and surface-to-core ratio do. This is noted by the slight increase of the magnetisation for the 5h-milled ensembles. In order to bring more light into the disordered state of the SPM $Tb_{0.1}Y_{0.9}Cu_2$ 5h milled NPs, hysteresis loops (not shown) have been performed at $T = 2$ K, where non-negligible values for both coercive field ($\mu_0H_C = 8.82(1)$ mT) and remanence ($M_r = 14.4(1)$ Am²/kg) have been found. These findings reveal that the magnetic state is that of a weakly interacting SPM, rather than a pure non-interacting one [60]. An estimation of the dipolar interaction contribution gives a very reduced value of $E_{d-d}/k_B \sim 0.22$ K, which is far from the observed $T_B \approx 3$ K. This low E_d value prevents the dipolar interactions to develop a cooperative glassy state, on the contrary of what happened for bulk $Tb_{0.1}Y_{0.9}Cu_2$.

Provided that the $M(T)$ results underlined the presence of FM interactions together with AF ones, the magnetic coupling to an external field should be inspected in closer detail. In this line, in order to elucidate these specific subtleties that deserve more attention, the **Arrott plots** for both $Tb_{0.5}Gd_{0.5}Cu_2$ and $Tb_{0.5}La_{0.5}Cu_2$ AF bulk alloys at several temperatures below T_N have been analysed (see Fig. 6.3). Indeed, the expected lineal shape for the curves measured close to T_N is retrieved, as it is non-surprising for antiferromagnets [111, 264]. Nevertheless, **what makes these analyses very interesting is the fact of having found non-negligible values of spontaneous magnetisation (M_{spt}), which corroborate the existence of the incipient FM interactions.** To the best of our knowledge, **this is the first time that the Arrott plots are used in a system revealing both FM and AF interactions** [67]. The evolution with the temperature for these M_{spt} follows a Brillouin-like function (see insets), as expected for FM ensembles. The obtained FM parameters for $Tb_{0.5}Gd_{0.5}Cu_2$ are $T_C = 28.5(1)$ K and $J = 4.75$, which agree with a proportion of 50 % of Tb^{3+} ($J = 6$) and 50 % of Gd^{3+} ($J = 7/2$). It is remarkable that these T_C values lie close to the obtained

θ_P ones (see Table 6.1). At this point, the presence of AF and FM interactions is experimentally probed, which leads then to understanding the outburst of a magnetically-disordered phase (irreversibility in the FC branches), that comes as a result of the competition between both kinds of RKKY couplings. Furthermore, the presence of this disorder phase leaves a trace in the Arrott plots², in the form of a right-curvature at low M^2 values [265]. This bending gets visible at $T \leq 25$ K for $Tb_{0.5}Gd_{0.5}Cu_2$ and $T \leq 15$ K for $Tb_{0.5}La_{0.5}Cu_2$, in good agreement with the $M(T)$ characterisation.

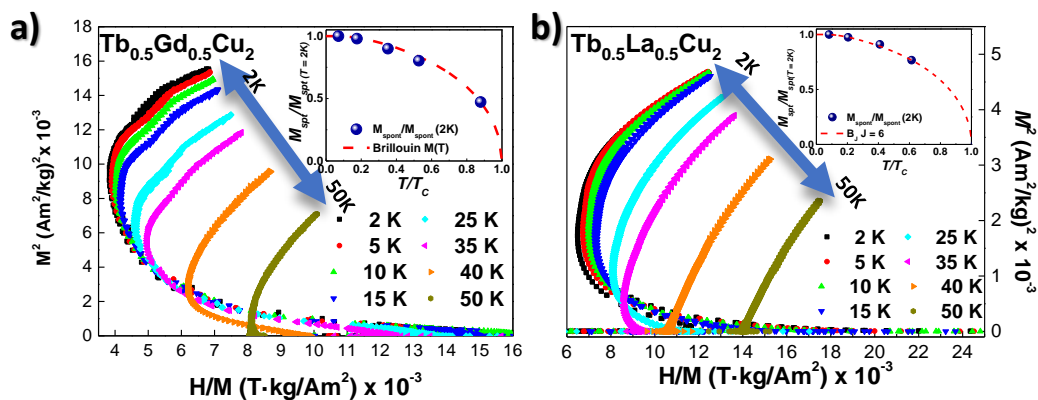


Figure 6.3: M^2 vs $\mu_0 H/M$ Arrott plots for (a) $Tb_{0.5}Gd_{0.5}Cu_2$ and (b) $Tb_{0.5}La_{0.5}Cu_2$ bulk alloys. The insets represent the relative spontaneous magnetisation $M_{spt}/M_{spt}(2K)$ obtained from the Arrott plots in a relative temperature scale respect T_C . The dashed red line represent a Brillouin curve with $J = 4.75$ and $J = 6$ respectively. Values of M_{spt} obtained for $T > T_C$ are equal to zero.

6.2.b Dynamic Magnetic Susceptibility

All the alloys display magnetic irreversibility; hence, a study on the magnetic dynamics becomes mandatory for completeness. First of all, Fig. 6.4a–i depicts the behaviour of the in-phase χ' (T) and out-of-phase χ'' (T) components for bulk, 2h, and 5h milled alloys. These measurements are coherent with the static M_{DC} , as the Néel transition is effectively absent for $Tb_{0.1}Y_{0.9}Cu_2$ alloy (bulk and MNPs), so it is for the $Tb_{0.5}Gd_{0.5}Cu_2$ MNPs. The observed rise of the χ'' (T) signal already at the bulk state observed for the $Tb_{0.5}Gd_{0.5}Cu_2$ ensembles at $T < 20$ K is connected to the conjectured existence of SG clusters. As it can be observed in Figs 6.4a–c, the SG cusp follows the expected right-shift frequency dependence in

²Arrott plots are a extremely powerful *loupe* to dip into the magnetic interactions of a sample, yet they are no so commonly found in the literature.

all the alloys, whereas the Néel transition is frequency independent [36, 50, 61, 87].

The most attractive study is the quantification of the observed T_f -shift with f in Fig. 6.4a–c by means of the critical exponents. Thereby, Table 6.2 includes the δ and fitting parameters obtained according to an exponential slowing down scaling values for the diluted MNPs. Beginning with the δ -parameter, it turns out that **the alloys containing 50 % of Tb display larger values (0.05–0.08) than the ones ascribed to the spin dynamics of canonical Spin Glasses** [50]. These values are **also greater than the ones reported for $TbCu_2$ [39], $GdCu_2$ or $NdCu_2$ MNPs**, yet they are still below the ones for SPM systems [60]. Actually, **these values fall close to those of CSG systems, $\delta \sim 0.06$** [72]. Values for the critical exponent $z\nu$ are included within the *fragile regime* behaviour ($5 < z\nu < 11$) [70]. Regarding the evolution of the spin dynamics with the milling time, nearly no-change follows the $Tb_{0.5}La_{0.5}Cu_2$ size reduction, whilst a clear decrease of the δ and $z\nu$ values is found for the $Tb_{0.5}Gd_{0.5}Cu_2$ MNPs, indicating a more glassy state [79]. Values of $T_{f \rightarrow 0}$ are slightly below the ones obtained for the freezing according to M_{DC} characterisation, which is expected, as the true phase transition is reached solely when $H, f \rightarrow 0$ [50].

On the other hand, the magnetic behaviour of the $Tb_{0.1}Y_{0.9}Cu_2$ alloys evolves clearly in a different way. For this alloy, an increase of δ , together with a reduction in both $z\nu$ and $T_{f,0}$, with milling time have been found. This implies weaker interactions for smaller NPs, as it has already been stated. In this way, **the values for δ clearly agree with the transformation from the bulk CSG ensemble to a SPM one for the 5h-milled MNPs.** This transformation from a freezing process to a blocking mechanism explains that the fitting of the experimental T_B for the $Tb_{0.1}Y_{0.9}Cu_2$ 5h according to a dynamic critical exponent fails, as no phase transition is established in this alloy.

To end with the magnetic characterisation, **in order to bring more light to the evolution of the $Tb_{0.1}Y_{0.9}Cu_2$ alloy from the interacting CSG to a weakly coupled SPM, we have judged interesting to represent the Cole–Cole diagrams.** This way, Fig. 6.5 compares the 2h and 5h-milled ensembles. These representations are a powerful tool to access information about the NP size distribution and anisotropy [266, 267]. While the Cole–Cole diagram of an ideal monodisperse ensemble of SPM NPs should be a perfect semi-circle, the 5h milled MNPs (Fig. 6.5b) are flattened and asymmetric semi-circles, which correspond to a polydisperse Log–Normal particle size distribution [60]. The occurrence of a broad peak (maximum) in $\chi''(\chi')$ further supports this deviation

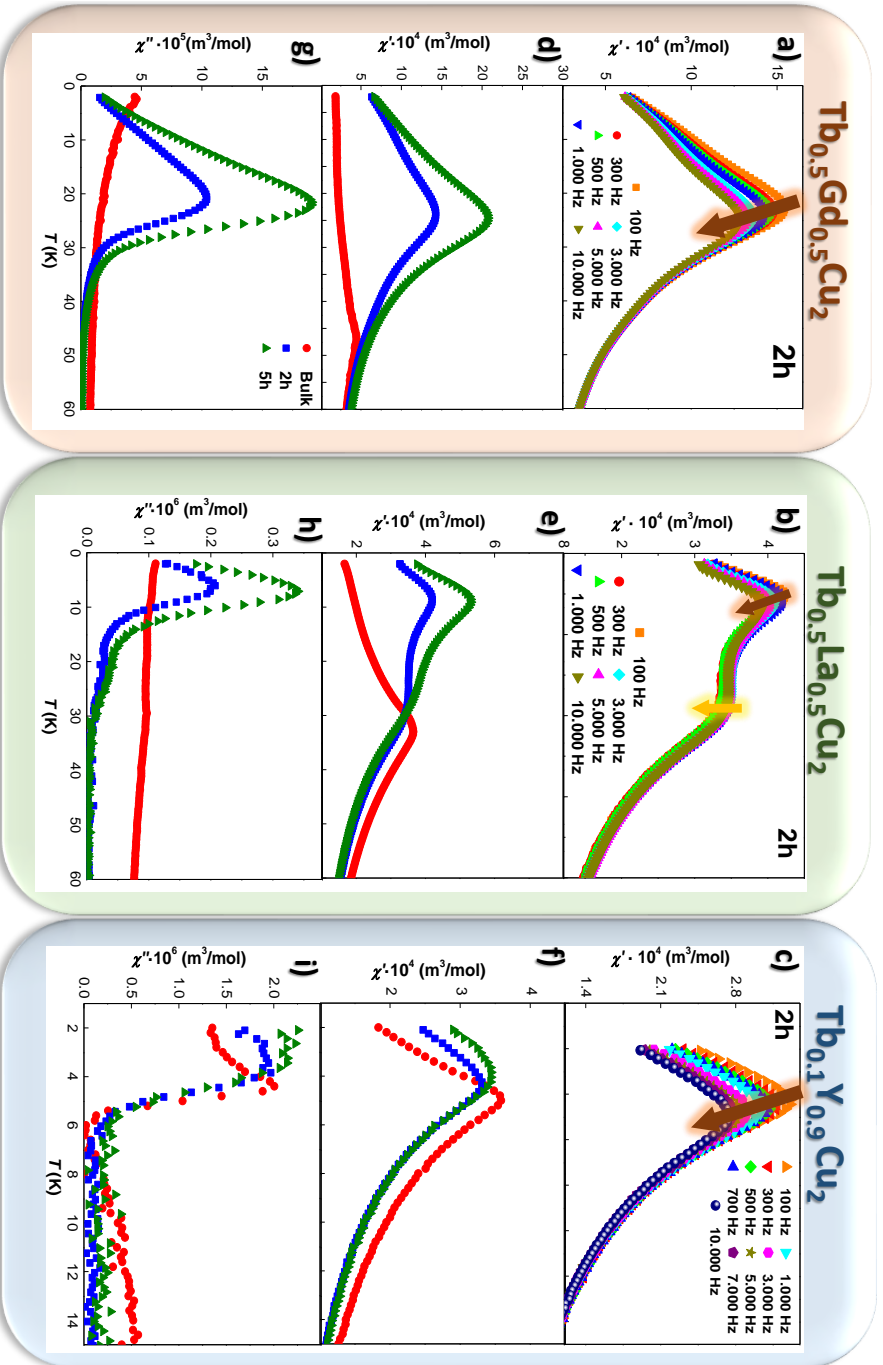


Figure 6.4: **a)–c)** In-phase $\chi'(T)$ recorded at $h = 0.313$ mT for the 2h-milled MNPs at several frequencies. The orange arrow marks the freezing transition, whereas the yellow one signals the Néel transition. **d)–f)** and **g)–i)** display the χ' and χ'' vs. T components for bulk (red circles), 2h (blue squares) and 5h (green triangles) milled NPs, measured at $f = 1000$ Hz [$f = 100$ Hz in **f)** and **i)**]. Left figures **a)**, **d)**, **g)** correspond to $\text{Tb}_{0.5}\text{Gd}_{0.5}\text{Cu}_2$, **b)**, **e)**, **h)**, to $\text{Tb}_{0.5}\text{La}_{0.5}\text{Cu}_2$, and **c)**, **f)**, **i)**, to $\text{Tb}_{0.1}\text{Y}_{0.9}\text{Cu}_2$ alloys.

Table 6.2: δ -shift parameter, relaxation time τ_0 of individual particles for $f \rightarrow 0$, freezing transition temperature T_f and critical exponent $z\nu$ for the diluted alloys. The fitting of the experimental data for 5h-milled $Tb_{0.1}Y_{0.9}Cu_2$ NPs didn't converge to a critical slowing down, according to the SPM relaxation undergone by these MNPs.

Alloy	t(h)	δ	τ_0 (s)	$z\nu$	$T_{f,0}$ (K)
$Tb_{0.5}Gd_{0.5}Cu_2$	2h	0.058(2)	10^{-8}	9.11(9)	18.7(5)
	5h	0.049(2)	10^{-8}	5.92(11)	21.51(7)
$Tb_{0.5}La_{0.5}Cu_2$	2h	0.070(4)	$5 \cdot 10^{-8}$	5.6(5)	7.4(1)
	5h	0.077(3)	$5 \cdot 10^{-8}$	5.4(2)	7.5(1)
$Tb_{0.1}Y_{0.9}Cu_2$	bulk	0.048(2)	10^{-8}	6.66(14)	4.00(2)
	2h	0.075(3)	10^{-8}	6.5(4)	3.80(5)
	5h	0.092(8)	—	—	—

from a monodisperse SPM ensemble of NPs. This maximum shows a right shift of $\chi'(T = 3.64K) - \chi'(T = 2.44K) \sim 0.017 \cdot 10^{-4} \text{ m}^3/\text{mol}$ to greater χ' values with increasing temperature. On the other hand, the Cole–Cole diagram of the CSG 2h-milled ensembles (Fig. 6.5a) displays a more drastic right-shift of this maximum with increasing temperature, as $\chi'(T = 4.4K) - \chi'(T = 2.44K) \sim 0.029 \cdot 10^{-4} \text{ m}^3/\text{mol}$. This is to say, ≈ 1.7 times greater than the one for 5h milled NPs. This is indicative of a narrower distribution of relaxation times, which is in good agreement with CSG state of 2h milled NPs, where the magnetic moments are more interacting.

The fact that the χ'' vs. χ' curves for the 2h-milled ensembles are flattened shifted downwards with respect to the situation for 5h-milled NPs further backs up the more interacting nature in these 2h-milled MNPs, as it is a typical signature of frustrated cooperative interactions [50]. Finally, a relative breadth $\sigma_{rel} \sim 0.33$ can be calculated for this peak, which is clearly larger than the of $\sigma_{rel} \sim 0.05$ corresponding to an archetypal canonical spin glass of $Au_{96}Fe_4$ [268]. This finding further corroborates the cooperative cluster behaviour of the magnetic moments rather than the individual response of SG ones.

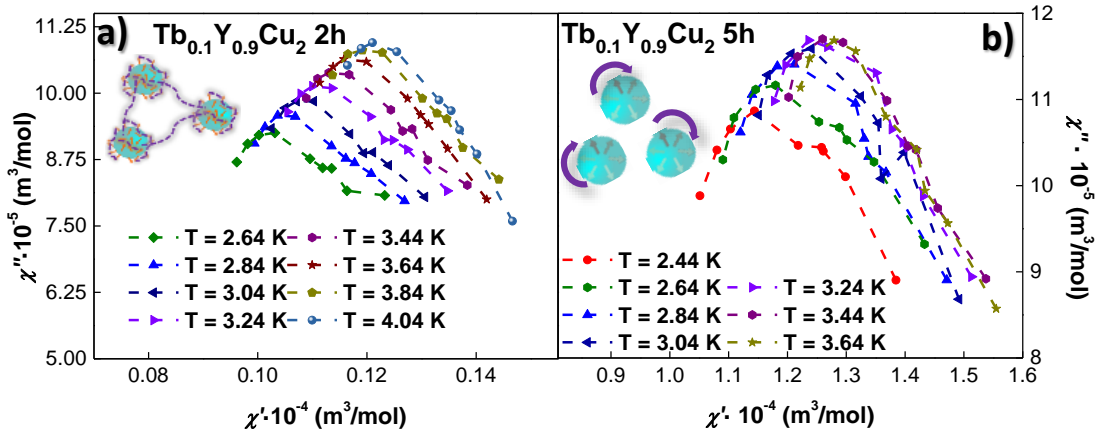


Figure 6.5: Cole–Cole diagrams for $Tb_{0.1}Y_{0.9}Cu_2$ (a) 2h and (b) 5h milled NPs measured at several temperatures close 2h and above T_f (T_B).

6.3 Specific heat measurements

It is obvious that, given the rich variety of magnetic order/disorder transitions observed in these alloys, having access to specific heat c_P measurements is of primer interest. Fortunately, we could gain access to measure the $Tb_{0.5}Gd_{0.5}Cu_2$ (bulk and 2h) and the $Tb_{0.5}La_{0.5}Cu_2$ (bulk, 2h and 5h–milled) ensembles. Just as a reminder, since no order transitions were found in the $Tb_{0.1}Y_{0.9}Cu_2$ ensembles, no c_P measurements have been performed in this series. The procedure to analyse the c_P data has already been explained in the precedent chapters, so further details are no required. Thereby, we will focus on the different nature of the transitions recovered in both $Tb_{0.5}R_{0.5}Cu_2$ ensembles.

Figs. 6.6a and d include the measured c_P , together with the c_{el+ph} and c_{mag} contributions, measured in the absence of external applied field. Needless to say, θ_D and γ have been taken from the non–magnetic isomorphous YCu_2 [160], with a renormalization correction applied subsequently [161]. The c_{mag} contribution represented in Figs. 6.6b and e deserves more attention. First of all, a clear peak associated with the second–order Néel transition shows at $T_N = 45.4(1)$ K in the **$Tb_{0.5}Gd_{0.5}Cu_2$ bulk alloy** (Fig. 6.6b). This peak shows the expected λ –anomaly profile, along with a decreasing intensity and temperature as the magnetic field is raised [208, 209, 210].

Below this λ –anomaly, a huge broadening can be noticed between $T \sim 20$ K

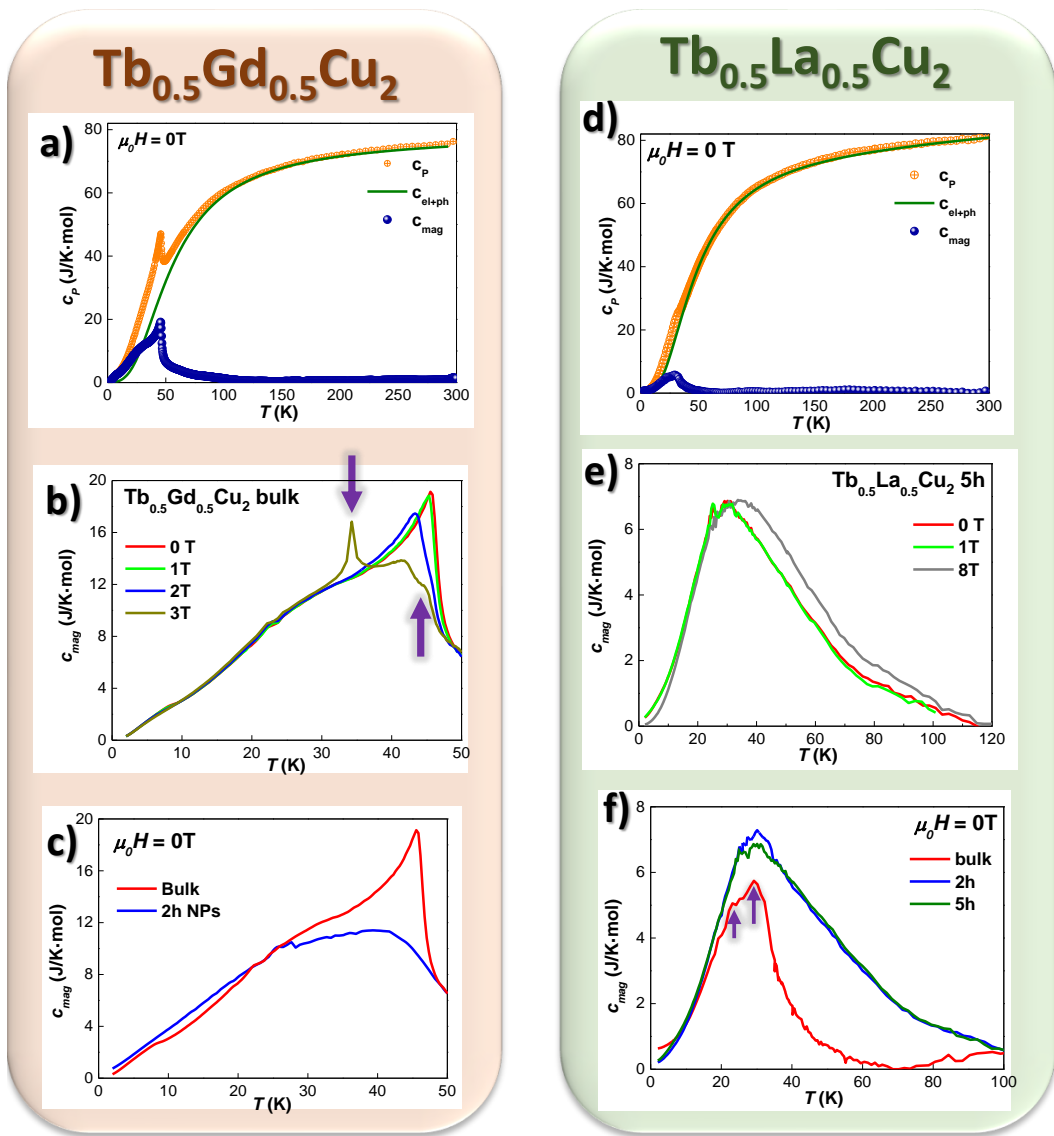


Figure 6.6: Experimental data for the specific heat c_p vs. T for $Tb_{0.5}Gd_{0.5}Cu_2$ (a) and $Tb_{0.5}La_{0.5}Cu_2$ (d) bulk alloys measured at $\mu_0H = 0$ T (orange), together with the c_{el+ph} (green line) and the c_{mag} (blue spheres) contributions. In (b) (e)), the c_{mag} vs. T is depicted in closer detail to compare the bulk and the NP contribution, also measured under no external applied field. Finally, (c) (f)) includes the bulk (5h-milled) c_{mag} contribution measured under a field of $\mu_0H = 0$ T (red line), 1 T (green), 2 T (blue), 3 T (dark yellow) and 8 T (gray). The purple arrows indicate the position of the extra peaks found at each alloy. The reason behind these humps is different for each alloy.

and $T \sim 35$ K. This shoulder, that constitutes a typical hint of an **amplitude-modulated (AM) magnetic structure**, may be ascribed to the propagation of spin waves within the ordered region. Given that both $GdCu_2$ [269] and $TbCu_2$ [39] display an AM–AF structure, it should not be surprising that a dilution containing both ions will be arranged as a AM structure as well. Of course, a tiny contribution stemming from CEF effects to this should could not be discarded, since Tb^{3+} is not a S–state ion [270]. Upon increasing the applied magnetic field (see bulk alloy in Fig. 6.6c), it is worth noting the outburst of two additional peaks located at $T = 34.3(1)$ K and $T = 45(1)$ K (marked with purple arrows) when $\mu_0 H = 3$ T. Whereas the narrow shape for former may be indicative of a first order transition associated with the existence of Ferromagnetic (FM) interactions, the shape of the latter could be more likely connected to a second order Néel transition. Considering the magnetic characterisation, it is plausible that, when the external applied field is strong enough, the magnetic response of the Tb^{3+} and Gd^{3+} ions would be, somehow, *decoupled*, yielding to two AF transitions that lead to a double peak structure in the c_{mag} .

The situation concerning the **$Tb_{0.5}La_{0.5}Cu_2$ series** (Fig. 6.6e and f) is somehow different. In this sense, the results corresponding to the bulk alloy (Fig. 6.6f) evidence two humps, one located at $T_N = 29.4(1)$ K, and a second one, which lies at $T_f = 23.0(1)$ K (marked with purple arrows). These two peaks survive in the NPs at $T_N = 29.7(5)$ K and $T_f = 24.9(5)$ K, in good agreement with the **SAF state of the MNPs**. Given that the values for both T_N and T_f transitions get closer when reducing the size, they collapse and form a single broad hump, instead of two different structures, in the MNP regime, with an increased c_{mag} intensity. In which concerns the field–dependence of the c_{mag} contribution corresponding to the 5h–milled $Tb_{0.5}La_{0.5}Cu_2$ MNPs (Fig. 6.6e), it can be observed that no extra transitions emerge at any applied field. Furthermore, the c_{mag} is almost field–independent at lower fields, although a slight shift towards higher temperatures is observed for $\mu_0 H = 8$ T, which may be indicative of the existence of magnetic short–range correlations promoted by the large magnetic field.

Finally, the latter Figs. 6.6c and f compare the c_{mag} between the bulk and MNP alloys. Accordingly, Fig. 6.6c includes both c_{mag} arising from the bulk alloy and the 2h–milled MNPs for $Tb_{0.5}Gd_{0.5}Cu_2$, whilst Fig. 6.6f accounts for the $Tb_{0.5}La_{0.5}Cu_2$ bulk, 2h and 5h–milled MNPs. In both compositions, the intensity of the bulk λ –anomaly is clearly reduced in the MNP state. **Furthermore, all the ensembles (bulk and MNPs) showcase a broad hump, located at around 25 K**, which is, as we have already commented above, mostly **triggered**

by the spin wave propagation. Therefore, this finding would reveal that the magnetic order survives within the nanoscale, but certainly weakened with respect to the bulk situation. This scenario is in very good agreement with the situation disclosed thanks to the INS measurements on the $NdCu_2$ ensembles (see Chapter 5). We could suggest, at this point, that it is very likely that the magnetic order should be ascribed to the RKKY interactions involving the Tb^{3+} ions, since the ones coming from Gd^{3+} have evidenced to be not strong enough to give rise to a magnetic collective order state at this NP size (see Chapter 4), and La^{3+} do not even display magnetic angular moment.

To sum up, this chapter serves as a *guide* to promote different degrees of magnetic disorder states on $Tb_xR_{1-x}Cu_2$ alloys, for both bulk and nanoparticle states. Starting from the less disordered state, **$Tb_{0.5}La_{0.5}Cu_2$ NPs showed a SAF arrangement** in which the AF order is retained within the NP core and the disordered SG phase is located at the shell. Then, progressing to a more disordered state, magnetic NPs of **$Tb_{0.5}Gd_{0.5}Cu_2$** revealed themselves to form a **SSG ensemble**, where all the magnetic moments have fallen into a frustrated state. Finally, the **$Tb_{0.1}Y_{0.9}Cu_2$ NPs could be placed at the most magnetically disordered extreme.** Here, the AF order is absent already at the bulk state, where a CSG is revealed. The evolution with the size reduction leads to a gradual *dilution* of the interactions among the magnetic $4f$ -moments, resulting in a **weakly interacting SPM** state for $\langle D \rangle \approx 7.5$ nm sized NPs.

Chapter 7

γ -Fe₂O₃ and Fe₃O₄ magnetic nanoparticles

*“Te voy a inyectar con la bacteria,
pa’ que dé vuelta como machina
de feria”*
Calle 13

Fe-oxides have been extensively studied along the history of Magnetism. Their ubiquity in Nature allowed humans to easily access them from a very early stage, which became quickly fascinated by their magnetic properties. Already in the Ancient Greece, there can be found plenty of references to *lodestone*, named *magnetite* after a mythical hero and the people who have inhabited the district where it was first recognised, *the Magnetis* [271]. Furthermore, not only have Fe-oxides been object of extensive studies due to their worldwide-presence, but also, because these materials display a plethora of applications in a great amount of fields, such as heritages or biomedical applications [23, 40]. Among these Fe-oxides, γ -Fe₂O₃ (maghemite) and Fe₃O₄ (magnetite) are two of the species gathering more attention. As a consequence of both **the magnetic response** stemming from these oxides¹, together with their **biocompatibility**, **a great deal of the present research work** on these compounds is performed **in ensembles of MNPs** [22, 272].

It is then not surprising the fact that **maghemite-based MNPs are already a standard in bio-nanomedicine** [22, 272, 273, 274]. Among the different γ -Fe₂O₃ nanoparticles, the ones that arrange in the form of a *flower* have deserved

¹see in Fig.7.1a a comparison between the M_{DC} vs. T response of maghemite Nanoflowers and magnetite bacterial magnetosome.

the majority of attention. In this particular shape, the nanoparticles consist on a multicore structure (see Fig. 7.1b), being the cores (*petals*) correlated among each other. The existence of a exchange coupling between these cores leads to a superferromagnetic magnetisation state, which takes place together with a significant degree of spin disorder caused by the grain boundaries. It is, precisely, due to the existence of this disorder that **the Magnetic Hyperthermia (MHT) performance of the flower-shaped nanoparticles is enhanced** with respect to other geometries/arrangements [28, 29, 275, 276].

Accordingly, the potential extensive use of the maghemite-based NFs for MHT and/or for drug delivery purposes has boosted their interest in the last two decades [277, 278, 279, 280]. To give an example, already in the early 2000s, Phase I clinical trials on magnetic hyperthermia were performed in Germany (MagForce Nanotechnologies, see [281]), and, more recently, new trials have been approved for treatment of specific type of cancers (e.g. glioblastoma and prostate) in several countries around the world, including Japan, Germany, USA, and China [273, 282, 283, 284, 285]. Generally speaking, **a slight bias of the scientific community towards maghemite, rather than magnetite-based MNPs**, is found nowadays. This has nothing to do with the hyperthermia performance itself, yet it is related to the **chemical stability, since maghemite is a more stable phase**, to which magnetite evolves, owing to an oxidation process [1, 40]. What is more, the vast majority of commercial MNPs developed for magnetic hyperthermia (MHT) purposes are made either of maghemite, or a magnetite core and an oxidized maghemite shell [286, 287, 288, 289, 290], meaning that **few attention has been devoted to compare the MHT performance** between $\gamma\text{-Fe}_2\text{O}_3$ and Fe_3O_4 MNPs. To the best of our knowledge, only [291] provides a comparison between maghemite Nanoflowers and magnetite nanospheres, although the mean nanoparticle size for the former was twice the one of the later. This mismatch *blurs* somehow the comparison, as it has been shown that **the mean NP size does affect the MHT performance** [292]. Therefore, an open question to be answered was **whether the MHT performance of purely maghemite MNPs was better than the one of purely magnetite MNPs of similar sizes or not**. The sticking point of such a comparison relies, indeed, on how to guarantee the chemical stability of magnetite, not only for the measuring processes, but also for their potential further application. As it is going to be explained a few lines below, the use of magnetotactic bacteria (MTB) will allow us to avoid this issue.

The main synthesis routes to obtain these Fe-based MNPs (either maghemite or magnetite MNPs) involve chemical methods, which contrast with the physical

top-down milling route followed to obtain RCu_2 -alloys. There are excellent reviews in the literature explaining these synthesis methods, e.g. [15], and it is obvious that the magnetic properties have also been extensively reviewed e.g. [40, 293]. In addition to these well-standardised chemical synthesis routes, in the last two decades, a lot of groups have devoted their main efforts **to obtain Fe_3O_4 from magnetotactic bacteria (MTB)**. These bacteria are aquatic motile microorganisms which display magnetotaxis² thanks to their intracellular magnetic organelles, called *magnetosomes*, which arrange in chains (see Fig. 7.1b top). The chemical stability of the magnetosome Fe_3O_4 phase is secured, as they are surrounded by a lipidic bilayer, which acts as a *shield* against oxidation. The MTB can be found in a widespread of marine environments, predominantly, at the oxic-anoxic transition zones [295], yet they can also be cultured in the laboratory by setting some specific conditions³ Thanks to their magnetosomes, these self-propulsed flagellated-microorganisms can be externally guided by the application of a magnetic field. This is an outstanding advantage, which makes them potential candidates to be used as *nanobiots* [24] in a widespread of applications, mainly connected to drug delivery and/or cancer treatments [279, 296, 297, 298]. Following this idea, **not only the MTB can be guided and manipulated by external magnetic fields, but they also retain the therapeutic and imaging capacities of the extracellular magnetosomes**. What is more, on the contrary of most of the bacteria currently tested in clinical trials for cancer therapy, **magnetotactic bacteria are not pathogenic**, and can also be engineered to deliver and/or express specific cytotoxic molecules [24].

The fascination about the potentialities of MTB does not stop at this point. Once the scientific community has been conscious about the high prospects of these bacteria as nanobiots, some groups have faced, in the last decade, the challenge of **tuning the composition of magnetosomes by doping them with different elements**. The aim of this research line is simply to broaden, even more, the applications and potentialities of MTB in, mainly, the biomedical field [35, 120, 122]. Just as an example, the coercive field value of magnetosomes can be greatly increased by doping magnetosomes with Co [34, 120]. The **magnetic anisotropy of these Co-doped MTB** is, consequently, **larger with respect to the one of the undoped MTB**, a fact that is **key for their Magnetic Hyperthermia Treatment (MHT) performance**. Given the exceptional potentialities and applications in the biomedicine field that Rare Earth elements have evidenced [299, 300], together with our solid background on the $4f$ magnetism, **tackling the**

²ability to passively align parallel to the Earth's geomagnetic field lines [294].

³already explained in Chapter 3.

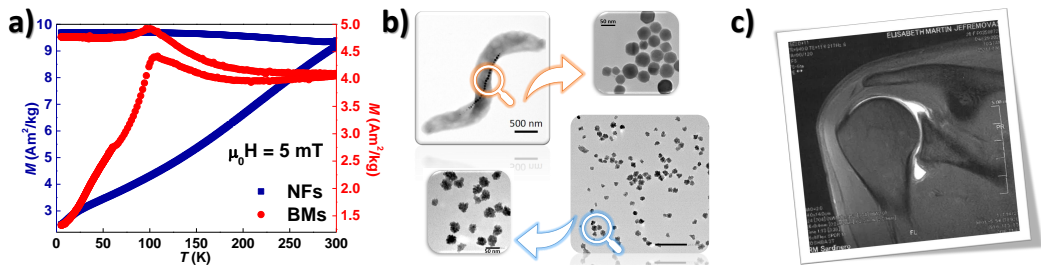


Figure 7.1: a) ZFC–FC measurements corresponding to Synomag NFs and bacterial magnetosome (BM). The Verwey transition is only retrieved for the Fe_3O_4 BMs. **b)** TEM images of MTB (inset zooms the magnetosomes) and Synomag Nanoflowers, where the cube–octahedral and multicore structure for each of them can be inspected. **c)** Contrast magnetic resonance imaging of my left shoulder. The use of Gd^{3+} as contrast agent was mandatory to observe the labrum (highlighted), the cup–shaped rim of cartilage which lines and reinforces the ball–and–socket joint of the shoulder.

doping MTB with R elements came naturally. Indeed, this constitutes a very exciting and challenging approach, since there are nearly no reported works, to the best of our knowledge, accounting for the doping of MTB with R. We have only found a single study on the incorporation of Sm to *Magnetospirillum magneticum* strain RSS-1, obtaining core/shell magnetosomes composed of magnetite in the core and samarium oxide at the shell [123]. Besides, it should be kept in mind the fact that high doses of R can be toxic for bacteria, which means that either their growing process may be arrested in the presence of R elements⁴, or, even if they achieve to grown, it is also possible that the R^{3+} ions would not be incorporated into the magnetosome structure. Among the different Rare Earth elements, in this work, we have selected the ones with the greatest de Gennes factor, **Gd and Tb**⁵, which have also evidenced amazing biomedical applications, mainly connected to **magnetic resonance imaging, MRI (Gd^{3+} [301]⁶) and fluorescent biomarker (Tb^{3+} [302])**. Along this Chapter, a detailed explanation of how the magnetic properties are altered by the R incorporation in the magnetosome structure will be provided.

Bearing this in mind, this chapter will describe the results and interpretation of two iron oxide nanoparticle ensembles of similar sizes, $\langle D \rangle \sim 40\text{--}45$ nm: Synomag maghemite nanoflowers (NF) and bacterial magnetosome (BMs), both undoped and Rare–Earth (Gd^{3+} and Tb^{3+}) doped. As it has already been indicated in

⁴this is why we had to determine the MICs, see Fig. 3.3 included in Chapter 3.

⁵see Chapter 4.

⁶see in Fig. 7.1c an actual example of the biomedical use of Gd^{3+} .

Chapter 3, the majority of the measurements have been performed by keeping intracellular the magnetosomes (*i.e.*, within the bacteria). We decided to proceed this way in order to take advantage from the bacteria body, that acts as a protection against oxidation. This shield, together with the magnetosome membrane itself, ensures the chemical stability of the Fe_3O_4 phase. We will first introduce a structural characterisation, where XRD and XANES are discussed in great detail. For the latter XANES, we have also included a comparison between the magnetosomes kept intracellular (BMs) and extracellular (OMs), which is useful to detect possible alterations on the magnetosome composition. The next analysis concerns the magnetic properties of both NFs and BMs, where we have not only scrutinised the magnetic transitions of $\gamma\text{-Fe}_2\text{O}_3$ and Fe_3O_4 phases, but we have also undergone a deep study on the magnetic properties concerning undoped BMs, Gd^{3+} and Tb^{3+} -doped BMs. Finally, a comparison between the MHT performance of both Synomag NFs and undoped bacteria magnetosomes (OMs, for meaningful comparisons) will be discussed.

7.1 Structural characterisation

XRD and TEM are powerful tools to access the IONPs microstructure, while the analyses of XANES provides information on the chemical composition, as it has already been pointed out in Chapter 3. For the case of our IONPs, **XRD** will be used, on the one hand, to **differentiate between maghemite and magnetite phases** [303, 304, 305], and also, **to verify both the crystallinity of the IONP ensembles** (NFs, undoped and doped BMs) **and the possible existence of extra phases** [132]. Moreover, thanks to Rietveld refinements, quantitative information on mean crystallite size (connected to the NP size by eq. 3.5) and strain are gained. On the other hand, **TEM** provides information on **the shape and morphology of the MNPs**. Besides, statistics on several TEM images brings good **estimations on the mean NP size**. The chemical composition of the maghemite and magnetite phases can be checked by means of **XANES**, which has been used to inspect **the oxidation state** of each ensemble [40].

We will begin by introducing the XRD and TEM measurements. Figs. 7.2a–d include the X–Ray Diffraction patterns, together with the Rietveld refinements, corresponding to γ -Fe₂O₃ Synomag NFs (Fig. 7.2a), Fe₃O₄ undoped BMs (Fig. 7.2b), Gd[100:100] doped BMs (Fig. 7.2c) and Tb[10:100] doped BMs (Fig. 7.2d). The measurements corresponding to the BMs have been performed keeping the magnetosomes intracellular, within the bacteria, to avoid an eventual oxidation. It is worth mentioning the fact that we decided to perform XRD for the two doping proportions, [10:100] and [100:100], to verify whether a ten–times increased proportion of R³⁺–ion could modify the crystalline structure.

The Rietveld refinements performed on the **Synomag NFs** (Fig. 7.2a) are consistent with a **single phase of cubic *Fd-3m* space group**, with a lattice parameter $a = 8.3451(3)$ Å, and a **mean nanoparticle size** $\langle D \rangle_{\gamma\text{-Fe}_2\text{O}_3} = 50.0(4)$ **nm** for the whole MNP core. The calculations also provide information on the microstrain, where a very reduced $\eta = 0.93(1)\%$ has been obtained. This ensures a good degree of crystallinity. The Refinements were cycled until a convergence is reached, giving a Bragg factor $R_B = 3.6\%$. This is a very low value, that guarantees the reliability of the fittings. **All the XRD peaks are indexed with those corresponding solely to the γ -Fe₂O₃ phase** [306]. Therefore, we can rely on these MNPs ensemble is purely formed by maghemite. A TEM image of these Synomag NFs is included in the inset, where the multi–core structure of the nanoparticles can be observed. Here, these nanoparticles, labelled as nanoflowers, are formed by ~ 10 cores (*petals*) of around 10 nm each one.

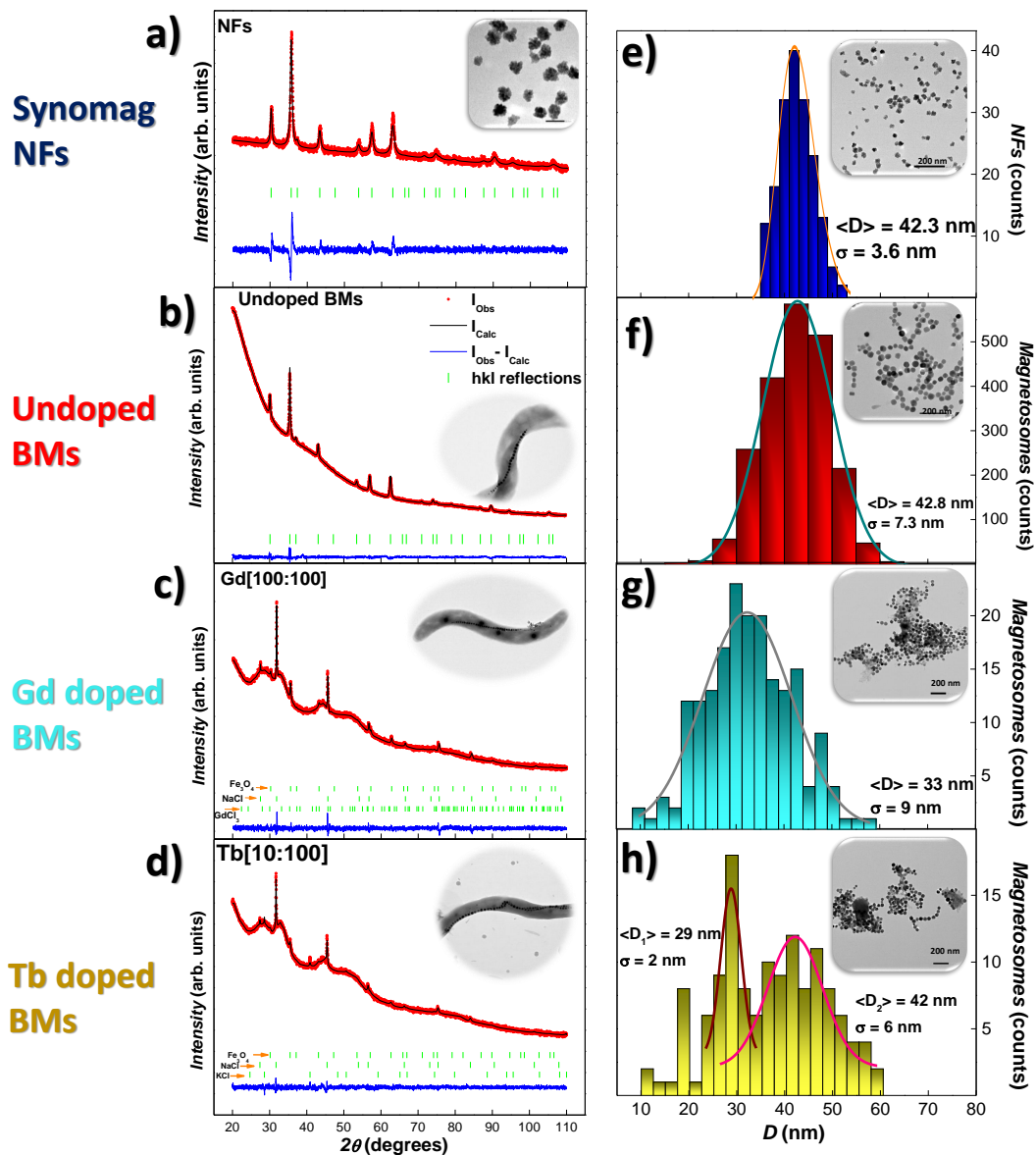


Figure 7.2: XRD patterns, together with the Rietveld refinements, **a)–d)**, and size distribution histograms, **e)–h)**, corresponding to **Synomag NFs**, **undoped**, **Gd[100:100]** and **Tb[10:100]** – doped bacteria, respectively. Insets show representative TEM images of the NFs (in **a)** and **e)** and the BMs arranged in chains (**b)–d)**) and extracted from the bacteria (**f)–h)**).

On the other hand, the XRD pattern, together with the Rietveld refinements performed on the **undoped bacteria magnetosomes** (intracellular) are shown in Fig. 7.2b. The results are consistent with a **single phase of cubic $Fd-3m$ structure**, with $a = 8.3985(2)$ Å, which corresponds to **magnetite** [307, 308], and agrees well with the ones reported for BMs [309]. No extra peaks apart from those corresponding to magnetite show up, which showcases the good crystallinity and the high chemical purity of the magnetosomes. The organic material surrounding the magnetite-composed magnetosomes give a contribution to the scattering intensity in the form of a background rise, which is specially noticeable at $2\theta < 50^\circ$. A **mean nano-crystallite size of $\langle D \rangle_{Fe_3O_4} = 45.1(3)$ nm** is obtained according to the Rietveld refinements. Here again, an even lower microstrain value of $\eta = 0.38(1)\%$ is found, which again, underlines the high crystallinity of the BMs. The low Bragg factor was, in this case, $R_B = 4.5\%$, which again supports our interpretations. The inset allows us to see an image of the magnetosomes arranged in chains within the bacteria. Each chain consists of ~ 20 magnetosomes, which is the usual number of magnetosomes for *Magnetospirillum gryphiswaldense* [32].

Going now to the **doped BMs**, Figs. 7.2c and d include the XRD characterisation for the Gd^{3+} and Tb^{3+} doped BMs, respectively. First of all, the (hkl) reflections corresponding to $Fd-3m$ Fe_3O_4 appear clearly in both patterns. This confirms the presence of **well-formed crystalline magnetite magnetosomes in both samples**. According to the Rietveld refinements, the Fe_3O_4 -content present on each sample is around 25% and 12 % for Gd and Tb-doped, respectively. In addition to the presence of magnetite, both XRD patterns show the presence of (hkl) reflections corresponding to NaCl (66% for Gd and 69% for Tb) and KCl (just for the Tb-doped, in 9%) phases. The Gd-doped also show a contribution coming from the $GdCl_3$ salts (in a proportion of 9%). These contributions come from the PBS medium employed for washing the harvested bacteria (NaCl and KCl), and from the $GdCl_3$ salts that remain, even after repeated washings, attached to the bacteria body, as it can be seen in the inset of Fig. 7.2c. The obtained lattice parameters corresponding to the magnetite Fe_3O_4 phase are $a = 8.360(3)$ Å for the Gd, and $a = 8.382(3)$ Å for the Tb-doped BMs. These values are slightly reduced ($\sim 0.4\%$) with respect to the one typically reported for bulk Fe_3O_4 ($a = 8.397$ Å) [308] and to the one (see above) of the undoped BMs. In principle, this slight contraction of the unit cell parameter could seem somehow contradictory, as one may expect it to increase owing to the larger ionic radius of Gd^{3+} ($r_{io} = 1.08$ Å) and Tb^{3+} ($r_{io} = 1.06$ Å [310]), in comparison to Fe^{3+} ($r_{io} = 0.63$ – 0.78 Å) or Fe^{2+} ($r_{io} = 0.92$ Å [311]) [312, 313]. However, similar reductions in the lattice

parameter have been reported in other R-doped Fe_3O_4 , argued in terms of strain [314] and/or the surface stress [309]. Rietveld refinements also give quantitative information on the mean crystallite size and microstrain, as we have already said. In this case, the obtained values of the **mean diameter $\langle D \rangle$ are found to be 34.8(2) nm for the Gd and 32.7(3) nm for Tb** doped BMs, together with microstrain values of $\eta = 1.92(9)\%$ (Gd) and $\eta = 3.9(1)\%$ (Tb). These low strain values indicate that the presence of both doping ions barely distorts the crystalline structure of the BMs, which is congruent with the literature about doped magnetosomes [33, 122, 315]. The Bragg factors were again satisfactory low (below 10% in both cases). Finally, as before, the inset in each figure includes a representative TEM image of the magnetosomes arranged in chains within the bacteria. Here, the number of magnetosomes per chain is found to be slightly greater (~ 27) with respect to the undoped ones. The reason for this will be given some lines below, when discussing the TEM results.

All in all, what is clear from the XRD characterisation is that: **(i)** the presence of **mixed and/or intermediate Fe-phases** in our IONPs is **discarded**, as Synomag NFs are purely $\gamma\text{-Fe}_2\text{O}_3$, whereas the BMs (undoped and doped) consist of a single phase of Fe_3O_4 ; and **(ii)** despite the R^{3+} incorporation, **the crystalline structure of the doped BMs is barely modified** by the presence of Gd and Tb ions *inside* the Fe_3O_4 lattice.

We will now focus on the analyses of the TEM measurements. Figs. 7.2e–h include the size distribution and representative TEM images of each ensemble of IONPs (insets). The main purpose of using this technique was to both determine the mean NP size, obtain information on the morphology and, in the case of the doped BMs, to also check possible alterations in magnetosome shape, size, and/or arrangement inside the bacteria due to the presence of R salts in the culture medium.

Accordingly, the size distribution histogram of the **NFs** presented in Fig. 7.2e is fitted to an average diameter $\langle D \rangle_{NF} = \mathbf{42.3\text{ nm}}$ and variance $\sigma = 3.6\text{ nm}$, according to a Log–Normal size distribution (orange line). This size is slightly smaller with respect to the one obtained by means of XRD, as expected [316]. The **flower–shape** of the MNPs can be inspected in the inset, where the size and morphology of the NFs is **homogeneous**. The situation concerning the BMs deserves more attention. First, the **undoped BMs** (Fig. 7.2f) display a Gaussian size distribution, centred at $\langle D \rangle_{MNP} = \mathbf{42.8\text{ nm}}$ with $\sigma = 7.3\text{ nm}$. By means

of just *visual* comparison, the **Gd[100:100] doped BMs** (Fig. 7.2g) point to a smaller value of mean diameter, as the size distribution is clearly shifted to lower values. By fitting the size distribution to a simple gaussian-function, a mean value of $\langle D \rangle$ **33 nm** with $\sigma = 9$ nm is found. The situation concerning **Tb [100:100]** (Fig. 7.2h) is, slightly different from the one of Gd[100:100], as **two size distributions** can be clearly distinguished, the main one centred at $\langle D \rangle =$ **42(6) nm**, and the smaller one, at $\langle D \rangle =$ **29(2) nm**. The presence of two size distributions is also typical in the case of undoped MTB, and it is related to the smaller size of the magnetosomes near both ends of the chains [33]. The situation concerning the [10:100] proportions (not shown) follows the same trend, as the same $\langle D \rangle$ values (~ 34 and 37 , respectively) are found. This reduction in the magnetosome size is not surprising, as it is well-known that the presence of additional dopant salts in the medium imposes a stress to the biomineralization process of the magnetotactic bacteria, leading to modifications in the shape, size, and arrangement of magnetosomes [34, 35, 122, 317, 318]. The magnetosomes display, for both undoped and doped situations, the expected **cube-octahedral shape**, being their size pretty uniform (see insets), except from those located at the end of the chains, whose growing process is to be completed [33, 317]. To end up with the comparison, it is worth recalling at this point the fact that the doped ensembles form longer chains with respect to the undoped BMs. In this way, since the doped BMs are smaller with respect to the undoped-ones, a reduction of the chain-net magnetic moment should follow, given the average diminution of the magnetic moment per magnetosome. In order to compensate this decrease, larger chains are formed.

Although XRD can give us crystallographic information about the different iron oxide phases present in our samples, **additional information on the electronic state is obtained by XANES**. As we have already commented in Chapter 3, XANES is a powerful technique that provides accurate data concerning the local environment and the oxidation state of the absorbing atoms, in our case, Fe [135]. Fig. 7.3 shows the Fe K-edge ($E_0 = 7112$ eV) XANES spectra corresponding to Fig. 7.3a the **NFs** and Fig. 7.3b to the BMs, both intracellular (**BMs**) and extracellular (**OMs**), together with reference patterns of γ -Fe₂O₃ [319] and Fe₃O₄, and the performed **Linear Combination Analyses** (LCA), according to eq. 3.13. These LCA allow us to quantify the content of each Fe-phase in the samples, as it has been shown in previous studies (e.g., [317]).

According to the XANES spectrum plotted in Fig. 7.3a, the edge position of the **NFs**, defined as the energy value at which the normalised absorption $\mu(E)$ reaches 0.5, is located at $E_0 \approx 7124$ eV, which is the **typical value of maghemite**, γ -

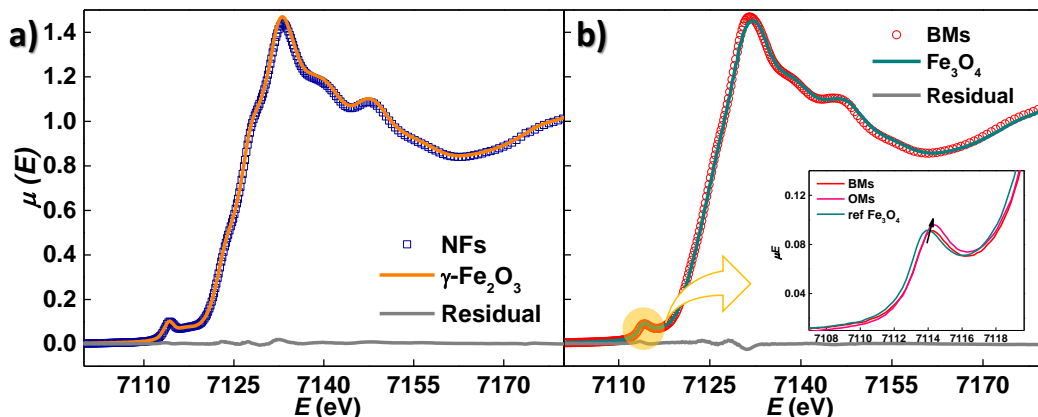


Figure 7.3: Normalised absorption $\mu(E)$ Fe K-edge XANES spectra corresponding to **a)** maghemite NFs and **b)** magnetite BMs. Reference patterns for γ - Fe_2O_3 (orange) and Fe_3O_4 (dark cyan) have been included for comparison purposes. The residual (gray) lines, that give account for the difference between the experimental and the calculated Linear Combination Analyses. Inset in **b)** zooms the pre-edge peak and provides also the experimental data for the OMs, which stands for the extracellular magnetosomes.

Fe_2O_3 [319, 320]. LCAs indicate a perfect match between the reference γ - Fe_2O_3 pattern and the experimental XAS data corresponding to the NFs. This allow us to **confirm the chemical purity of the NFs** that was pointed out by the XRD characterisation. On the other hand, XANES spectra corresponding to the **BMs** (Fig.7.3b) are left-shifted in energy with respect to the NFs (edge position $E_0 \approx 7122$ eV, i.e., $\Delta E_0 \approx 2$ eV). This indicates a lower Fe-oxidation state, which is expected, as magnetite combines both Fe^{2+} and Fe^{3+} , whereas for maghemite, only Fe^{3+} is present [135, 137]. Here, the **LCAs confirm the 100% magnetite-composition** of the magnetosomes, for both intracellular (BMs) and extracellular (OMs) cases. This allow us to unequivocally conclude that the NFs are fully composed of maghemite, whereas the BMs are fully composed of magnetite. A closer inspection to the pre-edge region (see inset in this Fig. 7.3b) allows us to detect a **tiny increased μE intensity in the case of the OMs** with respect to the BMs. This indicates a slightly **higher oxidation state for the magnetosomes** when they are extra-cellular. The fact of presenting a double membrane-shield (bacteria and magnetosomes' ones) rather than a single one (magnetosome) obviously isolates better the magnetite from air. In any case, the differences are minimal, yielding to a situation in which the **magnetite-phase is secured (stable) in both BMs and OMs forms**.

7.2 Magnetic properties

After determining the structural properties of the IONP ensembles, we have analysed their magnetic response by means of static $M_{DC}(T, \mu_0 H)$ and dynamic $\chi_{AC}(T, f, t)$ susceptibility. All the measurements were performed in whole bacteria (thus, BMs), where the magnetosomes arrange in chains, in order to minimise the effect of the inter-chain interactions [30, 34, 35].

When dealing with magnetic nanoparticles, it is important to know whether the sizes of these entities are on the single-domain or multi-domain regions. As we have already mentioned in the theoretical chapter, providing a preliminary set point of this state is important so as not to miss the interpretation of data, especially, those concerning $M_{DC}(T, \mu_0 H)$. To begin with, the **critical size for Fe-oxide nanoparticles to constitute a mono-domain ensemble** can be estimated according to [45] as:

$$r_c \approx 9 \frac{(AK_u)^{1/2}}{\mu_0 M_s^2} \quad (7.1)$$

which results in a value of $r_c \sim 45$ nm for maghemite and $r_c \sim 64$ nm for magnetite, in good agreement with the reported ones [321, 322]. **Therefore, both the NFs and the BMs are expected to be single-domain nano-ensembles.**

The point would now consist on determining the *blocking* temperature for both MNPs, as single-domain MNPs can be either magnetically *blocked* or *Superparamagnetic*. Each regime displays a different spin dynamics, which results in contrasting features. Values for the blocking temperature of each IONP ensemble can be estimated according to⁷:

$$T_B \approx \frac{KV}{25k_B} \quad (7.2)$$

This results in a value of $T_B \approx 277$ (NFs) and 393 K (BMs) for the case of our ensembles. According to the latter values, the **NFs** might be, in principle, **SPM** at $T = 300$ K (RT), whereas the **BMs would be magnetically blocked in the whole measuring range.**

⁷suitable only for DC magnetisation, where the measuring time is taken as 100 s.

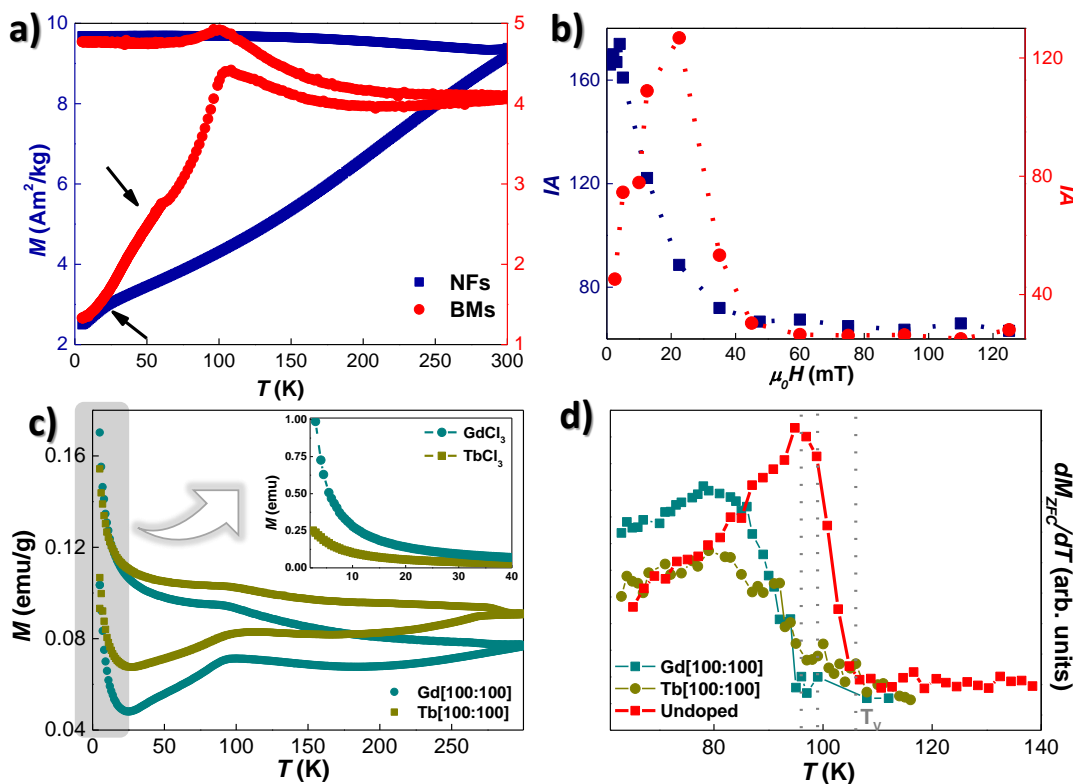


Figure 7.4: Static $M_{DC}(T)$ ZFC-FC curves, measured under $\mu_0 H = 5$ mT applied field of **a)** Synomag $\gamma\text{-Fe}_2\text{O}_3$ NFs (blue circles) and undoped Fe_3O_4 , (red squares) and **c)** Gd[100:100] (dark cyan) and Tb[100:100] (dark yellow) BMs. **b)** evolution of the I/A parameter vs. the magnetic applied field $\mu_0 H$ for Synomag NFs and undoped BMs. Inset in **c)** displays the ZFC-FC signal of GdCl_3 and TbCl_3 salts, measured under $\mu_0 H$ 100 mT where the typical fingerprint of PM is shown. The derivative of the ZFC branch for the BMs is shown in **d)**, as it eases the definition of the T_V , marked with gray dotted arrows.

Beginning with the static M_{DC} characterisation, we have measured, first of all, the ZFC–FC $M(\mu_0 H)$ curves at several applied fields to inspect the field–dependence of the magnetic transitions present in every IONPs. As an example, we are providing in Fig. 7.4 these ZFC–FC curves measured at $\mu_0 H = 5$ mT. We will start by comparing the magnetic response of the **maghemite NFs** and the **magnetite undoped BMs**, which can be inspected in Fig. 7.4a. There, it can be seen that already at $T = 300$ K, the **NFs** display magnetic irreversibility, as the ZFC and FC branches are separated in the whole temperature range. This is congruent with a **Superparamagnetic** state [60, 183], which is non–surprising for these NFs, according to our previous estimations (see above) and, especially, with [28], where the magnetic measurements at $T > 300$ K were measured as well. On the other hand, the situation concerning the **BMs** (red circles) is slightly different, despite the fact that the ZFC–FC branches appear again split in the whole temperature range. These BMs ensembles are **magnetically blocked**, instead of constitute a SPM state. **The same situation holds for the doped BMs** (Fig. 7.4c). Afterwards, the $M(\mu_0 H)$ measurements will confirm these different behaviours (SPM and blocking), as coercitivity and remanence hysteresis magnitudes will only be retrieved for the BMs. The difference between a SPM or a blocked ensemble of single–domain MNPs lies on their anisotropy energy barrier ($E_{\text{barrier}} \propto K \cdot V$). Accordingly, **the magnetisation state of a SPM nanoparticle is protected by a weak energy barrier**, which implies that the thermal energy perturbs easily this state (by flipping coherently the spins within the nanoparticles). On the other hand, the **magnetisation corresponding to a blocked state is robust**, meaning that it is **protected by a large energy barrier** that prevents the thermal agitation to destroy the collective spin up/down. As a result, **the BMs are revealing to constitute an ensemble displaying greater anisotropy with respect to the NFs**, given their similar V . Moreover, the value of the magnetisation measured at $T = 300$ K in the BMs ($M \approx 4.2$ Am²/kg) is almost half the value corresponding to the NFs ($M \approx 9.8$ Am²/kg), which reinforces again the higher K for the former. Finally, in order to attain more information concerning the *robustness* of the magnetic interactions among the moments (which are intimately connected to the effective anisotropy of the MNPs, K_{eff}), we have studied the dependence of the Irreversibility Area parameter (IA) with respect to the external applied field $\mu_0 H$ in the static regime. This K_{eff} is of fundamental interest to the biomedical applications, as the K_{eff} plays a key role in the heating efficiency of MNPs for magnetic hyperthermia purposes [323, 324]. As it can be seen in Fig. 7.4b, while BMs attain their maximum $IA = 174$ at $\mu_0 H = 12.5$ mT, NFs display a maximum $IA = 127$ at only $\mu_0 H = 4$ mT, *ie.*, one third of the field required to overcome the BMs' E_{barrier} . **This result confirms the greater K_{eff} for the**

BM in comparison to NFs.

As we have already said, the ZFC–FC protocols allow us to gain information on the magnetic transitions. By inspecting in closer detail the ZFC branch of the NFs, a **low–temperature hump**, located at $T_k \sim 50$ K, can be seen (marked by an arrow). This hump, even if it is weak, shows a field dependence, as it is not detectable for $\mu_0 H \geq 12.5$ mT. Very few could be added at this point to discuss about this feature, except from the fact that the $T_k(\mu_0 H)$ displacement failed to scale to a de Almeida–line (eq. 2.11) either with $m = 2/3$ (Ising–like SG) and $m = 2$ (Heisenberg–like SG). Later on, the dynamic χ_{AC} susceptibility will bring more light to this matter. On the other hand, the BMs evidence the expected **Verwey transition**, characteristic of Fe_3O_4 , which is marked by a sudden drop of the magnetisation with decreasing T . The T_V value is found at $T_V = 106, 95$ and **99 K for the undoped, Gd[100:100], and Tb[100:100] BMs, respectively**. These values can be seen in more detail by plotting the derivatives of the ZFC, displayed in Fig. 7.4d. The value corresponding to the undoped BMs agrees well with those previously reported for magnetosomes [137, 325] and it is below the $T_V \sim 120$ K corresponding to bulk magnetite⁸[41]. The fact that the T_V transition, that depends very strongly on the crystallinity and stoichiometry [33, 327, 328], **appears so clear for the doped ensembles is relevant**, and it reveals that **the R^{3+} incorporation to the magnetosomes is not distorting strongly the magnetite structure** [41]. Otherwise, this transition would be smeared or, even, almost wiped out, as it is the case of the Co–doped BMs [34].

A second transition is also observed for the BMs in the low–temperature range as a broad hump. That feature is more noticeable in the ZFC branch, and takes place in the temperature range $25 \lesssim T_f \lesssim 40$ K, yet it is more subtle than the one of the NFs. This additional transition is only visible for the undoped sample, due to the fact that a strong paramagnetic contribution appears $T \lesssim 25$ K in the doped ensembles (see Fig. 7.4c). This PM signal is related to the presence of the bacterioferritin and the Gd and Tb salts attached to the bacterial body, as can be seen in the ZFC–FC curves measured for these salts (see inset). Again, this transition, which has been generally attributed to the ordering of electron spins in magnetite [329, 330, 331], might deserve more attention. Again, the dynamic χ_{AC} characterisation will seed more light to this issue.

⁸needless to say, this Verwey transition is not present in the NFs, as expected for a pure maghemite system [28, 326].

We will now scrutinise the magnetic behaviour of the IONP ensembles by fixing the T at a constant value and varying the applied magnetic field. Figs. 7.5a–c include the M vs. $\mu_0 H$ loops measured at $T = 300$ K (RT) corresponding to: maghemite NFs (blue color) and magnetite undoped (red color) (Fig. 7.5a), Gd[100:100] (Fig. 7.5b), and Tb[100:100] (Fig. 7.5c) BMs. Beginning with Fig. 7.5a, **the SPM(blocked) state of the NFs(BMs) appears clear**. While a coercive field $H_C = 20$ mT and remanent magnetisation $M_r/M_s \sim 0.45$ are measured for the BMs, no trace for these hysteresis parameters can be observed for the NFs. This should, in principle, back up the SPM nature of these maghemite IONPs. Nevertheless, the data fitting to a Langevin function⁹ of the SPM-presumed NFs fails. Given the proximity of both measuring and blocking temperatures, it is very possible that some of the **Nanoflowers** could be blocked, with other ones are in the SPM regime. Furthermore, the $\chi_{AC}(T, f)$ characterisation (see below) will reveal the presence of **three hierarchical magnetic orders**, being the transition temperature of the second located at $T \sim 280$ K. This results in a wide range of time scales, which have already evidenced to be problematic in the definition of SPM systems macroscopically via the closed Langevin-type magnetisation curve [59]. The fact that the thermal equilibrium is often not achievable gives account for this happening.

In which concerns the **doped BMs**, Figs. 7.5b and c display the M vs. $\mu_0 H$ loops corresponding to Gd[100:100] and to Tb[100:100], respectively, together with the simulated $M(\mu_0 H)$ loops. These simulations are based on the Stoner–Wohlfarth model [332] with the modifications addressed in [32, 35]. Very briefly, this model considers each magnetosome chain as a collection of independent single domain nanoparticles, that are thermally stable. Inter-particle dipolar interactions occurring between the nearest magnetosome neighbours impose additional anisotropy contribution, whereas the chain–chain interactions are neglected. The equilibrium orientation of each magnetic dipole is calculated by minimising the single dipole energy density, which is formed by the sum of a magnetocrystalline term, a uniaxial one and a latter Zeeman term. Further details on the Stoner–Wohlfarth model are included in Append B. The good agreement between the calculated and the experimental profiles is clearly observed. These hysteresis loops evidence again the **magnetically blocked** state of the single-domain BMs, as non-negligible values for H_C and M_r are found. Particularly, $H_C = 18.3(1)$ and $15.8(1)$ mT, and $M_r/M_s = 0.39$ and 0.44 for the Gd and Tb-doped, respectively. Those values evidence slight deviations from the ones obtained for the undoped BMs, as it was

⁹ $M/M_{sat} = \mathcal{L}(a)$, being $a = \mu B/k_B T$.

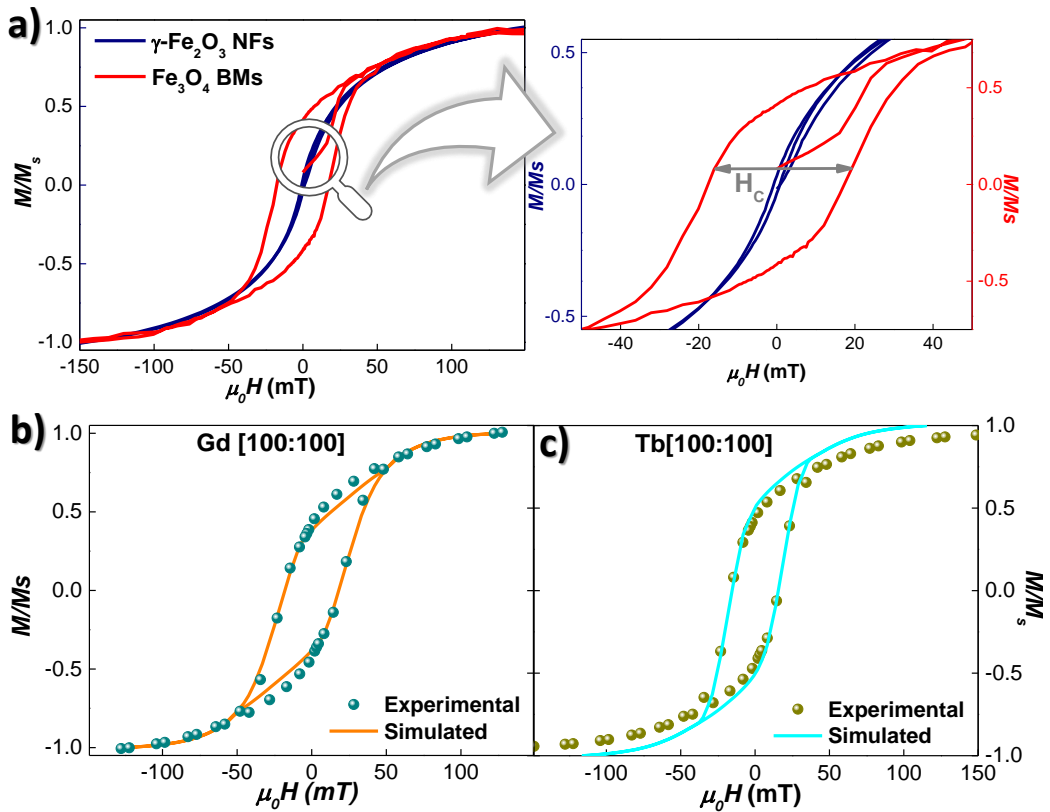


Figure 7.5: Static $M_{DC}(\mu_0H)$ hysteresis loops measured at $T = 300$ K for **a)** Synomag $\gamma\text{-Fe}_2\text{O}_3$ NFs (blue) and Fe_3O_4 BMs (red), **b)** Gd[100:100], and **c)** Tb[100:100]. Inset in **a)** zooms the central region, where coercivity is only retrieved for the BM ensembles. **b)** and **c)** include the simulated profiles with $K_C = 11$ and -12 , and $K_u = 12$ and 10 kJ/m³, respectively.

the case of the Mn or Co-doped BMs [34, 35]. The situation becomes much more interesting when the temperature is decreased, **where the R-doping effectively changes the anisotropy of the magnetosomes** and clear changes in the H_C and M_r trends are recovered. To inspect this in closer detail, Figs. 7.6a and b depict the evolution of these magnitudes with the temperature. Figs. 7.6c and d show the resulting K_C and K_u obtained thanks to the simulation of the measured hysteresis parameters.

Figs. 7.6a and b compare the evolution of the ΔH_C and the $\Delta M_r/M_s$ vs. T , respectively. The Δ symbol represents the difference between the measurements performed after a cooling process under an applied field of 1 T (FC) and without applied magnetic field (ZFC). Despite the fact that the 3 ensembles (**undoped**, **Gd[100:100]** and **Tb[100:100]**) behave in a similar way at RT, **the trend with**

decreasing T is clearly altered. In this way, especially for $T \lesssim T_V$, the **FC and ZFC loops of the doped/undoped BMs no longer overlap.** In this way, the undoped BMs show three clearly-differentiated regions: **(i)** above T_V , **(ii)** between T_V and T_f , and **(iii)** below T_f . The finding of these three differentiated regions indicate an evolution in the anisotropy of the magnetosomes: First, at T_V , the structure undergoes a transformation from the cubic system, with the chain easy axis pointing along the [111] direction, to a monoclinic arrangement, being the chain axis pointing now along the [100] direction [325]. Then, at T_f , the anisotropy changes again, probably as a consequence of a structural change from monoclinic structure to a lower symmetry arrangement (triclinic structure) [27, 333]. **The transformation of the structural arrangement alters the magnetocrystalline anisotropy term** (thus, the anisotropy barriers), and could also lead to the outburst of frustrating interactions that may develop the SG-like behaviour. It is also worth noting that the evolution of the doped BMs in the region between T_f and T_V gets much smoother in comparison, being even the *hump* observed in the undoped BMs almost wiped out, a fact that agrees well with the *smoothed Verwey* transition shown in the $M(T)$ characterisation. Besides, the values of H_C and M_r for the doped BMs are slightly smaller with respect to the ones of the undoped BMs at this low-temperature side. **This reveals a reduction of the anisotropy in the low-temperature region concerning the doped samples.**

These results agree very well with the ones recently published for Mn-doped BMs [35]. More precisely, they are very alike to the behaviour of the Mn[480:100] sample. Both Gd and Tb-doped behave in a very similar fashion, as it can be seen in the ΔH_C and/or $\Delta M_r/M_s$ evolution (see Fig. 7.6a and b). The situation concerning the NFs is much less interesting. The inset in each Fig. 7.6a and b depicts the evolution of the $\mu_0 H_C$ and M_r with the temperature after a cooling process with no applied field. Both magnitudes increase linearly, according to the progressive increase of the blocked entities. The slope of this trend gets more acute in the low-temperature region ($T_k \lesssim 50$ K), a fact that can be understood in terms of the incipient nanopetal-nanoflower correlations that are going to be revealed thanks to the dynamic χ_{AC} measurements.

At this point, it is clear that carrying out magnetic simulations of the $M(\mu_0 H)$ loops measured at different T values would be helpful to disclose the specific changes that are taking place in the intrinsic magnetic properties of Gd[100:100] and Tb[100:100] samples. As it has already been explained above, we have employed a modified Stoner-Wohlfarth approach, as it is common practice [32, 35].

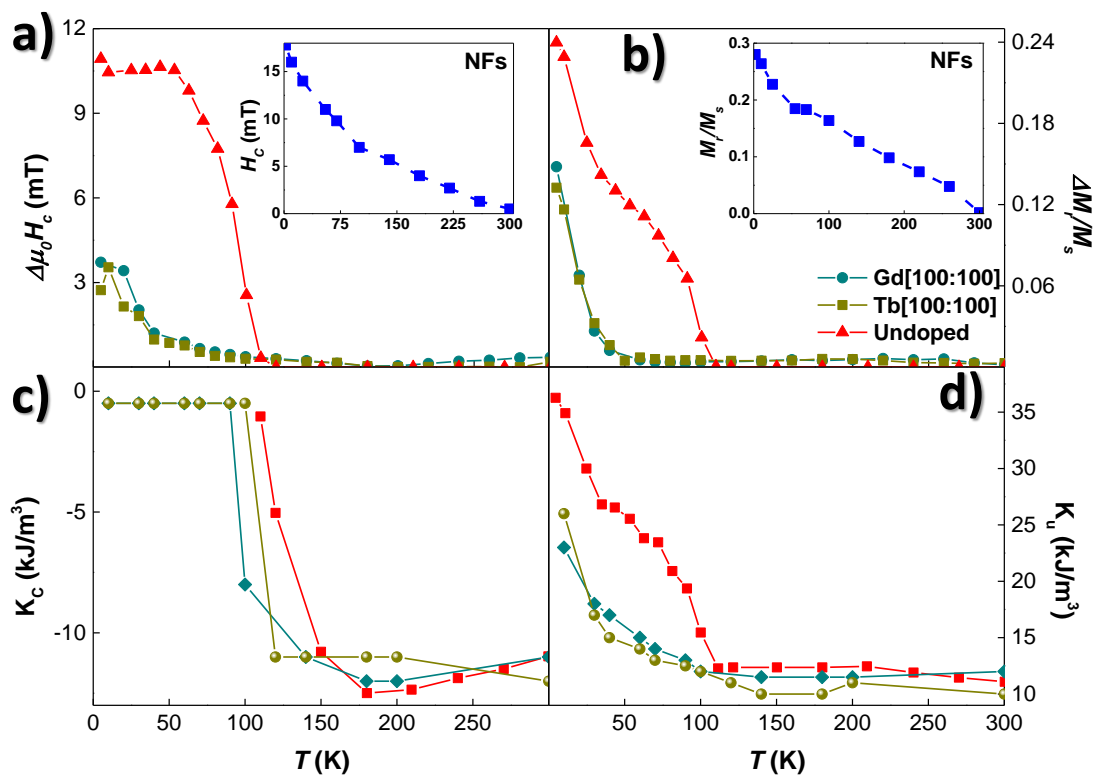


Figure 7.6: Temperature dependence of the a) $\Delta\mu_0 H_c$, b) M_r/M_s , c) K_c , and d) K_u for the Gd[100:100] (dark cyan), Tb[100:100] (dark yellow) and undoped (red) BMs. Insets in a) and b) give account for the NFs behaviour.

Figs. 7.6c and d display the thermal evolution of each anisotropy term for the **undoped (red)**, **Gd[100:100] (dark cyan)** and **Tb[100:100] (dark yellow)** BMs, obtained from the simulation of the $M(H)$ loops displayed in Fig. 7.5.

Beginning with the K_C term, Fig. 7.6c showcases that **the three BM ensembles showcase a very similar value at RT**, -11.0 kJ/m^3 for the undoped and Gd-doped, and -12.0 kJ/m^3 for the Tb-doped. These values are very close to the one corresponding to bulk magnetite, -10.8 kJ/m^3 [1, 32, 35]. Nevertheless, as the temperature is lowered, the absolute value of this term slightly increases for the undoped and Gd [100:100] samples, whereas the Tb [100:100]—one slightly decreases. Nevertheless, these modifications are really tiny, remaining this term $K_C \sim (-11)\text{--}(-12) \text{ kJ/m}^3$.

Notwithstanding, **the dramatic drop in the $|K_C|$ value retrieved in the undoped sample is displaced towards lower T in the doped ones**. This way, whereas it got null already from $T \sim 110 \text{ K}$ for the undoped BMs, this happened from $T \sim 90$ (Gd) and 100 (Tb). Given that the disappearance of the K_C contribution is triggered by the loss of the magnetocrystalline anisotropy driven by the structural change below T_V [34, 35, 41], the left-shift found in the doped BMs may be indicating that **the incorporation of R^{3+} ions into the magnetite structure** modifies the crystalline structure, **altering the Verwey transition**. The particular differences between Gd and Tb-doped BMs could be associated to a different incorporation of the Gd^{3+} and Tb^{3+} to the magnetosome structure.

Now we turn to the K_u term. Fig. 7.6d reflects very well the situation that has been explained for the M_r/M_s vs. T evolution. It turns out that K_u remains at an almost constant value of ~ 12 (undoped), 11.5 (Gd) and 10 (Tb) kJ/m^3 , down to T_V . As long as this term is mainly connected to the shape anisotropy and dipolar interactions, the differences between the K_u values (especially for the case of Tb) could be due to the **divergences between size distribution and/or morphology of the BMs** (see TEM results). Below T_V , a dramatic increase, up to 37 kJ/m^3 , is retrieved for the undoped BMs. Nevertheless, the K_u for the doped BMs rises at a slower pace, being the onset no so well-defined as for the case of the undoped ones. This is more noticeable below 50 K . At $T = 10 \text{ K}$; the doped BMs only achieve a maximum $K_u = 23$ and 26 kJ/m^3 , respectively. These values are very similar to the ones of Mn[480:100] [35].

All these findings point undoubtedly to an **actual modification of both magnetocrystalline and uniaxial anisotropy terms in the R-doped BMs**. Changes

above T_V may be triggered by the modifications of size and/or shape of the doped BMs compared to the pure ones. The situation concerning $T < T_V$ points to a scenario where the substitution of Fe^{3+} -ions by Gd^{3+} and Tb^{3+} -ones does effectively **modify the monoclinic crystalline arrangement**, which outcomes in a modification of the features associated with the T_V . This modification for magnetite doped with Gd and Tb appears as a relevant result that should lead to a more intense attention by the scientific community.

7.2.a Dynamic Magnetic Susceptibility

The main aim of the dynamic $\chi_{AC}(T, f, t)$ measurements was to access more information on the **spin dynamics of the low-temperature hump** that was observed in the $M_{DC}(T)$ ZFC-FC curves. This feature becomes more noticeable if a very low-field is applied, as it is the case of $\chi_{AC}(T)$ (see Fig. 7.7). The existence of **dissipation** connected to peaks in the in-phase component indicates the presence of **magnetically-disordered phases**, as it has been already shown along this work in the previous chapters. Accordingly, the inspection of the out-of-phase component of **Synomag NFs** in that Fig. 7.7 (left-side) shows **a clear peak located at $T \approx 40$ K**. This fingerprint of a disorder state has been a matter of debate in the last decades for both ensembles (magnetite and maghemite) [334, 335, 336], yet no unambiguous conclusions have been established. All the literature agrees with the occurrence of a broadening located in the range between $30 \lesssim T \lesssim 60$ K, but, whereas some studies claim for a Spin Glass dynamics, others point to a less-interacting disorder transition. In our case, provided the temperature range, this transition could be studied at the Synomag NFs, but on the magnetite-side, only the undoped bacteria could meet the criteria, as at the doped-ones, the signal coming from the PM R-salts got too intense at this low-temperature side, masking the signal stemming from the magnetosomes themselves.

Fig. 7.7 shows the in-phase $\chi'(T, f)$ (top) and out-of-phase $\chi''(T, f)$ (bottom) components for Synomag $\gamma\text{-Fe}_2\text{O}_3$ NFs (Figs. 7.7a and b) and undoped Fe_3O_4 BMs (Figs. 7.7c and d). The Verwey transition, T_V , marked by a sudden drop of the magnetisation with decreasing T , can be clearly seen in the BMs, whilst this transition is not present in the NFs, as expected for a pure maghemite system [28, 326]. The temperature for this T_V is determined to be $T_V \approx 106$ K (agreeing the M_{DC}), a value that agrees well with the reported for magnetosomes [137, 325], below $T_V \sim 120$ K for bulk magnetite [41]. The small drop in the $\chi'(T, f)$ observed at $T \geq T_k$ in Fig. 7.7c has already been argued in terms of particles below their

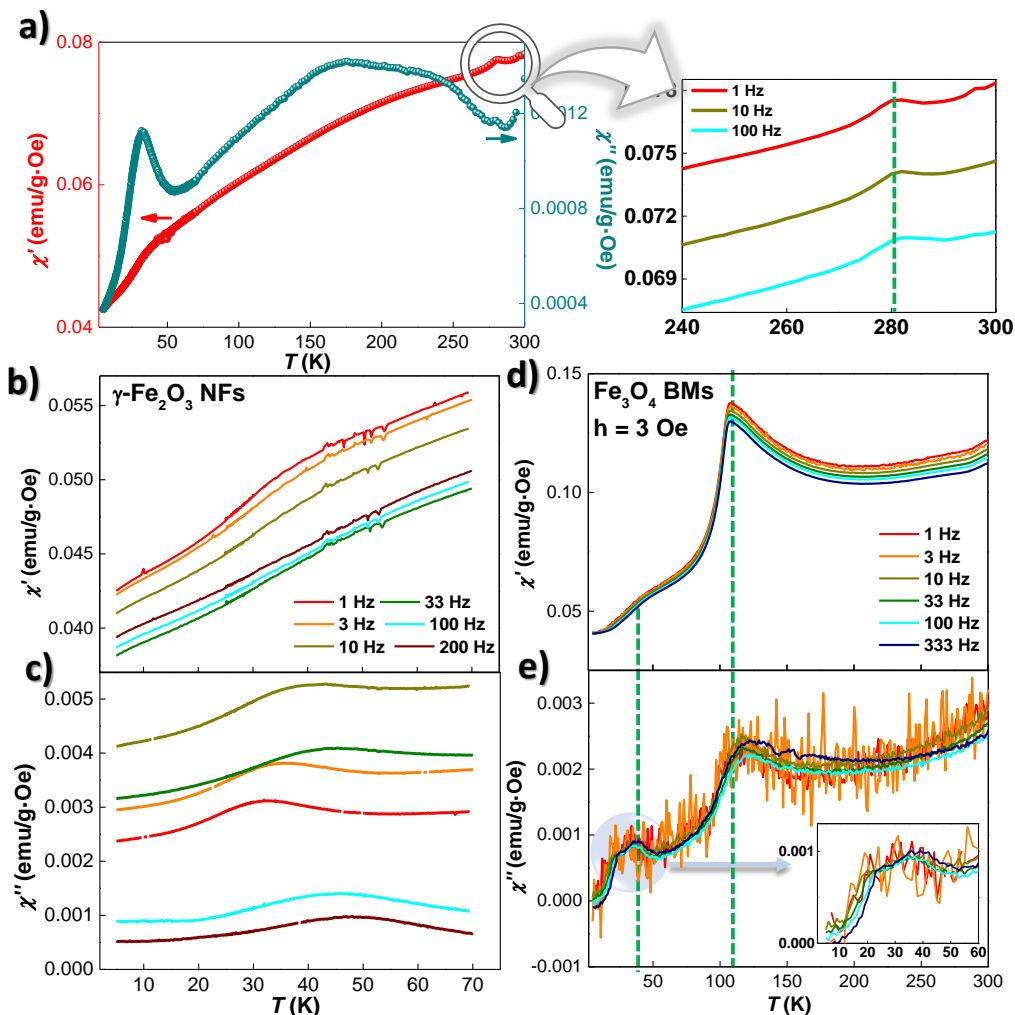


Figure 7.7: **a)** $\chi'(T)$ and $\chi''(T)$ components, measured at $f = 1$ Hz in the range T between 5 and 300 K, for Synomag NFs. The inset shows the extra high-temperature peak observed in the $\chi'(T)$, that holds for every measured frequency f (we have just included three of them for clarity purposes). **b)** and **c)** showcase the in-phase $\chi'(T)$ and out-of-phase $\chi''(T)$ components, respectively, measured in the low-temperature range ($T < 80$ K) at oscillating field $h = 0.313$ mT, for these γ - Fe_2O_3 MNPs. **d)** and **e)** display both $\chi'(T)$ and $\chi''(T)$ components for the Fe_3O_4 BM (within the bacteria), measured with $h = 0.1$ mT within the temperature range 5–300 K. The inset in **e)** zooms the low-temperature region ($T < 60$ K), where there is an extra dissipation. The occurrence, for both NFs and BMs, of dissipation in the low temperature region reveals the existence of magnetically-disordered phases.

critical Superparamagnetic (SPM) size [33]. Going now to the low-temperature side, the occurrence of a **hump for the in-phase component** can be detected for both IONP ensembles. This feature takes place at $T_k \approx \mathbf{60\ K\ for\ the\ NFs}$ and $T_f \approx \mathbf{35\ K\ for\ the\ BMs}$.

Although the occurrence of a hump is already observed in the $\chi'(T, f)$, this *kink* gets more noticeable in the out-of-phase component $\chi''(T, f)$. There are reports in the literature giving account for this fingerprint, *e.g.*, in 20 nm Fe- γ -Fe₂O₃ 20 nm NPs [334], or in magnetite, both bulk [337, 338, 339] and NP ensembles [335, 340]. Nevertheless, the spin dynamics behind this transition has been argued differently for both IONP ensembles. The most common scenario for magnetite relates this hump to a Super Spin Glass (SSG) freezing dynamics, caused by either the freezing of conduction electrons, or the rearrangement of electrons within domain walls [27, 41, 333], the situation concerning maghemite gets even more cumbersome, and it has only been reported to occur at the mesoscopic scale. Whilst the occurrence of a low-temperature hump is unambiguous, indicating the existence of distinct temperature-activated behaviours depending on the NP size and geometry [341, 342], the ultimate reason for this to happen is unclear and, even at some points, contradictory. In this sense, a research work claimed a SG-like phase for this transition [343], a recent investigation point to a non-interacting disorder-like transition for NF-shape maghemite [336].

In order to shed more light to this complex issue, we have undergone a complete analyses of the spin dynamics in both ensembles of IONPs. First, we have plot the Cole-Cole χ'' vs. χ' dependence at several temperatures close to the hump in Figs. 7.8a and b. As it has already been mentioned in the previous chapter, these representations are a powerful tool to obtain information about the NP size distribution and anisotropy [266, 267]. In a further step, we have fitted the $T_k(T_f)$ vs. f dependency by using different scaling models. The ones that fit the best were a non-interacting Néel-Arrhenius relaxation (eq. 2.1) and a critical power-law scaling (eq. 2.9), respectively. These fittings are represented in Figs. 7.8c and d. Additionally, we have obtained the δ -shift parameter. All the obtained values for these fits are inserted in Table 7.1. To end up with, we have performed ageing and memory effect measurements to follow whether the interactions among the magnetic moments are large enough to settle a collective frustrated disorder state.

Before moving forward to the subtleties concerning the low-temperature region, it is very worth mentioning the occurrence of a high-temperature bump in the in-phase component of the **NFs** (see left panel in Fig. 7.7). This hump, zoomed in

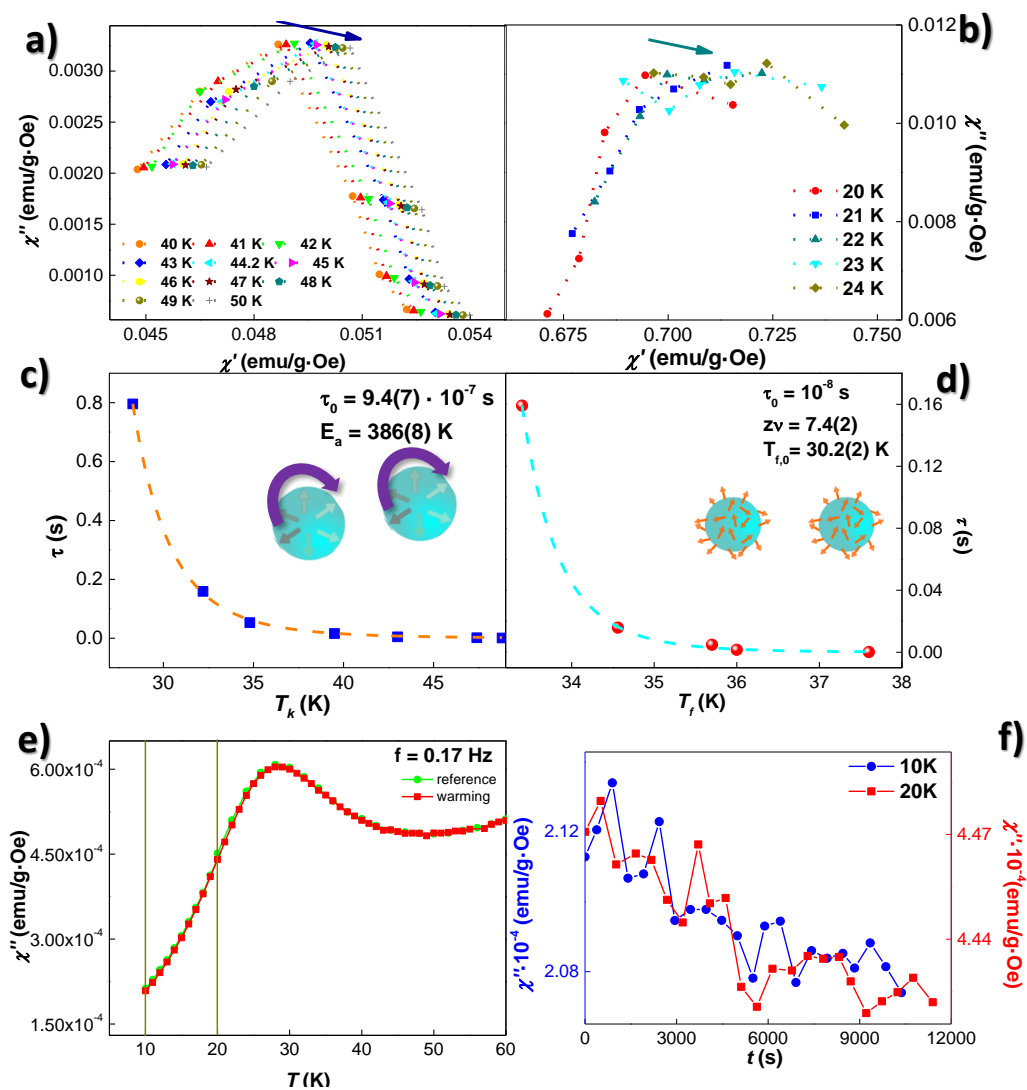


Figure 7.8: Cole–Cole diagrams for Synomag maghemite NFs (a) and magnetite BMs (b) at several temperatures nearby the low temperature hump, T_k and T_f . c) Néel–Brown (Arrhenius law) and d) critical slowing–down scaling for the NFs and the BMs, respectively, from which the SPM(CSG) behaviours can be inferred. e) and f) depict the memory effect and ageing measurements, respectively, performed in the Synomag NFs. No trace for any of these effects can be observed.

the inset, is located at $T_h \approx 280 \text{ K}$, and brings in more information about the structure of the NFs. Accordingly, given that this peak also carries dissipation, **an extra magnetic disorder-like transition is taking place**. At first, one may think of a two-step blocking mechanism to be beneath this double feature, one taking place at T_k , and the second, at this T_h , just in the same sense as it has already been reported in other magnetically-disordered NPs¹⁰ [37, 202, 334]. There, the freezing process for the magnetic moments located at the surface (lower T) and at the core (higher T) were decoupled, leading thus to two blocking/freezing processes. Nonetheless, the situation concerning our NFs is different, as the separation between both T_k and T_h is too great. Furthermore, the structure of the NFs, where several crystalline entities coexist, may be the shed of a **hierarchical magnetic structure [29], where three different correlation lengths coexist**. These are:

- i. the correlation length that builds up the ferrimagnetic order within each nanocrystallite ($\ell \lesssim 10 \text{ nm}$).
- ii. the correlation length that correlates the nanocrystallites ($\langle D \rangle \sim 10 \text{ nm}$, see TEM) to trigger the superferromagnetic coupling of petals (cores), forming nanoflowers ($\ell \sim 20\text{--}40 \text{ nm}$).
- iii. the correlation length that correlates the different nanoflowers to give rise to a supraferromagnetic arrangement ($\ell > 50 \text{ nm}$).

Consequently, the hump observed at 280 K can be mainly related the second level, i.e., the one where the individual nano-petals get correlated, building up the Nanoflower. The presence of strong interactions among the neighbouring nanocrystals within the NFs observed thanks to SANS [28] agrees with this scenario. It is also worth mentioning the fact that the out-of-phase component gets non-zero values all over the measured range, indicating a broad distribution of relaxation times.

Once the $\chi'(T, f)$ and $\chi''(T, f)$ curves have been discussed, we will focus now on the different analyses performed in the vicinity of the low T_k (T_f) transitions. We will begin with the Cole–Cole diagrams. Figs. 7.8a and b depict the χ'' vs. χ' dependence measured at different temperatures for the NFs and the BMs, respectively. The occurrence of a maximum is clear for both ensembles, which shows a positive frequency shift with the temperature. Nevertheless, the right-shift for the NFs is $\sim 1.9 \times 10^{-4} \text{ emu/g}\cdot\text{Oe}\cdot\text{K}$, whereas the one for the BMs is more drastic, \sim

¹⁰as it was the case of the GdCu₂ SSG MNPs shown in Chapter 4.

72×10^{-4} emu/g·Oe·K, *ie.*, almost 40–times greater. This indicates that the **BMs display a narrower distribution of relaxation times with respect to the NFs** [50]. Given the fact that the BMs display a broader size–distribution than the one for the NFs (see TEM measurements), this fact should be necessarily connected to the magnetic state itself. This way, whereas the SPM–like state of the NFs results in different entities that get *blocked* almost independently, the BMs would constitute a much more interacting ensemble, where the different entities are correlated and get frozen as a whole.

Second, regarding the shape of the Cole–Cole plots, we can see a striking difference between the NFs and the BMs. While the former display a relatively symmetric peak–shape, the curves for the latter are flattened and asymmetric. The latter feature is indicative of a polydisperse particle size distribution [60], which has been evidenced thanks to TEM measurements. Nonetheless, the peak shape of the NFs is much more congruent with the expected one for a monodisperse ensemble of SPM NPs, where a perfect semi–circle is retrieved [60]. This statement could be verified by applying intermediate frequencies between 1–3 and 3–10 Hz, as the number of points close to the maximum are just a few. Finally, the relative breadth of the peak can be obtained as $\sigma_{rel} = FWHM/\chi''_{max}$. A value of $\sigma_{rel} \sim 1.7$ is found for the NFs, whereas a greater one of $\sigma_{rel} \sim 2.1$ corresponds to the BMs. If we compare these values with the literature, the one achieved for the NFs is very similar to the one reported in [343] for maghemite NPs of several sizes. In which concerns the BMs, they display a larger value than the one of $\sigma_{rel} \sim 0.05$ corresponding to an archetypal canonical spin glass of $\text{Au}_{96}\text{Fe}_4$ [268] and/or the one corresponding to $\text{Tb}_{0.1}\text{Y}_{0.9}\text{Cu}_2$ 10 nm–sized MNPs, as indicated in Chapter 6. This finding supports the existence of a **broad magnetic size distribution** and clearly indicates a cooperative behaviour stemming from the magnetically–disordered moments, rather than an individual response.

After having discussed the Cole–Cole plots, we will bring to the fore the characterisation of the **spin dynamics** performed by means of the **critical exponents and power–law scalings**. Given that a frequency–dependence of the temperature value corresponding to the low–temperature broad peak has been traced in the $\chi'(T, f)$ component, several relaxation models have been employed in order to account for this displacement. The best fittings are the ones shown in Figs. 7.8c and d, where two different spin dynamics have been found depending upon the IONP ensemble. In this way, a **Néel–Brown model**¹¹ is the most suitable to

¹¹already introduced in eq. 2.1, $\tau = \tau_0 \exp\left(\frac{E_a}{k_B T}\right)$

reproduce the relaxation of the NFs, whilst for the case of the BMs, it is the critical power-law scaling¹². Therefore, with the analyses at hand, the spin dynamics of the NFs indicate a relaxation associated with weakly coupled magnetic entities. This finding is striking, considering that the magnetic entities should have some kind of interaction, given their proximity. It could be that the single-domain framework does not perfectly match with the behaviour of the NFs, where more complex magnetic structures can be playing a main role. On the other hand, a SG-like state is well-justified for the low-temperature transition found in the BMs [59]. The obtained values for the fitting parameters (NFs and BMs) are included in Table 7.1, together with the obtained δ -parameter for each IONP ensembles¹³

Paying attention to the quantitative values of the fitting parameters shown in this Table 7.1, the results concerning the NFs point to an activation energy E_a around 387 K. This may be indicative of a large anisotropy barrier, as a thermal energy above RT should be required to flip the (super)spins. The relaxation time, τ_0 , for the NFs is slightly greater than the traditional ones found in non-interacting SPM MNPs [60], which is an indication that we are dealing with magnetic entities, rather than with individual spins. δ -shift parameter values lie within the range of Cluster Glass (0.03–0.06) [182, 183], which underscores the existence of (weakly)-coupled entities (NFs). On the other hand, the displacement of T_f corresponding to the BMs was perfectly fitted to a critical slowing down behaviour (see Fig. 7.8d). The fitting parameters displayed in Tab. 7.1 lie within the range of Cluster Spin Glass-like state [50, 67, 84, 87]. This can be understood as a consequence of the strong interactions among these magnetic entities within the nanoparticles. The obtained δ is also congruent with a Cluster Glass regime, which reinforces the aforementioned CSG spin dynamics.

The last macroscopic *acid test* to investigate the actual nature of the low temperature hump would be $\chi_{AC}(t)$ measurements. This measuring protocol would be helpful to disclose whether a blocking or freezing mechanism takes place in the IONP ensembles. Unfortunately, the amount of magnetic mass inside the BMs, $\sim 30 \mu\text{g}$, gave rise to a signal that was below the detection limit. Thus, no safe conclusions can be attained. The same scenario held when we tried with, for example, a larger sample mass of $\sim 450 \mu\text{g}$. Hence, no sensible results are

¹²see eq. 2.9, $\tau = \tau_0 \left(\frac{T_f - T_{f,0}}{T_{f,0}} \right)^{-z\nu}$

¹³see eq. 2.10, $\delta = \frac{\ln(T_f)}{\log_{10}(2\pi f)} + k$

Table 7.1: Activation energy E_a /freezing transition temperature T_f , relaxation time τ_0 of individual particles for $f \rightarrow 0$, critical exponent $z\nu$ and δ -shift parameter values obtained for Synomag maghemite NFs and magnetite BMs.

	$E_a/T_{f,0}$ (K)	τ_0 (s)	$z\nu$	δ
NFs	386(8)	$9.4(7) \cdot 10^{-7}$	–	0.045(4)
BMs	30.2(2)	7.4(2)	10^{-8}	0.040(2)

conceivable at the present stage. On the other hand, the signal given by the NFs was more than enough to detect ageing and memory effect phenomena. Very interestingly, we could not observe any of these effects, even if we tried several temperatures between 5–70 K. As an example, we are including in Figs. 6.5e and f the memory effect protocol and the ageing measurements at $T = 10$ and 20 K. No trace of time-dependent phenomena are probed, which may indicate a non-interacting disorder-like phase taking place at this low temperature side. This would highlight the existence of a blocking, not a freezing, mechanism beneath this low-temperature disorder transition.

Given the subtleties associated to the low temperature relaxation mechanism of the NFs, it would be necessary to address this issue using powerful microscopic techniques, as high resolution TEM to really disclose the exact arrangement within the petals, and SANS, to determine the magnetic correlations among the petals forming the NF.

7.3 Magnetic Fluid Hyperthermia: NFs vs. Magnetosomes

To end this chapter, we will present a brief summary of the Magnetic Fluid Hyperthermia (MFH) measurements performed at the NF and BMs ensembles. These measurements were acquired with the help of PhD. Irati Rodrigo, at the University of the Basque Country (UPV/EHU). We refer the reader to [344], where the complete performed study is presented. But at this point, we will just give a small flavour of this MFH, as this Dissertation aims to deep on the fundamental mag-

netic phenomena, rather than on their potential applications.

Accordingly, **the heating efficiency of the NFs and the undoped OMs** (*ie.*, magnetosomes extracted from the bacteria) **has been evaluated by means of AC magnetometry measurements**. This technique allows to directly measure the AC hysteresis loops described by the magnetic moments of the nanoparticles in order to calculate their heating efficiency or *SAR* from the associated hysteresis losses. For this purpose, we have employed a novel home-made setup for AC magnetometry measurements¹⁴, which has allowed us to measure the *SAR* of the MNPs at 3 different frequencies, applying AC fields up to 88 mT. Thanks to this instrument, it has been possible to attain different heating ranges, getting a reliable *landscape* of the fields and frequencies that maximise the heating efficiency of these IONP ensembles under certain safety limits. One of the main advantages of this procedure is connected to the fact that the obtained *SAR* values are not affected by thermal parameters or conditions, which is more the case of AC-calorimetry [284]. Moreover, AC Calorimetry measurements require particular data analysis to remove artefacts from different error sources [346, 347]. The AC magnetometry method is, therefore, an excellent route to quantify magnetic losses when MNPs are inside biological matrices, like cells or tissues [348], and also avoids the struggles connected to the non-adiabatic conditions inherent to the measuring process.

The literature evaluating the heating efficiency of both ~ 45 nm-sized IONPs (NFs and undoped BMs) is really scarce. For instance, in the very recent publication (2021) [349], the heating curves of maghemite Nanoflowers with sizes ranging from $\langle D \rangle \sim 44$ to 162 nm is provided. On the other hand, in [350], the heating curves of magnetosomes within the bacteria are provided. These two works demonstrate the heating efficiency of these MNP ensembles by measuring the T vs. T curves. Nonetheless, there are no examples, to our knowledge, using the AC-magnetometry to determine the *SAR*. Considering all this, we decided to focus on this method to both determine this *SAR*, and to better understand the differences in the magnetic response of both systems.

Figs. 7.9a and b display the AC hysteresis loops measured for both NFs and OMs, respectively, dispersed in water (concentrations of ~ 3.1 mg/ml and ~ 1.5 mg/ml respectively). The AC loops were measured at three different frequencies, $f = 130, 300,$ and 530 kHz, with AC field amplitudes up to $\mu_0 H_{AC} = 88, 62,$ and

¹⁴we address the reader to Irati Rodrigo's PhD Thesis, ref. [345], to know more about this tool and the development process behind it.

50 mT, respectively. We have just included in this Fig. 7.9a the ones measured at $f = 300$ kHz, as this frequency value was the one corresponding to the maximum SAR_{limit} . The meaning of this magnitude will be explained when analysing the SAR parameter (see below). What is clear, according to these Figs. 7.9a and b, is that the shape of the AC loops changes when increasing the $\mu_0 H_{AC}$, given that both samples exhibit narrow and elongated AC loops at low field amplitudes, *ie.*, the typical lancet shape [351]. This gives rise to low hysteresis losses and low heating efficiencies. However, as the field amplitude increases, the AC loops become bigger and more squared until they reach a certain saturation at high enough fields, where the differences between the saturated loops are small. In addition, we can observe that the AC loops tend to become slightly wider and more squared at high enough field amplitudes. If we compare both IONP ensembles, quantitative differences can be already seen, especially at high field amplitudes: the coercive field value, $\mu_0 H_{C-AC}$, is up to ~ 85 % greater for OMs than for NFs, so does the M_{sat-AC} , which is ~ 26 % enhanced. **These results anticipate that the heating efficiency of OMs may be better than NFs—one, especially in the high field region.**

Powerful information related concerning the effective anisotropy, K_{eff} , can be gained by means of the coercive field, $\mu_0 H_{C-AC}$. In this way, following the approach described in [351], a good estimation on the K_{eff} for both IONP ensembles can be obtained. According to their model:

$$\mu_0 H_C = 0.96 \cdot \mu_0 H_\kappa (1 - \kappa^{0.8}) \quad (7.3)$$

where $H_\kappa = 2K_{eff}/\mu_0 M_{sat}$ is the anisotropy field, being κ a parameter given by:

$$\kappa = \frac{k_B T}{K_{eff} V} \ln \left(\frac{k_B T}{4\mu_0 H_{max} M_{sat} V f \tau_0} \right) \quad (7.4)$$

where $\tau_0 = 10^{-10}$ s, which lies within the typical ones in the literature [201, 351], $\mu_0 H_{max}$ is the maximum applied field, and V is the MNP volume.

The obtained values of this K_{eff} corresponding to each ensemble have been inserted in Table 7.2. According to the values inserted in that Table 7.2, **the OMs evidence greater effective anisotropy values** (more than twice for all the f), which results in wider AC loops, leading thus to **larger hysteresis losses**. This assessment is valid as long as the applied fields are strong enough: $\mu_0 H_{AC} \gg \mu_0 H_{c-hyp}$, being $\mu_0 H_{c-hyp}$ the field amplitude reached at the inflection point of

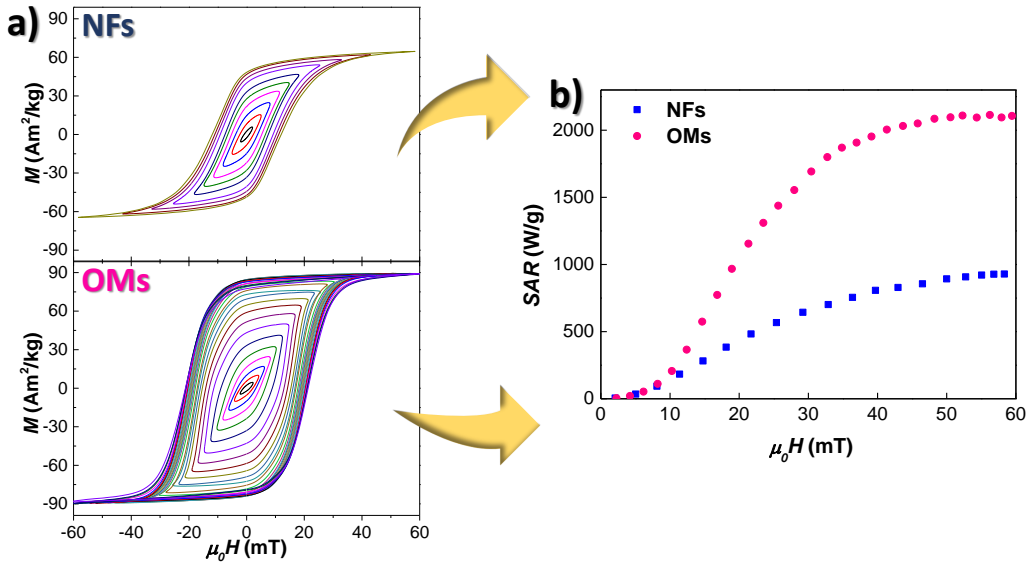


Figure 7.9: **a)** AC hysteresis loops measured up to $\mu_0 H_{AC} = 62$ mT for the NFs and the OMs at $f = 300$ kHz. In **b)**, the calculated SAR vs. $\mu_0 H_{AC}$ values for the NFs (blue squares) and the OMs (red circles) have been displayed. In all of the cases, the SAR corresponding to the OMs is more than twice the one of the NFs at high fields.

the SAR vs field curve [352, 353]. Finally, the K_{eff} values for the OMs agree well with the ones typically reported for other highly crystalline magnetite nanoparticles of similar size [354, 355].

We have included in Fig. 7.9b a depiction of the SAR vs. $\mu_0 H$ corresponding to the loops measured under $f = 300$ kHz. These SAR values, in W/g, were directly calculated from the area, *Area*, of the AC hysteresis loops, according to the following equation:

$$SAR = \frac{f}{c} \cdot Area = \frac{f}{c} \cdot \oint \mu_0 M_t dH_t \quad (7.5)$$

where M_t is the instantaneous magnetisation at time t , H_t the sinusoidal magnetic field of frequency f at time t , and c is the magnetic material weight concentration in the dispersing medium.

As it can be seen in this Fig. 7.9b, both the NFs and the OMs evidence nearly negligible SAR values at field amplitudes below 5 mT. Once the field amplitude is raised, the SAR starts increasing very fast until a saturation is reached above a certain field, $\mu_0 H_{sat}$. According to the values inserted in Table 7.2, **the maximum**

SAR values corresponding to the OMs are, at least, more than twice the ones obtained for NFs for all the measured frequencies. Both the magnetic moment and the effective anisotropy of each IONP ensemble is at the basis of this finding.

Table 7.2: Values corresponding to the effective anisotropy K_{eff} , maximum SAR_{max} and maximum SAR under chemical safety limits, SAR_{limit} , obtained for the NFs and OMs measured at $f = 130, 300$ and 530 kHz. Errors for the values are below 5%.

	NFs			OMs		
f (kHz)	130	300	530	130	300	530
K_{eff} (kJ/m ³)	4.0	4.6	5.1	9.8	11.0	12.1
SAR_{max} (W/g)	370	930	1820	880	2120	4120
SAR_{limit} (W/g)	335	455	350	805	1125	570

Finally, for **clinical applications** it is important to consider certain **safety limits** in the value of the field amplitude and frequency in order to avoid producing non-specific heating in the body that can harm the patient. There can be found different proposed safety limits, as it is the case of the Atkinson–Brezovich or Hergt criterion. According to the former, $H \cdot f$ should be lower than $4.85 \cdot 10^8$ A m⁻¹s⁻¹ [356, 357], while the second one extends this limit to $\sim 5 \cdot 10^9$ A m⁻¹s⁻¹ [358]. Even if this later Hergt criterion does not take into account the exposed volume to the magnetic field, it is, nowadays, the most accepted estimation. Of course, either the volume of exposed tissue or the heating time should be watched-out to avoid the possible inductance of damaging eddy currents connected to the use of high field amplitudes and/or frequencies. We have decided to follow this Hergt criterion to calculate the maximum achievable SAR of our samples. As indicated in Table 7.2, both samples achieve their maximum SAR_{limit} at $f = 300$ kHz (as it was already mentioned), with a maximum $\mu_0 H_{limit} = 20.7$ mT. Under this consideration, the $SAR_{limit} = 455$ and 1125 W/g for the NFs and OMs, respectively. This means, **the OMs are almost three-times more efficient than the NFs at the limit value.** This again supports the use of magnetite-based NPs for maximising the heating efficiency in magnetic hyperthermia under clinical conditions.

So, at this point, one may wonder about what are the limitations to perform MHT with magnetite, rather than maghemite-based MNPs. As it has already been stated, it is important to recall that **the sticking point was related to the**

chemical stability of the Fe_3O_4 phase (oxidation towards maghemite), not to the MHT performance itself. This is why maghemite-based IONPs, and, especially the case of the Synomag NFs, have been so extensively used. The fact that there are some degree of spin disorder and exchange coupling in their nanometric scale (already discussed above) promotes these NFs to display more than acceptable heating efficiency values [28]. Hence, a good chemical stability, together with a relatively good hyperthermia performance, large-scale production processes and high reproducibility, have finished to bias the interest of the scientific community towards maghemite-based IONPs. It is clear, however, that the OMs constitute a new player on the board, showing much better hyperthermia performance and avoiding the oxidation-issues thanks to their organic membrane. Indeed, the conditions of reproducibility and large-scale production of such biological MNPs are to be better defined, whereas Synomag NFs constitute already a high-available technological advanced product. Notwithstanding, it is our belief that **these OMs are a very promising IONP ensemble for being used in magnetic hyperthermia therapies** [344].

To sum up, the Magnetic Fluid Hyperthermia analyses discussed here set a perfect match of both fundamental and application worlds. This way, **the MFH results have evidenced experimentally the consequence of the larger magnetic moment and effective anisotropy corresponding to the magnetite bacteria magnetosomes, with respect to the maghemite Nanoflowers.**

Chapter 8

Conclusions

“¿Qué más, pues?”

J. Balvin feat. María Becerra

The evolution of the magnetic properties with respect to the size reduction and the microstrain has been analysed in ensembles of RCu_2 nanoparticles. In addition, we have studied the magnetic properties of commercial Synomag maghemite ($\gamma\text{-Fe}_2\text{O}_3$) Nanoflowers, and magnetite (Fe_3O_4) bacterial magnetosome, both undoped and Gd and Tb-doped bacteria.

Among the most relevant results, we would like to indicate:

- The bulk AF state in GdCu_2 evolves towards a Superantiferromagnetic arrangement, where the core keeps the AF order and the magnetic surface moments give rise to a Spin Glass disorder phase. The interactions among the SG disordered moments are maximised at a mean nanoparticle size of $\langle D \rangle \approx 25$ nm. When the nanoparticle size is below 10 nm, the AF order state does not hold anymore, and a Super Spin Glass state, involving all the magnetic moments in the nanoparticle, participate in this disordered state, whose spin dynamics follows a critical slowing down relaxation.
- The ensembles of NdCu_2 nanoparticles have evidenced the maintenance of the bulk AF commensurate structure at $\langle D \rangle \sim 13$ nm. The bulk commensurate-incommensurate transition ($T_R = 4.5$ K) is lost in the nanoparticle regime, where the surface moments arrange into an interacting Spin Glass phase. The bulk crystalline electric field level schemes, plus the magnon collective excitations, are well-maintained, not only in the

nanoparticles themselves, but **also at the nanoparticle surface**. A **shift of the magnon excitations towards larger energy values** is found, revealing the increasing anisotropy and a possibly stiffening in the magnon modes at the nanoparticle surface.

- Three different **Tb_xR_{1-x}Cu₂** alloys have been produced to explore the different degrees of magnetic disorder. **Tb_{0.5}Gd_{0.5}Cu₂** alloy keeps the AF state at the bulk stage, yet the magnetic order is lost in the nanoparticle regime, where a **Super Spin Glass** state is settled. The dilution with non-magnetic La³⁺ in the **Tb_{0.5}La_{0.5}Cu₂** alloy allows to preserve the bulk AF within the nanoparticle regime, for which a **Superantiferromagnetic state** takes place. On the other hand, the (magnetic) percolation limit is overcome for **Tb_{0.1}Y_{0.9}Cu₂** alloy already in the **bulk** state, where a **Cluster Spin Glass** state is settled. The **size reduction** to the nanoscale shows a progressive **loss of magnetic (disorder) interactions**, ending up in a Superparamagnetic picture. All in all, **three different spin (moment) dynamics are found for each of the compositions**.
- The commercial **Synomag Nanoflowers** are purely formed by maghemite, being in a **Superparamagnetic** state already at $T = 300$ K (RT). The purely magnetite **bacterial magnetosome** are, on the other hand, **magnetically blocked** at RT. The latter ensembles have evidenced a **larger magnetic anisotropy**, which leads to their improved Magnetic Hyperthermia performance with respect to the Synomag Nanoflowers.
- The **low temperature transitions** found in both the Nanoflowers and the (undoped) bacterial magnetosome display a **very different spin dynamics**, which needs to be further studied from a microscopic point of view.
- We **pioneering successfully the doping of bacterial magnetosome with Rare Earth ions Gd³⁺ and Tb³⁺**. These ions are incorporated within the magnetosome structure, mainly, in the octahedral B-type Fe³⁺ positions. The magnetic properties of the doped bacteria are very alike to the ones corresponding to the undoped BMs, with some **minor modifications on the anisotropy** due to the distortion of the magnetosome crystalline structure.

Bearing all these points in mind, it is clear that **this work has deepened into the fundamentals of the Magnetism in ensembles of nanoparticles containing Rare Earths**. The conclusions pave the way for further investigations, mainly concerning the analyses of single-ion and collective excitations in ensembles of 4f nanoparticles and to the determination of the correlations among the

magnetically-disordered moments. The latter could be very well studied by means of Small-Angle Neutron scattering.

On the other hand, **Fe-oxide compounds** have been shown as **excellent candidates for Magnetic Hyperthermia therapies**, that are mainly connected to cancer treatments. The high biocompatibility of bacteria magnetosomes, together with their **tunability**, make them excellent and promising candidates to be used as nanobiots. This not only could be used in magnetic hyperthermia treatments, but also they can be used as **double agents**, combining more than one potentiality. For instance, Gd^{3+} is already used as a contrast agent in magnetic resonance imaging, while Tb^{3+} is used with luminescence purposes. By combining both the potentialities of the bacterial magnetosomes, together with the ones coming from these R^{3+} would open the possibility to have, in a single biocompatible nanobiot, an amazing amount of applications. A natural future step will be to deepen into the details related to the magnetic correlations of magnetosomes. For this aim, it is clear that the SANS technique is the one that paves the way.

Conclusiones

La evolución de las propiedades magnética en función de la reducción de tamaño y de la micro-tensión (*microstrain*) ha sido analizada en aleaciones de la forma RCu_2 , tanto en material masivo (*bulk*) como en nanopartículas. Asimismo, se han estudiado las **propiedades magnéticas de nanopartículas de comerciales Synomag**, compuestas por $\gamma\text{-Fe}_2\text{O}_3$ y con forma de **Nanoflor**, así como para **magnetosomas de magnetita (Fe_3O_4) sintetizados por bacterias magnetotácticas**. Las propiedades magnéticas para estos magnetosomas se han estudiado **tanto para bacterias sin dopar, como en bacteria dopada con Gd y Tb**.

Entre los resultados más relevantes, conviene destacar los siguientes:

- El estado antiferromagnético (AF) de la aleación masiva (*bulk*) de GdCu_2 evoluciona hacia un estado Superantiferromagnético, dentro del cual, los momentos magnéticos situados en el interior de la nanopartícula (*core*) mantienen el ordenamiento AF, mientras que los situados en la superficie dan lugar a un estado magnético desordenado tipo vidrio de espín (*Spin Glass, SG*). **Las interacciones entre los momentos SG se encuentran maximizadas en las nanopartículas de $\langle D \rangle \approx 25$ nm**. El ordenamiento AF está destruido para tamaños de nanopartícula **por debajo de 10 nm**, estableciéndose entonces un estado conocido como **Super Spin Glass**, del cual participan todos los momentos magnéticos de la nanopartícula. La **dinámica de espín de este estado magnético desordenado obedece una relajación acorde a un ralentizamiento crítico (*critical slowing down relaxation*)**.
- Las nanopartículas de NdCu_2 evidencian el mantenimiento de la estructura AF conmensurada del estado masivo en nanopartículas de **13 nm**. La transición conmensurada–inconmensurada encontrada en $T_R = 4.5$ K para el estado masivo se pierde en las nanopartículas, donde los momentos magnéticos

de la superficie se encuentran de nuevo formando un estado interactuante tipo SG. **El esquema de niveles correspondiente al campo cristalino, junto con las excitaciones magnónicas colectivas, se mantienen, no sólo en la propia nanopartícula, sino también en su superficie, donde se ha observado un desplazamiento del pico magnónico hacia mayores energías.** Este desplazamiento revela una mayor anisotropía en la superficie de las nanopartículas, pudiendo ser igualmente indicativo de un endurecimiento (*stiffening*) de los modos magnónicos en dicha superficie.

- Se han producido tres aleaciones diferentes de la forma $\text{Tb}_x\text{R}_{1-x}\text{Cu}_2$ con el fin de explorar los diferentes grados de desorden magnético. La aleación de $\text{Tb}_{0.5}\text{Gd}_{0.5}\text{Cu}_2$ conserva el estado AF en su forma masiva, si bien, este orden magnético se pierde en el régimen de nanopartícula, donde se establece un estado **Super Spin Glass**. La dilución con el ion no magnético La^{3+} en la aleación $\text{Tb}_{0.5}\text{La}_{0.5}\text{Cu}_2$ sin embargo sí mantiene el orden AF en las nanopartículas, estableciéndose un estado **Superantiferromagnético**. Por último, aleación de composición $\text{Tb}_{0.1}\text{Y}_{0.9}\text{Cu}_2$ ofrece una situación en la que el límite de percolación magnético es ya sobrepasado en el propio estado masivo, estableciéndose los momentos magnéticos en un estado tipo **Cluster Glass**. La reducción de tamaño en la nanoescala evidencia la pérdida progresiva de las interacciones magnéticas (desordenadas), dando lugar a un estado **Superparamagnético para las nanopartículas de menor tamaño**. De esta manera, **se han evidenciado tres dinámicas de espín diferentes, en función de la composición de cada aleación.**
- Las **Nanoflores comerciales Synomag** están formadas puramente por maghemita, evidenciando un estado **Superparamagnético** a $T = 300$ K (RT). Los **magnetosomas sintetizados por bacteria** están compuestos puramente por magnetita, por el contrario, y se encuentran **magnéticamente bloqueados** a RT. Estos magnetosomas han evidenciado una **mayor anisotropía magnética**, lo que implica una mejor respuesta en hipertermia magnética respecto de la evidenciada por las Nanoflores comerciales Synomag.
- **Las transiciones de baja temperatura** halladas en las Nanoflores y en las bacterias sin dopar presentan **dos dinámicas de espín claramente distintas**. El uso de técnicas experimentales que permitan la caracterización de propiedades microscópicas permitirá el estudio de dichas sendas transiciones en mayor grado de detalle.

→ Hemos conseguido de manera pionera **el dopado de magnetosomas con los iones de tierra rara Gd^{3+} y Tb^{3+}** . Estos iones se incorporan a la estructura del magnetosoma, principalmente en las posiciones B octaédricas de los Fe^{3+} . Las propiedades magnéticas de las bacterias dopadas son muy similares a las correspondientes a las bacterias sin dopar, evidenciando **leves modificaciones de la anisotropía** debidas a la distorsión de la estructura cristalina del magnetosoma.

Teniendo en cuenta todo lo anterior, podemos concluir que **este trabajo presenta un estudio profundo del Magnetismo a nivel fundamental en nanopartículas cuya composición presenta iones de Tierra Rara**. Las conclusiones obtenidas abren camino para futuras investigaciones, principalmente relacionadas con el análisis de excitaciones, tanto de iones individuales como colectivas, en conjuntos de nanopartículas *4f*, así como aquellas relacionadas con la determinación de correlaciones entre momentos magnéticos desordenados. Estas últimas pueden estudiarse en detalle mediante la dispersión de neutrones de bajo ángulo (SANS).

Por otro lado, se ha observado la idoneidad de las nanopartículas de **óxidos de hierro** para su uso terapéutico mediante tratamientos de hipertermia magnética, principalmente relacionados con el cáncer. La alta biocompatibilidad de los magnetosomas de bacteria, junto con su **ajustabilidad**, los convierten en excelentes y prometedores candidatos para su uso como nano-robots (*nanobots*). De esta manera, no sólo pueden ser empleados en tratamientos de hipertermia magnética, sino que también pueden ser usados como **agentes dobles**, combinando en un único sistema dos o más potencialidades. Por ejemplo, el ion Gd^{3+} es empleado de manera extensa en resonancia magnética como agente de contraste, o el uso del ion de Tb^{3+} como biomarcador luminiscente. De esta manera, la combinación de las potencialidades tanto de los magnetosomas como de aquellas correspondientes a los iones R^{3+} permitirían atesorar, en un único nanobiot biocompatible, un conjunto inestimable de aplicaciones. Parece natural considerar que el siguiente paso a dar estaría relacionado con la investigación de las correlaciones magnéticas de los magnetosomas, para lo cual, la idoneidad de la técnica de SANS resulta evidente.

List of publications

Within this 3-years of Thesis activity, the following articles have been published directly connected to the development of the work:

- **E M Jefremovas**, J Alonso, M de la Fuente Rodríguez, Jesús Rodríguez Fernández, JI Espeso, DP Rojas, A García–Prieto, ML Fernández–Gubieda, L Fernández Barquín, “Investigating the Size and Microstrain Influence in the Magnetic Order/Disorder State of GdCu_2 Nanoparticles”, *Nanomaterials*, vol. 10, no 6, pp 1117–1133 (2020).
- **E M Jefremovas**, J Alonso, M de la Fuente Rodríguez, J Rodríguez Fernández, JI Espeso, DP Rojas, A García–Prieto, ML Fernández–Gubieda, L Fernández Barquín, “Exploring the Different Degrees of Magnetic Disorder in $\text{Tb}_x\text{R}_{1-x}\text{Cu}_2$ Nanoparticle Alloys”, *Nanomaterials*, vol. 10, no 11, pp 2148–2165 (2020).
- **E M Jefremovas**, L Gandarias, I Rodrigo, L Marcano, C Grüttner, JA García, E Garayo, I Orue, A García–Prieto, A Muela, ML Fernández–Gubieda, J Alonso, L Fernández Barquín, “Nanoflowers Versus Magnetosomes: Comparison Between Two Promising Candidates for Magnetic Hyperthermia Therapy”, *IEEE Access*, vol. 9, pp 99552–99561 (2021). This article was awarded by the editorial board with the distinction of *featured article*.
- **E M Jefremovas**, M de la Fuente Rodríguez, F Damay, B. Fåk, A Michels, JA Blanco, L Fernández Barquín, “Observation of surface magnons and crystalline electric field shifts in superantiferromagnetic NdCu_2 nanoparticles”, *Physical Review B*, vol. 104, no 13, pp 1344–1356 (2021).

In addition, two more contributions, with some connection to the work presented here, have also been published:

- J Soler–Morala, **E M Jefremovas**, L Martínez, A Mayoral, E H Sánchez, JA De Toro, E Navarro, Y Huttel, “Spontaneous Formation of Core@ shell Co@Cr Nanoparticles by Gas Phase Synthesis”, *Applied Nano*, vol. 1 no 1, pp 87–101 (2020).

- DP Rojas, JI Espeso, J Rodríguez, **E M Jefremovas**, “Unusual magnetic behaviour of binary YbNi₃ alloy”, *Journal of Magnetism and Magnetic Materials*, vol. 494, no 6, pp. 165815 (2020).

Appendix A

XRD diffraction

The use of X-Ray Diffraction has been extensive along this Dissertation. Fundamentals on the Rietveld refinement and how to connect the experimental hints with the actual crystal structure and nanoparticle size and/or strain have been provided in Chapter 3. This appendix will show and complete the XRD results concerning the GdCu_2 and NdCu_2 alloys. As it has already been mentioned, all the XRD patterns were collected at room temperature in a Bruker D8 Advance diffractometer working on Bragg-Brentano geometry, equipped with a high count rate Lynxeye detector. We used exclusively $\text{Cu-K}\alpha$ radiation, with $\lambda = 1.5418 \text{ \AA}$.

Beginning with the GdCu_2 alloy, the XRD characterisation and analyses of these GdCu_2 ensembles are included on the left hands side of Fig. A.1. Beginning with Fig. A.1a, a depiction of the XRD patterns corresponding to the bulk alloy ($t = 0 \text{ h}$) and the milled GdCu_2 powders ($t = 0.5, 1, 1.5, 1.75, 2$ and 5 h) is provided. All the peaks correspond to the orthorhombic *Imma* structure. A progressive peak broadening with the milling time is clearly observed, as expected, owing to the size reduction and the appearance of microstrain η [111, 114, 359]. Based on precedent works [39, 156], by keeping the milling time below 5h, the amorphisation of the alloys is well precluded.

We have decided to include the XRD pattern of the 2h milled alloy, as an example. In this way, Fig. A.1b includes the experimental XRD data of these MNPs (red points), together with the calculated Rietveld refinements (black line). The blue line at the bottom accounts for the difference between the experimental and calculated profiles, which is indicative of the fitting reliability. The Bragg positions for the (hkl) peaks corresponding to the *Imma* symmetry are displayed in green colour. Additionally to the results corresponding to the 2h-milled MNPs,

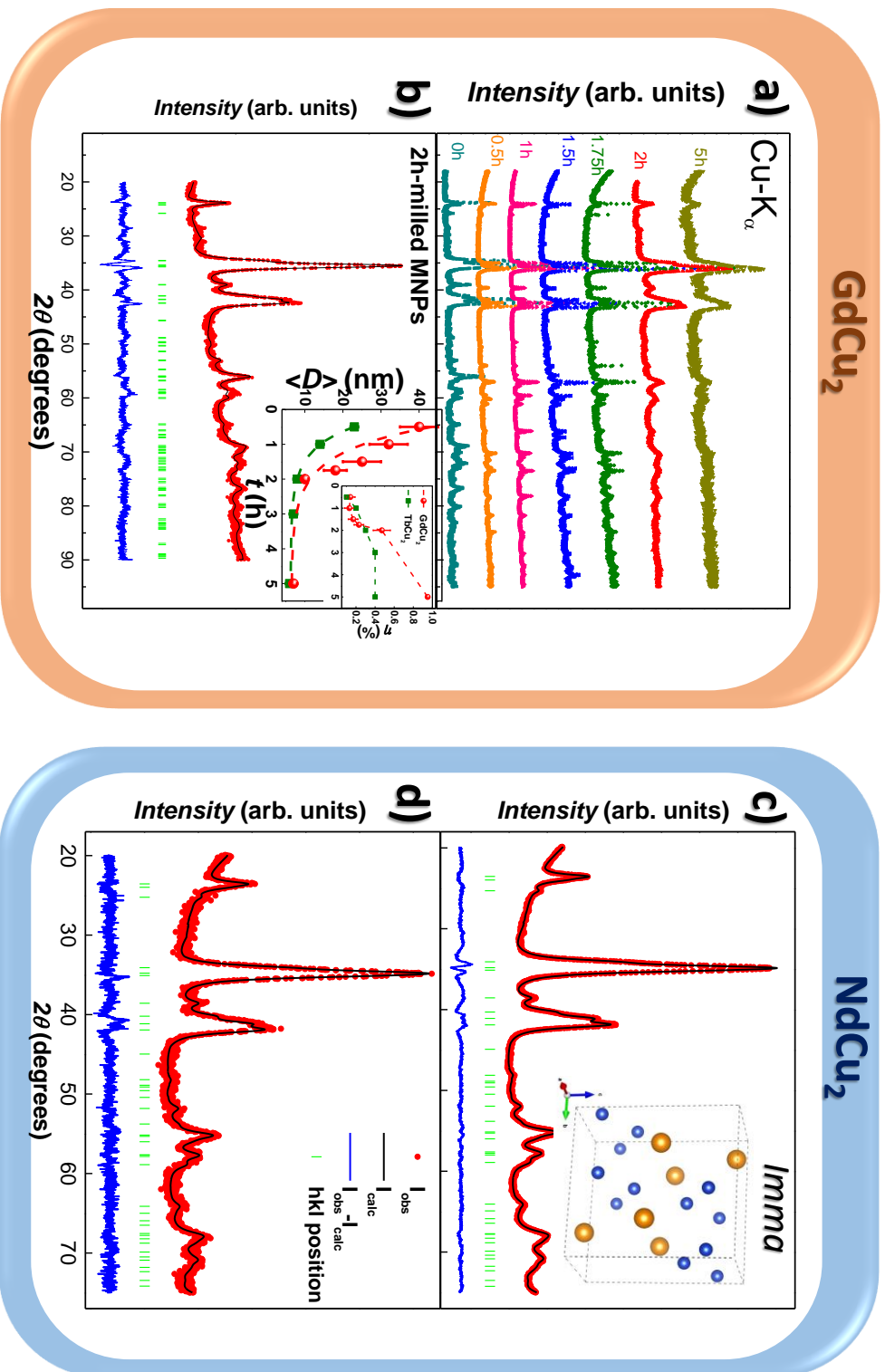


Figure A.1: **a)** and **b)** XRD profile for GdCu₂ alloys (shifted-up and re-scaled), and the XRD, together with the Rietveld refinements, for the 2h-milled ensembles, respectively. The inset in **b)** includes a comparison between the size and strain evolution vs. milling time between TbCu₂ [39] and GdCu₂. **c)** and **d)** give account for the XRD patterns plus Rietveld refinements performed on the NdCu₂ MNP ensembles (2h and 5h, respectively). Inset in **c)** sketches the orthorhombic *Imma* structure, where the orange (blue) spheres represent the Nd (Cu) atoms.

the main structural parameter for all the milled alloys have been inserted in Table A.1. There, a general trend to a positive unit cell expansion is retrieved when the alloys are nanoscaled, yet the expansion is kept low (ΔV are below 1 %). This guarantees that the bulk orthorhombic CeCu_2 -type crystal structure is well preserved in the nanoparticle state. Needless to say, the lattice parameters a , b and c agree well with the ones corresponding to bulk GdCu_2 [93]. The Bragg factors are kept below $R_B < 10\%$, which ensures the reliability of the fittings.

Table A.1: Orthorhombic mean lattice parameters (a, b and c); relative change in the unit size volume cell with respect to the unit cell in bulk alloy (ΔV), size $\langle D \rangle$, microstrain η and Bragg factor R_B of nanoparticles at different milling times (t). Bragg factors (R_B) close to 10% ensure the reliability of our refinements.

$t(\text{h})$	a (Å)	b (Å)	c (Å)	ΔV (%)	$\langle D \rangle$ (nm)	$\eta(\%)$	R_B (%)
0.5	4.329(4)	6.886(1)	7.342(1)	0.6	40(5)	0.14(5)	10.2
1	4.332(1)	6.903(2)	7.349(1)	0.3	32(5)	0.13(5)	11.5
1.5	4.326(1)	6.895(1)	7.340(2)	0.9	25(5)	0.17(5)	12.9
1.75	4.328(2)	6.903(2)	7.343(3)	0.1	18(3)	0.23(5)	6.7
2	4.314(3)	6.878(1)	7.304(2)	1.1	10(1)	0.47(9)	3.2
5	4.314(4)	6.887(1)	7.317(3)	0.8	7(1)	0.95(2)	2.0

Furthermore, we have considered that the size and microstrain evolution with the milling time could be better inspected not only by just including the values in Table A.1, but it would also be helpful to visually compare it with the one corresponding to TbCu_2 [39], which has been included in the inset in Fig. A.1b. As a matter of fact, the size (η) reduces (increases) as the milling time does. It is striking that, already for a grinding time as short as half an hour, nanoparticles around $\langle D \rangle \sim 40$ nm are already achieved. This contrasts with the long milling times $t \geq 20$ h usually employed in GdX_2 nano alloys (where X is a 3d metal) [360]. The size evolution is very alike to the one of TbCu_2 , as it can be seen in the inset in Fig. A.1b. Nevertheless, the MNP size decreases faster, for the low milling times, in GdCu_2 than in TbCu_2 . On the high milling time side, $t \geq 2$ h, the rise of η is more intense in the GdCu_2 ensembles. Given that both MNP ensembles are very close in size at this high milling time region, the greater η for GdCu_2 NPs would indicate an increased presence of defects in the particle core and surface with respect to the TbCu_2 case.

On the other hand, the right hands side of Fig. A.1 include the XRD patterns, together with the Rietveld refinements, corresponding to the NdCu₂ MNP alloys (2h in Fig. A.1c and 5h–milled in Fig. A.1d). Once again, both patterns are consistent with a single crystallographic phase of the orthorhombic CeCu₂–type crystal structure, *Imma* space group (see inset in Fig. A.1c), as it was also the case of the bulk alloy [93, 99, 213]. The volume unit cells are $V = 229.65(4) \text{ \AA}^3$ and $V = 229.77(1) \text{ \AA}^3$, respectively, values that are quite close to the bulk $V = 229.90(5) \text{ \AA}^3$. This ensures, once again, a minimal distortion of the lattice cell, yielding to a good degree of crystallinity of the MNPs despite the grinding. Rietveld refinements ($R_B < 2\%$) point to $\langle D \rangle = 18.3(1.0) \text{ nm}$ and $\eta = 0.62(7)\%$ (2h), and $\langle D \rangle = 13.0(5) \text{ nm}$ and $\eta = 0.59(1)\%$ (5h). These values are slightly greater with respect to the ones obtained for the GdCu₂ and/or Tb_xR_{1-x}Cu₂ ensembles, employing the same grinding times.

Finally, Fig. A.2 includes the XRD patterns with the performed Rietveld refinements corresponding to the three series of the Tb_xR_{1-x}Cu₂ produced alloys. Once again, all the patterns are consistent with a single crystallographic phase of the orthorhombic CeCu₂–type crystal structure (*Imma* space group), as it is found in the parent bulk RCu₂ alloys (R = Tb, Gd or Y). The R³⁺ ions occupy the *4e*-sites (0, 0.25, z), whereas Cu atoms are located at the *8h* position (0, x, y). Values for x, y, and z are found to lie near $x \approx 0.006$, $y \approx 0.163$, and $z \approx 0.547$. However, LaCu₂ is an exception for this orthorhombic *Imma* structure, as it crystallises in a hexagonal *P6/mmm* AB₂-type one [254]. Although the crystalline structure of the Tb_{0.5}La_{0.5}Cu₂ alloy could consist of a mixture of both orthorhombic and hexagonal phases, the Rietveld refinements included in Figs. A.2b, e and h reveal unambiguously that only a single phase of the orthorhombic *Imma* structure is present. This fact is in agreement with the lower energy-cost of an orthorhombic structure with respect to the hexagonal AB₂-type [93].

The main structural parameters for the bulk and NP alloys are summarised in Table A.2. First of all, the Bragg error factors R_B are kept below 10%, which is a sign of a reliable refinement. The lattice parameters of the bulk diluted alloys are slightly decreased with respect to the ones of the bulk parent TbCu₂ and GdCu₂ [93], leading to a small reduction of the unit cell volume. This general trend is in good agreement with the one previously observed in a Gd_xY_{1-x}Cu₂ bulk alloy [160]. Nevertheless, an exception for this trend is found in Tb_{0.5}La_{0.5}Cu₂, where the unit cell is expanded with respect to the TbCu₂ bulk alloy. The greater ionic radii of La³⁺ ions ($r = 1.032 \text{ \AA}$ [263]) in comparison to Tb³⁺ ($r = 0.923 \text{ \AA}$ [263]) could be beneath this fact.

Figs. A.2d–i display the XRD patterns for the nanoscaled alloys ($t = 2\text{h}$ and $t = 5\text{h}$, respectively). According to the Rietveld refinements, the orthorhombic *Imma* crystalline structure is maintained. As it can be observed from the values included in Table A.2, the unit cell tends to expand when the bulk powders are milled for the La^{3+} and Y^{3+} alloys, whereas the dilution with Gd^{3+} provokes a unit cell contraction. This effect can be attributed to the different metallurgical behaviour of the alloys [114, 359].

In which concerns the mean NP size, according to Table A.2, both $\text{Tb}_{0.5}\text{Gd}_{0.5}\text{Cu}_2$ and $\text{Tb}_{0.1}\text{Y}_{0.9}\text{Cu}_2$ reach a mean diameter size $\langle D \rangle \sim 10\text{ nm}$ after milling for $t = 2\text{h}$, and $\langle D \rangle \sim 7\text{ nm}$ after $t = 5\text{h}$. Nevertheless, $\text{Tb}_{0.5}\text{La}_{0.5}\text{Cu}_2$ NPs display greater sizes and smaller microstrain values. This may suggest that including La^{3+} ions could favour a harder metallurgical resistance to the grinding. All of the produced alloys display microstrain values below $\sim 1\%$, which ensures their good crystallinity.

Finally, a TEM image for $\text{Tb}_{0.5}\text{Gd}_{0.5}\text{Cu}_2$ -2h milled NPs is shown in the inset of Fig. A.2d. This technique has been employed to check the crystalline microscopic structure of the $\text{Tb}_{0.5}\text{Gd}_{0.5}\text{Cu}_2$ NPs, as no ND measurements could be performed for this dilution due to the high neutron absorption rate of Gd [181]. The clearly depicted crystallographic planes confirm the crystallinity of the NPs. Furthermore, the size-distribution (inset) reveals the usually found LogNormal distribution for mean NP sizes, with a mean size diameter of $D_{TEM} = 10.5(2)\text{ nm}$. This result is in good agreement with the $\langle D \rangle = 9.0(8)\text{ nm}$ obtained from the Rietveld refinements of the XRD patterns.

Table A.2: Orthorhombic mean lattice parameters (a, b and c); unit size cell volume V , mean NP diameter $\langle D \rangle$, microstrain η , and Bragg factor R_B for the produced diluted alloys.

Alloy	t(h)	a (Å)	b (Å)	c (Å)	V (nm³)	$\langle D \rangle$ (nm)	η(%)	R_B (%)
Tb _{0.5} Gd _{0.5} Cu ₂	bulk	4.312(2)	6.858(5)	7.325(5)	216.6(3)	—	—	13.3
	2h	4.319(3)	6.842(4)	7.313(4)	216.1(2)	9.0(8)	0.5(1)	6.6
	5h	4.320(5)	6.839(6)	7.312(7)	216.0(1)	7.0(9)	0.6(1)	5.8
Tb _{0.5} La _{0.5} Cu ₂	bulk	4.381(5)	7.057(1)	7.416(1)	229.3(3)	—	—	24.5
	2h	4.400(2)	7.084(4)	7.429(5)	231.6(2)	12.9(8)	0.4(1)	9.7
	5h	4.421(5)	7.116(6)	7.478(8)	235.6(2)	9.0(9)	0.4(1)	8.7
Tb _{0.1} Y _{0.9} Cu ₂	bulk	4.302(4)	6.865(2)	7.295(2)	215.4(1)	—	—	16.2
	2h	4.314(3)	6.878(2)	7.304(1)	216.7(1)	9.0(8)	0.47(9)	3.2
	5h	4.310(4)	6.887(2)	7.317(3)	217.2(1)	7.5(4)	0.95(2)	1.7

Appendix B

Simulation of the $M(H)$ loops in bacteria

Magnetic simulations of the $M(H)$ loops measured in the bacteria (doped and undoped) at different temperatures have been carried employing a modified Stoner-Wohlfarth approach [361, 362]. Briefly, the equilibrium configuration of the magnetic moment of each magnetosome is calculated as the sum of three contributions: **(i)** the magnetocrystalline anisotropy energy, E_C ; **(ii)** the effective uniaxial anisotropy energy, E_{uni} , that arises from the competition between the magnetosome shape anisotropy and the dipolar interactions between magnetosomes within the chain; and **(iii)** the Zeeman energy term, E_Z [32, 35]. In spherical coordinates, considering the $\langle 100 \rangle$ crystallographic directions of magnetite as the reference system, the total energy density is given by:

$$E(\theta, \phi) = E_C(\theta, \phi) + E_{uni}(\theta, \phi) + E_Z(\theta, \phi) \quad (\text{B.1})$$

being

$$\begin{aligned} E_C(\theta, \phi) &= K_C \left[\sin^4 \theta \sin^2 \phi + \frac{\sin^2 2\theta}{4} \right] \\ E_{uni}(\theta, \phi) &= K_{uni} [1 - (\hat{u}_m \hat{u}_{uni})^2] \\ E_Z(\theta, \phi) &= -\mu_0 M H (\hat{u}_m \cdot \hat{u}_H) \end{aligned} \quad (\text{B.2})$$

in the above-mentioned expressions, θ and ϕ give account for the polar and azimuthal angles of the magnetic moment corresponding to each magnetosome, respectively. K_C and K_{uni} stand for the magnetocrystalline and uniaxial anisotropy constants, respectively. The \hat{u}_i represents the unitary vector along the magnetic moment (\hat{u}_m), the uniaxial anisotropy vector (\hat{u}_{uni}) and the external magnetic field (\hat{u}_H) directions, respectively. As it has been probed by means of SANS and Electron cryotomography imaging, mainly, the \hat{u}_m forms an angle of $\sim 20^\circ$ with the

chain axis direction, $\langle 111 \rangle$ [32, 363]. Therefore, the magnetic simulations of the ZFC $M(H)$ loops at different temperatures have been simulated, employing the dynamical approach described in [32, 364]. A program developed by PhD. Iñaki Orue (Sglker) has been employed to calculate the results. This program runs on standard PC.

Appendix C

Surface contribution to the INS patterns: The choice of the N ratio

In order to verify that the prevalence of both CEF and collective magnon excitations in the MNPs, we have tried several values of the ratio $N = N_{core}/N_{MNP}$ in eq. 5.3. The resulting $S_{surface}(q, \hbar\omega)$ are shown in Fig. C.1. The situation concerning both the PM region ($T = 10$ K, Figs. C.1a, c and e) and the magnetic region ($T = 1.5$ K, Figs. C.1b, d and f) clearly showcases the presence of both single and collective excitations, as the peaks associated with both the CEF and the magnons do remain in all of the patterns, no matter the N value. In order to ease the tracking of peaks throughout the different N , the orange arrow marks the position for the most intense CEF peak (P2). It is beyond all doubts that this peak, located at $\hbar\omega = 4.6$ meV, is perfectly-defined for all the N values. We have also marked the position of the transverse spin wave mode peak (M) that emerges within the AF region ($T = 1.5$ K). Also for this case, the peak, located at $\hbar\omega = 1.6$ meV, is clearly observable for all the N considered. Bearing this in mind, in order to determine the most reliable N ratio, we have estimated the geometrical core-to-volume ratio corresponding to a MNP size of $\langle D \rangle = 13$ nm according to:

$$N = \frac{V_{core}}{V_{MNP}} = \left(\frac{D_{core}}{D_{MNP}} \right)^3 = \left(\frac{9}{13} \right)^3 \approx 0.33 \quad (\text{C.1})$$

where the MNPs have been assumed to be spherical and a shell thickness of 2 nm is considered [43, 55, 56]. A sketch of the MNP core and surface dimensions is included in the inset of Fig. C.1a.

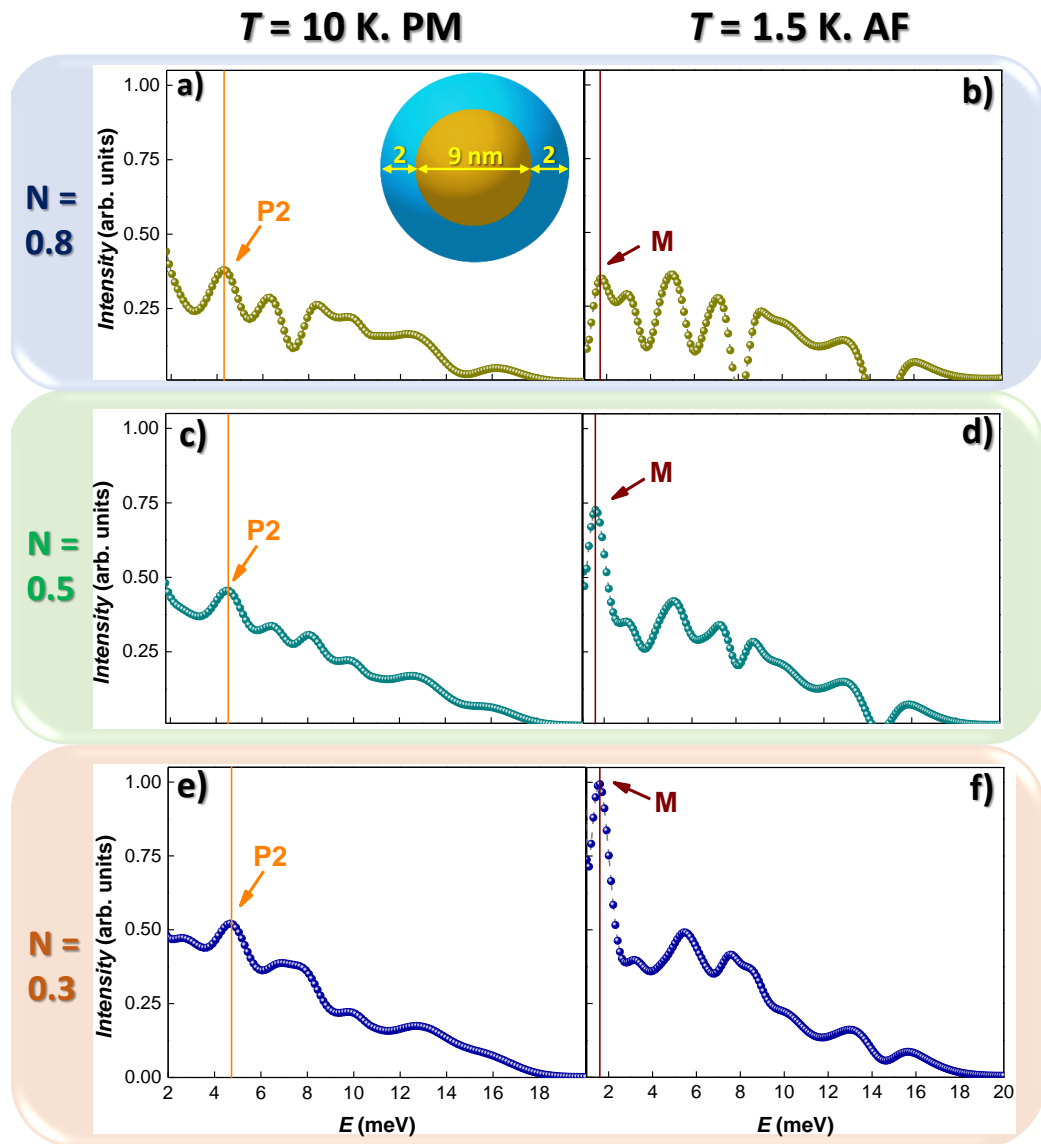


Figure C.1: $S_{\text{surface}}(q, \hbar\omega)$ obtained following eq. 5.3 at the PM region ($T = 10$ K [a], c) and e)] and the AF-region ($T = 1.5$ K [b], d) and f)) for the 5h-milled NdCu_2 MNPs as a function of energy transfer for a wave vector of $q = 1.75 \pm 0.5 \text{ \AA}^{-1}$. The CEF and magnon collective excitations do remain in all the patterns, no matter the different N values. Orange and brown arrows point the position of the CEF $|2\rangle$ multiplet (labelled as P2), and the one corresponding to the magnon modes (M). These are found at $\hbar\omega = 4.6$ and 1.6 meV, respectively. Inset in a) includes a schematic representation of the $\langle D \rangle \approx 13$ nm NdCu_2 MNPs, where the core $\langle D \rangle \approx 9$ nm.

Bibliography

- [1] John MD Coey. *Magnetism and magnetic materials*. Cambridge university press, 2010.
- [2] Stephen Blundell. *Magnetism in condensed matter*, 2003.
- [3] V Franco, JS Blázquez, JJ Ipus, JY Law, LM Moreno-Ramírez, and A Conde. Magnetocaloric effect: From materials research to refrigeration devices. *Progress in Materials Science*, 93:112–232, 2018.
- [4] Karin Everschor-Sitte, Jan Masell, Robert M Reeve, and Mathias Kläui. Perspective: Magnetic skyrmions—overview of recent progress in an active research field. *Journal of Applied Physics*, 124(24):240901, 2018.
- [5] Manfred Fiebig, Thomas Lottermoser, Dennis Meier, and Morgan Trassin. The evolution of multiferroics. *Nature Reviews Materials*, 1(8):1–14, 2016.
- [6] Bhaskar Das, Balamurugan Balasubramanian, Ralph Skomski, Pinaki Mukherjee, Shah R Valloppilly, George C Hadjipanayis, and David J Sellmyer. Effect of size confinement on skyrmionic properties of MnSi nanomagnets. *Nanoscale*, 10(20):9504–9508, 2018.
- [7] N Marcano, PA Algarabel, J Rodríguez Fernández, JP Araujo, AM Pereira, JH Belo, C Magén, L Morellón, and MR Ibarra. Pressure dependence of the griffiths-like phase in 5: 4 intermetallics. *Physical Review B*, 102(17):174416, 2020.
- [8] See <https://www.science-community.org/en/node/186626> for additional information.
- [9] Sandra H Skjærvø, Christopher H Marrows, Robert L Stamps, and Laura J Heyderman. Advances in artificial spin ice. *Nature Reviews Physics*, 2(1):13–28, 2020.

- [10] Liang-Juan Chang, Yen-Fu Liu, Ming-Yi Kao, Li-Zai Tsai, Jun-Zhi Liang, and Shang-Fan Lee. Ferromagnetic domain walls as spin wave filters and the interplay between domain walls and spin waves. *Scientific reports*, 8(1):1–7, 2018.
- [11] James L Hart, Andrew C Lang, Asher C Leff, Paolo Longo, Colin Trevor, Ray D Twosten, and Mitra L Taheri. Direct detection electron energy-loss spectroscopy: a method to push the limits of resolution and sensitivity. *Scientific reports*, 7(1):1–14, 2017.
- [12] J Dai, E Frantzeskakis, N Aryal, K-W Chen, F Fortuna, JE Rault, P Le Fèvre, L Balicas, K Miyamoto, T Okuda, et al. Experimental observation and spin texture of Dirac node arcs in tetradymite topological metals. *arXiv preprint arXiv:2105.07515*, 2021.
- [13] Andreas Michels. *Magnetic Small-Angle Neutron Scattering: A Probe for Mesoscale Magnetism Analysis*, volume 16. Oxford University Press, 2021.
- [14] I Radu, K Vahaplar, C Stamm, T Kachel, N Pontius, HA Dürr, TA Ostler, J Barker, RFL Evans, RW Chantrell, et al. Transient ferromagnetic-like state mediating ultrafast reversal of antiferromagnetically coupled spins. *Nature*, 472(7342):205–208, 2011.
- [15] AG Roca, R Costo, AF Rebolledo, S Veintemillas-Verdaguer, P Tartaj, T Gonzalez-Carreno, MP Morales, and CJ Serna. Progress in the preparation of magnetic nanoparticles for applications in biomedicine. *Journal of Physics D: Applied Physics*, 42(22):224002, 2009.
- [16] Josep Nogués and Ivan K Schuller. Exchange bias. *Journal of Magnetism and Magnetic Materials*, 192(2):203–232, 1999.
- [17] Josep Nogués, J Sort, V Langlais, V Skumryev, S Suriñach, JS Muñoz, and MD Baró. Exchange bias in nanostructures. *Physics reports*, 422(3):65–117, 2005.
- [18] AE Berkowitz and Kentaro Takano. Exchange anisotropy—a review. *Journal of Magnetism and Magnetic materials*, 200(1-3):552–570, 1999.
- [19] S Karmakar, S Kumar, R Rinaldi, and G Maruccio. Nano-electronics and spintronics with nanoparticles. In *Journal of Physics: Conference Series*, volume 292, page 012002. IOP Publishing, 2011.

- [20] Abu Sebastian, Manuel Le Gallo, Riduan Khaddam-Aljameh, and Evangelos Eleftheriou. Memory devices and applications for in-memory computing. *Nature nanotechnology*, 15(7):529–544, 2020.
- [21] Ahmed A El Gendy, Jose Manuel Barandiaran, and Ravi L Hadimani. *Magnetic nanostructured materials: from lab to fab*. Elsevier, 2018.
- [22] Quentin A Pankhurst, J Connolly, Stephen K Jones, and J Dobson. Applications of magnetic nanoparticles in biomedicine. *Journal of physics D: Applied physics*, 36(13):R167, 2003.
- [23] Nguyen TK Thanh. *Clinical applications of magnetic nanoparticles: From Fabrication to Clinical Applications*. CRC Press, 2018.
- [24] ML Fdez-Gubieda, J Alonso, A García-Prieto, A García-Arribas, L Fernández Barquín, and A Muela. Magnetotactic bacteria for cancer therapy. *Journal of Applied Physics*, 128(7):070902, 2020.
- [25] Damien Faivre and Dirk Schuler. Magnetotactic bacteria and magnetosomes. *Chemical reviews*, 108(11):4875–4898, 2008.
- [26] See <https://www.nanomag-project.eu/> for additional information.
- [27] David González-Alonso, Jose I Espeso, Helena Gavilán, LJ Zeng, Maria Teresa Fernández-Díaz, Gloria Subías, Imanol de Pedro, J Rodríguez Fernández, Philipp Bender, L Fernández Barquín, et al. Identifying the presence of magnetite in an ensemble of iron–oxide nanoparticles: a comparative neutron diffraction study between bulk and nanoscale. *Nanoscale Advances*, 2021.
- [28] Philipp Bender, Jeppe Fock, Cathrine Frandsen, Mikkel F Hansen, Christoph Balceris, Frank Ludwig, Oliver Posth, Erik Wetterskog, Lara K Bogart, Paul Southern, et al. Relating magnetic properties and high hyperthermia performance of iron oxide nanoflowers. *The Journal of Physical Chemistry C*, 122(5):3068–3077, 2018.
- [29] Philipp Bender, Dirk Honecker, and Luis Fernández Barquín. Supraferromagnetic correlations in clusters of magnetic nanoflowers. *Applied Physics Letters*, 115(13):132406, 2019.
- [30] Philipp Bender, Lourdes Marcano, Iñaki Orue, Diego Alba Venero, Dirk Honecker, Luis Fernández Barquín, Alicia Muela, and M Luisa Fdez-Gubieda.

- Probing the stability and magnetic properties of magnetosome chains in freeze-dried magnetotactic bacteria. *Nanoscale Advances*, 2(3):1115–1121, 2020.
- [31] GF Goya, TS Berquo, FC Fonseca, and MP Morales. Static and dynamic magnetic properties of spherical magnetite nanoparticles. *Journal of applied physics*, 94(5):3520–3528, 2003.
- [32] I Orue, L Marcano, P Bender, A García-Prieto, S Valencia, MA Mawass, D Gil-Cartón, D Alba Venero, D Honecker, A García-Arribas, et al. Configuration of the magnetosome chain: a natural magnetic nanoarchitecture. *Nanoscale*, 10(16):7407–7419, 2018.
- [33] L Marcano, A García-Prieto, D Muñoz, L Fernández Barquín, I Orue, J Alonso, A Muela, and ML Fdez-Gubieda. Influence of the bacterial growth phase on the magnetic properties of magnetosomes synthesized by *Magnetospirillum gryphiswaldense*. *Biochimica et Biophysica Acta (BBA)-General Subjects*, 1861(6):1507–1514, 2017.
- [34] Lourdes Marcano Prieto. *Magnetic and structural characterization of magnetite nanoparticles synthesized by magnetotactic bacteria*. PhD thesis, Universidad del País Vasco UPV/EHU, 2018.
- [35] Lourdes Marcano, Inaki Orue, Ana Garcia-Prieto, Radu Abrudan, Javier Alonso, Luis Fernandez Barquin, Sergio Valencia, Alicia Muela, and M Luisa Fdez-Gubieda. Controlled magnetic anisotropy in single domain Mn-doped biosynthesized nanoparticles. *The Journal of Physical Chemistry C*, 124(41):22827–22838, 2020.
- [36] G. F. Zhou and H. Bakker. Spin-glass behaviour of mechanically milled crystalline GdAl_2 . *Physical Review Letters*, 73:2, 1994.
- [37] E M Jefremovas, J Alonso, M De la Fuente Rodríguez, Jesús Rodríguez Fernández, JI Espeso, DP Rojas, Ana García-Prieto, ML Fernández-Gubieda, and Luis Fernández Barquín. Investigating the size and microstrain influence in the magnetic order/disorder state of GdCu_2 nanoparticles. *Nanomaterials*, 10(6):1117, 2020.
- [38] H-G Purwins, JG Houmann, P Bak, and E Walker. Interaction between magnons and magnetic excitons in TbAl_2 . *Physical Review Letters*, 31(27):1585, 1973.

- [39] Cristina Echevarria-Bonet, DP Rojas, JI Espeso, J Rodríguez Fernández, M De la Fuente Rodríguez, L Fernández Barquín, L Rodríguez Fernández, Pedro Gorria, JA Blanco, M Luisa Fdez-Gubieda, et al. Magnetic phase diagram of superantiferromagnetic TbCu₂ nanoparticles. *Journal of Physics: Condensed Matter*, 27(49):496002, 2015.
- [40] Damien Faivre. *Iron oxides: from nature to applications*. John Wiley & Sons, 2016.
- [41] Friedrich Walz. The Verwey transition—a topical review. *Journal of Physics: Condensed Matter*, 14(12):R285, 2002.
- [42] DP Rojas, L Fernández Barquín, J Rodríguez Fernández, JI Espeso, and JC Gómez Sal. Size effects in the magnetic behaviour of TbAl₂ milled alloys. *Journal of Physics: Condensed Matter*, 19(18):186214, 2007.
- [43] C Echevarria-Bonet, D P Rojas, J I Espeso, J Rodríguez Fernández, M de la Fuente Rodríguez, L Fernández Barquín, L Rodríguez Fernández, P Gorria, J A Blanco, M L Fdez-Gubieda, E Bauer, and F Damay. Size-induced superantiferromagnetism with reentrant spin-glass behavior in metallic nanoparticles of tbcu₂. *Phys. Rev. B*, 87:180407(R), 2013.
- [44] DP Rojas, L Fernández Barquín, J Sánchez Marcos, C Echevarria-Bonet, JI Espeso, J Rodríguez Fernández, L Rodríguez Fernández, and MH Mathon. Magnetic disorder in TbAl₂ nanoparticles. *Materials Research Express*, 2(7):075001, 2015.
- [45] Robert C O'handley. *Modern magnetic materials: principles and applications*. 1999.
- [46] E Tronc. Magnetic relaxation in fine-particle systems. *Adv Chem Phys*, 283:283–449, 1997.
- [47] Hari Singh Nalwa et al. *Magnetic nanostructures*. American scientific publishers USA, 2002.
- [48] Cristina Echevarría Bonet. *Influencia de la reducción del tamaño en las propiedades electrónicas y magnéticas de aleaciones binarias de Tierras Raras*. PhD thesis, Universidad de Cantabria, 2014.
- [49] María de la Fuente Rodríguez. *Supermagnetismo en aleaciones binarias nanométricas de Tierras Raras*. PhD thesis, Universidad de Cantabria, 2017.

- [50] John A Mydosh. *Spin glasses: an experimental introduction*. CRC Press, 2014.
- [51] Oleg V Salata. Applications of nanoparticles in biology and medicine. *Journal of nanobiotechnology*, 2(1):1–6, 2004.
- [52] Shan X Wang and Guanxiong Li. Advances in giant magnetoresistance biosensors with magnetic nanoparticle tags: Review and outlook. *IEEE transactions on Magnetics*, 44(7):1687–1702, 2008.
- [53] Cedric Bouzigues, Thierry Gacoin, and Antigoni Alexandrou. Biological applications of rare-earth based nanoparticles. *ACS nano*, 5(11):8488–8505, 2011.
- [54] JL Dormann, D Fiorani, and E Tronc. On the models for interparticle interactions in nanoparticle assemblies: comparison with experimental results. *Journal of Magnetism and Magnetic Materials*, 202(1):251–267, 1999.
- [55] LAJM Del Bianco, D Fiorani, AM Testa, E Bonetti, L Savini, and S Signoretti. Magnetothermal behavior of a nanoscale Fe/Fe oxide granular system. *Physical Review B*, 66(17):174418, 2002.
- [56] Quentin A Pankhurst, Ángel Yedra Martínez, and Luis Fernández Barquín. Interfacial exchange pinning in amorphous iron-boron nanoparticles. *Physical Review B*, 69(21):212401, 2004.
- [57] Elizabeth Martín Jefremovas. Desorden magnético en aleaciones nanométricas de tierras raras-Cu₂ (RCu₂). 2017.
- [58] JL Dormann, L Bessais, and D Fiorani. A dynamic study of small interacting particles: superparamagnetic model and spin-glass laws. *Journal of Physics C: Solid State Physics*, 21(10):2015, 1988.
- [59] Subhankar Bedanta, Oleg Petracic, and Wolfgang Kleemann. Supermagnetism. In *Handbook of magnetic materials*, volume 23, pages 1–83. Elsevier, 2015.
- [60] S Bedanta and W Kleemann. Topical review superparamagnetism. *J. of Phys. D: Appl. Phys.*, 42:013001, 2009.
- [61] Roland Mathieu and Per Nordblad. Collective magnetic behaviour. In *New Trends in Nanoparticle Magnetism*, pages 65–84. Springer, 2021.

- [62] José A De Toro, Daniel P Marques, Pablo Muñiz, Vassil Skumryev, Jordi Sort, Dominique Givord, and Josep Nogués. High temperature magnetic stabilization of cobalt nanoparticles by an antiferromagnetic proximity effect. *Physical review letters*, 115(5):057201, 2015.
- [63] Dmitry Zakharov, Hans-Albrecht Krug von Nidda, Mikhail Eremin, Joachim Deisenhofer, Rushana Eremina, and Alois Loidl. Anisotropic exchange in spin chains. In *Quantum Magnetism*, pages 193–238. Springer, 2008.
- [64] D Altbir, J d'Albuquerque e Castro, and P Vargas. Magnetic coupling in metallic granular systems. *Physical Review B*, 54(10):R6823, 1996.
- [65] Dora Altbir, Miguel Kiwi, Ricardo Ramírez, and Ivan K Schuller. Dipolar interaction and its interplay with interface roughness. *Journal of Magnetism and Magnetic Materials*, 149(3):L246–L250, 1995.
- [66] John E Greedan, NP Raju, AS Wills, C Morin, SM Shaw, and JN Reimers. Structure and magnetism in λ - MnO_2 . geometric frustration in a defect spinel. *Chemistry of materials*, 10(10):3058–3067, 1998.
- [67] E. M. Jefremovas, M. de la Fuente Rodríguez, J. Alonso, J. Rodríguez Fernández, J.I. Espeso, I. Puente-Orench, D.P. Rojas, A. García-Prieto, M.L. Fdez-Gubieda, L. Rodríguez Fernández, and L.Fernández Barquín. Exploring the different degrees of magnetic disorder in $\text{Tb}_x\text{R}_{1-x}\text{Cu}_2$ nanoparticle alloys. *Nanomaterials*, 10(11):2148, 2020.
- [68] Petra Jönsson. *Anisotropy, disorder and frustration in magnetic nanoparticle systems and spin glasses*. PhD thesis, Acta Universitatis Upsaliensis, 2002.
- [69] Samuel Frederick Edwards and Phil W Anderson. Theory of spin glasses. *Journal of Physics F: Metal Physics*, 5(5):965, 1975.
- [70] J Souletie and JL Tholence. Critical slowing down in spin glasses and other glasses: Fulcher versus power law. *Phys. Rev. B*, 32(1):516, 1985.
- [71] PV Prakash Madduri and SN Kaul. Intrinsic chiral-spin glass and spin glass transitions in compacted $\text{Ni}_5\text{Al}_3/\text{NiO}$ core/shell nanoparticles. *Physical Review Materials*, 3(12):126003, 2019.
- [72] L. Fernández Barquín, J. C. Gómez Sal, P. Gorria, J. S. Garitaonandia, and J. M. Barandiarán. Dynamic susceptibility of reentrant Fe-rich inhomogeneous amorphous alloys. *The European Physical Journal B - Condensed Matter and Complex Systems*, 35(1):3–12, Sep 2003.

- [73] Sayan Chandra, H Khurshid, Wanfeng Li, GC Hadjipanayis, MH Phan, and H Srikanth. Spin dynamics and criteria for onset of exchange bias in superspin glass Fe/ γ -Fe₂O₃ core-shell nanoparticles. *Physical Review B*, 86(1):014426, 2012.
- [74] MB Weissman. What is a spin glass? a glimpse via mesoscopic noise. *Reviews of Modern Physics*, 65(3):829, 1993.
- [75] T Jonsson, K Jonason, Petra Jönsson, and P Nordblad. Nonequilibrium dynamics in a three-dimensional spin glass. *Physical Review B*, 59(13):8770, 1999.
- [76] P Svedlindh, K Gunnarsson, Jan-Olov Andersson, H Aruga Katori, and A Ito. Time-dependent ac susceptibility in spin glasses. *Physical Review B*, 46(21):13867, 1992.
- [77] K Jonason, E Vincent, J Hammann, JP Bouchaud, and P Nordblad. Memory and chaos effects in spin glasses. *Physical Review Letters*, 81(15):3243, 1998.
- [78] T Jonsson, J Mattsson, C Djurberg, FA Khan, P Nordblad, and P Svedlindh. Aging in a magnetic particle system. *Physical review letters*, 75(22):4138, 1995.
- [79] Xi Chen, S. Bedanta, O. Petravic, W. Kleemann, S. Sahoo, S. Cardoso, and P. P. Freitas. Superparamagnetism versus superspin glass behavior in dilute magnetic nanoparticle systems. *Phys. Rev. B*, 72:214436, Dec 2005.
- [80] Malay Bandyopadhyay and Sushanta Dattagupta. Memory in nanomagnetic systems: Superparamagnetism versus spin-glass behavior. *Physical Review B*, 74(21):214410, 2006.
- [81] HT Diep et al. *Frustrated spin systems*. World Scientific, 2013.
- [82] J P Bouchaud, LF Cugliandolo, J Kurchan, and M Mézard. Spin glasses and random fields. *Directions in Condensed Matter Physics*, 12:443, 1998.
- [83] E Vincent, F Alet, M Alba, J Hammann, M Ocio, and JP Bouchaud. Aging phenomena in spin glasses and frustrated ferromagnets. *Physica B: Condensed Matter*, 280(1-4):260–261, 2000.
- [84] P Nordblad and P Svedlindh. Spin glasses and random fields. *AP Young, World Scientific, Singapore*, 1998.

- [85] Jean-Philippe Bouchaud, Vincent Dupuis, Jacques Hammann, and Eric Vincent. Separation of time and length scales in spin glasses: Temperature as a microscope. *Physical review B*, 65(2):024439, 2001.
- [86] M Lederman, R Orbach, JM Hammann, M Ocio, and E Vincent. Dynamics in spin glasses. *Physical Review B*, 44(14):7403, 1991.
- [87] Per Nordblad and Peter Svedlindh. Experiments on spin glasses. In *Spin Glasses and Random Fields*, pages 1–27. World Scientific, 1998.
- [88] P Koželj, S Vrtnik, M Krnel, A Jelen, D Gačnik, M Wencka, Z Jagličić, A Meden, G Dražić, F Danoix, et al. Spin-glass magnetism of the non-equiatomic CoCrFeMnNi high-entropy alloy. *Journal of Magnetism and Magnetic Materials*, 523:167579, 2021.
- [89] J Dolinšek, J Slanovec, Z Jagličić, M Heggen, S Balanetsky, M Feuerbacher, and K Urban. Broken ergodicity, memory effect, and rejuvenation in taylor-phase and decagonal al₃(mn, pd, fe) complex intermetallics. *Physical Review B*, 77(6):064430, 2008.
- [90] Janez Dolinšek, M Feuerbacher, M Jagodič, Z Jagličić, M Heggen, and K Urban. A thermal memory cell. *Journal of applied physics*, 106(4):043917, 2009.
- [91] MD Sturge. The Jahn–Teller effect in solids. In *Solid state physics*, volume 20, pages 91–211. Elsevier, 1968.
- [92] Jens Jensen and Allan R Mackintosh. *Rare earth magnetism*. Clarendon Press Oxford, 1991.
- [93] Nguyen Hoang Luong and JJM Franse. Magnetic properties of rare earth-Cu₂ compounds. *Handbook of Magnetic Materials*, 8:415–492, 1995.
- [94] Peter Fulde and Michael Loewenhaupt. Magnetic excitations in crystal-field split 4f systems. *Advances in Physics*, 34(5):589–661, 1985.
- [95] M T Hutchings. Point-charge calculations of energy levels of magnetic ions in crystalline electric fields. In *Solid state physics*, volume 16, pages 227–273. Elsevier, 1964.
- [96] KWH Stevens. The theory of paramagnetic relaxation. *Reports on Progress in Physics*, 30(1):189, 1967.

- [97] Do J Newman. Theory of lanthanide crystal fields. *Advances in Physics*, 20(84):197–256, 1971.
- [98] D Schmitt, P Morin, and J Pierre. Crystal field and magnetic properties in some cubic holmium compounds. *Physical Review B*, 15(4):1698, 1977.
- [99] E Gratz, M Loewenhaupt, M Divis, W Steiner, E Bauer, N Pillmayr, H Muller, H Nowotny, and B Frick. Structural, magnetic, electronic and transport properties of ndcu2. *J. Phys.: Condens. Matter*, 3(47):9297, 1991.
- [100] M Loewenhaupt, Th Reif, W Hahn, and B Frick. Magnetic excitation spectra of NdCu₂. *J. Magn. Magn. Mater.*, 177-181:1050–1051, 1998.
- [101] M Rotter, M Loewenhaupt, S Kramp, Th Reif, N M Pyka, W Schmidt, and R van de Kamp. Anisotropic magnetic exchange in orthorhombic RCu₂ compounds (R=rare earth). *Eur. Phys. J. B*, 14:29–42, 2000.
- [102] M Rotter, S Kramp, M Loewenhaupt, E Gratz, W Schmidt, N M Pyka, B Hennion, and R van de Kamp. Magnetic excitations in the antiferromagnetic phase NdCu₂ compound. *Appl. Phys. A*, 74(Suppl.):S751–S753, 2002.
- [103] J. H. van Vleck. chapter 9. Oxford University Press, London, 1932.
- [104] Allan R Mackintosh. *Rare earth magnetism: structures and excitations*. Clarendon Press, 1991.
- [105] Neil W Ashcroft, N David Mermin, et al. *Solid state physics*, 1976.
- [106] Steen Mørup, Daniel E Madsen, Cathrine Frandsen, Christian RH Bahl, and Mikkel F Hansen. Experimental and theoretical studies of nanoparticles of antiferromagnetic materials. *Journal of Physics: Condensed Matter*, 19(21):213202, 2007.
- [107] Keith A McEwen, Uschi Steigenberger, and Jens Jensen. Spin waves, phonons, and crystal-field excitations in thulium. *Physical Review B*, 43(4):3298, 1991.
- [108] RM Nicklow and N Wakabayashi. Spin excitations in the longitudinally modulated magnetic phase of erbium. *Physical Review B*, 51(18):12425, 1995.

- [109] Earl Callen and Herbert Callen. Ferromagnetic transitions and the one-third-power law. *Journal of Applied Physics*, 36(3):1140–1142, 1965.
- [110] P Morin and D Schmitt. Quadrupolar interactions and magneto-elastic effects in rare earth intermetallic compounds. *Handbook of Ferromagnetic Materials*, 5:1–132, 1990.
- [111] Etienne du Tremolet De Lacheisserie, Damien Gignoux, and Michel Schlenker. *Magnetism*, volume 1. Springer Science & Business Media, 2005.
- [112] M de la Fuente Rodríguez, JI Espeso, JA González, J Rodríguez Fernández, DP Rojas, L Rodríguez Fernández, A Garcia-Arribas, ML Fdez-Gubieda, C Echevarria-Bonet, ÉA Périgo, et al. Surfactant-assisted production of tbcu 2 nanoparticles. *Journal of Nanoparticle Research*, 19(7):231, 2017.
- [113] B Mutelet, N Keller, S Roux, MA Flores-Gonzales, F Lux, M Martini, O Tillement, C Billotey, M Janier, C Villiers, et al. Size-induced effect upon the Néel temperature of the antiferro/paramagnetic transition in gadolinium oxide nanoparticles. *Applied Physics A*, 105(1):215–219, 2011.
- [114] Cury Suryanarayana. Mechanical alloying and milling. *Progress in materials science*, 46(1-2):1–184, 2001.
- [115] Oliver Posth, Mikkel Fougt Hansen, Uwe Steinhoff, Lara Bogart, Paul Southern, Peter Svedlindh, Cordula Grüttner, L Fernández Barquin, Wojciech Szczerba, Frank Ludwig, et al. Classification of analysis methods for characterization of magnetic nanoparticle properties. In *Imeko XXI World Congress*, pages 1362–1367. Czech Technical University, Prague, 2015.
- [116] Helena Gavilán, Anja Kowalski, David Heinke, Abhilash Sugunan, Jens Sommertune, Miriam Varón, Lara K Bogart, Oliver Posth, Lunjie Zeng, David González-Alonso, et al. Colloidal flower-shaped iron oxide nanoparticles: Synthesis strategies and coatings. *Particle & particle systems characterization*, 34(7):1700094, 2017.
- [117] Lenaic Lartigue, Pierre Hugounenq, Damien Alloyeau, Sarah P Clarke, Michael Levy, Jean-Claude Bacri, Rana Bazzi, Dermot F Brougham, Claire Wilhelm, and Florence Gazeau. Cooperative organization in iron oxide multi-core nanoparticles potentiates their efficiency as heating mediators and MRI contrast agents. *ACS nano*, 6(12):10935–10949, 2012.

- [118] U Heyen and D Schüler. Growth and magnetosome formation by microaerophilic magnetospirillum strains in an oxygen-controlled fermentor. *Applied microbiology and biotechnology*, 61(5-6):536–544, 2003.
- [119] Karen Grünberg, Cathrin Wawer, Bradley M Tebo, and Dirk Schüler. A large gene cluster encoding several magnetosome proteins is conserved in different species of magnetotactic bacteria. *Applied and environmental microbiology*, 67(10):4573–4582, 2001.
- [120] Sarah Staniland, WYN Williams, Neil Telling, Gerrit Van Der Laan, Andrew Harrison, and Bruce Ward. Controlled cobalt doping of magnetosomes in vivo. *Nature nanotechnology*, 3(3):158–162, 2008.
- [121] Tanya Prozorov, Teresa Perez-Gonzalez, Carmen Valverde-Tercedor, Concepcion Jimenez-Lopez, Africa Yebra-Rodríguez, André Körnig, Damien Faivre, Surya K Mallapragada, Paul A Howse, Dennis A Bazylinski, et al. Manganese incorporation into the magnetosome magnetite: magnetic signature of doping. *European Journal of Mineralogy*, 26(4):457–471, 2014.
- [122] Masayoshi Tanaka, Rosemary Brown, Nicole Hondow, Atsushi Arakaki, Tadashi Matsunaga, and Sarah Staniland. Highest levels of Cu, Mn and Co doped into nanomagnetic magnetosomes through optimized biomineralisation. *Journal of Materials Chemistry*, 22(24):11919–11921, 2012.
- [123] Hirokazu Shimoshige, Yoshikata Nakajima, Hideki Kobayashi, Keiichi Yanagisawa, Yutaka Nagaoka, Shigeru Shimamura, Toru Mizuki, Akira Inoue, and Toru Maekawa. Formation of core-shell nanoparticles composed of magnetite and samarium oxide in magnetospirillum magneticum strain RSS-1. *PloS one*, 12(1):e0170932, 2017.
- [124] J Rodríguez-Carvajal. Recent advances in magnetic structure determination by neutron powder diffraction. *Physica B*, 192:55–69, 1993.
- [125] Bruce Ravel and MATHENA Newville. Athena, artemis, hephaestus: data analysis for X-ray absorption spectroscopy using ifeffit. *Journal of synchrotron radiation*, 12(4):537–541, 2005.
- [126] Hugo M Rietveld. A profile refinement method for nuclear and magnetic structures. *Journal of applied Crystallography*, 2(2):65–71, 1969.
- [127] R García Calderón, L Fernández Barquín, SN Kaul, JC Gómez Sal, Pedro Gorria, JS Pedersen, and RK Heenan. Small-angle neutron scattering study

- of a magnetically inhomogeneous amorphous alloy with reentrant behavior. *Physical Review B*, 71(13):134413, 2005.
- [128] Vitalij Pecharsky and Peter Zavalij. *Fundamentals of powder diffraction and structural characterization of materials*. Springer Science & Business Media, 2008.
- [129] PI Varghese and T Pradeep. *A textbook of nanoscience and nanotechnology*. Tata McGraw-Hill Education, 2003.
- [130] G Caglioti, A t Paoletti, and FP Ricci. Choice of collimators for a crystal spectrometer for neutron diffraction. *Nuclear Instruments*, 3(4):223–228, 1958.
- [131] G Caglioti, A t Paoletti, and FP Ricci. On resolution and luminosity of a neutron diffraction spectrometer for single crystal analysis. *Nuclear Instruments and Methods*, 9(2):195–198, 1960.
- [132] André Guinier. *X-ray diffraction in crystals, imperfect crystals, and amorphous bodies*. Courier Corporation, 1994.
- [133] P Thompson, DE Cox, and JB Hastings. Rietveld refinement of Debye–Scherrer synchrotron X-ray data from Al_2O_3 . *Journal of Applied Crystallography*, 20(2):79–83, 1987.
- [134] DC Koningsberger and Roelof Prins. *X-ray absorption: principles, applications, techniques of EXAFS, SEXAFS and XANES*. John Wiley and Sons Inc., New York, NY, 1987.
- [135] M Luisa Fdez-Gubieda, Ana García-Prieto, Javier Alonso, and Carlo Meneghini. X-ray absorption fine structure spectroscopy in Fe oxides and oxyhydroxides. *Iron Oxides*, pages 397–422, 2016.
- [136] D Grolimund, M Senn, M Trottmann, M Janousch, I Bonhoure, AM Scheidegger, and M Marcus. Shedding new light on historical metal samples using micro-focused synchrotron X-ray fluorescence and spectroscopy. *Spectrochimica Acta Part B: Atomic Spectroscopy*, 59(10-11):1627–1635, 2004.
- [137] M Luisa Fdez-Gubieda, Alicia Muela, Javier Alonso, Ana García-Prieto, Luca Olivi, Rodrigo Fernández-Pacheco, and Jose Manuel Barandiarán. Magnetite biomineralization in *Magnetospirillum gryphiswaldense*: time-resolved magnetic and structural studies. *ACS nano*, 7(4):3297–3305, 2013.

- [138] Tapan Chatterji. *Neutron scattering from magnetic materials*. Elsevier, 2005.
- [139] Albert Furrer, Joel F Mesot, and Thierry Strässle. *Neutron scattering in condensed matter physics*, volume 4. World Scientific Publishing Company, 2009.
- [140] VE Naish, Ruslan Pavlovich Ozerov, et al. *Neutron diffraction of magnetic materials*. Springer Science & Business Media, 2012.
- [141] COLIN G Windsor. An introduction to small-angle neutron scattering. *Journal of Applied Crystallography*, 21(6):582–588, 1988.
- [142] LA Feigin, Dimitrij I Svergun, et al. *Structure analysis by small-angle X-ray and neutron scattering*, volume 1. Springer, 1987.
- [143] Sebastian Mühlbauer, Dirk Honecker, Élio A Périgo, Frank Bergner, Sabrina Disch, André Heinemann, Sergey Erokhin, Dmitry Berkov, Chris Leighton, Morten Ring Eskildsen, et al. Magnetic small-angle neutron scattering. *Reviews of Modern Physics*, 91(1):015004, 2019.
- [144] Boualem Hammouda. A new guinier–porod model. *Journal of Applied Crystallography*, 43(4):716–719, 2010.
- [145] Andreas Michels, Artem Malyeyev, Ivan Titov, Dirk Honecker, Robert Cubitt, Elizabeth Blackburn, and Kiyonori Suzuki. Magnetic guinier law. *IUCrJ*, 7(1):136–142, 2020.
- [146] R Przeniosło, R Winter, H Natter, M Schmelzer, R Hempelmann, and W Wagner. Fractal pore distribution and magnetic microstructure of pulse-electrodeposited nanocrystalline Ni and Co. *Physical Review B*, 63(5):054408, 2001.
- [147] Mathias Bersweiler, Evelyn Pratami Sinaga, Inma Peral, Nozomu Adachi, Philipp Bender, Nina-Juliane Steinke, Elliot Paul Gilbert, Yoshikazu Todaka, Andreas Michels, and Yojiro Oba. Revealing defect-induced spin disorder in nanocrystalline Ni. *Physical Review Materials*, 5(4):044409, 2021.
- [148] Sabrina Disch, Raphael P Hermann, Erik Wetterskog, Andrey A Podlesnyak, Kwangjin An, Taeghwan Hyeon, German Salazar-Alvarez, Lennart Bergström, and Th Brückel. Spin excitations in cubic maghemite nanoparticles studied by time-of-flight neutron spectroscopy. *Phys. Rev. B*, 89(6):064402, 2014.

- [149] Claude Fermon and Francis Tasset. *Neutrons et magnétisme: JDN 9, Colleville, France, mai 2000*, volume 11. EDP Sciences, 2001.
- [150] R Scherm and B Fåk. Inelastic neutron scattering: introduction. In *Neutron and X-ray Spectroscopy*, pages 361–381. Springer, 2006.
- [151] H Bjerrum Møller and JC Gylden Houmann. Inelastic scattering of neutrons by spin waves in terbium. *Physical Review Letters*, 16(17):737, 1966.
- [152] Caroline A Schneider, Wayne S Rasband, and Kevin W Eliceiri. NIH Image to ImageJ: 25 years of image analysis. *Nature methods*, 9(7):671–675, 2012.
- [153] Petra Jönsson, Mikkel F Hansen, Peter Svedlindh, and Per Nordblad. Memory effects in an interacting magnetic nano-particle sample. *Physica B: Condensed Matter*, 284:1754–1755, 2000.
- [154] DC Joshi, G Gebresenbut, C Pay Gomez, and R Mathieu. Memory and rejuvenation in a quasicrystal. *EPL (Europhysics Letters)*, 132(2):27002, 2020.
- [155] R Bachmann, FJ DiSalvo Jr, TH Geballe, RL Greene, RE Howard, CN King, HC Kirsch, KN Lee, RE Schwall, H-U Thomas, et al. Heat capacity measurements on small samples at low temperatures. *Review of Scientific Instruments*, 43(2):205–214, 1972.
- [156] DP Rojas, LCJ Pereira, EB Lopes, JC Waerenborgh, LM da Silva, FG Gandra, and AN Medina. Transport and magnetic properties of Ce_2NiIn_3 . *Journal of alloys and compounds*, 432(1-2):34–38, 2007.
- [157] DP Rojas, L Fernández Barquín, J Rodríguez Fernández, L Rodríguez Fernández, and J Gonzalez. Phonon softening on the specific heat of nanocrystalline metals. *Nanotechnology*, 21(44):445702, 2010.
- [158] Bu-Xuan Wang, Le-Ping Zhou, and Xiao-Feng Peng. Surface and size effects on the specific heat capacity of nanoparticles. *International journal of thermophysics*, 27(1):139–151, 2006.
- [159] AA Azhar, CD Mitescu, WR Johanson, CB Zimm, and JA Barclay. Specific heat of GdRh. *Journal of Applied Physics*, 57(8):3235–3237, 1985.
- [160] Nguyen Hoang Luong, JJM Franse, and Than Duc Hien. Specific heat and thermal expansion in $\text{Gd}_x\text{Y}_{1-x}\text{Cu}_2$. *Journal of Physics F: Metal Physics*, 15(8):1751, 1985.

- [161] M Bouvier, P Lethuillier, and D Schmitt. Specific heat in some gadolinium compounds. I. Experimental. *Phys. Rev. B*, 43(16):13137, 1991.
- [162] D.P. Rojas, J.I. Espeso, L. Rodríguez Fernández, and L. Fernández Barquín. Heat capacity of nanocrystalline Yb_2O_3 . *Ceramics International*, 2021.
- [163] M. Rotter, A. Lindbaum, E. Gratz, G. Hilscher, H. Sassik, H.E. Fischer, M.T. Fernández-Díaz, R Arons, and Erwin Seidl. The magnetic structure of GdCu_2 . *Journal of Magnetism and Magnetic Materials (2000)*, 214:281–290, 2000.
- [164] CA Poldy and E Gratz. Electrical resistivity and magnetic investigations of the orthorhombic $\text{Tb}(\text{Ni},\text{Cu})_2$ system. *Journal of Magnetism and Magnetic Materials*, 8(3):223–231, 1978.
- [165] P Morin and D Schmitt. Magnetoelastic and quadrupolar couplings in ErZn and HoZn . *Journal of Physics F: Metal Physics*, 8(5):951, 1978.
- [166] JF Herbst. $\text{R}_2\text{Fe}_{14}\text{B}$ materials: Intrinsic properties and technological aspects. *Reviews of Modern Physics*, 63(4):819, 1991.
- [167] E Pina, FJ Palomares, MA Garcia, F Cebollada, A De Hoyos, JJ Romero, A Hernando, and JM Gonzalez. Coercivity in SmCo hard magnetic films for mems applications. *Journal of Magnetism and Magnetic Materials*, 290:1234–1236, 2005.
- [168] Yongsheng Liu, Datao Tu, Haomiao Zhu, and Xueyuan Chen. Lanthanide-doped luminescent nanoprobe: controlled synthesis, optical spectroscopy, and bioapplications. *Chemical Society Reviews*, 42(16):6924–6958, 2013.
- [169] Xiaoyong Wang, Zijian Zhou, Zhiyong Wang, Yunxin Xue, Yun Zeng, Jinhao Gao, Lei Zhu, Xianzhong Zhang, Gang Liu, and Xiaoyuan Chen. Gadolinium embedded iron oxide nanoclusters as T1–T2 dual-modal MRI-visible vectors for safe and efficient sirna delivery. *Nanoscale*, 5(17):8098–8104, 2013.
- [170] Richard H Kodama, Salah A Makhlof, and Ami E Berkowitz. Finite size effects in antiferromagnetic NiO nanoparticles. *Physical Review Letters*, 79(7):1393, 1997.
- [171] Xavier Batlle and Am Icar Labarta. Finite-size effects in fine particles: magnetic and transport properties. *Journal of Physics-London-D Applied Physics*, 35(6):R15–R42, 2002.

- [172] DS Williams, Paul M Shand, Thomas M Pekarek, Ralph Skomski, V Petkov, and DL Leslie-Pelecky. Magnetic transitions in disordered GdAl_2 . *Physical Review B*, 68(21):214404, 2003.
- [173] G. F. Zhou and H. Bakker. Mechanically induced structural and magnetic changes in the GdAl_2 laves phase. *Phys. Rev. B*, 52:9437–9445, Oct 1995.
- [174] EM Levin, VK Pecharsky, and KA Gschneidner Jr. Real and imaginary components of the alternating current magnetic susceptibility of RAl_2 ($\text{R} = \text{Gd}, \text{Dy}, \text{and Er}$) in the ferromagnetic region. *Journal of Applied Physics*, 90(12):6255–6262, 2001.
- [175] GF Zhou and H Bakker. Spin-glass behavior of mechanically milled crystalline GdAl_2 . *Phys. Rev. Lett.*, 73(2):344, 1994.
- [176] MA Morales, DS Williams, Paul M Shand, C Stark, Thomas M Pekarek, LP Yue, V Petkov, and DL Leslie-Pelecky. Disorder-induced depression of the Curie temperature in mechanically milled GdAl_2 . *Physical Review B*, 70(18):184407, 2004.
- [177] Z Smetana and V Šíma. Magnetic structures of $\text{R}(\text{Cu}, \text{Ni})_2$ compounds ($\text{R} = \text{heavy rare earth}$) studied by neutron diffraction. *Czechoslovak Journal of Physics B*, 35(11):1232–1238, 1985.
- [178] V Šíma, Z Smetana, Bente Lebech, and E Gratz. Temperature dependence of the magnetic structure of TbCu_2 . *Journal of Magnetism and Magnetic Materials*, 54:1357–1358, 1986.
- [179] F Fernández Barquín, JC Gómez Sal, P Gorria, JS Garitaonandia, and JM Barandiarán. Dynamic susceptibility of reentrant Fe-rich inhomogeneous amorphous alloys. *The European Physical Journal B-Condensed Matter and Complex Systems*, 35(1):3–12, 2003.
- [180] Pablo Álvarez, Jorge Sánchez Marcos, Pedro Gorria, Luis Fernández Barquín, and Jesús A Blanco. Magneto-caloric effect in FeZrB amorphous alloys near room temperature. *Journal of Alloys and Compounds*, 504:S150–S154, 2010.
- [181] H Rauch, M Zawisky, Ch Stellmach, and P Geltenbort. Giant absorption cross section of ultracold neutrons in gadolinium. *Physical Review Letters*, 83(24):4955, 1999.

- [182] J. Alonso, M. L. Fdez-Gubieda, J. M. Barandiarán, A. Svalov, L. Fernández Barquín, D. Alba Venero, and I. Orue. Crossover from superspin glass to superferromagnet in $\text{Fe}_x\text{Ag}_{100-x}$ nanostructured thin films ($20 \leq x \leq 50$). *Phys. Rev. B*, 82:054406, Aug 2010.
- [183] Xi Chen, S. Bedanta, O. Petravic, W. Kleemann, S. Sahoo, S. Cardoso, and P. P. Freitas. Superparamagnetism versus superspin glass behavior in dilute magnetic nanoparticle systems. *Phys. Rev. B*, 72:214436, Dec 2005.
- [184] JRL De Almeida and David J Thouless. Stability of the sherrington-kirkpatrick solution of a spin glass model. *Journal of Physics A: Mathematical and General*, 11(5):983, 1978.
- [185] Arun Kumar, Anatoliy Senyshyn, and Dhananjai Pandey. Evidence for cluster spin glass phase with precursor short-range antiferromagnetic correlations in the B-site disordered $\text{Ca}(\text{Fe}_{0.5}\text{Nb}_{0.5})\text{O}_3$ perovskite. *Physical Review B*, 99:214425, 2019.
- [186] MK Borombaev, RZ Levitin, AS Markosyan, VA Rejmer, EV Sinitsyn, and Z Smetana. Magnetic properties of the GdCu_2 single crystal. *Zhurnal Eksperimental'noj i Teoreticheskoy Fiziki*, 93(10):1517–1525, 1987.
- [187] H De Graaf, RC Thiel, and KHJ Buschow. Charge transfer and 155Gd isomer shift in various intermetallic compounds of Gd. *Journal of Physics F: Metal Physics*, 12(9):2079, 1982.
- [188] Michael Bauer, MSS Brooks, and Elmar Dormann. Orbital polarization of the conduction electrons in ferromagnetically ordered GdAl_2 . *Phys. Rev. B*, 48(2):1014, 1993.
- [189] G Aeppli, SM Shapiro, RJ Birgeneau, and HS Chen. Spin correlations and reentrant spin-glass behavior in amorphous Fe–Mn alloys. ii. dynamics. *Physical Review B*, 29(5):2589, 1984.
- [190] Mikkel F Hansen, Franz Bødker, Steen Mørup, Kim Lefmann, Kurt N Clausen, and Per-Anker Lindgård. Dynamics of magnetic nanoparticles studied by neutron scattering. *Physical review letters*, 79(24):4910, 1997.
- [191] Mikkel Fougth Hansen, Petra E Jönsson, Per Nordblad, and Peter Svedlindh. Critical dynamics of an interacting magnetic nanoparticle system. *Journal of Physics: Condensed Matter*, 14(19):4901, 2002.

- [192] Kentaro Takano, RH Kodama, AE Berkowitz, W Cao, and G Thomas. Interfacial uncompensated antiferromagnetic spins: Role in unidirectional anisotropy in polycrystalline $\text{Ni}_{81}\text{Fe}_{19}/\text{CoO}$ bilayers. *Physical Review Letters*, 79(6):1130, 1997.
- [193] M Rotter, Andreas Lindbaum, Ernst Gratz, Gerfried Hilscher, Herbert Sassik, HE Fischer, MT Fernández-Díaz, R Arons, and Erwin Seidl. The magnetic structure of GdCu_2 . *Journal of Magnetism and Magnetic Materials*, 214(3):281–290, 2000.
- [194] FN Gygax, D Andreica, A Schenck, and Y Ōnuki. Probing the magnetic structure of GdCu_2 by μSR spectroscopy. *Journal of Magnetism and Magnetic Materials*, 246(1-2):101–109, 2002.
- [195] M Rotter, A Schneidewind, M Loewenhaupt, M Doerr, A Stunault, A Hiess, A Lindbaum, E Gratz, G Hilscher, and H Sassik. Magnetic scattering on GdCu_2 . *Physica B: Condensed Matter*, 284:1329–1330, 2000.
- [196] Jin Lan, Weichao Yu, and Jiang Xiao. Antiferromagnetic domain wall as spin wave polarizer and retarder. *Nature communications*, 8(1):1–7, 2017.
- [197] Matthias B Jungfleisch, Wei Zhang, and Axel Hoffmann. Perspectives of antiferromagnetic spintronics. *Physics Letters A*, 382(13):865–871, 2018.
- [198] K Gunnarsson, P Svedlindh, P Nordblad, L Lundgren, H Aruga, and A Ito. Static scaling in a short-range Ising spin glass. *Physical Review B*, 43(10):8199, 1991.
- [199] A Ito, H Aruga, M Kikuchi, Y Syono, and H Takei. Phase diagram and reentrant spin-glass behavior in a random mixture of two Ising–antiferromagnets $\text{Fe}_x\text{Mn}_{1-x}\text{TiO}_3$. *Solid state communications*, 66(5):475–479, 1988.
- [200] Zhendong Fu, Yanzhen Zheng, Yinguo Xiao, Subhankar Bedanta, Anatoliy Senyshyn, Giovanna Giulia Simeoni, Yixi Su, Ulrich Rucker, Paul Kögerler, and Thomas Brückel. Coexistence of magnetic order and spin-glass-like phase in the pyrochlore antiferromagnet $\text{Na}_3\text{Co}(\text{CO}_3)_2\text{Cl}$. *Phys. Rev. B*, 87(21):214406, 2013.
- [201] Claes Djurberg, Peter Svedlindh, Per Nordblad, Mikkel Fougt Hansen, Franz Bødker, and Steen Mørup. Dynamics of an interacting particle system: evidence of critical slowing down. *Physical review letters*, 79(25):5154, 1997.

- [202] Z Nemati, H Khurshid, J Alonso, MH Phan, P Mukherjee, and H Srikanth. From core/shell to hollow Fe/ γ -Fe₂O₃ nanoparticles: evolution of the magnetic behavior. *Nanotechnology*, 26(40):405705, 2015.
- [203] K Binder and AP Young. Logarithmic dynamic scaling in spin-glasses. *Physical Review B*, 29(5):2864, 1984.
- [204] R Mathieu, P Jönsson, DNH Nam, and P Nordblad. Memory and superposition in a spin glass. *Physical Review B*, 63(9):092401, 2001.
- [205] S Sahoo, O Petravic, W Kleemann, P Nordblad, S Cardoso, and PP Freitas. Aging and memory in a superspin glass. *Physical Review B*, 67(21):214422, 2003.
- [206] Frank Döbrich, M Elmas, A Ferdinand, J Markmann, M Sharp, H Eckerlebe, J Kohlbrecher, R Birringer, and Andreas Michels. Grain-boundary-induced spin disorder in nanocrystalline gadolinium. *Journal of Physics: Condensed Matter*, 21(15):156003, 2009.
- [207] SM Podgornykh and NI Kourov. Low-temperature specific heat of GdCu, GdCu₂, and GdCu₅ antiferromagnets. *bulletin of the russian academy of sciences: Physics*, 71(8):1079–1080, 2007.
- [208] Abel García-Saiz, Imanol de Pedro, Pedro Migowski, Oriol Vallcorba, Javier Junquera, Jesus Angel Blanco, Oscar Fabelo, Denis Sheptyakov, Joao Carlos Waerenborgh, María Teresa Fernandez-Díaz, et al. Anion- π and Halide-Halide nonbonding interactions in a new ionic liquid based on imidazolium cation with three-dimensional magnetic ordering in the solid state. *Inorganic chemistry*, 53(16):8384–8396, 2014.
- [209] Bernard Chevalier, Samir F Matar, Michel Ménétrier, J Sanchez Marcos, and J Rodríguez Fernández. Influence of Ce–H bonding on the physical properties of the hydrides CeCoSiH_{1.0} and CeCoGeH_{1.0}. *Journal of Physics: Condensed Matter*, 18(26):6045, 2006.
- [210] Erode Gopal. *Specific heats at low temperatures*. Springer Science & Business Media, 2012.
- [211] Atsushi Koyanagi, Yoshiyuki Yoshida, Yasushi Kimura, Rikio Settai, Kiyohiro Sugiyama, and Yoshichika Ōnuki. Magnetic and electrical properties of GdCu₂. *Journal of the Physical Society of Japan*, 67(7):2510–2513, 1998.

- [212] Douglas L Martin. Specific heat of spin-glass CuMn below 3 K. *Physical Review B*, 20(1):368, 1979.
- [213] RR Arons, M Loewenhaupt, Th Reif, and E Gratz. The magnetic structures of NdCu₂ in zero field. *J. Phys Condens. Matter*, 6(34):6789, 1994.
- [214] M Loewenhaupt, Th Reif, RR Arons, E Gratz, M Rotter, and B Lebeck. The magnetic structures of NdCu₂ determined by single crystal neutron diffraction. *Zeitschrift für Physik B Condensed Matter*, 96(4):491–496, 1995.
- [215] M Ellerby, KA McEwen, M De Podesta, M Rotter, and E Gratz. Detailed magnetization study of ndcu2 at low temperatures. *Journal of Physics: Condensed Matter*, 7(9):1897, 1995.
- [216] Alexander A Baker, Jonathan RI Lee, Christine A Orme, Tony van Buuren, and Scott K McCall. Suppression of low temperature magnetic ordering in samarium nanoparticles. *J. Phys.: Condens. Matter*, 32(49):495803, 2020.
- [217] L Bozukov, A Gilewski, E Gratz, A Apostolov, and K Kamenov. High field magnetization and magneto-resistance of NdCu₂. *Physica B: Condensed Matter*, 177(1-4):299–301, 1992.
- [218] K Shibata, XZ Yu, T Hara, D Morikawa, N Kanazawa, K Kimoto, S Ishiwata, Y Matsui, and Y Tokura. Towards control of the size and helicity of skyrmions in helimagnetic alloys by spin-orbit coupling. *Nature nanotechnology*, 8(10):723–728, 2013.
- [219] E. M. Jefremovas, M. de la Fuente Rodríguez, F. Damay, B. Fåk, A. Michels, J. A. Blanco, and L. F. Barquín. Observation of surface magnons and crystalline electric field shifts in superantiferromagnetic NdCu₂ nanoparticles. *Phys. Rev. B*, 104:134404, Oct 2021.
- [220] Mathias Doerr, M Rotter, and Andreas Lindbaum. Magnetostriction in rare-earth based antiferromagnets. *Advances in Physics*, 54(1):1–66, 2005.
- [221] J Weissmüller and Andreas Michels. Comment on “magnetic correlations in nanostructured ferromagnets”. *Physical review letters*, 87(14):149701, 2001.
- [222] Paul W Schmidt. Small-angle scattering studies of disordered, porous and fractal systems. *Journal of Applied Crystallography*, 24(5):414–435, 1991.

- [223] Thomas Lucatorto, Marc De Graef, and Po-Zen Wong. *Methods of the physics of porous media*. Academic Press, 1999.
- [224] M Veith, S Faber, R Hempelmann, S Janssen, J Prewo, and H Eckerlebe. Synthesis and microstructure of nanostructured Al/Al₂O₃(H)-composite. *Journal of materials science*, 31(8):2009–2017, 1996.
- [225] Andreas Michels, M Elmas, Frank Döbrich, M Ames, J Markmann, M Sharp, H Eckerlebe, J Kohlbrecher, and R Birringer. Porosity-induced spin disorder in nanocrystalline inert-gas-condensed iron. *EPL (Europhysics Letters)*, 85(4):47003, 2009.
- [226] Jun-ichi Suzuki, Yasuo Endoh, Masatoshi Arai, Michihiro Furusaka, and Hideki Yoshizawa. Small angle neutron scattering studies on Fe_{0.715}Al_{0.285} reentrant spin glass. *Journal of the Physical Society of Japan*, 59(2):718–724, 1990.
- [227] D Martín Rodríguez, F Plazaola, JJ Del Val, José S Garitaonandia, GJ Cuello, and C Dewhurst. Small-angle neutron-scattering studies of reentrant spin-glass behavior in Fe–Al alloys. *Journal of applied physics*, 99(8):08H502, 2006.
- [228] A Tomou, D Gournis, I Panagiotopoulos, Y Huang, GC Hadjipanayis, and BJ Kooi. Weak ferromagnetism and exchange biasing in cobalt oxide nanoparticle systems. *J. App. Phys*, 99(12):123915, 2006.
- [229] AH Morrish. *The Physical Principles of Magnetism*. Wiley, New York, 1965.
- [230] Stine Nyborg Klausen, Kim Lefmann, P-A Lindgård, L Theil Kuhn, Christian Robert Haffenden Bahl, Cathrine Frandsen, Steen Mørup, Bertrand Roessli, N Cavadini, and Ch Niedermayer. Magnetic anisotropy and quantized spin waves in hematite nanoparticles. *Phys. Rev. B*, 70(21):214411, 2004.
- [231] Julien Robert, Elsa Lhotel, Gyorgy Remenyi, S Sahling, Isabelle Mirebeau, Claudia Decorse, Benjamin Canals, and Sylvain Petit. Spin dynamics in the presence of competing ferromagnetic and antiferromagnetic correlations in Yb₂Ti₂O₇. *Phys. Rev. B*, 92(6):064425, 2015.
- [232] Maciej Dabrowski, Takafumi Nakano, David M Burn, Andreas Frisk, David G Newman, Christoph Klewe, Qian Li, Mengmeng Yang, Padraic Shafer, Elke Arenholz, et al. Coherent transfer of spin angular momentum by evanescent spin waves within antiferromagnetic NiO. *Phys. Rev. Lett.*, 124(21):217201, 2020.

- [233] Y Nambu, J Barker, Y Okino, T Kikkawa, Y Shiomi, M Enderle, T Weber, B Winn, M Graves-Brook, JM Tranquada, et al. Observation of Magnon Polarization. *Phys. Rev. Lett.*, 125(2):027201, 2020.
- [234] Michael Hermele, Matthew PA Fisher, and Leon Balents. Pyrochlore photons: The U (1) spin liquid in a $S=1/2$ three-dimensional frustrated magnet. *Physical Review B*, 69(6):064404, 2004.
- [235] Michel JP Gingras and Paul A McClarty. Quantum spin ice: a search for gapless quantum spin liquids in pyrochlore magnets. *Reports on Progress in Physics*, 77(5):056501, 2014.
- [236] Yao Shen, Yao-Dong Li, Hongliang Wo, Yuesheng Li, Shoudong Shen, Bingying Pan, Qisi Wang, HC Walker, Paul Steffens, Martin Boehm, et al. Evidence for a spinon Fermi surface in a triangular-lattice quantum-spin-liquid candidate. *Nature*, 540(7634):559–562, 2016.
- [237] Oliver Gutfleisch, Matthew A Willard, Ekkes Brück, Christina H Chen, SG Sankar, and J Ping Liu. Magnetic mat. and devices for the 21st century: stronger, lighter, and more energy efficient. *Advanced Mater.*, 23(7):821–842, 2011.
- [238] VK Pecharsky and KA Gschneidner Jr. Effect of alloying on the giant magnetocaloric effect of $Gd_5(Si_2Ge_2)$. *J. Magn. Magn. Mater.*, 167(3):L179–L184, 1997.
- [239] E Gratz, N Pillmayr, E Bauer, H Muller, B Barbara, and M Loewenhaupt. Low-temperature X-ray diffraction, transport properties, specific-heat, thermal expansion and magnetic investigations of $SmCu_2$. *J. Phys.: Condens. Matter*, 2(6):1485, 1990.
- [240] M Rotter, M Loewenhaupt, S Kramp, T Reif, NM Pyka, W Schmidt, and R van de Kamp. Anisotropic magnetic exchange in orthorhombic RCu_2 compounds (R= rare earth). *The European Physical Journal B-Condensed Matter and Complex Systems*, 14(1):29–42, 2000.
- [241] LT Baczewski, M Piecuch, J Durand, G Marchal, and P Delcroix. Influence of interface effects on a rare-earth crystal field in iron–rare-earth multilayers. *Physical Review B*, 40(16):11237, 1989.
- [242] KR Lea, MJM Leask, and WP Wolf. The raising of angular momentum degeneracy of f–electron terms by cubic crystal fields. *J. of Physics and Chem. of Solids*, 23(10):1381–1405, 1962.

- [243] RJ Birgeneau. Transition probabilities for f-electron J-multiplets in cubic crystal fields. *J. Phys. and Chem. of Solids*, 33(1):59–68, 1972.
- [244] Pinaki Das, P-F Lory, Rebecca Flint, Tai Kong, T Hiroto, Sergey L Bud'ko, Paul C Canfield, M de Boissieu, Andreas Kreyssig, and Alan I Goldman. Crystal electric field excitations in the quasicrystal approximant TbCd₆ studied by inelastic neutron scattering. *Phys. Rev. B*, 95(5):054408, 2017.
- [245] Stefan Philippi, Jürgen Markmann, Rainer Birringer, and Andreas Michels. Grain-size-dependent magnetic susceptibility of nanocrystalline terbium. *J. of Appl. Phys.*, 105(7):07A701, 2009.
- [246] M Hennion, C Bellouard, I Mirebeau, JL Dormann, and M Nogues. Dual spin dynamics of small Fe particles. *EPL (Europhysics Letters)*, 25(1):43, 1994.
- [247] P Talagala, Petru S Fodor, D Haddad, R Naik, LE Wenger, PP Vaishnava, and VM Naik. Determination of magnetic exchange stiffness and surface anisotropy constants in epitaxial Ni_{1-x}Co_x (001) films. *Physical Review B*, 66(14):144426, 2002.
- [248] Nguyen Hoang Luong, Than Duc Hien, and Nguyen Huu Duc. Magnetic properties of Tb_xY_{1-x}Cu₂ compounds at low temperatures. *Physica B+ C*, 109:2135–2137, 1982.
- [249] P Svoboda, J Vejpravová, M Doerr, M Rotter, J-U Hoffmann, I Satoh, and T Komatsubara. Ising-axis conversion in Tb_{0.5}Y_{0.5}Cu₂. *Journal of Magnetism and Magnetic Materials*, 310(2):1767–1769, 2007.
- [250] R Rajivgandhi, J Arout Chelvane, AK Nigam, SK Malik, and R Nirmala. Preservation of large low temperature magnetocaloric effect in metamagnetic intermetallic compounds RCu₂ (R= Gd, Tb, Dy, Ho and Er) upon rapid solidification. *Journal of Alloys and Compounds*, 815:152659, 2020.
- [251] Vitalij K Pecharsky and Karl A Gschneidner Jr. Giant magnetocaloric effect in Gd₅(Si₂Ge₂). *Physical review letters*, 78(23):4494, 1997.
- [252] P Poddar, J Gass, DJ Rebar, S Srinath, H Srikanth, SA Morrison, and EE Carpenter. Magnetocaloric effect in ferrite nanoparticles. *Journal of Magnetism and Magnetic Materials*, 307(2):227–231, 2006.

- [253] Ram Kumar, Kartik K Iyer, PL Paulose, and EV Sampathkumaran. Magnetic and transport anomalies in R_2RhSi_3 ($R= Gd, Tb, \text{ and } Dy$) resembling those of the exotic magnetic material Gd_2PdSi_3 . *Physical Review B*, 101(14):144440, 2020.
- [254] A Lindbaum, S Heathman, G Kresse, M Rotter, E Gratz, A Schneidewind, G Behr, K Litfin, T Le Bihan, and P Svoboda. Structural stability of $LaCu_2$ and YCu_2 studied by high-pressure X-ray diffraction and ab initio total energy calculations. *Journal of Physics: Condensed Matter*, 12(14):3219, 2000.
- [255] DP Rojas, JI Espeso, L Fernández Barquín, J Rodríguez Fernández, and JC Gómez Sal. Spin-glass behavior of mechanically milled $TbCu_2$. *Journal of Magnetism and Magnetic Materials*, 310(2):e506–e508, 2007.
- [256] Y Hashimoto et al. Magnetic properties of single crystal rare earth intermetallic compounds RCu_2 . 1979.
- [257] Š Zajac, M Diviš, V Šíma, and Z Smetana. Magnetization in $(Tb_xY_{1-x})Cu_2$. *Le Journal de Physique Colloques*, 49(C8):C8–413, 1988.
- [258] Z Smetana, V Šíma, E Gratz, and JJM Franse. Neutron diffraction study of the $R(Cu_{1-x}Ni_x)_2$ ($R= Tb, Ho$) system. *Journal of Magnetism and Magnetic Materials*, 31:633–634, 1983.
- [259] Ram Kumar, Jyoti Sharma, Kartik K Iyer, and EV Sampathkumaran. Reentrant spin-glass and transport behavior of Gd_4PtAl , a compound with three sites for Gd. *Journal of Magnetism and Magnetic Materials*, 490:165515, 2019.
- [260] N Rinaldi-Montes, P Gorria, David Martínez-Blanco, AB Fuentes, L Fernández Barquín, Inés Puente-Orench, and JA Blanco. Scrutinizing the role of size reduction on the exchange bias and dynamic magnetic behavior in NiO nanoparticles. *Nanotechnology*, 26(30):305705, 2015.
- [261] TD Hien, NH Luong, NH Duc, NP Thuy, PH Frings, and JJM Franse. Magnetic properties of Rcu_2 ($R= Dy, Ho, Er$) and $Dy_xY_{1-x}Cu_2$ compounds. *Journal of Magnetism and Magnetic Materials*, 31:245–246, 1983.
- [262] Nguyen Hoang Luong and JJM Franse. Thermal expansion, forced magnetostriction, and pressure dependence of the Néel temperature in $GdCu_2$ and $TbCu_2$. *physica status solidi (a)*, 66(1):399–406, 1981.

- [263] Robert D Shannon. Revised effective ionic radii and systematic studies of interatomic distances in halides and chalcogenides. *Acta crystallographica section A: crystal physics, diffraction, theoretical and general crystallography*, 32(5):751–767, 1976.
- [264] Rebeca Garcia Calderon. *Efectos cooperativos en la relajación magnética de aleaciones nanométricas de Fe–Cu–Ag*. PhD thesis, Universidad de Cantabria, 2006.
- [265] Yoshihiro Yamada and Akihiko Sakata. Weak antiferromagnetism in NbFe_2 . *Journal of the Physical Society of Japan*, 57(1):46–49, 1988.
- [266] Kenneth S Cole and Robert H Cole. Dispersion and absorption in dielectrics I. alternating current characteristics. *The Journal of chemical physics*, 9(4):341–351, 1941.
- [267] PH Fang. Cole—cole diagram and the distribution of relaxation times. *The Journal of Chemical Physics*, 42(10):3411–3413, 1965.
- [268] T Bitoh, K Ohba, M Takamatsu, T Shirane, and S Chikazawa. Comparative study of linear and nonlinear susceptibilities of fine-particle and spin-glass systems: quantitative analysis based on the superparamagnetic blocking model. *Journal of Magnetism and Magnetic Materials*, 154(1):59–65, 1996.
- [269] M Rotter, M Loewenhaupt, M Doerr, A Lindbaum, and H Michor. Non-collinear amplitude-modulated magnetic order in Gd compounds. *Physical Review B*, 64(1):014402, 2001.
- [270] Nguyen Hoang Luong. Crystalline-electric-field effect in some rare-earth intermetallic compounds. *Physica B: Condensed Matter*, 319(1-4):90–104, 2002.
- [271] Vasilios Melfos, Bruno Helly, and Panagiotis Voudouris. The ancient Greek names “Magnesia” and “Magnetes” and their origin from the magnetite occurrences at the Mavrovouni mountain of Thessaly, central Greece. A mineralogical–geochemical approach. *Archaeological and Anthropological Sciences*, 3(2):165–172, 2011.
- [272] QA Pankhurst, NTK Thanh, SK Jones, and J Dobson. Progress in applications of magnetic nanoparticles in biomedicine. *Journal of Physics D: Applied Physics*, 42(22):224001, 2009.

- [273] Burghard Thiesen and Andreas Jordan. Clinical applications of magnetic nanoparticles for hyperthermia. *International journal of hyperthermia*, 24(6):467–474, 2008.
- [274] HJJOM Shokrollahi. A review of the magnetic properties, synthesis methods and applications of maghemite. *Journal of Magnetism and Magnetic Materials*, 426:74–81, 2017.
- [275] Pierre Hugounenq, Michael Levy, Damien Alloyeau, Lenaïc Lartigue, Emmanuelle Dubois, Valerie Cabuil, Christian Ricolleau, Stephane Roux, Claire Wilhelm, Florence Gazeau, et al. Iron oxide monocrystalline nanoflowers for highly efficient magnetic hyperthermia. *The Journal of Physical Chemistry C*, 116(29):15702–15712, 2012.
- [276] SK Shaw, A Biswas, A Gangwar, P Maiti, CL Prajapat, Sher Singh Meena, and NK Prasad. Synthesis of exchange coupled nanoflowers for efficient magnetic hyperthermia. *Journal of Magnetism and Magnetic Materials*, 484:437–444, 2019.
- [277] Joshua E Rosen, Lorena Chan, Dar-Bin Shieh, and Frank X Gu. Iron oxide nanoparticles for targeted cancer imaging and diagnostics. *Nanomedicine: Nanotechnology, Biology and Medicine*, 8(3):275–290, 2012.
- [278] Sophie Laurent and Morteza Mahmoudi. Superparamagnetic iron oxide nanoparticles: promises for diagnosis and treatment of cancer. *International journal of molecular epidemiology and genetics*, 2(4):367, 2011.
- [279] Beata Chertok, Bradford A Moffat, Allan E David, Faquan Yu, Christian Bergemann, Brian D Ross, and Victor C Yang. Iron oxide nanoparticles as a drug delivery vehicle for MRI monitored magnetic targeting of brain tumors. *Biomaterials*, 29(4):487–496, 2008.
- [280] Thomas Vangijzegem, Dimitri Stanicki, and Sophie Laurent. Magnetic iron oxide nanoparticles for drug delivery: applications and characteristics. *Expert opinion on drug delivery*, 16(1):69–78, 2019.
- [281] See <https://www.magforce.com/> for additional information.
- [282] S Luo, LF Wang, WJ Ding, H Wang, JM Zhou, HK Jin, SF Su, and WW Ouyang. Clinical trials of magnetic induction hyperthermia for treatment of tumours. *OA Cancer*, 2(2), 2014.

- [283] Esther Cazares-Cortes, Sonia Cabana, Charlotte Boitard, Emilie Nehlig, Nébéwia Griffete, Jérôme Fresnais, Claire Wilhelm, Ali Abou-Hassan, and Christine Ménager. Recent insights in magnetic hyperthermia: From the “hot-spot” effect for local delivery to combined magneto-photo-thermia using magneto-plasmonic hybrids. *Advanced drug delivery reviews*, 138:233–246, 2019.
- [284] Irene Rubia-Rodríguez, Antonio Santana-Otero, Simo Spassov, Etelka Tombácz, Christer Johansson, Patricia De La Presa, Francisco J Teran, María del Puerto Morales, Sabino Veintemillas-Verdaguer, Nguyen TK Thanh, et al. Whither magnetic Hyperthermia? A tentative roadmap. *Materials*, 14(4):706, 2021.
- [285] Aaron C Anselmo and Samir Mitragotri. A review of clinical translation of inorganic nanoparticles. *The AAPS journal*, 17(5):1041–1054, 2015.
- [286] EM Múzquiz-Ramos, V Guerrero-Chávez, BI Macías-Martínez, CM López-Badillo, and LA García-Cerda. Synthesis and characterization of maghemite nanoparticles for hyperthermia applications. *Ceramics International*, 41(1):397–402, 2015.
- [287] Michael Lévy, Claire Wilhelm, Jean-Michel Siaugue, Olivier Horner, Jean-Claude Bacri, and Florence Gazeau. Magnetically induced hyperthermia: size-dependent heating power of γ -Fe₂O₃ nanoparticles. *Journal of Physics: Condensed Matter*, 20(20):204133, 2008.
- [288] K Simeonidis, C Martinez-Boubeta, D Serantes, S Ruta, O Chubykalo-Fesenko, R Chantrell, J Oró-Solé, LI Balcells, AS Kamzin, RA Nazipov, et al. Controlling magnetization reversal and hyperthermia efficiency in core-shell iron-iron oxide magnetic nanoparticles by tuning the interphase coupling. *ACS applied nano materials*, 3(5):4465–4476, 2020.
- [289] R Hergt, R Hiergeist, I Hilger, Werner A Kaiser, Y Lapatnikov, S Margel, and Uwe Richter. Maghemite nanoparticles with very high AC-losses for application in RF-magnetic hyperthermia. *Journal of Magnetism and Magnetic Materials*, 270(3):345–357, 2004.
- [290] Alberto Curcio, Amanda KA Silva, Sonia Cabana, Ana Espinosa, Benoit Baptiste, Nicolas Menguy, Claire Wilhelm, and Ali Abou-Hassan. Iron oxide nanoflowers@ CuS hybrids for cancer tri-therapy: interplay of photothermal therapy, magnetic hyperthermia and photodynamic therapy. *Theranostics*, 9(5):1288, 2019.

- [291] Sonia Cabana, Alberto Curcio, Aude Michel, Claire Wilhelm, and Ali Abou-Hassan. Iron oxide mediated photothermal therapy in the second biological window: A comparative study between magnetite/maghemite nanospheres and nanoflowers. *Nanomaterials*, 10(8):1548, 2020.
- [292] Gerardo F Goya, Enio Lima Jr, Amanda D Arelaro, Teobaldo Torres, Hercilio R Rechenberg, Liane Rossi, Clara Marquina, and M Ricardo Ibarra. Magnetic hyperthermia with Fe_3O_4 nanoparticles: The influence of particle size on energy absorption. *IEEE Transactions on Magnetics*, 44(11):4444–4447, 2008.
- [293] Manuel Arruebo, Rodrigo Fernández-Pacheco, M Ricardo Ibarra, and Jesús Santamaría. Magnetic nanoparticles for drug delivery. *Nano today*, 2(3):22–32, 2007.
- [294] Richard Blakemore. Magnetotactic bacteria. *Science*, 190(4212):377–379, 1975.
- [295] Christopher T Lefèvre and Dennis A Bazylinski. Ecology, diversity, and evolution of magnetotactic bacteria. *Microbiology and Molecular Biology Reviews*, 77(3):497–526, 2013.
- [296] Edouard Alphanbéry. Applications of magnetosomes synthesized by magnetotactic bacteria in medicine. *Frontiers in bioengineering and biotechnology*, 2:5, 2014.
- [297] Edouard Alphanbéry. Bio-synthesized iron oxide nanoparticles for cancer treatment. *International journal of pharmaceutics*, 586:119472, 2020.
- [298] Edouard Alphanbéry. Applications of magnetotactic bacteria and magnetosome for cancer treatment: a review emphasizing on practical and mechanistic aspects. *Drug Discovery Today*, 25(8):1444–1452, 2020.
- [299] RM Kershi, FM Ali, and MA Sayed. Influence of rare earth ion substitutions on the structural, optical, transport, dielectric, and magnetic properties of superparamagnetic iron oxide nanoparticles. *Journal of Advanced Ceramics*, 7(3):218–228, 2018.
- [300] Parvesh Sharma, Scott C Brown, Glenn Walter, Swadeshmukul Santra, Edward Scott, Hideki Ichikawa, Yoshinobu Fukumori, and Brij M Moudgil. Gd nanoparticulates: from magnetic resonance imaging to neutron capture therapy. *Advanced Powder Technology*, 18(6):663–698, 2007.

- [301] Guilong Zhang, Ruohong Du, Lele Zhang, Dongqing Cai, Xiao Sun, Yong Zhou, Jian Zhou, Junchao Qian, Kai Zhong, Kang Zheng, et al. Gadolinium-doped iron oxide nanoprobe as multifunctional bioimaging agent and drug delivery system. *Advanced Functional Materials*, 25(38):6101–6111, 2015.
- [302] Rodrigo M Petoral Jr, Fredrik Soderlind, Anna Klasson, Anke Suska, Marc A Fortin, Natalia Abrikosova, Linnéa Selegård, Per-Olov Kall, Maria Engstrom, and Kajsa Uvdal. Synthesis and characterization of Tb³⁺-doped Gd₂O₃ nanocrystals: a bifunctional material with combined fluorescent labeling and MRI contrast agent properties. *The Journal of Physical Chemistry C*, 113(17):6913–6920, 2009.
- [303] Alejandro G Roca, Jose F Marco, María del Puerto Morales, and Carlos J Serna. Effect of nature and particle size on properties of uniform magnetite and maghemite nanoparticles. *The Journal of Physical Chemistry C*, 111(50):18577–18584, 2007.
- [304] Fernando Vereda, Juan de Vicente, María del Puerto Morales, Fernando Rull, and Roque Hidalgo-Álvarez. Synthesis and characterization of single-domain monocrystalline magnetite particles by oxidative aging of Fe(OH)₂. *The Journal of Physical Chemistry C*, 112(15):5843–5849, 2008.
- [305] Wonbaek Kim, Chang-Yul Suh, Sung-Wook Cho, Ki-Min Roh, Hanjung Kwon, Kyungsun Song, and In-Jin Shon. A new method for the identification and quantification of magnetite–maghemite mixture using conventional X-ray diffraction technique. *Talanta*, 94:348–352, 2012.
- [306] CJ Serna, F Bødker, kS Mørup, MP Morales, F Sandiumenge, and S Veintemillas-Verdaguer. Spin frustration in maghemite nanoparticles. *Solid state communications*, 118(9):437–440, 2001.
- [307] Jiro Yoshida and Shuichi Iida. X-ray study of the phase transition in magnetite. *Journal of the Physical Society of Japan*, 47(5):1627–1633, 1979.
- [308] ME Fleet. The structure of magnetite. *Acta Crystallographica Section B: Structural Crystallography and Crystal Chemistry*, 37(4):917–920, 1981.
- [309] Anna Fischer, Manuel Schmitz, Barbara Aichmayer, Peter Fratzl, and Damien Faivre. Structural purity of magnetite nanoparticles in magnetotactic bacteria. *Journal of The Royal Society Interface*, 8(60):1011–1018, 2011.

- [310] YQ Jia. Crystal radii and effective ionic radii of the rare earth ions. *Journal of Solid State Chemistry*, 95(1):184–187, 1991.
- [311] RD T Shannon and C Tfc Prewitt. Effective ionic radii in oxides and fluorides. *Acta Crystallographica Section B: Structural Crystallography and Crystal Chemistry*, 25(5):925–946, 1969.
- [312] Honghu Zhang, Vikash Malik, Surya Mallapragada, and Mufit Akinc. Synthesis and characterization of Gd-doped magnetite nanoparticles. *Journal of Magnetism and Magnetic Materials*, 423:386–394, 2017.
- [313] Aleksandra Rekorajska, Grzegorz Cichowicz, Michał K Cyranski, Marek Pekala, and Pawel Kryszynski. Synthesis and characterization of Gd³⁺- and Tb³⁺-doped iron oxide nanoparticles for possible endoradiotherapy and hyperthermia. *Journal of Magnetism and Magnetic Materials*, 479:50–58, 2019.
- [314] Suvra S Laha, Ehab Abdelhamid, Maheshika P Arachchige, Ajay Kumar, and Ambesh Dixit. Ferroic ordering and charge-spin-lattice order coupling in Gd-doped Fe₃O₄ nanoparticles relaxor multiferroic system. *Journal of the American Ceramic Society*, 100(4):1534–1541, 2017.
- [315] Jinhua Li, Nicolas Menguy, Marie-Anne Arrio, Philippe Saintavit, Amélie Juhin, Yinzhao Wang, Haitao Chen, Oana Bunau, Edwige Otero, Philippe Ohresser, et al. Controlled cobalt doping in the spinel structure of magnetosome magnetite: new evidences from element-and site-specific X-ray magnetic circular dichroism analyses. *Journal of The Royal Society Interface*, 13(121):20160355, 2016.
- [316] Henrik Jensen, Joergen H Pedersen, JE Jørgensen, J Skov Pedersen, Karsten Dan Joensen, Steen B Iversen, and EG Søgaard. Determination of size distributions in nanosized powders by TEM, XRD, and SAXS. *Journal of Experimental Nanoscience*, 1(3):355–373, 2006.
- [317] D Muñoz, L Marcano, R Martín-Rodríguez, L Simonelli, A Serrano, A García-Prieto, ML Fdez-Gubieda, and A Muela. Magnetosomes could be protective shields against metal stress in magnetotactic bacteria. *Scientific Reports*, 10(1):1–12, 2020.
- [318] David Muñoz Rodríguez. *Nanopartículas magnéticas de origen biológico: síntesis y aplicaciones en biomedicina*. PhD thesis, Universidad del País Vasco UPV/EHU, 2019.

- [319] Anna Corrias, Guido Ennas, Gavin Mountjoy, and Giorgio Paschina. An X-ray absorption spectroscopy study of the Fe K-edge in nanosized maghemite and in Fe₂O₃-SiO₂ nanocomposites. *Physical Chemistry Chemical Physics*, 2(5):1045–1050, 2000.
- [320] Max Wilke, François Farges, Pierre-Emmanuel Petit, Gordon E Brown Jr, and François Martin. Oxidation state and coordination of Fe in minerals: A Fe K-XANES spectroscopic study. *American Mineralogist*, 86(5-6):714–730, 2001.
- [321] An-Hui Lu, E emsp14L Salabas, and Ferdi Schüth. Magnetic nanoparticles: synthesis, protection, functionalization, and application. *Angewandte Chemie International Edition*, 46(8):1222–1244, 2007.
- [322] Srikanth Singamaneni, Valery N Bliznyuk, Christian Binek, and Evgeny Y Tsymbal. Magnetic nanoparticles: recent advances in synthesis, self-assembly and applications. *Journal of Materials Chemistry*, 21(42):16819–16845, 2011.
- [323] D Fiorani, AM Testa, F Lucari, F D’orazio, and H Romero. Magnetic properties of maghemite nanoparticle systems: surface anisotropy and interparticle interaction effects. *Physica B: Condensed Matter*, 320(1-4):122–126, 2002.
- [324] Bernard Dennis Cullity and Chad D Graham. *Introduction to magnetic materials*. John Wiley & Sons, 2011.
- [325] Ruslan Prozorov, Tanya Prozorov, Surya K Mallapragada, Balaji Narasimhan, Timothy J Williams, and Dennis A Bazylinski. Magnetic irreversibility and the Verwey transition in nanocrystalline bacterial magnetite. *Physical Review B*, 76(5):054406, 2007.
- [326] A Espinosa, A Serrano, A Llavona, J Jimenez de la Morena, M Abuin, A Figuerola, T Pellegrino, JF Fernández, M Garcia-Hernandez, GR Castro, et al. On the discrimination between magnetite and maghemite by xanes measurements in fluorescence mode. *Measurement Science and Technology*, 23(1):015602, 2011.
- [327] VAM Brabers, F Walz, and H Kronmüller. Impurity effects upon the Verwey transition in magnetite. *Physical Review B*, 58(21):14163, 1998.
- [328] Joaquín García and Gloria Subías. The Verwey transition—a new perspective. *Journal of Physics: Condensed Matter*, 16(7):R145, 2004.

- [329] Håkon Fischer, Giovanni Mastrogiacomo, Jörg F Löffler, Rolf J Warthmann, Peter G Weidler, and Andreas U Gehring. Ferromagnetic resonance and magnetic characteristics of intact magnetosome chains in *Magnetospirillum gryphiswaldense*. *Earth and Planetary Science Letters*, 270(3-4):200–208, 2008.
- [330] H Kronmüller and F Walz. Magnetic after-effects in Fe_3O_4 and vacancy-doped magnetite. *Philosophical Magazine B*, 42(3):433–452, 1980.
- [331] AR Muxworthy and E McClelland. Review of the low-temperature magnetic properties of magnetite from a rock magnetic perspective. *Geophysical Journal International*, 140(1):101–114, 2000.
- [332] Edmund Clifton Stoner and EP Wohlfarth. A mechanism of magnetic hysteresis in heterogeneous alloys. *Philosophical Transactions of the Royal Society of London. Series A, Mathematical and Physical Sciences*, 240(826):599–642, 1948.
- [333] David González-Alonso, Jesús González, Helena Gavilán, Jeppe Fock, Lunjie Zeng, Kerstin Witte, Philipp Bender, Luis Fernández Barquín, and Christer Johansson. Revealing a masked Verwey transition in nanoparticles of coexisting Fe-oxide phases. *RSC Advances*, 11(1):390–396, 2021.
- [334] Sayan Chandra, H Khurshid, Wanfeng Li, GC Hadjipanayis, MH Phan, and H Srikanth. Spin dynamics and criteria for onset of exchange bias in superspin glass $\text{Fe}/\gamma\text{-Fe}_2\text{O}_3$ core-shell nanoparticles. *Physical Review B*, 86(1):014426, 2012.
- [335] KL Lopez Maldonado, P De La Presa, E Flores Tavizón, JR Farias Mancilla, JA Matutes Aquino, Antonio Hernando Grande, and JT Elizalde Galindo. Magnetic susceptibility studies of the spin-glass and Verwey transitions in magnetite nanoparticles. *Journal of Applied Physics*, 113(17):17E132, 2013.
- [336] M Basini, S Sanna, T Orlando, L Bordonali, M Cobianchi, P Arosio, M Mariani, D Peddis, V Bonanni, R Mathieu, et al. Low-temperature anomalies in muon spin relaxation of solid and hollow $\gamma\text{-Fe}_2\text{O}_3$ nanoparticles: A pathway to detect unusual local spin dynamics. *Physical Review B*, 102(19):195424, 2020.
- [337] Russell W Millar. The heat capacities at low temperatures of “ferrous oxide,” magnetite and cuprous and cupric oxides. *Journal of the American Chemical Society*, 51(1):215–222, 1929.

- [338] Toshihiko Okamura. Transformation of magnetite at a low temperature. *Scientific Reports of the Research Institutes of Tohoku University*, 21:231, 1932.
- [339] Javier Blasco, Joaquín García, and Gloria Subías. Structural transformation in magnetite below the Verwey transition. *Physical Review B*, 83(10):104105, 2011.
- [340] Z Švindrych, Z Jan, A Kozłowski, and Jurgen M Honig. Low-temperature magnetic anomaly in magnetite. *Physical Review B*, 86(21):214406, 2012.
- [341] D Vollath, DV Szabo, RD Taylor, and JO Willis. Synthesis and magnetic properties of nanostructured maghemite. *Journal of materials research*, 12(8):2175–2182, 1997.
- [342] Andreu Cabot, A Paul Alivisatos, Víctor F Puentes, Lluís Balcells, Óscar Iglesias, and Amílcar Labarta. Magnetic domains and surface effects in hollow maghemite nanoparticles. *Physical Review B*, 79(9):094419, 2009.
- [343] S Mo, F Bo, Peter Vang Hendriksen, Søren Linderøth, et al. Spin-glass-like ordering of the magnetic moments of interacting nanosized maghemite particles. *Physical Review B*, 52(1):287, 1995.
- [344] Elizabeth M Jefremovas, Lucía Gandarias, Irati Rodrigo, Lourdes Marcano, Cordula Grüttner, José Ángel García, Eneko Garayo, Iñaki Orue, Ana García-Prieto, Alicia Muela, et al. Nanoflowers versus Magnetosomes: Comparison between two promising candidates for magnetic hyperthermia therapy. *IEEE Access*, 9:99552–99561, 2021.
- [345] Irati Rodrigo Arrizabalaga. *High field, high frequency and temperature adjustable AC magnetometer for magnetic hyperthermia characterization*. PhD thesis, Universidad del País Vasco UPV/EHU, 2020.
- [346] RR Wildeboer, P Southern, and QA Pankhurst. On the reliable measurement of specific absorption rates and intrinsic loss parameters in magnetic hyperthermia materials. *Journal of Physics D: Applied Physics*, 47(49):495003, 2014.
- [347] Shu-Yi Wang, Shujuan Huang, and Diana-Andra Borca-Tasciuc. Potential sources of errors in measuring and evaluating the specific loss power of magnetic nanoparticles in an alternating magnetic field. *IEEE Transactions on magnetics*, 49(1):255–262, 2012.

- [348] David Cabrera, Annelies Coene, Jonathan Leliaert, Emilio J Artés-Ibáñez, Luc Dupré, Neil D Telling, and Francisco J Teran. Dynamical magnetic response of iron oxide nanoparticles inside live cells. *ACS nano*, 12(3):2741–2752, 2018.
- [349] SK Shaw, J Kailashiya, A Gangwar, SK Alla, Santosh K Gupta, CL Prajapat, Sher Singh Meena, D Dash, P Maiti, and NK Prasad. γ -Fe₂O₃ nanoflowers as efficient magnetic hyperthermia and photothermal agent. *Applied Surface Science*, 560:150025, 2021.
- [350] David Gandia, Lucía Gandarias, Irati Rodrigo, Joshua Robles-García, Raja Das, Eneko Garaio, José Ángel García, Manh-Huong Phan, Hariharan Srikanth, Iñaki Orue, et al. Unlocking the potential of magnetotactic bacteria as magnetic hyperthermia agents. *Small*, 15(41):1902626, 2019.
- [351] B Mehdaoui, RP Tan, A Meffre, J Carrey, S Lachaize, B Chaudret, and M Respaud. Increase of magnetic hyperthermia efficiency due to dipolar interactions in low-anisotropy magnetic nanoparticles: Theoretical and experimental results. *Physical Review B*, 87(17):174419, 2013.
- [352] NA Usov and B Ya Liubimov. Dynamics of magnetic nanoparticle in a viscous liquid: Application to magnetic nanoparticle hyperthermia. *Journal of Applied Physics*, 112(2):023901, 2012.
- [353] Ivan Conde-Leboran, Daniel Baldomir, Carlos Martinez-Boubeta, Oksana Chubykalo-Fesenko, María del Puerto Morales, Gorka Salas, David Cabrera, Julio Camarero, Francisco J Teran, and David Serantes. A single picture explains diversity of hyperthermia response of magnetic nanoparticles. *The Journal of Physical Chemistry C*, 119(27):15698–15706, 2015.
- [354] Alicia Muela, David Muñoz, Rosa Martín-Rodríguez, Iñaki Orue, Eneko Garaio, Ana Abad Diaz de Cerio, Javier Alonso, Jose Angel García, and M Luisa Fdez-Gubieda. Optimal parameters for hyperthermia treatment using biomineralized magnetite nanoparticles: theoretical and experimental approach. *The Journal of Physical Chemistry C*, 120(42):24437–24448, 2016.
- [355] Idoia Castellanos-Rubio, Irati Rodrigo, Rahul Munshi, Oihane Arriortua, José S Garitaonandia, Ana Martínez-Amesti, Fernando Plazaola, Iñaki Orue, Arnd Pralle, and Maite Insausti. Outstanding heat loss via nano–octahedra above 20 nm in size: from wustite–rich nanoparticles to magnetite single–crystals. *Nanoscale*, 11(35):16635–16649, 2019.

- [356] William J Atkinson, Ivan A Brezovich, and Dev P Chakraborty. Usable frequencies in hyperthermia with thermal seeds. *IEEE Transactions on Biomedical Engineering*, (1):70–75, 1984.
- [357] Ivan A Brezovich. Low frequency hyperthermia: capacitive and ferromagnetic thermoseed methods. *Med. Phys. Monogr*, 16:82–111, 1988.
- [358] Rudolf Hergt, Silvio Dutz, and Matthias Zeisberger. Validity limits of the Néel relaxation model of magnetic nanoparticles for hyperthermia. *Nanotechnology*, 21(1):015706, 2009.
- [359] C Suryanarayana, E Ivanov, and VV Boldyrev. The science and technology of mechanical alloying. *Materials Science and Engineering: A*, 304:151–158, 2001.
- [360] IW Modder, H Bakker, and GF Zhou. Defects and magnetism in cubic GdX_2 laves phase compounds. *Physica B: Condensed Matter*, 262(1-2):141–158, 1999.
- [361] C Tannous and J Gieraltowski. The Stoner–Wohlfarth model of ferromagnetism. *European journal of physics*, 29(3):475, 2008.
- [362] Marcos F de Campos, Fernanda A Sampaio da Silva, Elio A Perigo, and José A de Castro. Stoner–Wohlfarth model for the anisotropic case. *Journal of Magnetism and Magnetic Materials*, 345:147–152, 2013.
- [363] David Gandia, Lucía Gandarias, Lourdes Marcano, Iñaki Orue, David Gil-Cartón, Javier Alonso, Alfredo García-Arribas, Alicia Muela, and M^a Luisa Fdez-Gubieda. Elucidating the role of shape anisotropy in faceted magnetic nanoparticles using biogenic magnetosomes as a model. *Nanoscale*, 12(30):16081–16090, 2020.
- [364] Julian Carrey, Boubker Mehdaoui, and Marc Respaud. Simple models for dynamic hysteresis loop calculations of magnetic single-domain nanoparticles: Application to magnetic hyperthermia optimization. *Journal of Applied Physics*, 109(8):083921, 2011.

